Cardiff University
School Of Chemistry

Design, Synthesis And Application Of Luminescent Rhenium Complexes In Cell Imaging

Thesis submitted for the degree of Doctor of Philosophy

by:

Vanesa Fernández Moreira

Supervisors: Dr. M. P. Coogan
Dr. A. J. Amoroso

July, 2008

ProQuest LLC
789 East Eisenhower Parkway
P.O. Box 1346
Ann Arbor, MI 48106-1346

DECLARATION

This work has not previously been accepted in substance for any degree and is not concurrently submitted in candidature for any degree.

Signed.................................. (candidate) Date....01/05/08.....

STATEMENT 1

This thesis is being submitted in partial fulfilment of the requirements for the degree of Doctor of Philosophy.

Signed.................................. (candidate) Date....01/05/08.....

STATEMENT 2

This thesis is the result of my own independent work/investigation, except where otherwise stated. Other sources are acknowledged by explicit references.

Signed.................................. (candidate) Date....01/05/08.....

STATEMENT 3

I hereby give consent for my thesis, if accepted, to be available for photocopying and for interlibrary loan, and for the title and summary to be made available to outside organisations.

Signed.................................. (candidate) Date....01/05/08.....

Acknowledgements

First of all I would like to thank my supervisors Dr. Michael. P. Coogan and Dr. Angelo. J. Amoroso for their unconditional support and help throughout these three and a half years, which has made possible to accomplish this work.

I am also grateful to Dr. Simon J. A. Pope for his luminescence tutorials and advices, and especially to Dr. Sarah Oakley for her help in the lab and during my writing up, correcting my *Spanglish*.

Especial acknowledgment goes to Prof. David Lloyd and Coralie Millet who have put the icing on the cake with their amazing cell-image work.

Not to forget everybody in lab 1.86 who have made enjoyable not only the working hours, but also Friday evenings and weekends: Leni, Txell, Richard, Soraya, Stephane, Damian and to my babies, the B.Sc. students, Jenny, Craig, Jack and Jenny-2 for their contributions to this thesis, many thanks guys.

I also thank Grazia and Lino who had share with me *from the beginning* the incredible experience of living abroad, for all those chats, weekend-meals, and relaxing shopping strolls.

I would like to extend my grateful thanks to all those people who have accepted me as one more of the group and made my time in Cardiff unforgettable: Caterina, Debs, Eugene, Frenchie, Dave, Eli, Paula and also to those who have joined the gang later Dirk, Vince, Anabel, Vero, Niek...it has been a pleasure to meet you all!!!

My kindest gratitude goes to Manuel who has always encouraged and supported me and without whom I do not know if I would ever have made it.

Finally, I would like to thank my family, especially my parents for their help and understanding through all these years, and to whom I dedicate this thesis.

Abstract

This thesis describes the development of a new variety of lumophores, in particular luminescent rhenium(I) complexes of the type $[Re(bisim)(CO)_3L]^{n+}$, where bisim represents a bisimine derivative, *e.g.* bipyridine, and L is a pyridine derivative (n = 1) or a chloride (n = 0), suitable for specific cell imaging and whose modified photophysical properties overcome some of the problems associated with traditional imaging agents (small Stokes shift, short lifetimes, *etc*).

Specifically the successful synthesis and photophysical studies of a chemical model to validate the concept of a membrane permeable cell-imaging device, *fac*-$[Re(bipy)(CO)_3(PyCH_2COO(CH_2)_3OTBD)]^+$, are presented. Further investigations towards and improved cell imaging agent, considering different issues like water solubility, lipophilicity and cell encapsulation rate, are then undertaken. Consequently, a new range of water soluble rhenium complexes, *fac*-$[Re(bisim)(CO)_3(L)]^{n-}$ where bisim is a water soluble bathophenanthroline and L is a pyridine derivative (n = 2) or a chloride (n = 1), as well as a variety of novel *fac*-$[Re(bisim)(CO)_3Cl]$ complexes, where bisim is a terpyridine derivative bearing a *self destruction device* which can be triggered by nitroreductase, are also presented. Additionally, the synthesis and structural description of a trinuclear rhenium complex is reported, along with a discussion of its use in inclusion experiments and attempts at analogue formation.

The design and synthesis of a thiol selective luminescent rhenium complex, *fac*-$[Re(bipy)(CO)_3(PyCH_2Cl)]^+$, is described, along with the demonstration of its thiol selectivity both *in vitro* and *in vivo* as demonstrated by specific mitochondrial localization. Finally, studies of membrane permeability in liposome models, cellular uptake and localization in different cells such as *Spironucleous vortens*, yeast cells and human breast cancer cells of a variety of rhenium complexes above cited are also reported.

These results combine to demonstrate the promising future of this new class of imaging probes as specific cell imaging agents and therefore, this work represents the initial step in the growing area of the development of transition metal based imaging agents.

Abbreviations

Å	Angstroms
Ar	Aryl
Atm	Atmosphere
bs	Broad singlet
bd	Broad doublet
bt	Broad triplet
Bu	Butyl
bipy	Bipyridine
ca	*Circa*
cm	Centimetre
d	Doublet
δ	Chemical shift (in ppm)
DCE	1,2-Dichloroethane
DCM	Dichloromethane
dd	Doublet of doublets
dfppy	2-(2,4-difluorophenyl)pyridine
DME	Dimethoxyethane
DMF	N,N'-Dimethylformamide
DMSO	Dimethylsulphoxide
DNS-Cl	Dansyl chloride
ddpz	dipyrido[3,2-a:2',3'-c]-phenazine
EB	Ethidium bromide
Ed(s)	Editor(s)
ed	Edition
e.g.	*Exempli gratia* (for example)
Eq	Equivalent
ES-MS	Electrospray mass spectrometry
et al.	*Et alii* (and others)
FITC	Fluorescein-5-isothiocyanate
FRET	Fluorescence-resonance energy transfer
g	Gramme

h	Hour
HOMO	Highest occupied molecular orbital
HRMS	High resolution mass spectrometry
HSA	Human serum albumin
hν	Irradiation with light
Hz	Hertz
IAF	5-iodoacetamidofluorescein
i-Pr	*Iso*-propyl
IR	Infrared spectroscopy
L	Ligand
LUMO	Lowest unoccupied molecular orbital
m	Multiplet
m	*Meta*
MLC	Metal-ligand complex
MLCT	Metal-ligand charge transfer (state)
m.p.	Melting point
Me	Methyl
mg	Milligram
MHz	Megahertz
min	Minute
ml	Millilitre
mmol	Millimoles
ν	Wavenumber
NIR	Near infrared
nm	Nanometre
NMR	Nuclear magnetic resonance
o	Ortho
ORTEP	Oak-Ridge thermal ellipsoid plot
°C	Degrees Celsius
p	Para
p	Pentuplet
PET	Photoinduced electron transfer
Ph	Phenyl

ppm	Parts per million
p-TsOH	*Para*-toluensulphonic acid
p-TsCl	*Para*-toluensulphonyl chloride
Phen	phenanthroline
py	Pyridine
q	Quartet
QDs	Quantum dots
quint	Quintuplet
R	Alkyl or aryl
rbf	Round bottom flask
ref	Reference
rt	Room temperature
s	Singlet
t	Triplet
t-Bu	*Tert*-butyl
TBAF	Tetrabutylammonium fluoride
TBDCl	*Tert*-butyldimethylchloride
THF	Tetrahydrofuran
TLC	Thin layer chromatography
TRITC	Tetramethylrhodamine-5-(and-6)isothiocyanate
Ts	Tosyl (*p*-toluenesulfonyl)
UV	Ultraviolet
YFP	Yellow fluorescent protein

Index

Chapter 1: Introduction to ^{3}MLCT Complexes as Biological Imaging Agents.

Chapter 2: Synthetic Studies Directed Towards A Luminescent Rhenium(I) Complex For Specific Cell Imaging.

Chapter 3: Structural Modifications Directed Towards Improved Modulation Of Emission, Rate Of Cyclisation And Tuning Solubility In Re(I) Complexes.

Chapter 5: Electrochemistry, Membrane Permeability and Confocal Fluorescence Microscopy Studies.

Chapter 1

Introduction to ^{3}MLCT Complexes as Biological Imaging Agents.

1.1 Introduction.

Optimum detection of individual biomolecules, cell components and other biological entities, as well as the proper distribution and targeting of drugs, is becoming one of the most important issues in medicine. Traditionally, organic dyes such as Malachite green, Fluorescein, Rhodamine, *etc.* have been used to visualize biological tissue or cell organelles.[1] Recently, however, the demand for more precise information about biological processes and the biodistribution of drugs or biomolecules, in addition to the technological advances of the last decade, have led to the development of a new range of biological luminescent probes including quantum dots (QDots) and transition metal and lanthanide complexes. In particular, transition metal complexes as light-emitting markers have exceptional characteristics as lumophores.[2] Not only do they offer obvious advantages over the traditional dyes, but also over quantum dots and lanthanide complexes as they can be used in a new range of experiments, *i.e.* anisotropy measurement.

1.1.1 Organic dyes: Simple colour staining and fluorescence techniques.

In the early nineteenth century there was an interest in the development of organic dyes for biological and microscopy applications as some of these dyes allowed specific staining of biological tissues and showed a preference for particular inner cell organelles.[3] These pioneering dyes include Malachite green, Sudan black, Coomassire blue and also Hematoxylin, which is an organic dye whose affinity for negatively charged molecules reveals the distribution of DNA, RNA and acidic proteins in the cell **Figure 1.1.** However, achieving an adequate level of sensitivity that enabled selective staining in order to reveal the localisation of specific proteins or macromolecules within the cell, as well as to overcome interference from other coloured materials, was difficult.

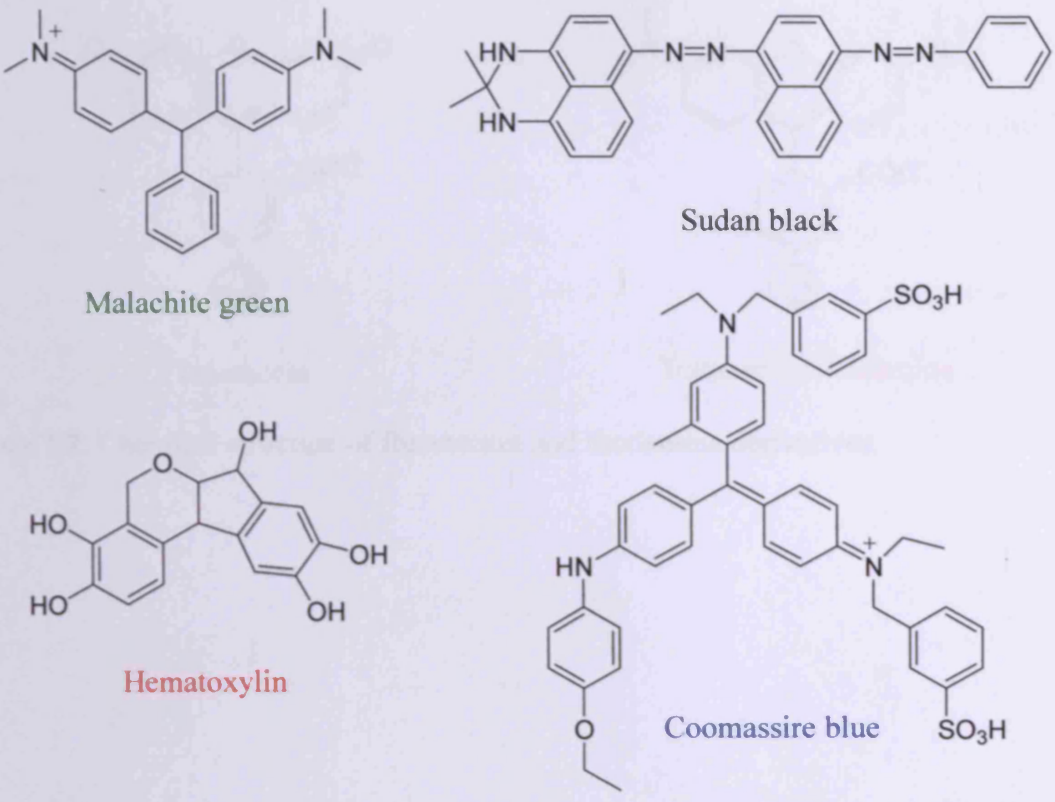

Figure 1.1. The chemical structures of Malachite green, Sudan black, Hematoxylin and Coomassire blue.

An alternative method that overcomes these drawbacks was pioneered with the use of fluorescent dyes, revolutionising the biological imaging field. Two fluorescent dyes commonly used for biological applications are fluorescein, which emits an intense green fluorescence when excited with blue light, and rhodamine, which emits a deep red when excited with green-yellow light (see **Figure 1.2.**). The coupling of an antibody[a] to either of the fluorescent dyes allows visualization of, for example, the biodistribution of an antibody's target or monitoring changes in concentration and location of the target inside living cells.

---

[a] Which often binds extremely strongly to a specific target foreign molecule or cell, thereby inactivating it or marking it for destruction.

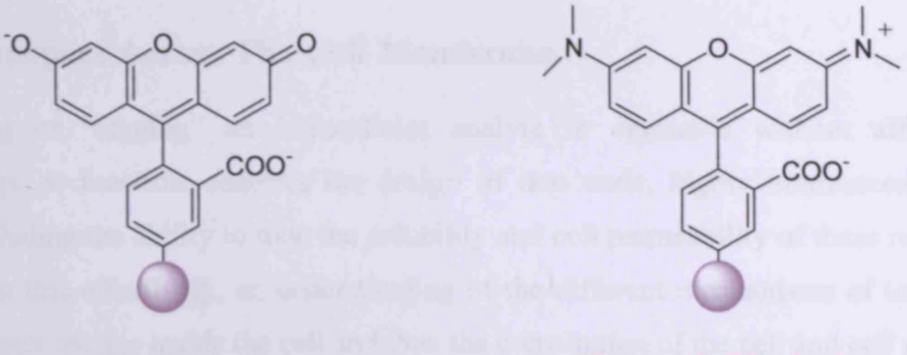

Fluorescein Tetramethylrhodamine

Figure 1.2. Chemical structure of fluorescein and rhodamine derivatives.

1.2 Transport Across The Cell Membrane.

Monitoring or "tagging" an intracellular analyte or organelle without affecting its morphology or function, requires the design of non toxic, highly luminescent contrast agents including the ability to tune the solubility and cell permeability of these reagents. In order to do this effectively, an understanding of the different mechanisms of transporting an exogenous species inside the cell and thus the constitution of the cell and cell membrane is necessary. **Figure 1.3** depicts a schematic of a typical animal cell.

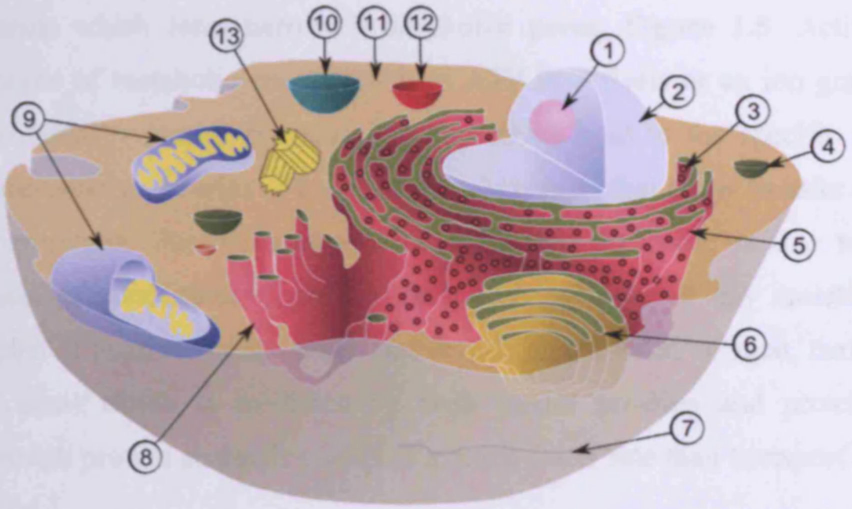

Within the cytoplasm, the major organelles and cellular structures include (1) nucleolus (2) nucleus (3) ribosome (4) vesicle (5) rough endoplasmic reticulum (6) Golgi apparatus (7) cytoskeleton (8) smooth endoplasmic reticulum (9) mitochondria (10) vacuole (11) cytosol (12) lysosome and (13) centriole.

Figure 1. 3. Schematic drawing of a typical animal cell. (Reproduced with permission of, and Copyright ©, 2000, 2001, 2002 Free Software Foundation)

The cell membrane is a lipid bilayer mainly constituted of phospholipids, amphiphilic entities with a hydrocarbon tail and a polar head, and, to a smaller extent, cholesterol and membrane proteins, known as transmembrane proteins. The cell membranes are dynamic fluid structures which are crucial for many membrane functions, such as transport processes and enzymatic activity. See **Figure 1.4**.

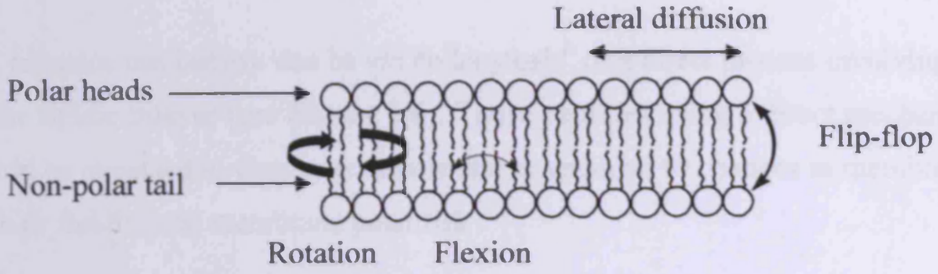

Figure 1.4. The types of movement possible for phospholipid molecules in a lipid bilayer.

Transmembrane proteins are responsible for transferring solutes such as water, nutrients and waste into and out of the cell. They can be divided in two major classes; carrier proteins which have moving parts to shift specific molecules across the membrane and channel proteins which form narrow hydrophobic pores, **Figure 1.5**. Active transport requires a source of metabolic energy, such as ATP hydrolysis or an ion gradient and is generally mediated by carrier proteins. These proteins bind to the specific solute to be transported and undergo a series of conformational changes that allow transfer of the solute across the membrane. Passive transport, or facilitated diffusion, is due to a positive electrochemical or concentration gradient and does not involve any metabolic energy. Some examples of passive transport are simple diffusion (water, oxygen, carbon dioxide, ethanol and urea) which is mediated by both carrier proteins and protein channels. Transport through protein channels occurs at a much faster rate than transport mediated by carrier proteins.

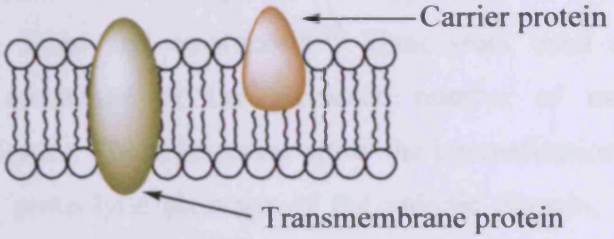

Figure 1.5 Schematic drawings showing two-dimensional view of a cell membrane.

In addition, short peptide sequences are known to cross the plasma membrane, *e.g.* Tat-peptide,[4] or polyarginines. These peptide sequences are used to transport diverse substrates such as polymers,[5] nanoparticles,[6] DNA[7] and liposomes[8] across the cell membrane. The cell entrance mechanism can be *via* endocytosis[b] or a direct process involving translocation of the lipidic bilayer (see **Figure 1.6**). Those peptides using a direct mechanism of uptake would be expected to display transport that is sensitive to changes in membrane properties, such as fluidity and membrane potential.

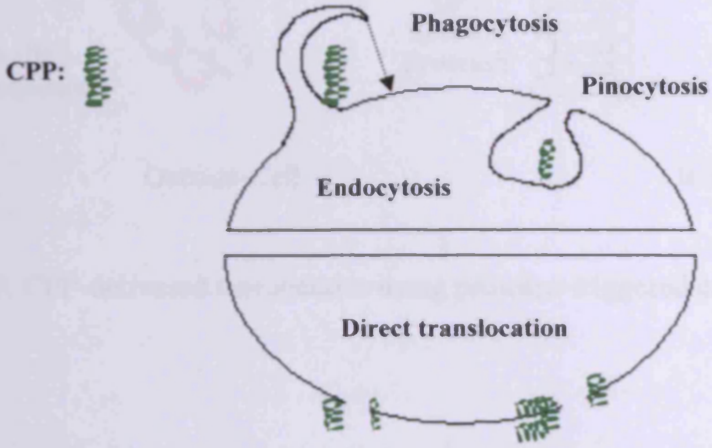

Figure 1.6. Schematic representation of entrance mechanism of cell membrane.

Later investigations reveal that the route of entry of a cell *via* a penetrating peptide (CPP) can be dependent on the identity of the attached cargo[9] (*e.g.* drug, fluorophore, nanoparticle, protein *etc.*) and on the cell type.[10] CPPs have been proven to be effective at increasing the efficacy of several therapeutics by improving cellular uptake and also their use as molecular vehicles offers several advantages such as lower toxicity and more controlled administration.[11] An example of the application of CPPs for imaging was recently reported by Tsien and co-workers.[12] Their work used a fluorescein-peptide hairpin[c] that takes advantage of the increased number of extracellular proteases surrounding tumour tissues. These proteases allow the internalization of the cargo, *i.e.* the imaging agent, upon proteolytic cleavage of the anionic domain, *i.e.* the impermeable domain. Thus the imaging marker is taken up specifically by the cancer cells. (See **Figure 1.7**).

---

[b] Endocytosis, includes phagocytosis and pinocytosis, where the difference is that in the first one there is a enlargement of the cell membrane (pseudopods) that surround the external agent, whereas in the second type vesicles of fluid are formed in the cell membrane (no pseudopods).

[c] It is the simplest protein motif involving two beta strands that aligns with itself to form a needle like structure

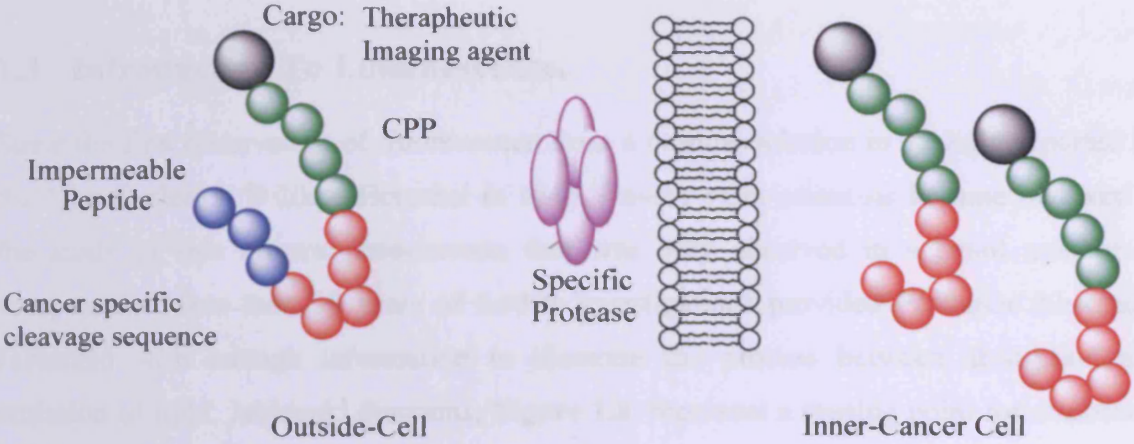

Figure 1.7. CPP-delivered therapeutics using protease-triggered cellular uptake.

1.3 Introduction To Luminescence.

Since the first observation of fluorescence from a quinine solution in sunlight reported by Sir John Frederick William Herschel in 1845,[13] many other scientists became involved in the study of this bizarre phenomenon that was only observed in a small number of compounds. More than 50 years of further investigations provided Professor Alexander Jablonski with enough information to illustrate the process between absorption and emission of light. Jablonski diagrams, **Figure 1.8**, represent a starting point for discussing the process of luminescence.

Luminescence can be divided into fluorescence and phosphorescence, distinguished by the excited state from which the emission of light comes: from the singlet excited state for fluorescence and the triplet excited state for phosphorescence. In both cases, once the molecule is irradiated there is an electronic transition from the ground state (S_0) to the excited states (S_1) and (S_2); the time that it takes is extremely brief, in the order of femtoseconds. The molecule can then release the energy through different pathways – radiation-less (vibrational relaxation, internal conversion and intersystem crossing) and emission of light (fluorescence and phosphorescence). The emission of light typically takes place from the lowest vibrational level of S_1 or T_1 to any of the ground state vibrational levels after removal of excess of energy by vibrational relaxation, internal conversion or/and intersystem crossing.

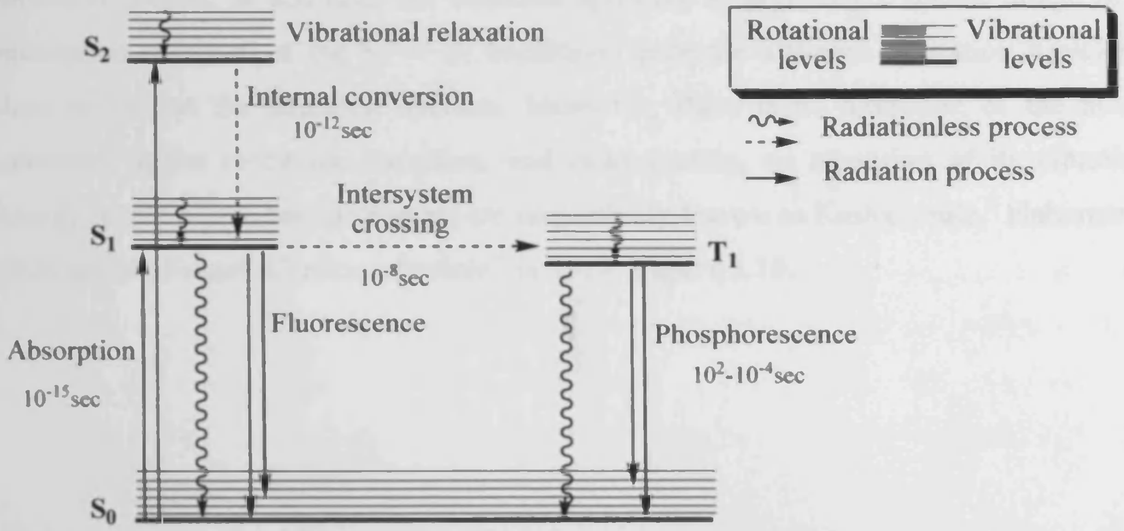

Figure 1.8. Jablonski diagram.

An interesting consequence of the energy pathways involved is that the emitted light has a longer wavelength than that absorbed, first observed in 1852 by Sir George Gabriel Stokes[14] at the University of Cambridge after performing an incredibly simple experiment, **Figure 1.9**. The experiment did not need any electronic equipment, only the intelligence of a scientist like Sir Stokes. The source of ultraviolet light was provided by the sun and was then filtered by a stained glass window which only transmitted light below 400 nm. This light was absorbed by the quinine solution and was then filtered again using yellow glass, in fact a glass of wine, which only transmits light above 400 nm. Quinine emission is near 450 nm and therefore easily visible.

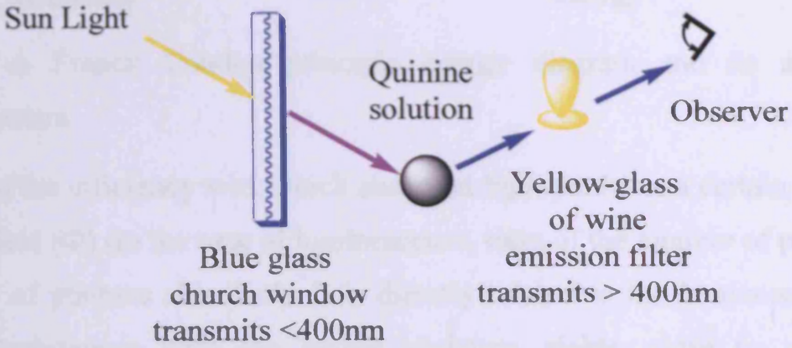

Figure 1.9. Experimental schematic for the detection of the Stokes shift.

As a result of this experiment, the Stokes shift, an intrinsic property of a luminescent substance, became an important concept in luminescent processes. It is defined as the difference, in wavelength or frequency units, between the maxima of the absorption and emission spectra. In addition, the emission spectrum is generally a mirror image of the absorption spectrum of the $S_0 \rightarrow S_1$ transition, since the different excitation wavelength does not affect the emission maxima. Moreover, there is no alteration of the nuclear geometry in the electronic transition, and consequently, no alteration of its vibrational energy levels. These two statements are respectively known as Kasha´s rule,[d] elaborated in 1926 and the Franck-Condon principle,[e] in 1927. **Figure 1.10.**

---

[d] Exceptions to this rule arise when there are large energy gaps between excited states, e.g. azulene.

[e] Named after James Franck and Edward Ulher Condon, a German physicist and an American nuclear physicist respectively.

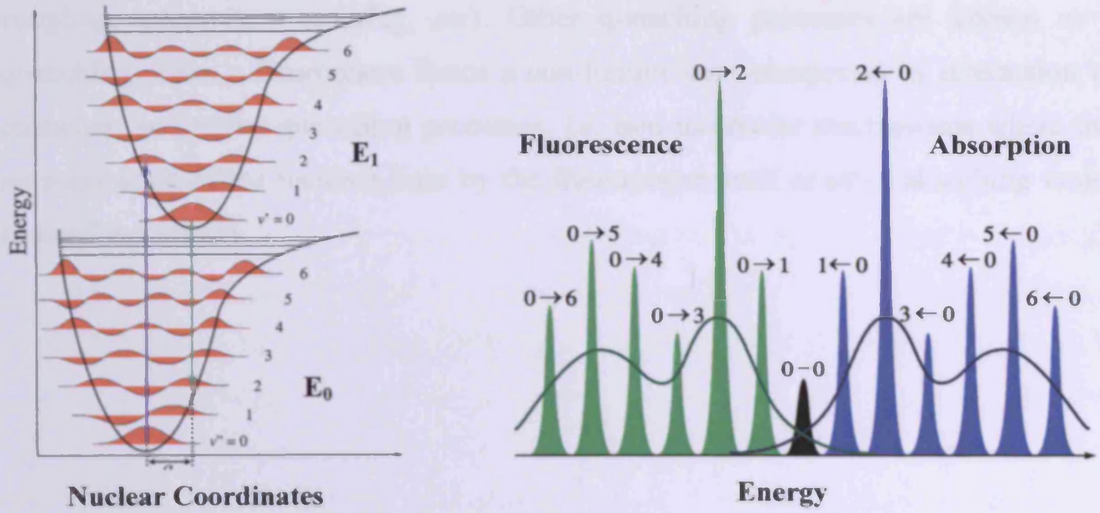

Figure 1.10. A Franck Condon principle energy diagram and its absorption and fluorescence spectra.

The measure of the efficiency with which absorbed light produces a certain effect is called the quantum yield (Φ) (in the case of luminescence, ratio of the number of photons emitted to the number of photons absorbed). It is directly related to the luminescence intensity, whereby the substances with the largest quantum yields, close to unity, such as rhodamines, display the brightest emission. Other essential features in a fluorophore[f] are the molar absorption coefficient (ε) and lifetime (τ). The molar absorption coefficient is an intrinsic characteristic of the fluorophore that indicates how strong the absorption is at a given wavelength.[g] The lifetime of a species is inversely proportional to the radioactive decay rate and can be defined as the average time that the molecule remains excited before yielding a photon and hence, it is the time available to interact with, or diffuse in its environment. These interactions affect the intensity of the emission spectra.

The particular case of a loss of luminescence is known as luminescence quenching which can occur by various mechanisms. The most common quenching process is due to the collision of the excited state of the fluorophore with certain other molecules, known as quenchers, releasing the excess energy in this way. A wide range of molecules can act as collisional quenchers, for example; oxygen, halogens, amines. The mechanism of quenching varies between the fluorophore-quencher pairs (*e.g.* electron transfer, spin-orbit

---

[f] Although the term fluorophore strictly includes only those molecules that display only fluorescence not phosphorescence, it is used in this work as a generic term for lumophore, as is common in fluorescence microscopy related work.

[g] Lambert-Beer law: $A = \varepsilon cl$, where A is the absorbance, c sample concentration and l path length.

coupling, intersystem crossing, *etc*). Other quenching processes are known as static quenching, when a fluorophore forms a non-luminescent compound by interaction with a quencher, and trivial quenching processes, *i.e.* non molecular mechanisms where there is an attenuation of the incident light by the fluorophore itself or other absorbing molecules (inner-filter effect).

1.4 Fluorophores.

The search for suitable fluorophores is one of the major issues in fluorescence spectroscopy and thus in biological imaging. Fluorophores can be divided broadly into two main classes, intrinsic and extrinsic, where the intrinsic fluorophores are those belonging to biological media and whose fluorescence occurs naturally (*e.g.* aromatic amino acids, NADPH, flavins, *etc*). Extrinsic fluorophores are those added to the studied sample in order to change its spectral properties. Nowadays there is a wide range of commercially available extrinsic fluorophores[15] that can be used to tag or label bio-molecules. Organic chromophores are incredibly abundant in contrast to lanthanide or transition metal compounds. Examples of commercial fluorophores used in protein labelling *via* a coupling reaction with amines or sulfhydryl in proteins are illustrated below, **Figure 1.11**.

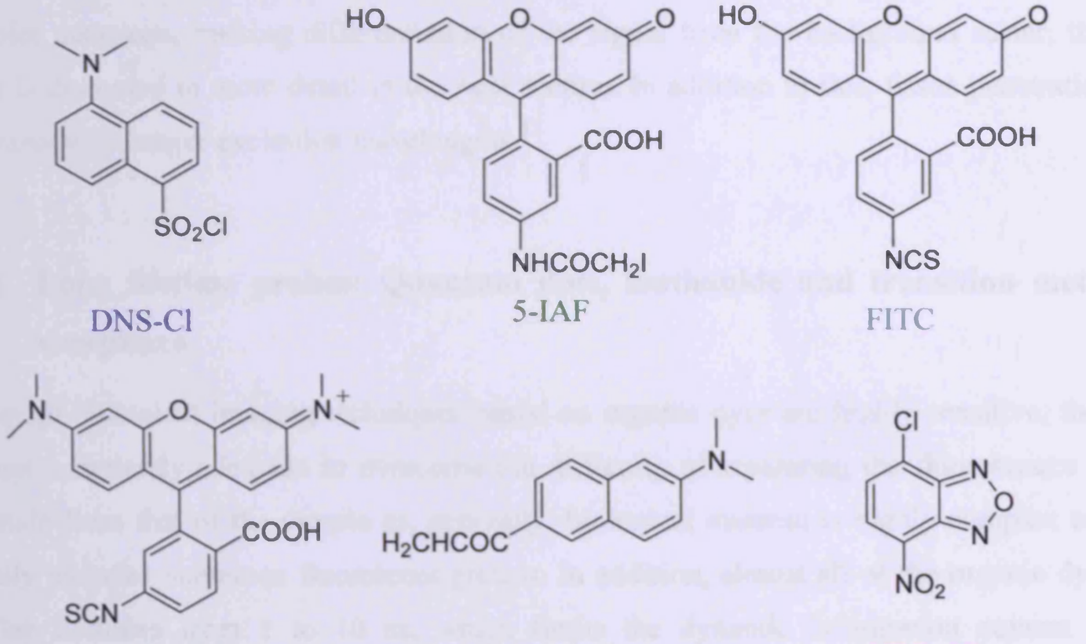

DNS-Cl 5-IAF FITC

TRITC Acrylodan NBD-Cl

Figure 1.11. Commercial organic fluorophores

To illustrate the photophysical properties of these extrinsic fluorophores, dansyl chloride (DNS-Cl), originally described by Weber,[16] will be discussed. It has excitation and emission maxima at 350 and 520 nm respectively and a lifetime of 10 ns. Unfortunately, not all the organic fluorophores display such a big Stokes shift, 170 nm, and long lifetime as this compound. Thus, this is the reason why there is currently an increase in interest in exploring the area of lanthanides and transition metal complexes as new extrinsic fluorophores.

Fluorophores with small Stokes shifts are likely to self-quench if, for example, they are being used to label proteins where various fluorophores are attached close to each other in the same protein. Therefore, energy transfer between these fluorophores can occur (Förster resonance energy transfer (FRET) may also be referred to as fluorescence resonance energy transfer), due to the small distance between the imaging probes, which have a high probability of being within the Förster distance.[h]

Photostability is another important characteristic that the extrinsic fluorophores should have to be used in biological imaging, and regrettably almost all existing organic fluorophores are photobleached[i] upon continuous illumination.

Long-wavelength probes are also an interesting area of investigation as the sensitivity of fluorescence detection is generally limited by autofluorescence[j] of biological samples. Therefore, as the excitation wavelength becomes longer, the autofluorescence of biological samples decreases, making differentiation of the signal from the background easier; this topic is discussed in more detail in the next section. In addition to this, tissue penetration increases with longer excitation wavelengths.[17]

1.4.1 Long lifetime probes: Quantum dots, lanthanide and transition metal complexes.

Although biological imaging techniques based on organic dyes are highly sensitive, they are not completely adequate to overcome the difficulty of separating the fluorescence of the stain from that of the sample as, generally, biological material is highly complex and usually includes numerous fluorescent groups. In addition, almost all of the organic dyes display lifetimes from 1 to 10 ns, which limits the dynamic information content of fluorescence, for example anisotropy measurements,[k] (see **Section 1.4.5**). Semi conductor nanoparticles (quantum dots) and lanthanide and transition metal complexes are taking advantage of the limitations of organic dyes and are becoming the subject of many recent studies in the field. These compounds show emission *via* phosphorescent processes,

---

[h] Donor-to-acceptor separation distance.

[i] The photochemical destruction of a fluorophore.

[j] Fluorescent of the intrinsic biological components (see **Chapter 5**).

[k] Measurement of protein denaturalization, protein association, internal viscosity of membranes, effect of lipid composition in the phase-transition temperature, *etc.*

providing emission bands well separated from the emission of organic moieties. Moreover, their photophysical properties (emission wavelength, excited state lifetime, quantum yield, *etc.*) can be tuned by changing the coordinated ligands (especially in transition metal complexes) or the chemical composition in the case of QDots. However, there are problems to overcome as many of the relevant metal ions are toxic. Therefore, not only is it desirable to synthesise kinetically stable complexes, but also to improve features such as solubility or cell permeability, especially when they are designed for biological purposes. The synthesis of the right ligand system is the key to achieving this objective.

1.4.2 Quantum dots (QDots).

QDots have shown their suitability as fluorescent biological labels since the first studies in 1988.[18] Their composition consists of a core, usually CdSe or CdS, and a shell, usually ZnS, to coat the core from the outside and hence confer the chemical and photostability needed. In addition, a polymer or a silica layer surrounding the shell modulates the solubility properties and a final coating with biocompatible molecules ensure its specific binding to biomolecules and hence its localization, see **Figure 1.12**.

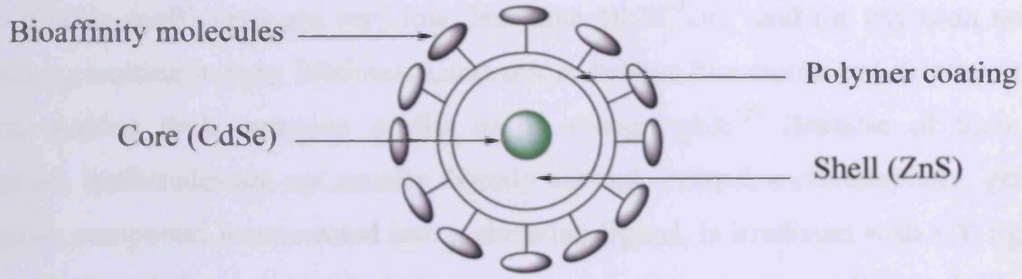

Figure 1.12. Schematic drawing of typical QDots.

Some spectral properties of QDots that make them useful for biological fluorescent probes are listed below:

i. Homogeneous sized QDots display emission spectra twofold narrower than conventional fluorophores.

ii. QDots do not exhibit a long-wavelength emission tail.

iii. Large extinction coefficients.

iv. High photostability.

v. Emission wavelength depends on the size and chemical composition.[19]

Examples of QDots being used as specific labels in live cells can be found in various reports, principally by Jaisawal[20] and Wargnier.[21]

1.4.3 Lanthanides.

The first interest in lanthanide complexes in biology was due to their similarity to calcium ions. Although they have a higher charge (Ln^{3+} vs. Ca^{2+}), their ionic radii confer a high affinity for Ca^{2+} sites in biological molecules, acting as either Ca^{2+} inhibitors or probes.[22] Currently, their luminescent properties have drawn attention to their potential for use in medical imaging as emitted light is the most convenient and sensitive medium to detect and image, and even single-molecule detection is often within reach.

Lanthanides, or 4*f* elements, are the series from lanthanum to lutetium, and have a trivalent charge in aqueous solution. The rare earth designation generally includes scandium and yttrium. Their characteristic decrease in atomic size and radius with increasing atomic number is known as the lanthanide contraction. In addition, the shielding of the 4*f* orbitals results in special spectroscopic properties such as lanthanide emissions resulting from transitions involving these 4*f* orbitals, which are forbidden by the Laporte rules.[1] Therefore, the absorption coefficients are very low, less than 10 $M^{-1}cm^{-1}$ and the emission rates are very slow, resulting in long lifetimes. Lanthanides behave like atoms and display line-like spectra, making their emission profile easily recognizable.[23] Because of their weak absorption, lanthanides are not usually directly excited, instead, a chromophore, generally an organic compound incorporated into a chelating ligand, is irradiated with UV light and then the lanthanide becomes excited *via* an energy transfer process, see **Figure 1.13**.

---

[1] Named after Otto Laporte, 1925. The electronic transitions conserving either symmetry or asymmetry with respect to an inversion center (*e.g.*, *g* (gerade) → *g*, or *u* (ungerade) → *u*) are forbidden i.e. transitions within a given set of *p* or *d* orbitals.

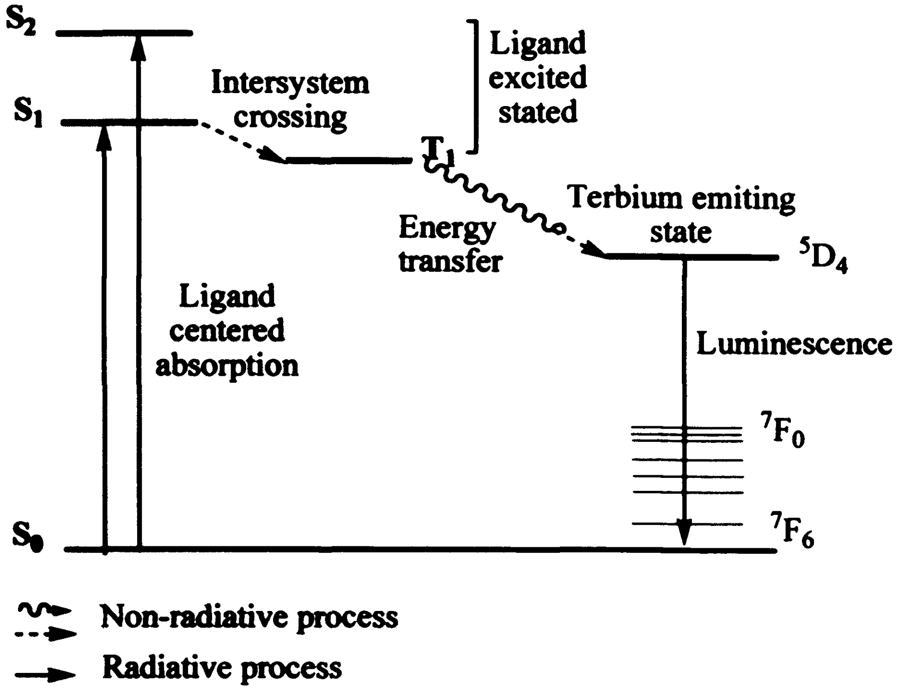

Figure 1.13. Jablonski diagram for terbium excitation.

However, there are also non-radiative paths that release energy and which must be minimized in order to increase the quantum yield of the process. Vibrational deactivation is one of the most efficient deactivation processes. It is temperature dependent and has a major impact when a donor atom involved in the vibration is directly attached to the metal ion. For instance, there is severe quenching of the luminescence of lanthanides via O-H interactions of the aqueous solution (*e.g.* biological media) with the metal centre and so the metal must be protected from the aqueous environment by encapsulation using a multidentate ligand. It is also important to have efficient sensitization of the lanthanide by matching the energy gap between the lowest triplet state of the ligand and the emissive state. Another deactivation process is energy back transfer, which is also avoided with a suitable energy level gap. Therefore the design of luminescent lanthanide complexes for biological imaging requires a broad knowledge of their intrinsic properties.[24] **(Figure 1.14)**

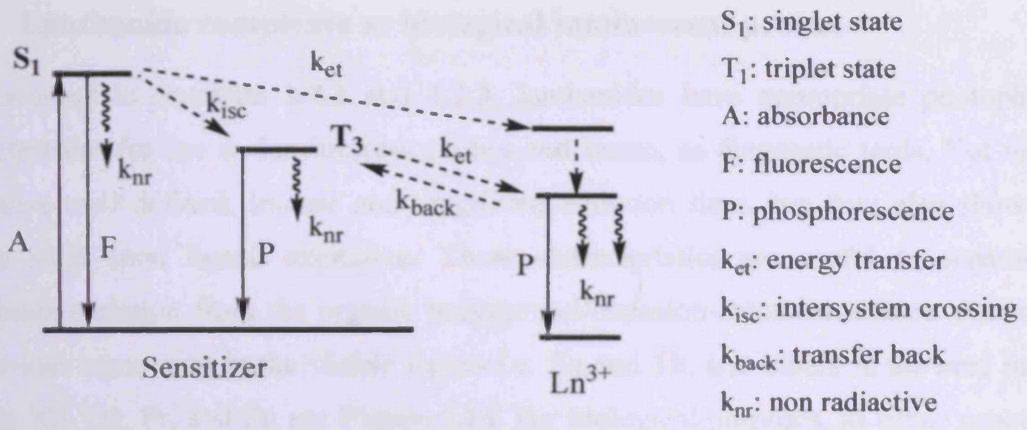

Figure 1.14. Radiative and non-radiative processes.

The coordination number of lanthanide complexes varies from 6 to 12, the preferred being 8 and 9. The major challenge for a chemist is ligand design in order to control the coordination sphere through the conformational restrictions of the ligand. Moreover, the ligand design must provide a strong metal-ligand interaction in order to have a high thermodynamic stability and kinetic inertness. In biological media, *i.e.* aqueous solutions, the stability of lanthanide complexes increases upon substitution of the bonded water molecules for a polydentate ligand due to the chelate effect. As the preorganization of the ligand increases this also raises its thermodynamic stability in the case of macrocyclic ligands due to the macrocyclic effect. Therefore, by encapsulating the metal in a complex scaffold, not only does the stability of the complex improve, but also the vibrational deactivation processes are avoided as water molecules from the environment are not able to reach the metal centre. Many different ligands have been used for this purpose; some examples are shown in **Figure 1.5.**

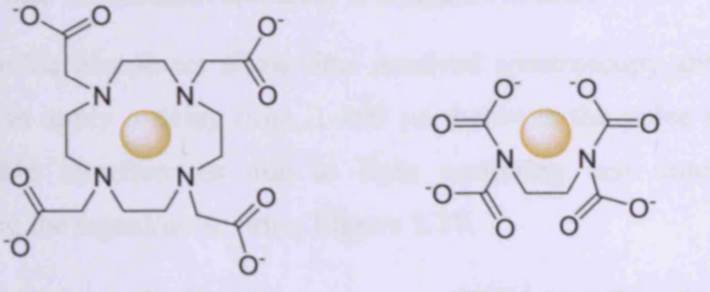

Macrocyclic ligands

EDTA type ligands

Figure 1.15. Types of suitable ligands for lanthanides.[25]

1.4.4 Lanthanide complexes as biological luminescent probes.

As discussed in **Sections 1.2.1** and **1.2.3**, lanthanides have appropriate photophysical characteristics for use as luminescent probes and hence, as diagnostic tools. Not only do they have well defined, intense and long-lived emission lines, but they also show large Stokes shift upon ligand excitation. These characteristics are useful to separate the lanthanide emission from the organic background-emission-autofluorescence. Among the lanthanides some emit in the visible region *i.e.* Eu and Tb, and others in the near infrared *i.e.* Yb, Nd, Dy, Pr, and Er, see **Figure 1.16**. For biological purposes, as tissue penetration by light increases with wavelength, near IR-emitting probes are ideal, although their lifetimes are shorter, in the order of microseconds (μs), than those that emit in the visible range, in the order of milliseconds (ms).

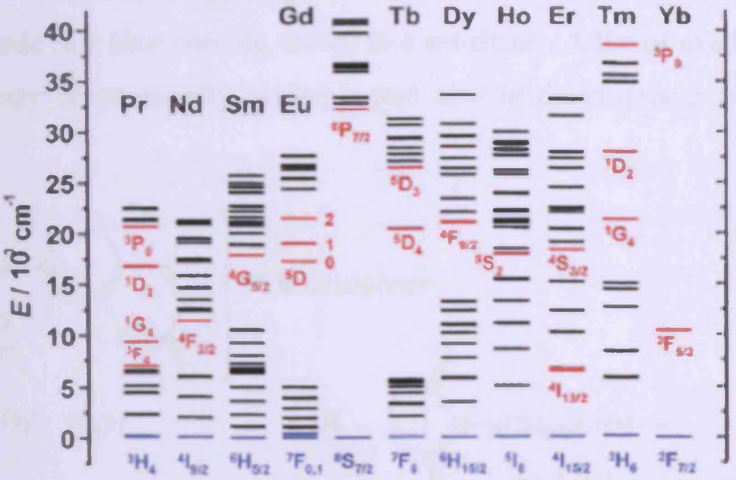

Figure 1.16. Partial energy diagrams for lanthanide aquo ions.[26] Main luminescent levels are drawn in red while the fundamental level is indicated in blue.

In addition, lanthanide complexes allow time resolved spectroscopy and microscopy, the basis of which is to apply a delay time, 1-100 μs, between the pulse and the detection, eliminating possible interferences due to light scattering and autofluorescence and therefore enhancing the signal/noise ratio, **Figure 1.17**.

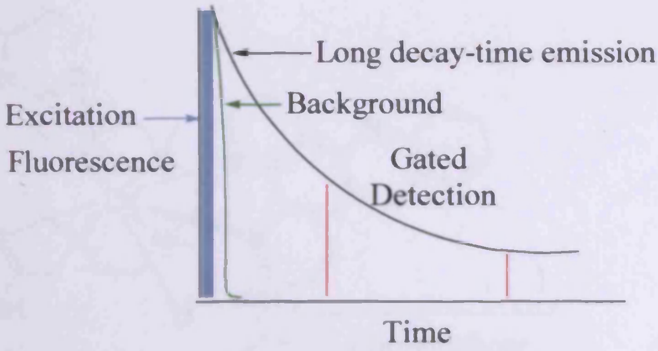

Figure 1.17. Principle of time resolved techniques.

All the different examples of lanthanide complexes for biological imaging applications found in the literature follow the same general structure. The lanthanide ion is isolated from the media by a chelator, *i.e.* a scaffold, whose function is not only to increase the quantum yield of the unit by displacing the water molecules, but also to provide a means to bind the lanthanide to a biomolecule and/or to a sensitizer. A list of examples of lanthanide complexes already commercially available and also in development is shown in **Figure 1.18** and **1.19**

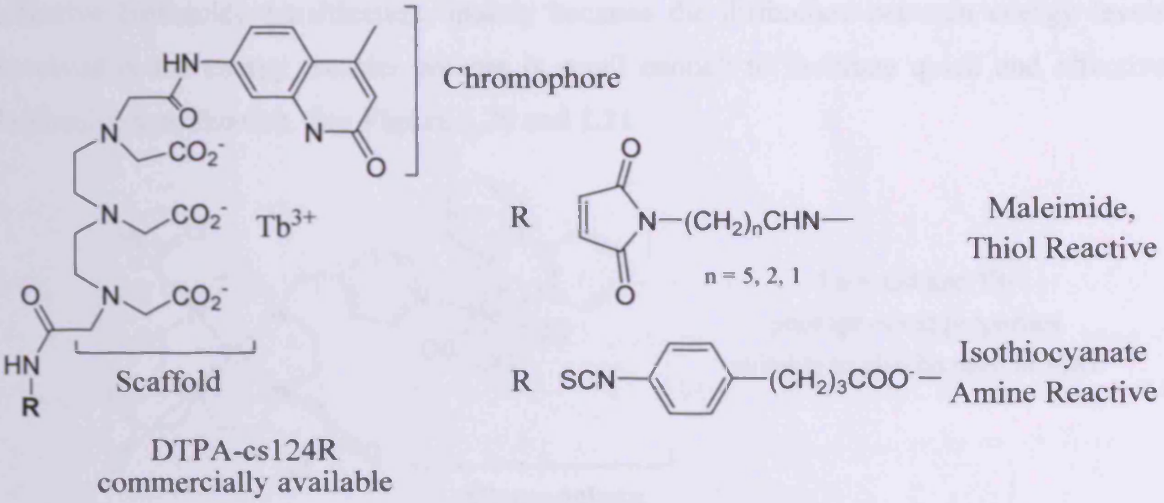

Figure 1.18. Chemical structure of DTPA-cs124R.[27]

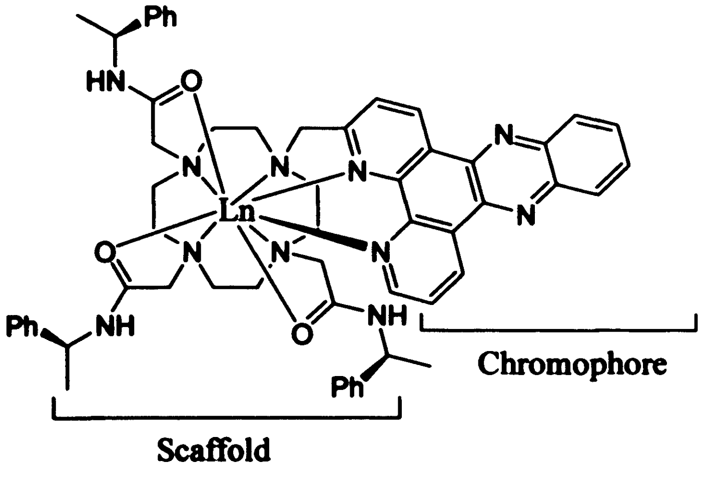

Ln: Eu, Gd, Tb

Ln = Tb used in cell
Mouse skin fibroblasts
(NIH-3T3 cells).

Localization in the cell
nucleus and defining the
nuclear cell membrane

Figure 1.19. Lanthanide complex whose antenna is an organic chromophore designed by Parker *et al.*[28]

There are now also examples of transition metals acting as chromophores in these systems. They offer the advantage over organic molecules of larger absorption maxima and more effective lanthanide sensitization, mainly because the difference between energy levels involved in the energy transfer process is small enough to facilitate quick and effective lanthanide sensitization. See **Figure 1.20** and **1.21**.

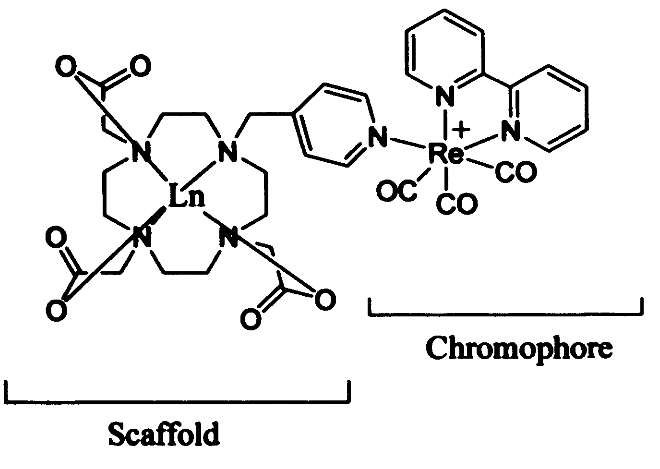

Ln: Gd, Tb

Ln = Gd and Yb
photophysical properties
suitable to also be used in MRI

Figure 1.20. Lanthanide complex whose antenna is a transition metal complex designed by Faulkner *et al.*[29]

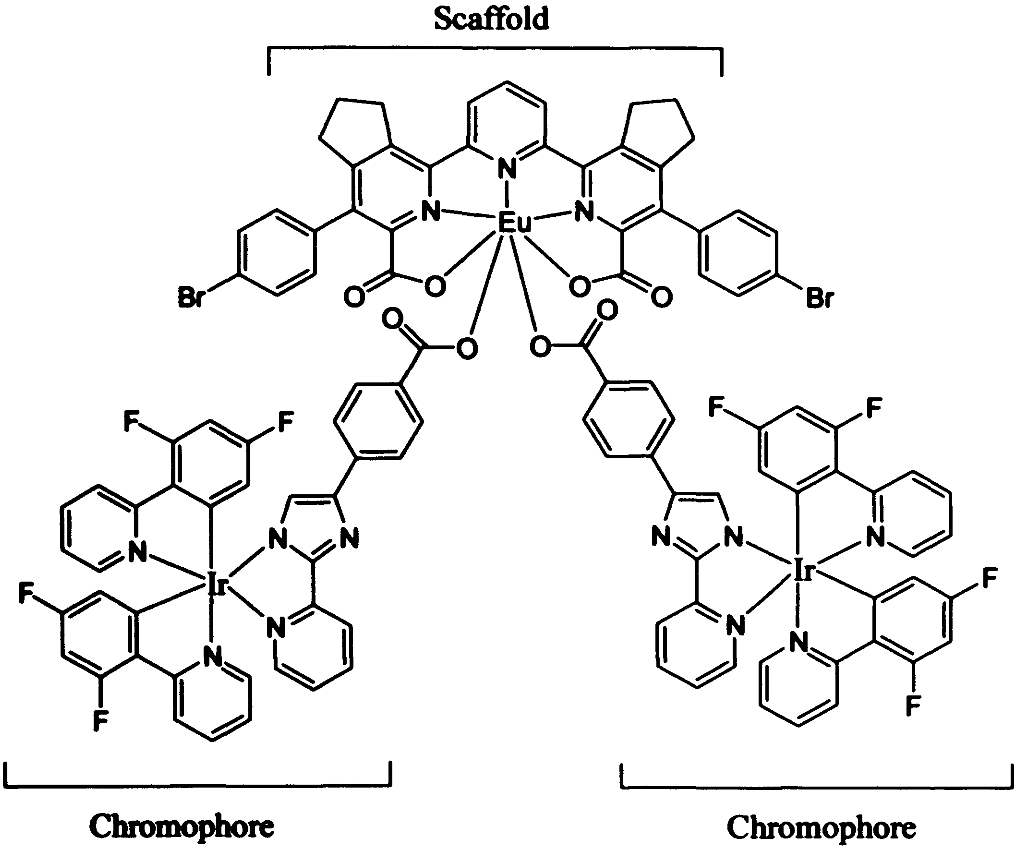

Figure 1.21. Lanthanide complex whose antennae are transition metal complexes designed by De Cola *et al.*[30]

1.4.5 Transition metal complexes.

Transition metal complexes, particularly those with metal electronic configurations defined by a d^6 system, have been the subject of much attention mostly because of their unique photophysical and photochemical properties.[31,32,33] Complexes of Re(I), Ru(II), Os(II) and Ir(III) have been widely studied over the last three decades as possible candidates for biological probes for imaging or therapeutic purposes. Generally, d^6 metal complexes display an octahedral geometry; the presence of the ligands around the metal split the d-orbitals into three lower and two higher levels. The energy difference between them depends on the crystal field strength which is dictated by the nature of the ligands. See **Figure 1.22.**

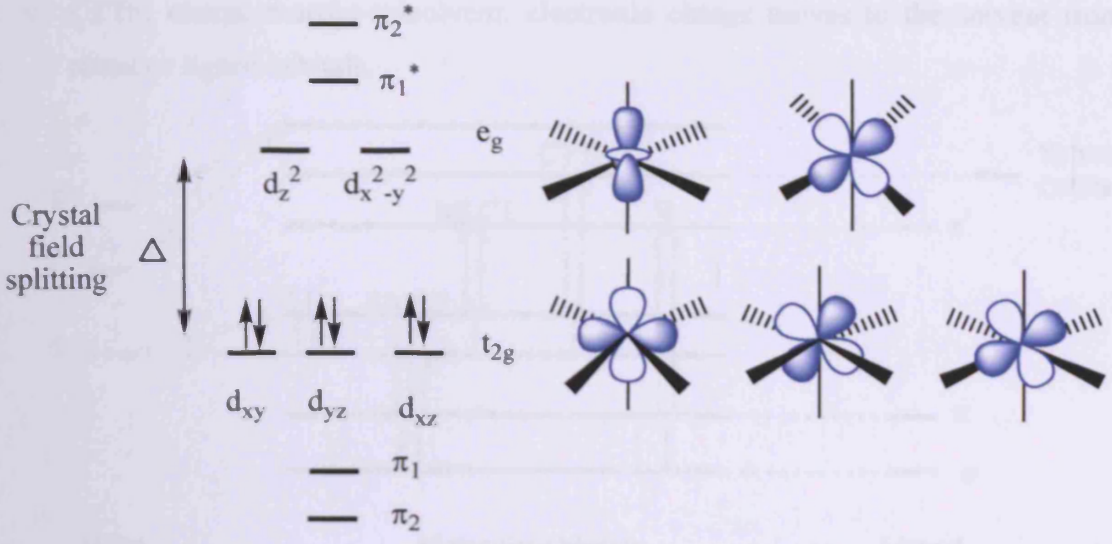

Figure 1.22. Metal and ligand orbitals.

The spectrochemical series of ligands, **Figure 1.23**, shows common ligands in order of increasing crystal field splitting, Δ, and hence, in increasing π acceptor and strong σ donor ligand character.

$$I^- < Br^- < Cl^- < F^- < H_2O < NH_3 < CO, H < SnCl_3^-$$

← Low Δ High Δ →

← π donor π acceptor/ σ donor →

Figure 1.22. Spectrochemical series of ligands.[34]

The electronic transitions in a metal complex are classified depending on the molecular orbitals between which the transitions occur. Therefore, for an octahedral complex, the electronic transitions are as follows: see **Figure 1.23.**

i. IL, intraligand bands: transitions between energy levels of the ligands, which are relatively unaffected by the metal centre.

ii. LF, ligand-field bands: transitions between energy levels of the metal d-orbitals. They are the lowest intensity transitions, usually in the visible region.

iii. LMCT, Ligand-to-metal-charge-transfer: transitions in which the electronic charge is transferred from the ligands to the coordinated metal.

iv. MLCT, metal-to-ligand-charge-transfer: electronic transition in which the electronic charge is transferred from the coordinated metal to the ligands.

v. CTTS, charge-transfer-to-solvent: electronic charge moves to the solvent from the metal or ligand orbitals.

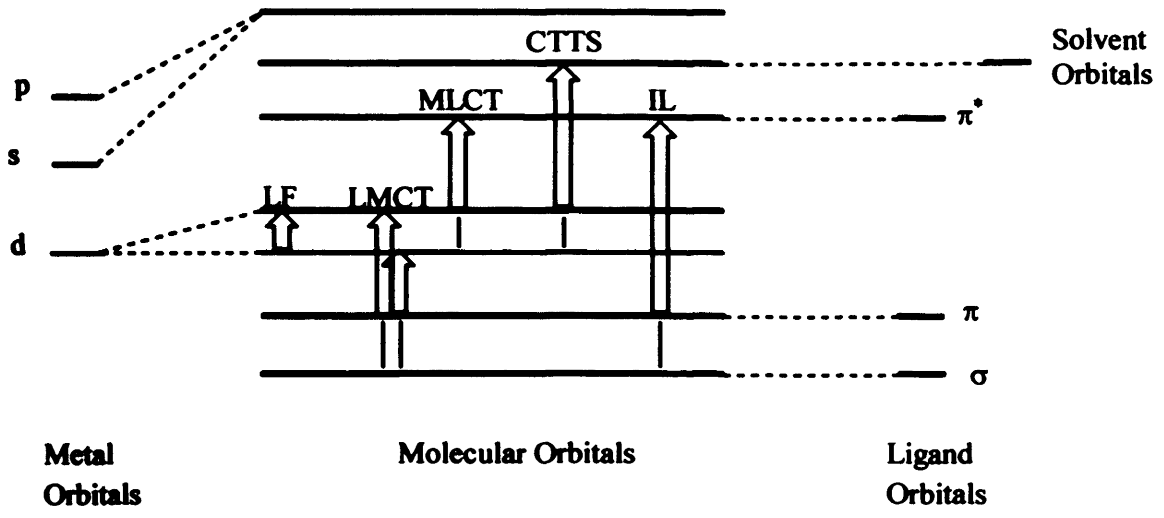

Figure 1.23. Molecular orbital diagram for an octahedral coordination complex and the different electronic transitions.[35]

In d^6 metal complexes, especially when the metal is Re(I), Ru(II), Os(II) and Ir(III), the emission arises from an MLCT transition. The luminescence from these metal complexes is formally phosphorescence and generally short lived compared to that of lanthanides (microseconds), due to the efficient spin-orbit coupling[m] with a heavy atom which allows radiationless deactivation, **Figure 1.24.**

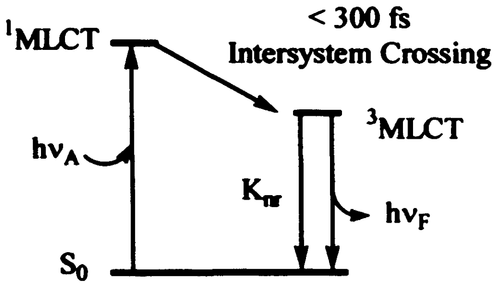

Figure 1.24. Jablonski diagram for a d^6 metal complex.

For a metal complex to be luminescent several criteria must be fulfilled. The crystal field must be strong enough to raise the d-d state above the MLCT state in order to have an emissive MLCT complex. In addition, the separation between the excited state, MLCT, and the ground state should be reasonably large to avoid radiationless decay, as smaller energy gaps result in a more rapid deactivation. Furthermore, the relative levels of MLCT and d-d states determine the sensitivity of the transition metal complex decay time to the

---

[m] Interaction between the intrinsic angular momenta associated with the particle spin and the orbital motion.

temperature. Hence, if the d-d levels are close to the MLCT level, then the d-d levels are thermally accessible, decreasing the life time of the probe, as the d-d level can become populated. **Figure 1.25**

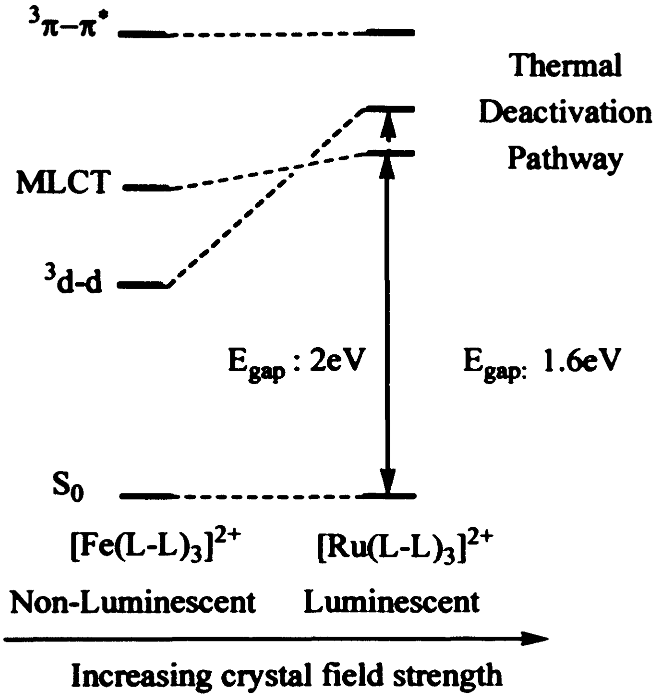

Figure 1.25. Energy states for non-luminescent, luminescent and weakly luminescent complexes.[36]

1.4.6 Transition metal complexes as biological luminescent probes.

The high photostability, large Stokes shifts, long wavelength excitation and long decay times give transition metal complexes significant potential as biophysical probes.[37] Their polarized emission[a] (unlike lanthanide complexes) makes transition metal complexes useful for the measurement of dynamic processes on the microsecond scale. Furthermore, their long decay times allow an easy separation of the luminescence of the imaging probe from any autofluorescence, using time gating techniques, as in the case of the lanthanide probes.

The metal-ligand covalent bonds and their high photostability confer the stability necessary in order not to dissociate under physiological conditions, avoiding any toxicity that the free

---

[a] Emission from a partially oriented population in the fluorophores which were excited with polarized light as fluorophores preferentially absorb photons whose electric vector is aligned parallel to their transition moment.

metal can confer to the imaging agent and also preventing photobleaching. Moreover, metal complexes overcome the problem of the self-quenching found in organic chromophores, *e.g.* fluorescein, as a result of their large Stokes shift.

Their applications range from being used as lipid probes, measuring domain-to-domain motion in proteins,[38] or measuring DNA dynamics[39] to ion sensing complexes.[40] Therefore, transition metal complexes seem to have a promising future as luminescent biological probes. Some examples are listed below in **Figure 1.26**.

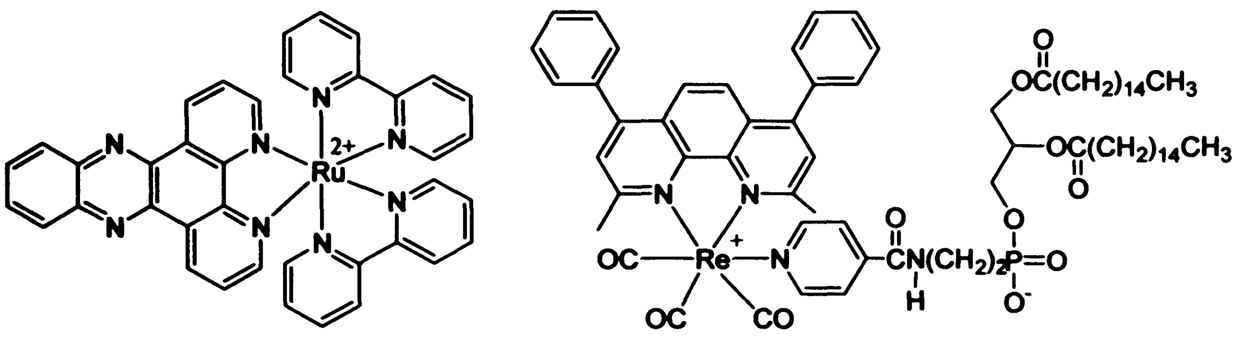

Example A

Example B

[Ru(bpy)$_2$(dppz)](PF$_6$)$_2$

Re(bcp)(CO)$_3$(pyCOOH)-PE-lipid

Figure 1.26. DNA and lipid luminescent probes.

[Ru(bpy)$_2$(dppz)](PF$_6$)$_2$ (**Figure 1.26**, example A)[39] is used to study DNA dynamics as it intercalates into the double-helix and displays polarized emission. It is highly luminescent after its interaction with DNA. Transition metal complexes represent an important breakthrough in these kinds of studies as the organic molecules, *e.g.* EB,[o] acridine orange, *etc*,[41] used so far for this purpose display decay times of around 30 nanoseconds (ns) whereas the expected motion for DNA ranges from ns to μs. Anisotropy decay[p] can typically be measured for up to three times the lifetime of the fluorophore; therefore transition metal complexes can be used to measure all the expected DNA motions. Specifically, complex **A** can be used to study DNA dynamics of 300 ns or longer. For that reason, these luminescent probes allow extended observation to the microsecond scale, offering the opportunity to increase the information content in time-resolved measurement of nuclei acids. Complex **B**,[38] on the other hand, is an example of a long lifetime lipid

---

[o] Ethidium bromide.

[p] Polarized emission.

probe which can be used to study rotational motions of entire lipid vesicles or to measure diffusions by their effect on resonance energy transfer.

Transition metal complexes sensitive to different ions and pH are another important area of investigation within the biological imaging field and also in the detection of toxic substances. **Figure 1.27** shows an example of each category. Example C[42] shows a luminescent probe that can be used for measurement of blood pH due to its high sensitivity to pH variations between 7.35 and 7.46, pH values of clinical relevance. On the other hand, example D[40] shows a cyanide sensitive probe whose emission decreases as cyanide concentration increases.

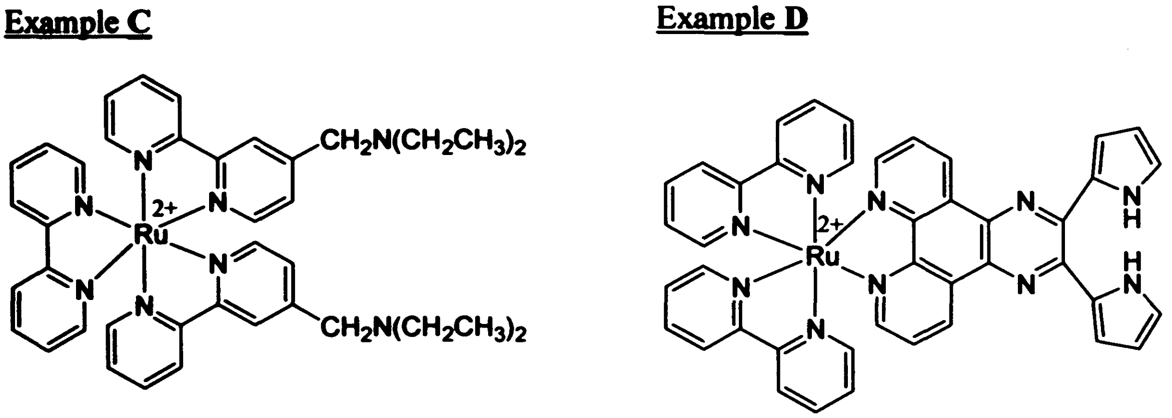

[Ru(bpy)$_2$(deabpy)](PF$_6$)$_2$ [Ru(bpy)$_2$(dcbpy)](PF$_6$)$_2$

Figure 1.27. pH and ion sensitive luminescent probes.

In the last year different research groups such as Lo's group[43] from Hong Kong, Li's group[44] from Shanghai and the work described in this thesis,[45] have demonstrated the viability of using novel d^6 MLCT transition metal complexes as fluorophores in cell microscopy. Cell uptake, low toxicity and in some cases their demonstrated localization in inner organelles represent a great breakthrough in this area. These earliest investigations symbolize an initial step towards the development of other metal complexes, whose luminescent properties could help to overcome the difficulties found with conventional dyes in cell imaging. Examples from other groups organised in chronological order are shown in **Figures 1.28** to **1.30**. No examples of work from this group will be presented at this point as they are discussed in the following chapters of this thesis.

Example **E**

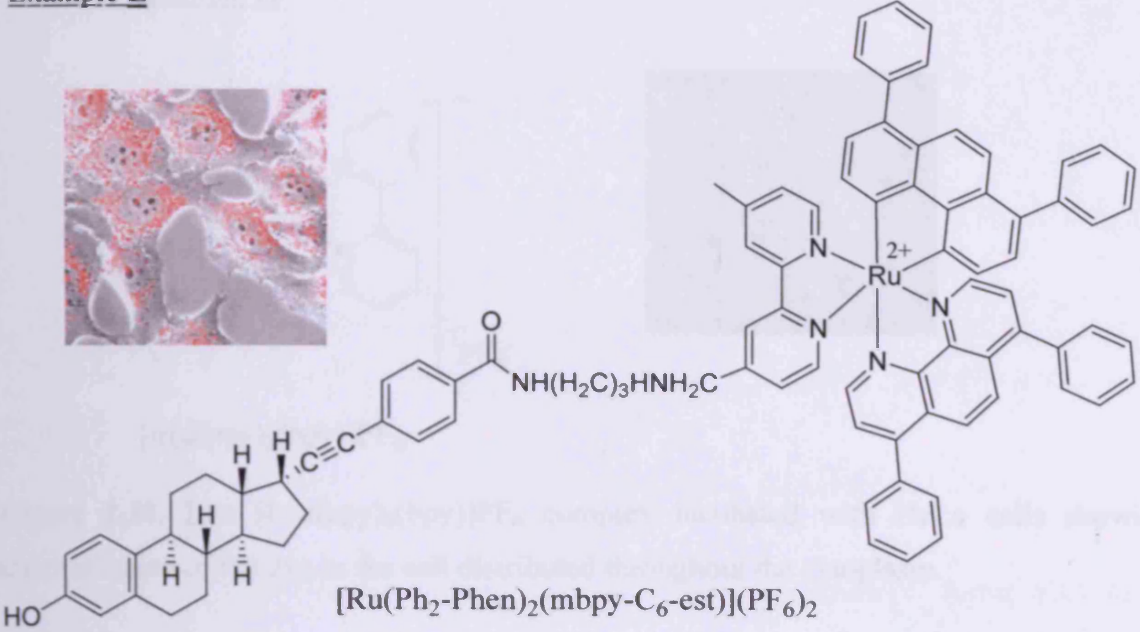

[Ru(Ph$_2$-Phen)$_2$(mbpy-C$_6$-est)](PF$_6$)$_2$

Figure 1.28. Lo's [Ru(Ph2-phen)$_2$(mbpy-C6-est)](PF$_6$)$_2$ complex incubated with HeLa cells showing distribution inside the cytoplasm with a lower extent of nuclear uptake.

Example **F**

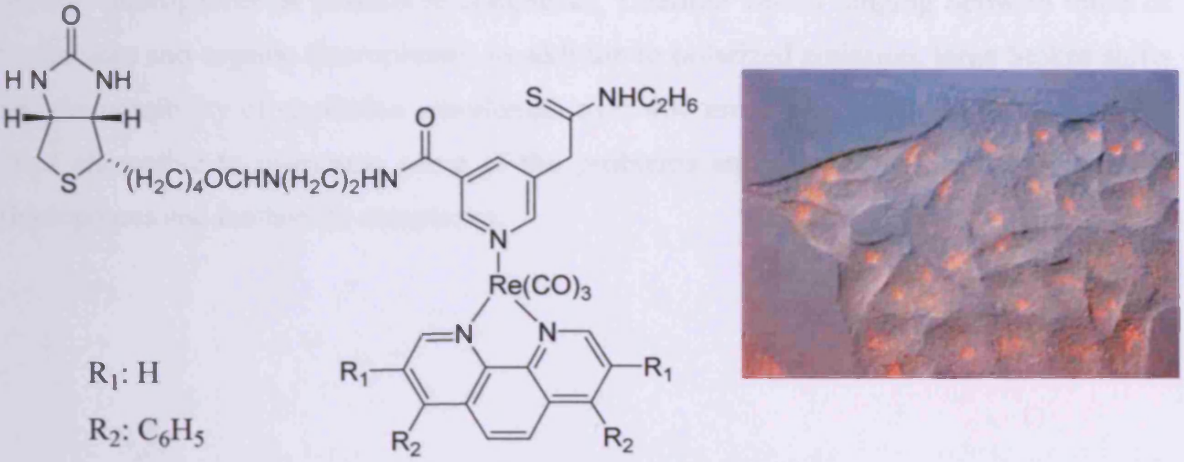

[Re(Ph$_2$-phen)(CO)$_3$(py-biotin-TU-Et)]PF$_6$

Figure 1.29. Lo's [Re(Ph$_2$-phen)(CO)$_3$(py-biotin-TU-Et)]PF$_6$ complex incubated with HeLa cells showing not homogeneous distribution within the cytoplasm but localized in the perinuclear region.

Example G

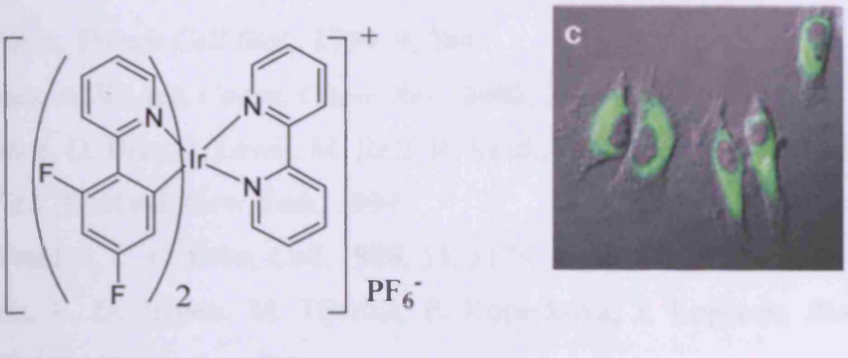

$[Ir(dfppy)_2(bpy)]PF_6$

Figure 1.30. Li's $[Ir(dfppy)_2(bpy)]PF_6$ complex incubated with HeLa cells showing internalization of the dye in the cell distributed throughout the cytoplasm.

1.5 Conclusions.

A new door is open to the application of transition metal complexes in biological recognition and cell imaging as they offer some unique features not available with either organic fluorophores or lanthanide complexes. Lifetime values ranging between those of lanthanides and organic fluorophores, in addition to polarized emission, large Stokes shifts and the possibility of excitation wavelength over 400 nm, make transition metal probes a great alternative to overcome some of the problems encountered in the use of organic fluorophores and lanthanide complexes.

1.6 References.

[1] J. C. Politz, *Trends Cell Biol.*, **1999**, 9, 284.

[2] S.-S. Sun, A, J. Lees, *Coord. Chem. Rev.*, **2002**, 230, 171.

[3] B. Alberts, D. Bray, J. Lewis, M. Raff, R. Keith, J. D. Watson, *Molecular Biology Of The Cell*, 3rd ed., Garland, New York, **1994**.

[4] A. D. Frankel, C. O. Pabo, *Cell*, **1988**, 55, 1179.

[5] A. Nori, K. D. Jensen, M. Tijerina, P. Kopeckova, J. Kopecek, *Bioconjugate Chem.*, **2003**, 14, 44.

[6] M. Zhao, M. F. Kircher, L. Josephson, R. Weissleder, *Bioconjugate Chem.*, **2002**, 13, 840.

[7] A. Astriab-Fisher, D. Sergueev, M. Fisher, B. R. Shaw, R. L. Juliano, *Pharm. Res.*, **2002**, 19, 744.

[8] V. P. Torchilin, R. Rammohan, V. Weissig, T. S. Levchenko, *Proc. Natl. Acad. Sci. U. S. A.*, **2001**, 98, 8786.

[9] **a)** J. R. Maiolo, M. Ferrer, E. A. Ottinger, *Biochim. Biophys. Acta*, **2005**, 1712, 161; **b)** G. Tunnemann, R. M. Martin, S. Haupt, C. Patsch, F. Edenhofer, M. C. Cardoso, *FASEB J.*, **2006**, 20, 1775.

[10] X. Zhang, L. Wan, S. Pooyan, Y. Su, C. R. Gardner, M. J. Leibowitz, S. Stein and P. J. Sinko, *Mol. Pharm.*, **2004**, 1, 145.

[11] S. Veldhoen, S. D. Laufer, A. Trampe, T. Restle, *Nucleic Acids Res.*, **2006**, 34, 6561

[12] T. Jiang, E. S. Olson, Q. T. Nguyen, M. Roy, P. A. Jennings, R. Y. Tsien, *Proc. Natl. Acad. Sci. U. S. A.*, **2004**, 101, 17867.

[13] Sir J. F. W. Herschel, *Phil. Trans. Royal*, **1845**, 143.

[14] Sir G. G. Stokes, *Phil. Trans. Royal*, **1852**, 463.

[15] R. P. Haugland, *Handbook Of Fluorescent Probes And Research Chemicals*, 6th ed., Molecular Probes, Eugene, **1996**.

[16] G. Weber, *Biochem. J.*, **1951**, 51, 155.

[17] P. Lenz, *Applied Optics*, **1999**, 38, 3662.

[18] M. Bruchez, M. Moronnne, P. Gin, S. Weiss, A. P. Alivisatos, *Science*, **1988**, 2013.

[19] A. Watson, X. Wu, M. Bruchez, *Biotechnol.*, **2003**, 34, 296.

[20] J. K. Jaisawal, H. Mattossi, J. M. Mauro, S. M. Simon, *Nature Biotechnol.*, **2003**, 21, 41.

[21] R. Wargnier, A. V. Baranov, V. G. Maslov, V. Stsiapura, M. Artemyev, M. Pluot, A. Sukhahanove, I. Nabiev, *Nanotechnol. Lett.*, **2004**, 4, 451.

[22] C. H. Evans, *Trends Biochem. Sci.*, **1983**, 445.

[23] F. S. Richardson, *Chem. Rev.*, **1982**, 82, 541.

[24] J.-C. G. Bünzli, C. Piguet, *Encyclopedia of Materials: Science and Technology*, Vol. 10 K. H. J. Buschow, R. W. Cahn, M. C. Flemings, B. Ilschner, E. J. Kramer, S. Mahajan (Eds.), Elsevier Science, Oxford, **2001**.

[25] A. Sigel, H. Sigel (Eds.), *Metal Ions in Biological System*, 1st edn, Marcel Dekker Inc., New York, **2004**.

[26] J.-C. G. Bünzli, C. Piguet, *Chem. Soc. Rev.*, **2005**, 34, 1048.

[27] P. R. Selvin, *Applied Fluorescence In Chemistry, Biology And Medicine*, W. Rettig, B. Strechmel, S. Scharder, H. Seifert(Eds.), 1st ed., Springer, New York, **1999**.

[28] R. A. Poole, G. Bobba, M. J. Cann, J.-C. Frias, D. Parker, R. D. Peacock, *Org. Biomol. Chem.*, **2005**, 3, 1013.

[29] T. Koullourou, L. S. Natrajan, H. Bhavsar, S. J. A. Pope, Ji. Feng, J. Narvainen, R. Shaw, E. Scales, R. Kauppinen, A. M. Kenwright, S. Faulkner, *J. Am. Chem. Soc.* **2008**, 130, 2178.

[30] P. Coppo, M. Duati, V. N. Kozhevnikov, J. W. Hofstraat, L. De Cola, *Angew. Chem. Int. Ed.*, **2005**, 44, 1806.

[31] V. Balzani, N. Sabbatini, *Chem. Rev.*, **1986**, 86, 319.

[32] P. Chen, T. J. Meyer, *Chem. Rev.*, **1998**, 98, 1439.

[33] S-S. Sun, A. J. Lees, *Coord. Chem. Rev.*, **2002**, 230, 171.

[34] R. H. Crabtree (Ed.), *The Organometallic Chemistry Of The Transition Metals*, 3rd ed., Wiley, New York, **2001**.

[35] O. Horváth, K. L. Stevenson (Eds.), *Charge Transfer Photochemistry Of Coordination Compounds*, 1st ed., VCH, New York, **1993**.

[36] J. N. Demas, B. A. DeGraff, *Anal. Chem.*, **1991**, 63, 829.

[37] J. R. Lakowicz, E. Terpetschnig, Z. Murtaza, H. Szmacinski, *J. Fluoresc.*, **1997**, 240, 54.

[38] L. Li, H. Szmzcinski, J. R. Lakowicz, *Anal. Biochem.*, **1997**, 244, 80.

[39] R. E. Holmin, E. D. A. Stemp, J. K. Barton, *Inorg. Chem.*, **1998**, 37, 29.

[40] P. Anzenbacher, D. S. Tyson, K. Jursiková, F. N. Castellano, *J. Am. Chem. Soc.*, **2002**, 124, 6332.

[41] D. Suh, J. B. Chaires, *Bioorg. Med. Chem.*, **1995**, 3, 723.

[42] Z. Murtaza, Q. Chang, G. Rao, H. Lin, J. R. Lakowicz, *Anal. Biochem.*, **1997**, 247, 216.

[43] **a)** K. K.-W. Lo, M.-W. Louie, K.-S. Sze, J. S.-Y. Lau, *Inorg. Chem.*, **2008**, 47, 602, **b)** K. K.-W. Lo, T. K.-M. Lee, J. S.-Y. Lau, W.-L. Poon, S.-H. Cheng, *Inorg. Chem.*, **2008**, 47, 200.

[44] M. Yu, Q. Zhao, Li. Shi, F. Li, Z. Zhou, H. Yang, T. Yia, C. Huang, *Chem. Commun.*, **2008**, 2115.

[45] **a)** A. J. Amoroso, M. P. Coogan, J. E. Dunne, V. Fernández-Moreira, J. B. Hess, A. J. Hayes, D. Lloyd, C. Millet, S. J. A. Pope, C. Williams, *Chem. Commun.*, **2007**, 3066; **b)** A. J. Amoroso, R. J. Arthur, M. P. Coogan, J. B. Court, V. Fernández-Moreira, A. J. Hayes, D. Lloyd, C. Millet, S. J. A. Pope, *New J. Chem.*, **2008**, 32, 1097.

Chapter 2

Synthetic Studies Directed Towards A Luminescent Rhenium(I) Complex For Specific Cell Imaging.

2.1 Aims.

This chapter is focused on the synthesis of luminescent, membrane-permeable rhenium complexes that will act as chemical models to validate the concept of a membrane permeable cell-imaging device. The device is comprised of three parts - a luminescent core, a lipophilic 'tail' and a sensor. These compounds are formulated as part of the development of a delivery system that will introduce an imaging device through a bilipidic membrane into a cell.

2.2 Introduction.

2.2.1 Transport across the cell membrane: R. Y. Tsien's Quin2 system.

A range of membrane-permeable devices for medical imaging and biodiagnostic analysis has been developed in the last few years. In many cases, transport of these devices across the cell membrane is facilitated by the lipophilicity of the substrate, which provides the permeability required to cross the lipidic bilayer.

One method of providing this lipophilicity to a device that, in its active state, is not able to pass through the membrane bilayer, was designed by Tsien *et al.* in order to monitor intracellular Ca(II) ion concentrations.[1] The device (or system) is based on a simple Ca(II)-selective chelator acetoxymethyl tetraester, that is made temporarily membrane permeable. This is achieved by esterifying the four carboxylate groups to make the molecule lipophilic affording a acetoxymethyl tetraester. This then allows the system to enter the cell without perturbing membrane integrity. Once in the cell, the esters are hydrolysed by acetylesterases,[a] reforming the original Ca(II) chelator (**Figure 2.1**). The lipophilicity and thus, membrane permeability of the whole system can thereby be changed by a simple esterification process.

---

[a] Enzymes belonging to the hydrolase family that act specifically on carboxylic ester bonds.

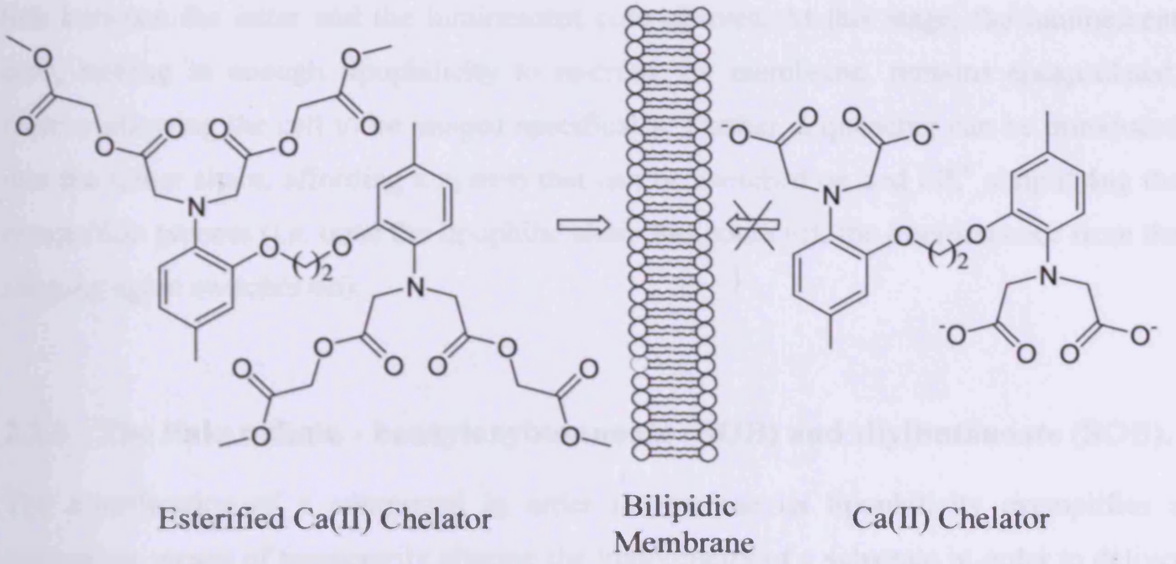

Figure 2.1. Tsien's Ca(II) chelator.

2.2.2 Premises.

Tsien's idea is for a compound with a lipophilic "tail" that crosses a cell membrane where it undergoes a modification of its chemical structure, ensuring its encapsulation. This concept provides the basis for the development of a similar system that will deliver lumophores into target cells **Scheme 2.2.** The general scheme shows the target molecule divided in three parts: a luminescent core, the imaging agent, linked to a lipophilic chain, for membrane permeability of the whole unit, and a sensor, the nature of which depends on the analyte to be monitored.

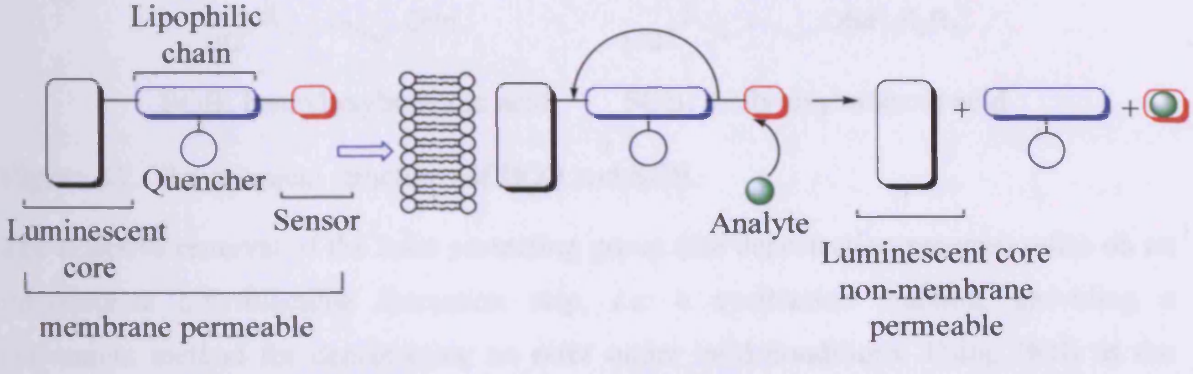

Scheme 2.1. General concept.

In the presence of an analyte (*e.g.* an intracellular enzyme) which reacts with the sensor, not only does the linkage break between the sensor and the lipophilic chain, but also the link between the latter and the luminescent core cleaves. At this stage, the luminescent core, lacking in enough lipophilicity to re-cross the membrane, remains encapsulated, thereby allowing the cell to be imaged specifically. Further, a quencher can be introduced into the linker chain, affording a system that can be switched on and off,[b] simplifying the recognition process (*i.e.* once the lipophilic chain has come off, the luminescence from the imaging agent switches on).

2.2.3 The linker chain - benzyloxybutanoate (BOB) and silylbutanoate (SOB).

The esterification of a compound in order to increase its lipophilicity exemplifies a convenient means of temporarily altering the lipophilicity of a substrate in order to deliver a diagnostic device (system) to a cell without altering the active part of the device. Other means of esterification include the use of butyrate–based molecules as ester protecting groups. These protecting groups can also be viewed as linker chains connecting the sensor to the lumophore and also serve as a means to deliver the lumophore to the target within the cell.

In the last decade, a series of studies by Ganem[2] and Gala[3] concerning the application of benzyloxybutanoate (BOB) and silyloxybutanoate (SOB) as ester protecting groups have been carried out. They have shown in their work that not only are both protecting groups easily synthesized, but also that their selective removal is possible in the presence of other ester groups. **Figure 2.2.**

BOB: benzyloxybutanoic acid SOB: 4-silyloxybutanoic acid

Figure 2.2. The chemical structures of BOB and SOB.

The selective removal of the ester protecting group (the deprotection process) relies on an intermediate butyrolactone formation step, *i.e.* a cyclization reaction, providing a convenient method for deprotecting an ester under mild conditions. Using BOB as the esterification agent, debenzylation and the addition of a base is needed prior to the lactonisation reaction. In contrast, when SOB is used, the removal of the silyl compound

---

[b] On/off devices that can be flipped from being non emissive to emissive or *vice versa* by interaction with an external agent.

takes place before the lactonisation reaction. The optimum conditions found for the de-esterification processes are shown in **Scheme 2.2**.

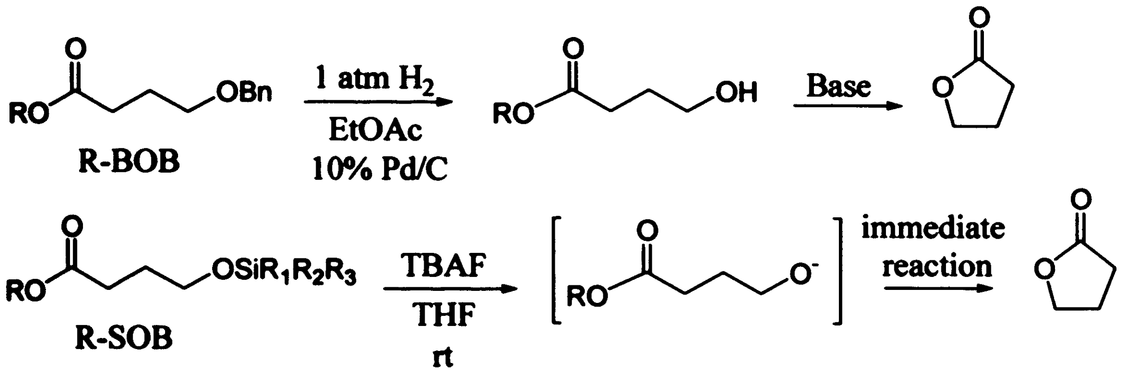

$SiR_1R_2R_3$: $SiMe_2{}^tBu$

Scheme 2.2. Lactonisation reaction.

2.2.4 The sensor.

The SOB group, silyloxybutanoate, was chosen as the linker chain in our system due to the work published by Gala in 2001,[3] showing that there is a strong driving force for the chain to "self destruct", leading to a butyrolactone. In addition, $SiMe_2{}^tBu$ group is known to be stable in water across a wide pH range (stable between pH 4 and 12), a feature necessary if it is to be used in biological media. Furthermore, Si-O systems are very sensitive to fluoride ions which can be used as a trigger in the first instance to test the viability of the system.

2.2.5 Specific imaging agent design.

A chemically activated model molecule consisting of a luminescent core, a lipophilic chain and a sensor, designed to comply with the premises enunciated in **Section 2.2.2**, is shown in **Scheme 2.3**.

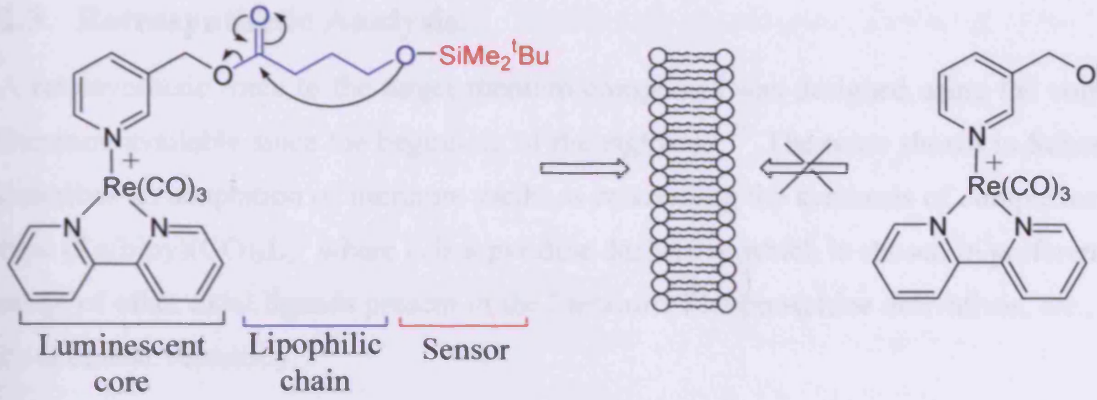

Scheme 2.3. Specific models.

The strategy involves binding the well known imaging unit [Re(bisim)(CO)$_3$L]$^{+}$ [4,5,6] (bisim represents a bisimine ligand *i.e.* a bipyridine, phenanthroline or derivative, and L is a pyridine derivative) to a sensor, through a linker chain. This linker chain will "self destruct", that is, cut itself away from the ligand upon the loss of the sensor. **Scheme 2.4.** No quencher has been considered for the specific model molecule, contrary to the original design **Scheme 2.1,** as the initial objective is to probe the chain "*self-destruction*" mechanism.

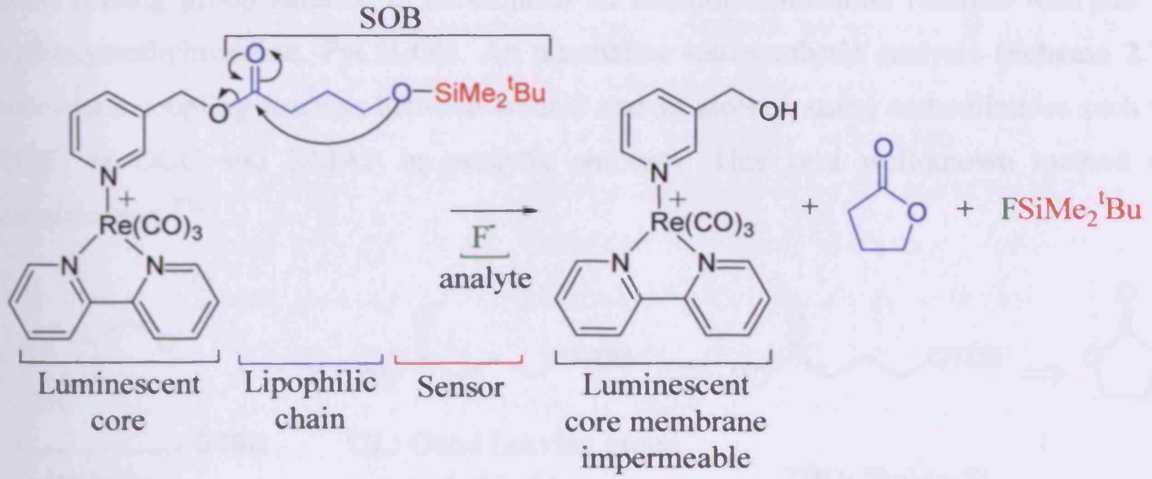

Scheme 2.4. The *self destruct* mechanism.

2.3 Retrosynthetic Analysis.

A retrosynthetic route to the target rhenium complexes was designed using the volume of literature available since the beginning of the eighties.[7,8,9] The route shown in **Scheme 2.5** describes an adaptation of literature methods concerning the synthesis of complexes of the type $[Re(bipy)(CO)_3L]^+$ where L is a pyridine derivative which is chosen in preference to a range of other axial ligands present in the literature, like phosphine derivatives, *etc.*, due to its chemical versatility.

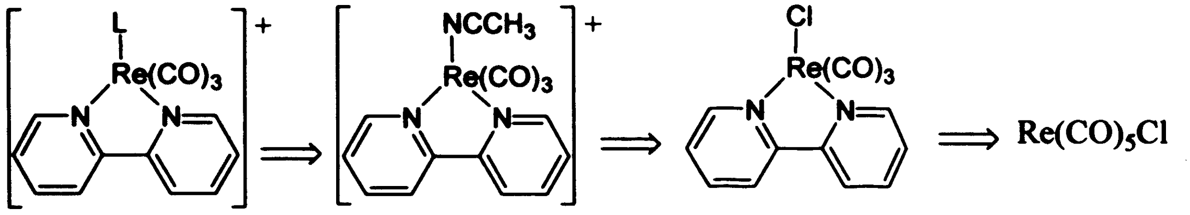

L: axial ligand, pyridine derivative

Scheme 2.5. Rhenium complex retrosynthesis.

The first approach to the synthesis of the axial ligand, L, was based upon consecutive reactions of a butyrolactone fragment, **Scheme 2.6.** This would give a derivative bearing a good leaving group suitable to accomplish an addition/elimination reaction with the 3-hydroxymethylpyridine, $PyCH_2OH$. An alternative retrosynthetic analysis (**Scheme 2.7**) involves a coupling reaction between an acid and an alcohol, using carbodiimides such as EDCI or DCC and DMAP in catalytic amounts. This is a well-known method of esterification.[10,11]

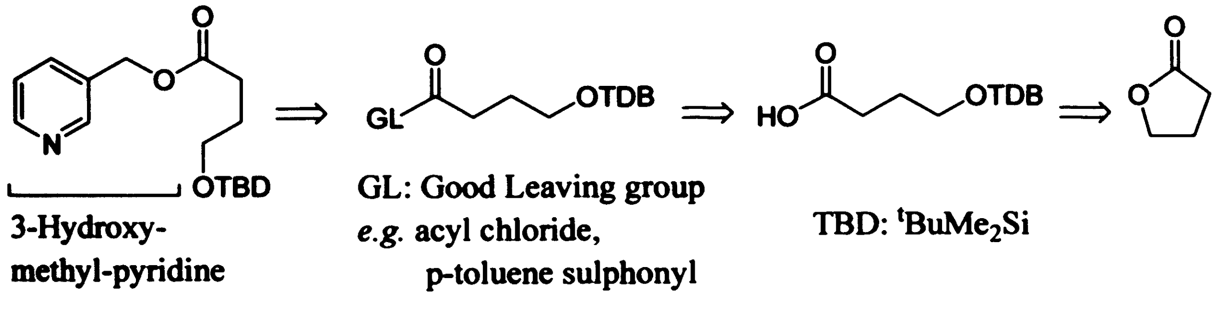

3-Hydroxy-
methyl-pyridine

GL: Good Leaving group
e.g. acyl chloride,
p-toluene sulphonyl

TBD: $^tBuMe_2Si$

Scheme 2.6. Initial retrosynthetic analysis of the pyridine derivative.

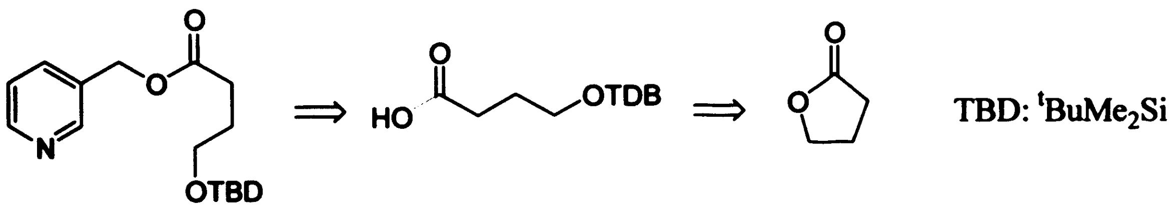

TBD: $^tBuMe_2Si$

Scheme 2.7. Final retrosynthetic analysis of the pyridine derivative.

2.4 Results And Discussion: Synthesis Attempts Toward The Axial Ligand.

2.4.1 Synthesis of the axial ligand, L, *via* an acyl chloride adduct.

The first step towards the final target molecule 3-(4-tertbutyldimethylsilyloxybutanoatomethyl)pyridine was the ring opening of butyrolactone, **Scheme 2.8.** Step (i) in the procedure, using sodium hydroxide in DMF, was published by Marvel in 1929.[12] The product was obtained as its sodium salt in good yield (88 %).

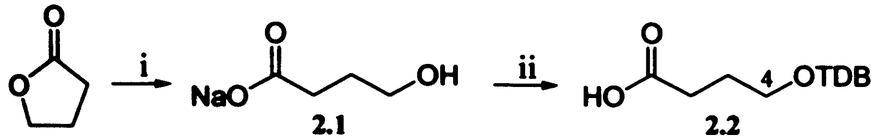

i: NaOH, DMF, 88 %
ii: TBDCl, Py, 28 %

Scheme 2.8. Synthesis of compounds **2.1** and **2.2**.

Step (ii) was the protection of the terminal alcohol using *tert*-butyldimethylsilyl chloride, TBDCl. Pyridine was used as a solvent in order to overcome the problem of the low solubility of compound **2.1** in solvents such as DMF and at the same time to act as a base and neutralize the HCl formed during the reaction. However, the salt **2.1** is only sparingly soluble in this solvent and the reaction mixture remained heterogeneous even after 12 hours stirring at room temperature. After 72 hours, an aqueous work up was done to isolate the product. If some pyridine remained, further extractions with copper sulphate were performed to purify the product. The reaction was monitored by following the shift of the $CH_2(4)$ protons from 3.45 ppm in the alcohol to 3.56 ppm, which is a typical value for aliphatic protons contiguous to a protected alcohol.[13] Also, the strong band observed in the IR spectrum at 1714 cm^{-1} indicative of a carbonyl stretching band of a carboxylic acid (typical range 1700-1725 cm^{-1})[14] suggested, in stage (ii), that the alcohol protection had been successfully accomplished. These spectroscopic data agree with those given in the literature for compound **2.2**.[15]

The reason why such a long reaction time is required in order to synthesise compound **2.2** is that the silylation occurs initially at the carboxyl group rather than the hydroxyl group. This is followed by silyl migration to the hydroxyl group under these reaction conditions as depicted in **Scheme 2.8.** This transformation was studied by Renton in 2002.[15]

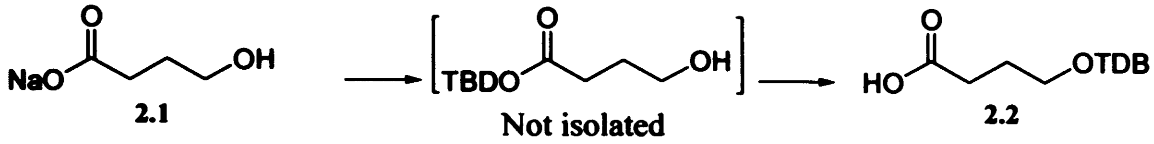

Scheme 2.9. TBD migration.

The next step in the synthesis (see **Scheme 2.6**) was the transformation of the carboxylic acid, **2.2**, into a carbonyl compound bearing a good leaving group. This required the transformation of **2.2** into its potassium salt, **2.3**, in order to improve the nucleophilicity of the oxygen atom so that its reaction with oxalyl chloride would yield the acyl chloride compound, **2.4**. **Scheme 2.10.**

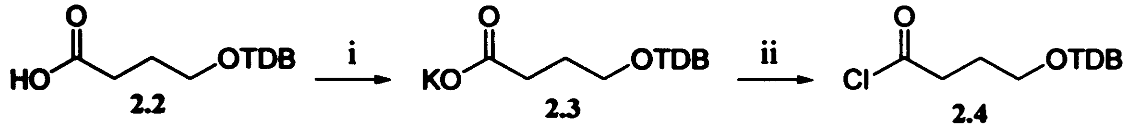

i: ^{t}BuOK, MeOH, 75 %
ii: $(COCl)_2$, $CHCl_3$

Scheme 2.10. Leaving group improvement.

The transformation of the carboxylic acid, **2.2**, into its potassium salt, **2.3**, was achieved with ^{t}BuOK in methanol and it was monitored by ^{1}H-NMR, in which there was a clear shift to higher field of the protons closer to the carbonyl group (from 2.30 to 2.10 ppm). The attempt to synthesise the acyl chloride **2.4** was then carried out. The potassium salt **2.3**, was stirred at room temperature with oxalyl chloride in chloroform for 12 hours under a nitrogen atmosphere. Initially, the reaction mixture effervesced as CO and CO_2 were released as by-products of the transformation. The reaction mechanism is shown below in **Scheme 2.11.**

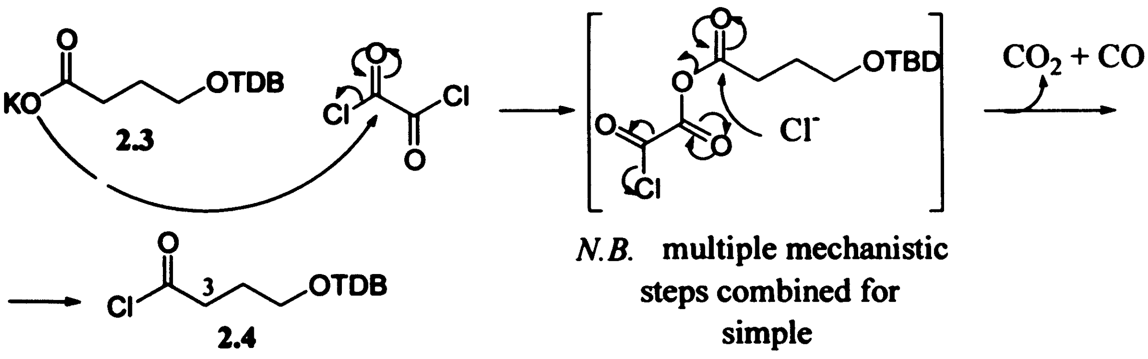

N.B. multiple mechanistic steps combined for simple

Scheme 2.11. Reaction mechanism.

Unfortunately, although the acyl chloride adduct, **2.4**, was obtained (as shown by a change in the $CH_2(3)$ hydrogen chemical shift from 2.10 ppm to 2.94 ppm) the butyrolactone was also produced in a 1:1.4 ratio (acyl chloride adduct:butyrolactone). This is because of alcohol deprotection followed by a cyclisation reaction, **Scheme 2.12.** It was likely that some HCl formation took place during the reaction leading to the unprotected alcohol.

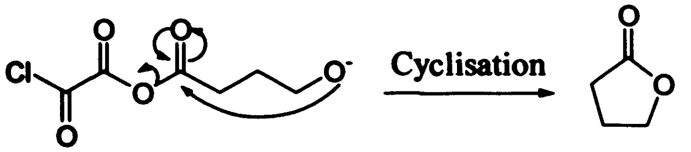

Scheme 2.12. Cyclisation reaction.

Attempts to purify compound **2.4** by fractional distillation were unsuccessful and the product decomposed to a mixture of species impossible to identify. As a result, another attempt to synthesise the final target was performed, *via* a one-pot reaction. Oxalyl chloride and compound **2.3** were stirred at room temperature until the effervescence finished. Then, without any isolation or purification, 3-hydroxymethylpyridine and triethylamine were added to the reaction mixture, **Scheme 2.13.** The latter was added not only to keep the reaction basic and prevent alcohol deprotection, but also to facilitate the addition/elimination reaction with the acyl chloride by forming the salt Et_3NHCl. **Scheme 2.14.**

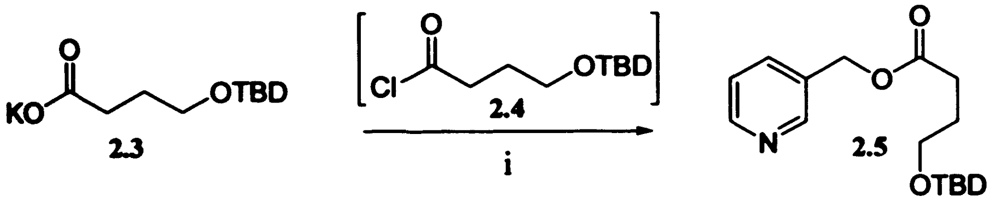

i: $(COCl)_2$, $CHCl_3$, after 25 min., $PyCH_2OH$, Et_3N, 10 %

Sheme 2.13. One pot reaction *via* an acyl choride adduct.

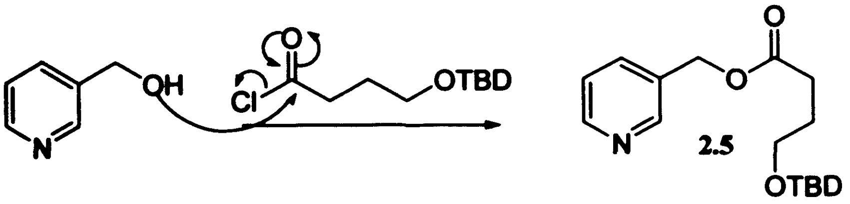

Scheme 2.14. Proposed addition-elimination reaction mechanism.

The final product, **2.5**, was obtained as colourless oil. IR experiments clearly showed the presence of **2.5** as the CO band observed at 1714 cm^{-1} is shifted to 1769 cm^{-1} which is the normal frequency for an ester.[16] Moreover, ^{1}H-NMR spectroscopy also showed a clear shift to lower field (from 4.6 to 5.0 ppm) of the methylene protons of the oxy-methyl pyridine upon esterification, indicating a reduction in shielding. On the other hand, the methylene protons belonging to the butanoyl fragment are barely shifted, only those closest to the carbonyl group show a significant change in chemical shift from 2.30 to 2.42 ppm, again indicating a decrease in shielding. Although full characterisation confirmed the structure of the target molecule, a new route for its synthesis was required due to the low yield (less than 10%).

2.4.2 Synthesis of the axial ligand, L, *via* a mixed anhydride.

Next, attention turned to the use of the *p*-toluene-sulfonyl group as an alternative leaving group in an attempt to form the mixed anhydride of the acid **2.2**. The reaction was performed in dry DCM, stirring the potassium salt, which is partially soluble in this solvent, in the presence of *p*-toluene sulfonyl chloride under a nitrogen atmosphere at room temperature for 2 hours. The product, **2.6**, a moisture sensitive white solid, was obtained in 35 % yield. **Scheme 2.15.**

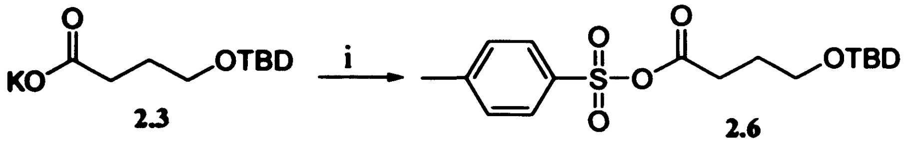

i: TsCl, DCM, 35 %

Scheme 2.15. Synthesis of compound **2.6.**

Unfortunately, several attempts at further characterisation of **2.6** were hindered by its ease of hydrolysis, and so only ^{1}H-NMR spectroscopic studies were carried out. Once again, a slight shift to lower field is visible for the methylene unit adjacent to the carbonyl group (2.10 ppm to 2.46 ppm), comparable to the shift observed for compound **2.5**. This mixed anhydride was immediately stirred with 3-hydroxymethyl pyridine in the presence of a base in dry chloroform. However, the result was a mixture of decomposition products indicating the un-viability of obtaining the desired product in this way. Nevertheless, a one-pot reaction was tried again, as the final product, **2.5**, is known to be more stable and so easier to handle than the mixed anhydride, **Scheme 2.16.**

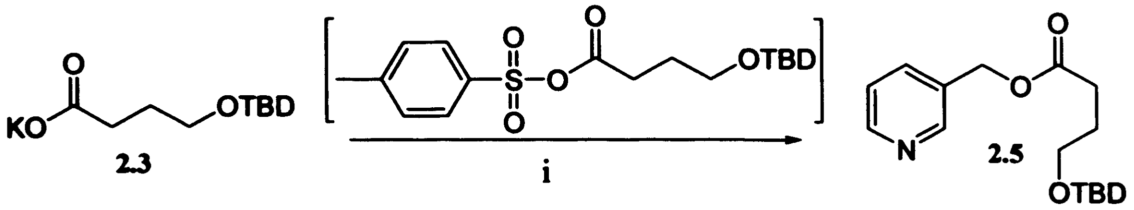

i: TsCl, DCM, after 4 hours, $PyCH_2OH$, Et_3N

Scheme 2.16. One pot reaction *via* a mixed anhydride adduct.

The potassium salt and *p*-toluene sulfonyl chloride were stirred for 4 hours in dry DCM under a nitrogen atmosphere to generate the mixed anhydride **2.6** *in situ*. 3-hydroxymethylpyridine ($PyCH_2OH$) was then added and the reactants stirred for a further 12 hours. After an aqueous work up, ^{1}H-NMR spectroscopy showed a mixture of compounds including the desired product **2.5** together with unreacted *p*-TsCl and unknown species containing the butanoyl fragment. The product was unable to be purified and this synthetic route to synthesise **2.5** was abandoned.

2.4.3 Synthesis of the axial ligand, L, *via* a coupling reaction.

A third route to the target molecule **2.5** was described in the retrosynthetic analysis discussed in **Section 2.3.2.** This route utilizes the direct coupling reaction between an acid and an alcohol using a carbodiimide derivative such as EDCI as a coupling agent, **Scheme 2.17.** As discussed in **Section 2.3.2.** several examples of this coupling reaction are described in the literature.[10,11,17] Specifically, research groups headed by Roush[18] and Zhang[19] describe the coupling reaction between the acid **2.2** and an alcohol (3-hydroxymethyl pyridine). The accepted mechanism of the reaction is presented in **Scheme 2.18.**[20]

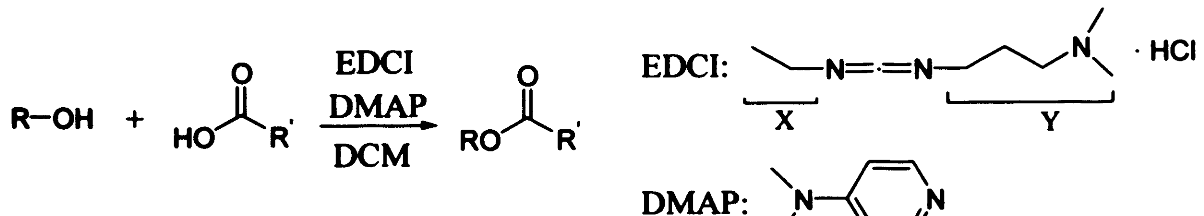

R, R': Generic hydrocarbon chain

Scheme 2.17. Generic acid-alcohol coupling reaction scheme.

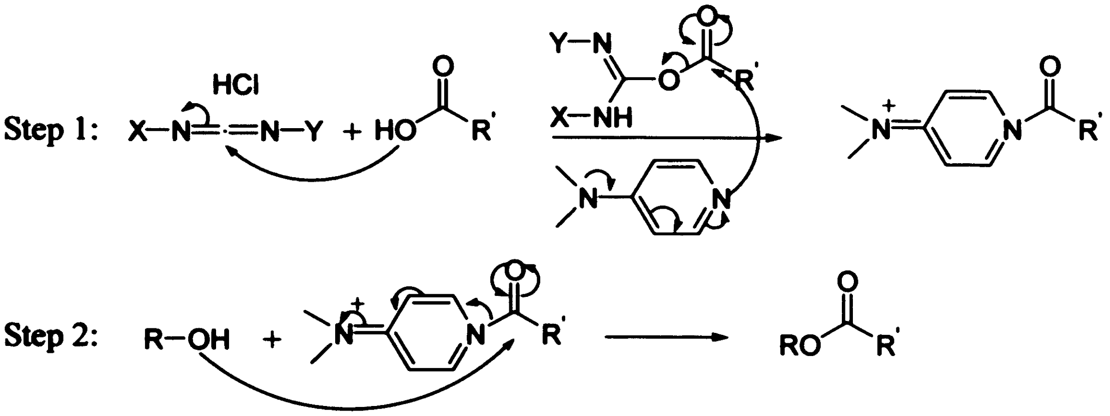

R, R'. Generic hydrocarbon chain
X, Y: indicated in **Scheme 2.16.**

Scheme 2.18. Accepted mechanism for an acid-alcohol coupling reaction.

^{1}H-NMR spectroscopy confirmed the formation of the target compound **2.5**, with the characteristic shift of the hydroxymethylpyridine CH_2 proton from 4.60 ppm to 5.1 ppm upon esterification as discussed in **Section 2.4.1**. An aqueous work up and chromatographic purification afforded a clean product in 46 % yield. **Scheme 2.19.**

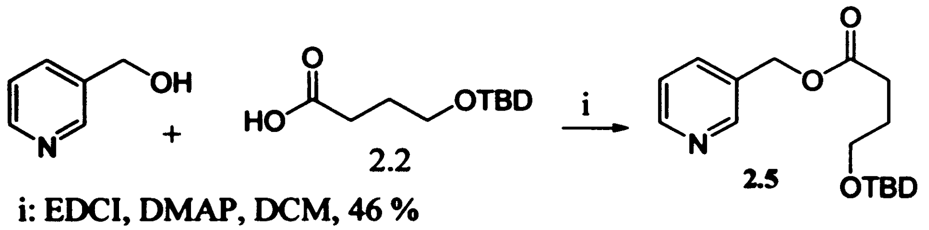

EDCI, DMAP
see **Scheme 2.18.**

Scheme 2.19. Successful synthesis of the desired target, **2.5**.

The advantage of not having to pre-synthesise an activated acid derivative represented a successful outcome in the synthesis of the pyridine derivative that would act as the axial ligand in the rhenium complex. The generality of this route to a range of ligands used throughout this thesis will be discussed in subsequent chapters.

2.5 Results And Discussion: Synthetic Studies Directed Towards Hydroxybutanoate Substituted Complexes.

2.5.1 Synthesis of imaging target *via* an activated tetrafluoroborate rhenium salt.

Following the synthesis proposed in **Scheme 2.5, Section 2.3** (*vide supra*), the second part of this discussion focuses on rhenium coordination chemistry. Taking the synthesis presented in the first instance by Caspar *et al.* in 1983[7] as a guideline, the complex Re(bipy)(CO)$_3$Cl **2.7** was successfully synthesized by the reaction of Re(CO)$_5$Cl in toluene with one equivalent of bipyridine (bipy). The desired product **2.7** was obtained in excellent yield, 98 %, after 1 h. As IR data observed from the synthesised Re(bipy)(CO)$_3$Cl were similar to those previously reported by Caspar no further characterization was carried out.[7]

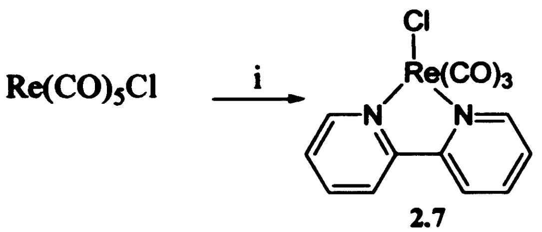

2.7

i: bipy, toluene, 98 %

Scheme 2.20. Synthesis of complex **2.7.**

Halide abstraction was the next step in the synthesis in order to access more easily the hydroxybutanoate substituted complex *via* an activated complex. Silver tetrafluoroborate was used to abstract the chloride because of the high affinity of silver for chloride. The reaction was carried out by heating both reagents in acetonitrile at reflux in the dark (because of the photosensitivity of silver salts), and under an inert atmosphere, **Scheme 2.21.** A coordinating solvent is needed to achieve the final product in order to fill the coordination sphere about the metal centre. However, the choice of solvent is critical as a too strongly bound solvent (*i.e.* pyridine or DMSO) would not dissociate readily in the following derivatisation step.

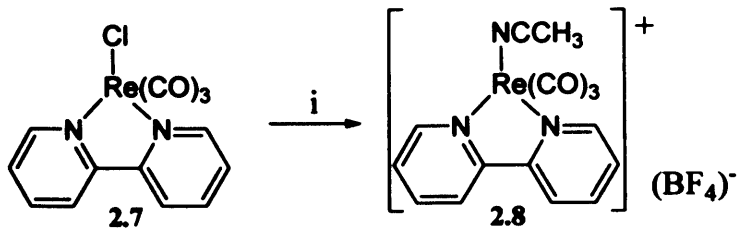

i: AgBF$_4$, CH$_3$CN, 88 %

Scheme 2.21. Halide abstraction with AgBF$_4$.

IR showed the expected change for the transformation of a neutral complex into a cationic species: υ(CO) moved from 2020, 1895 and 1880 cm^{-1} to 2035 and 1918 cm^{-1} (the latter is a broad band) as Re has less electron density to back donate into the carbonyl π^* orbital, thereby increasing the CO bond strength.[21] ^1H-NMR spectroscopic studies in deuterated chloroform corroborated this result, showing a distinctive shift of the coordinated CH_3CN resonance to 2.10 ppm (the resonance for non-coordinated CH_3CN occurs at 2.00 ppm).

The substitution of acetonitrile for the desired axial ligand, **2.5** is the last step in the proposed synthesis shown in **Section 2.3, Scheme 2.5.** Optimisation of the substitution procedure was carried out using simpler pyridine derivative before using the target molecule **2.5** due to the limited supply of this compound.

$[Re(bipy)(CO)_3(CH_3CN)][BF_4]$, **2.8**, was heated at reflux with 10 equivalents of 3-hydroxymethylpyridine in dry THF under a nitrogen atmosphere. Precipitation by addition of diethyl ether to the reaction mixture afforded $[Re(bipy)(CO)_3(PyCH_2OH)][BF_4]$, **2.8** in a 62 % yield. Yellow crystals suitable for X-ray diffraction analysis were grown from a THF/Et_2O solution. Discussion of the crystal structure of **2.9** is in **Section 2.6**.

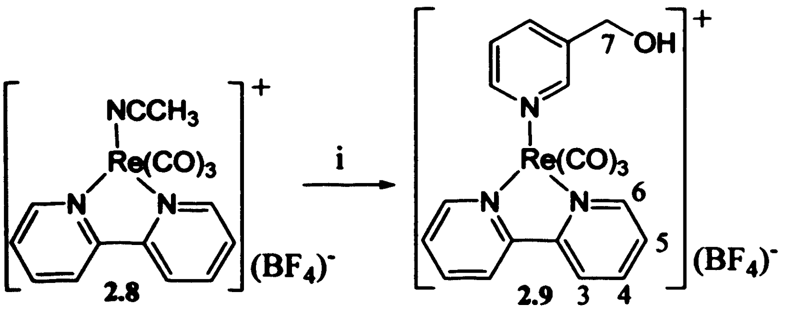

i: $PyCH_2OH$, THF, 62 %

Scheme 2.22. Acetonitrile substitution reaction.

^1H-NMR spectroscopy on a CD_3CN solution of **2.9** indicated a successful reaction as demonstrated by a shift in the resonance for the 3-pyridyl-methylene group $CH_2(7)$ from 4.6 ppm in the free ligand to 4.3 ppm upon coordination. This difference cannot just be due to the loss of electron density from the ligand upon coordination as this would cause a shift to higher frequency as electron density is donated into the metal centre. It is likely that an interaction with the bipyridine π system is responsible for this displacement. The signals observed for the bipyridine moiety have also changed, with chemical shifts that are characteristic of a complex with a pyridine derivative in an axial position (CH(6): from 8.85 to 9.18 ppm; CH(3): from 8.49 to 8.30 ppm; CH(5) from 7.57 to 7.70 ppm). The IR υ(CO) bands also shift to lower frequencies upon coordination of 3-

hydroxymethylpyridine. This is due to the better π-acceptor properties of the ligand in comparison to acetonitrile, in concordance with axial ligand electronic effects over the carbonyls. (The better π-acceptor properties of the axial ligand, the higher vibration frequencies of the carbonyls as the retrodonation from the metal to the antibonding orbitals of the CO decreases).

Once the synthetic route to the target molecule analogue was optimised, the same reaction conditions were employed in an attempt to form [Re(bipy)$(CO)_3$L][BF_4] where L is 3-(4-tert-butyldimethylsilyloxybutanoatomethyl)pyridine **2.5**. However, the isolated product was not the expected complex but of its desilylated derivative, **Scheme 2.23.**

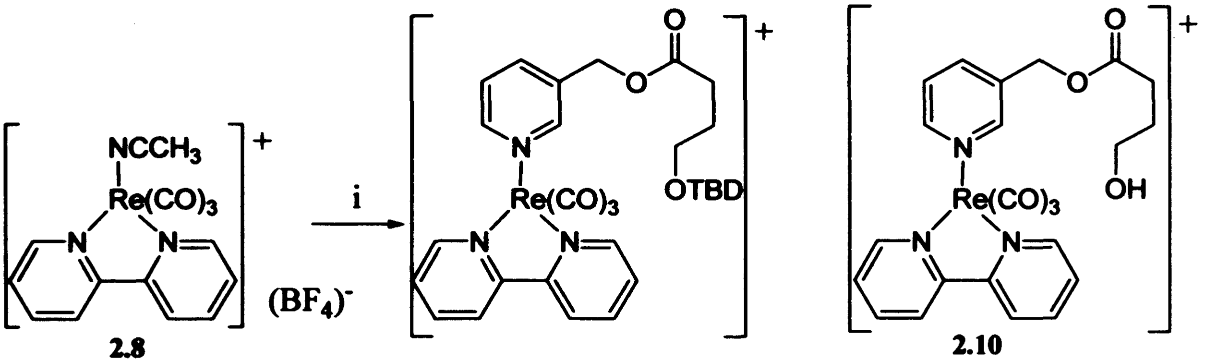

2.8

2.10

Expected complex

Obtained complex

i: **2.5**, THF, 20 %

Scheme 2.23. Synthesis of the desilylated rhenium complex **2.10**.

Mass spectrometry studies confirmed the desilylated structure, no fragments containing $SiMe_2{}^tBu$ were found, *m/z* (ESI) 622.1 $[MH]^+$, 536.1 $[M\text{-}CO(CH_2)_3O]^+$, 427.0 $[M\text{-}BF_4\text{-}PyCH_2OCO(CH_2)OH]^+$. A possible explanation for the desilylation reaction is that the counter anion, BF_4^-, acts as fluoride ion donor which reacts with the silyl group, breaking the Si-O bond, **Scheme 2.4.**

2.5.2 Synthesis of imaging target *via* an activated nitrate rhenium salt.

In order to overcome the desilylation problem a different anion with no reactive fluoride was required. The first approach was to use silver nitrate ($AgNO_3$), instead of silver tetrafluoroborate ($AgBF_4$) for the halide abstraction as the nitrate is a non-coordinating anion which does not contain any fluoride. The same reaction conditions as in **Scheme 2.21** were used; in this case however, the product, complex **2.11**, was very difficult to handle due to its low solubility in a wide range of solvents (chloroform, THF, acetonitrile).

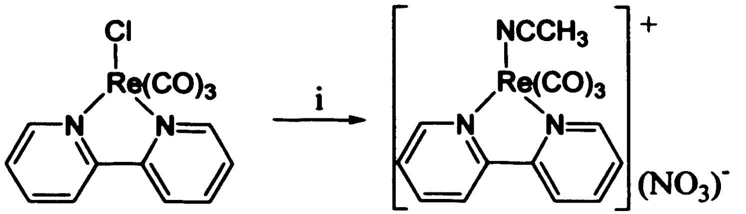

2.7 2.11

i: $AgNO_3$, CH_3CN

Scheme 2.24. Halide abstraction with $AgNO_3$.

Examples of this reaction found in the literature solve this solubility problem by precipitating the product as a PF_6 salt by addition of aqueous ammonium hexafluorophospate (NH_4PF_6) to the reaction mixture.[22] However, it was very likely that the same desilylation reaction would occur if PF_6 was used as the counter ion. Therefore a second abstraction reaction using silver trifluoromethylsulfonate ($AgCF_3SO_3$) was attempted.[6]

2.5.3 Synthesis of imaging target *via* an activated trifluoromethanesulphonate rhenium salt.

Even though silver trifluoromethylsulfonate contains fluorine atoms, they are more strongly bound to carbon *via* a covalent bond than those in BF_4. Presumably, this would prevent any fluoride donation in subsequent reactions. Following the same conditions as described for the halide abstraction, $[Re(bipy)(CO)_3CH_3CN][CF_3SO_3]$ complex **2.12** was synthesised in 74% yield.

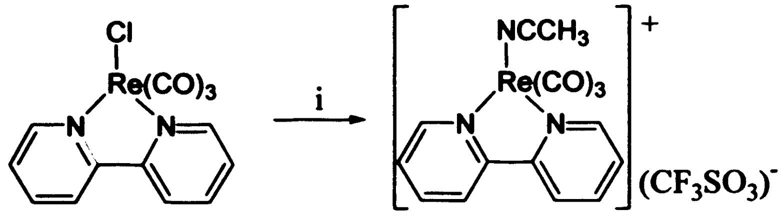

2.7 2.12

i: $AgCF_3SO_3$, CH_3CN, 74 %

Scheme 2.25. Halide abstraction with $AgCF_3SO_3$.

After the reaction of **2.12** and 1.1 equivalents of **2.5** in dry THF, the acetonitrile ligand was successfully substituted and the final target (complex **2.13**) thus synthesised. Confirmation was given by ^{1}H-NMR spectra in CD_3CN which showing the characteristic shift from 5.1 to 5.0 ppm of the resonance for the 3-pyridylmethylene group CH_2(7), indicating that coordination had occurred, **Scheme 2.25.** The aromatic protons on bipy are also shifted due to the presence of the new axial ligand. These shifts are in concordance with the data reported for complex **2.9**: CH(6) from 8.88 to 9.08 ppm, CH(3) from 8.61 to 8.79 ppm and CH(5) from 7.59 to 7.80-7.71 ppm. Yellow crystals were obtained after addition of petroleum ether to the reaction mixture, which were too small for standard X-ray diffraction and so were analysed using synchrotron X-ray studies (*vide infra*).

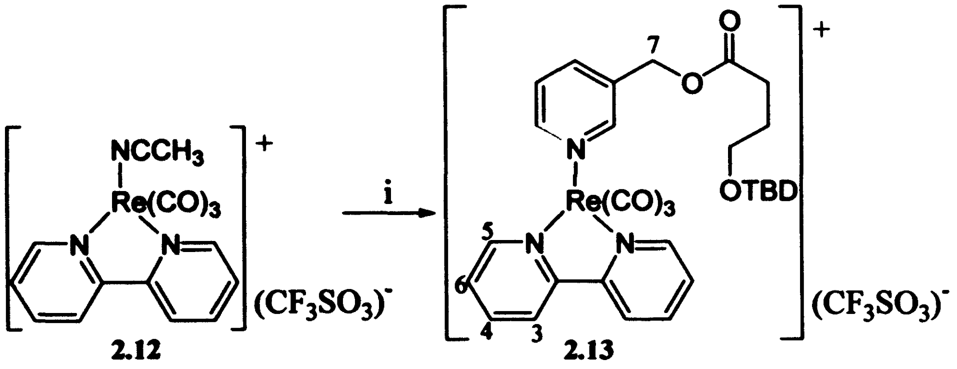

i: **2.5**, THF, 45 %

Scheme 2.26. Synthesis of the designed target **2.13**.

2.6 Crystalline Structures Discussion.

Solid state structures of complexes **2.9**[c] and **2.13**[d] were determined by standard X-ray crystallography and Synchrotron X-ray[23] respectively. The structures are presented as ORTEP drawings in **Figure 2.3** and **Figure 2.4**. Details of collection and refinement data and selected bond lengths and angles for **2.9** and **2.13** are given in **Table 2.1**, **Table 2.2**, **Table 2.3**, **Table 2.4** respectively.

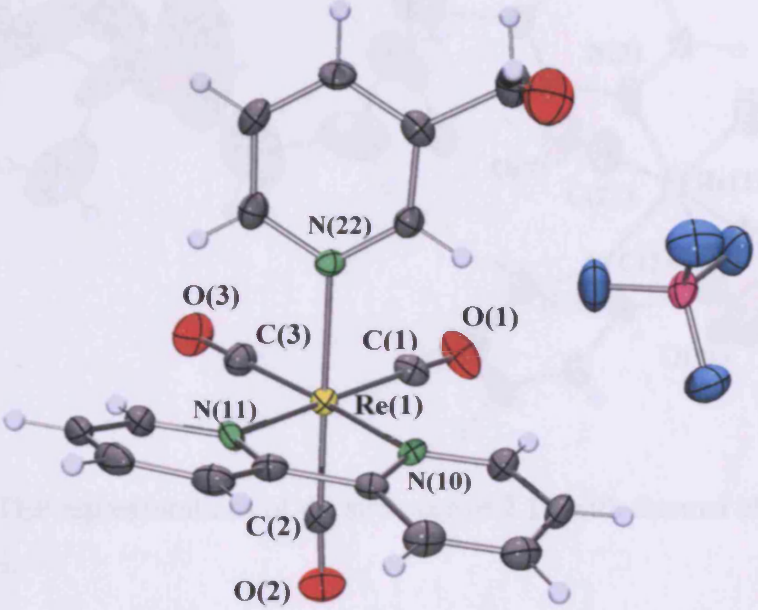

Figure 2.3. ORTEP representations of the structure of **2.9** with thermal ellipsoids drawn at the 50 % level.

---

[c] Crystal structure measured and solved by Dr Elena Davis at Cardiff University.

[d] Crystal structure measured and solved by Dr. Madeleine Helliwel at Daresbury Laboratory.

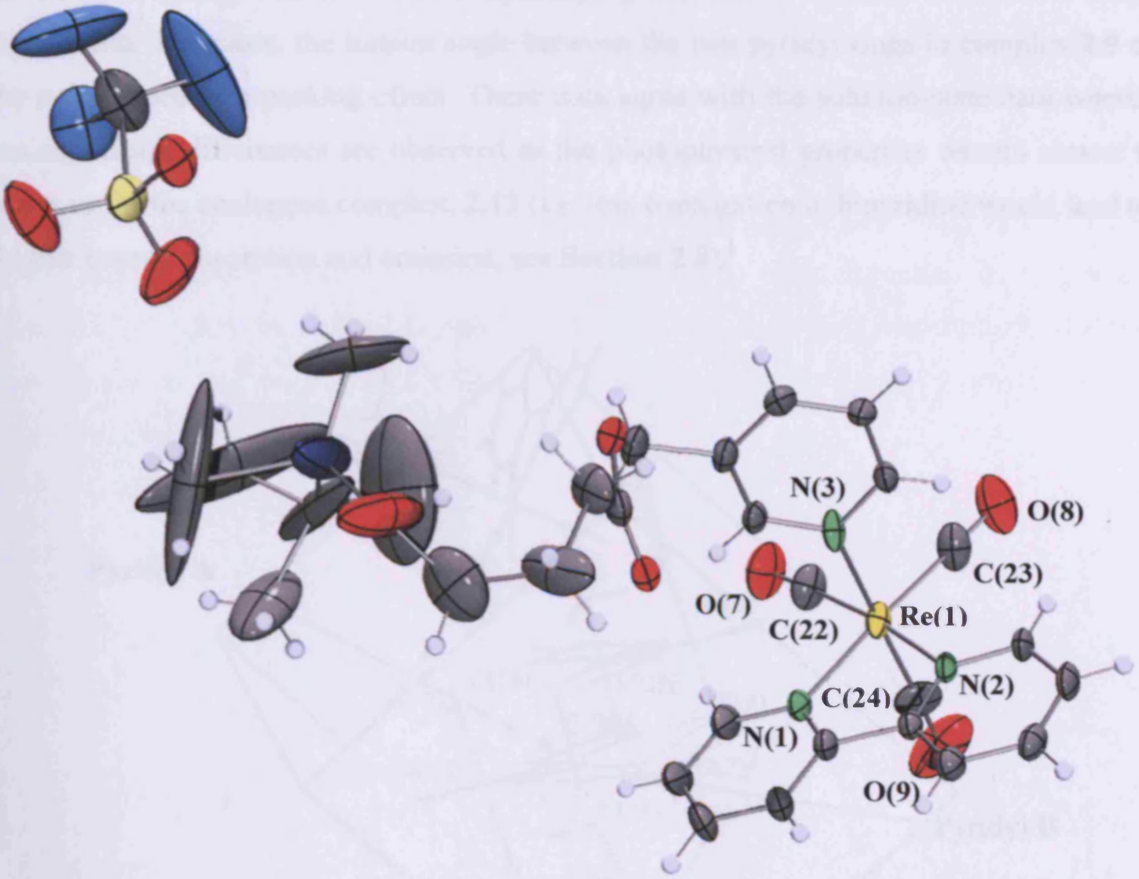

Figure 2.4. ORTEP representations of the structure of **2.13** with thermal ellipsoids drawn at the 50 % level.

Both complexes feature a distorted octahedral coordination geometry around the Re(I) centre. The Re-to-bipyridine nitrogen bonds are *ca*. 2.172 Å in length which is typical for Re(I) complexes.[24] Furthermore, the two pyridine rings of the bipyridine ligand in complex **2.13** are almost coplanar (0.14° torsion angle between the two rings). This may promote better delocalization of the π-electronic system and confer better π-acceptor properties on this ligand than in the case of complex **2.9** where the bipyridine ligand displays an inter ring angle of about 14.73°.

Examination of the packing in complex **2.9** shows a different environment and interactions of each pyridyl unit within the bipyridine, **Figure 2.5**. Pyridyl A displays a short interaction with a fluorine atom from one of the counterions surrounding the molecule, as well as a non-symmetrical π stacking interaction with a bipyridine of an adjacent molecule. Not only are the same interactions observed for Pyridyl B but also interactions with two axial carbonyls belonging to two other molecules within the unit cell. Moreover, Pyridyl B is within bonding distance with a hydroxyl group and a fluorine atom of a second counterion. Therefore, the torsion angle between the two pyridyl rings in complex **2.9** can be rationalized as a packing effect. These data agree with the solution-state data whereby no significant differences are observed as the photophysical properties remain almost the same as for the analogous complex, **2.13** (*i.e.* less conjugation in bipyridine would lead to a higher energy absorption and emission, see **Section 2.8**).

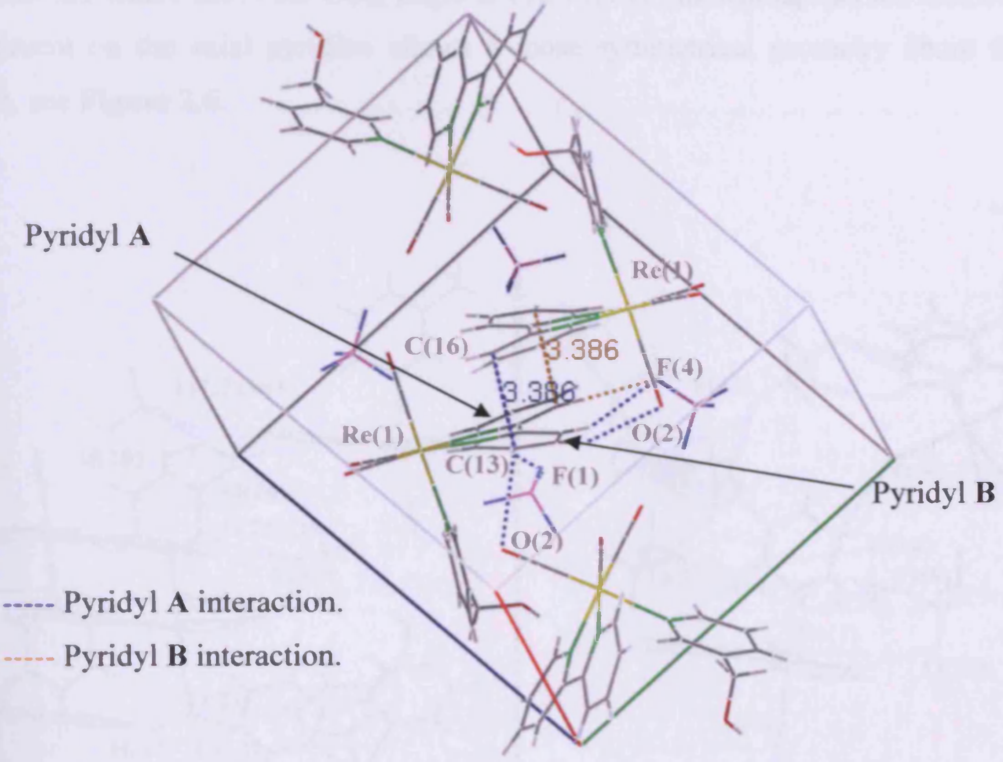

Figure 2.5. Packing of complex **2.9** and short interactions of the two pyridyl units.

The distance between the metal and the carbon atom of the carbonyl units *trans* to the chelated ligand, which define the equatorial plane, in species **2.9** and **2.13** range between 1.912(6) and 1.929(8) Å respectively, and agree with the corresponding values found in the literature for complexes of the same type *i.e* $[Re(CO)_3(\alpha\text{-diimide})]^+$.[23] The $Re\text{-}CO_{ax}$ distance (the carbonyl in the *cis* position to both of the bipyridine nitrogen atoms is referred to as the axial CO ligand) is affected by the nature of the ligand *trans* to it. In both cases the *trans* ligand is a pyridine derivative, 3-hydroxymethylpyridine and 3-(4-tertbutyldimethylsilyloxybutanoatomethyl)pyridine. The N-Re distances are 2.221(4) Å and 2.184(5) Å respectively. The shorter bond length in complex **2.13** (2.184(5) Å) suggests better π-acceptor versus σ-donor properties for **2.5** over that of 3-

hydroxymethylpyridine. This is also reflected in the Re-CO$_{ax}$ and C-O$_{ax}$ bond lengths being 1.929(8) and 1.137(11) Å respectively. These distances are slightly longer and shorter in that order than the analogous bonds in complex **2.9** (Re-CO$_{ax}$: 1.912(6) and C-O$_{ax}$: 1.150(7) Å).

The long chain attached to the pyridine derivative in complex **2.13** distorts the N-Re-CO$_{ax}$ angle from perfect octahedral geometry to 176.4(2)°. Less distortion is observed in complex **2.9** where the N-Re-CO$_{ax}$ angle is 178.27(18)°, indicating that the lack of a bulky substituent on the axial pyridine allows a more symmetrical geometry about the metal centre, see **Figure 2.6.**

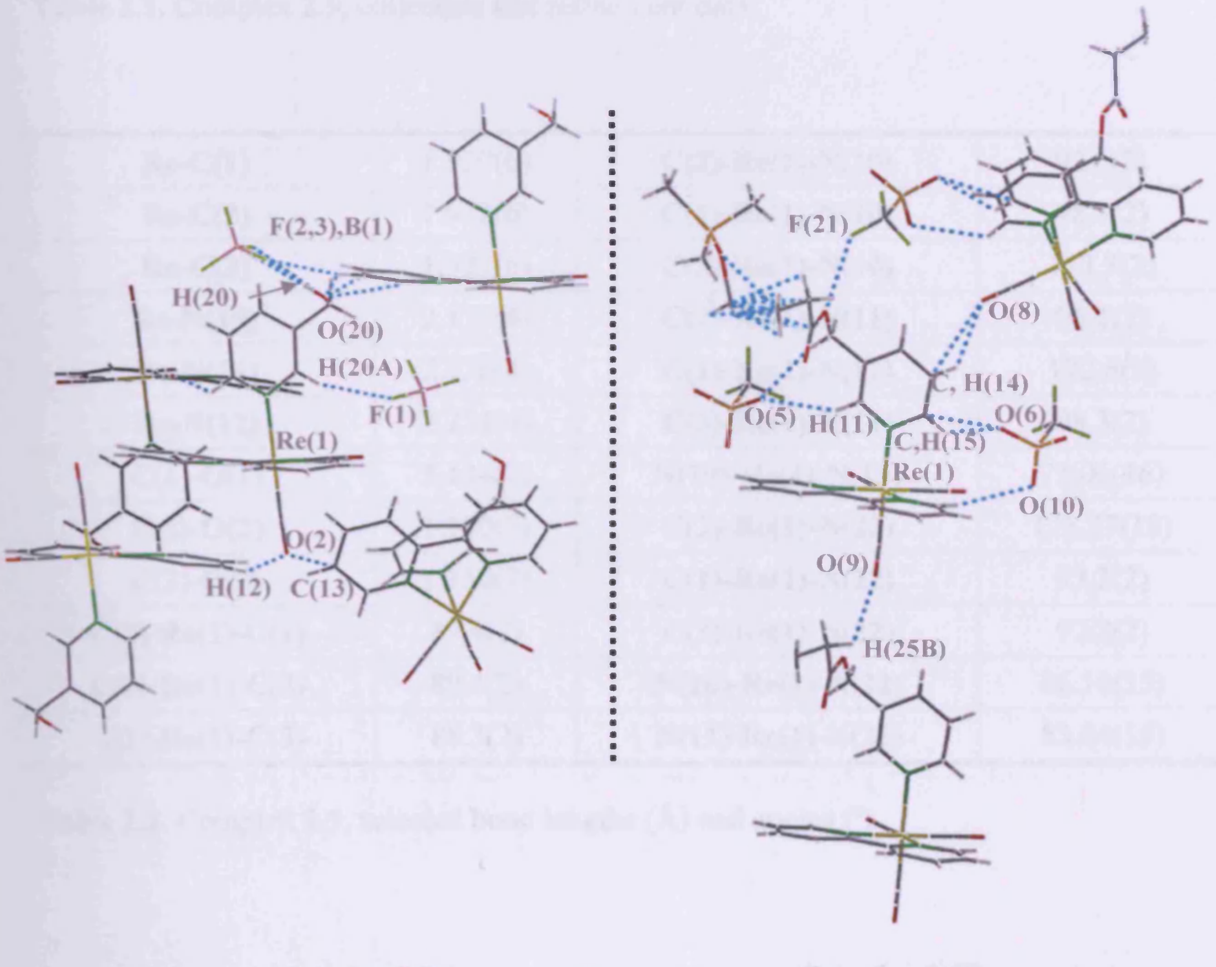

Complex **2.9** Complex **2.13**

Figure 2.6. Short intermolecular interactions of the complexes **2.9** (left picture) and **2.13** (right picture).

Empirical Formula	$C_{19}H_{15}BF_4N_3O_4Re$	**a (Å)**	10.2550
Molecular weight	622.35	**b (Å)**	12.5820
Crystal system	monoclinic	**c (Å)**	15.6370
Space group	$P\ 2_1/c$	**α (°)**	90
Volume (Å^3)	2012.69	**β (°)**	94.006
Z	4	**γ (°)**	90

Table 2.1. Complex 2.9, collection and refinement data.

Re-C(1)	1.920(6)	**C(2)-Re(1)-N(10)**	92.2(2)
Re-C(2)	1.912(6)	**C(1)-Re(1)-N(10)**	98.3(2)
Re-C(3)	1.922(6)	**C(3)-Re(1)-N(10)**	173.3(2)
Re-N(10)	2.172(4)	**C(2)-Re(1)-N(11)**	96.1(2)
Re-N(11)	2.176(4)	**C(1)-Re(1)-N(11)**	172.6(2)
Re-N(12)	2.221(4)	**C(3)-Re(1)-N(11)**	98.3(2)
C(1)-O(1)	1.144(7)	**N(10)-Re(1)-N(11)**	75.06(16)
C(2)-O(2)	1.150(7)	**C(2)-Re(1)-N(22)**	178.27(18)
C(3)-O(3)	1.150(7)	**C(1)-Re(1)-N(22)**	93.3(2)
C(2)-Re(1)-C(1)	87.4(2)	**C(3)-Re(1)-N(22)**	92.2(2)
C(2)-Re(1)-C(3)	89.4(2)	**N(10)-Re(1)-N(22)**	86.16(15)
C(1)-Re(1)-C(3)	88.3(2)	**N(11)-Re(1)-N(22)**	83.04(16)

Table 2.2. Complex 2.9, selected bond lengths (Å) and angles (°).

Empirical Formula	$C_{30}H_{35}F_3N_3O_9ReSSi$	**a (Å)**	11.1847(8)
Molecular weight	884.96	**b (Å)**	13.3116(10)
Crystal system	monoclinic	**c (Å)**	24.0160(18)
Space group	$P2_1/c$	**α (°)**	90
Volume (Å^3)	3558.7(5)	**β (°)**	95.5780(10)
Z	4	**γ (°)**	90

Table 2.3. Complex 2.13, collection and refinement data.

Re(1)-C(24)	1.907(8)	**C(24)-Re(1)-N(1)**	92.8(3)
Re(1)-C(22)	1.927(7)	**C(22)-Re(1)-N(1)**	97.3(3)
Re(1)-C(23)	1.942(8)	**C(23)-Re(1)-N(1)**	174.2(2)
Re(1)-N(1)	2.171(5)	**C(24)-Re(1)-N(2)**	92.4(2)
Re(1)-N(2)	2.169(5)	**C(22)-Re(1)-N(2)**	172.1(3)
Re(1)-N(3)	2.201(5)	**C(23)-Re(1)-N(2)**	99.4(2)
O(7)-C(22)	1.138(9)	**N(1)-Re(1)-N(2)**	74.94(18)
O(8)-C(23)	1.112(10)	**C(24)-Re(1)-N(3)**	176.2(2)
O(9)-C(24)	1.163(10)	**C(22)-Re(1)-N(3)**	94.2(3)
C(24)-Re(1)-C(22)	89.4(3)	**C(23)-Re(1)-N(3)**	93.0(3)
C(24)-Re(1)-C(23)	88.4(4)	**N(1)-Re(1)-N(3)**	85.39(19)
C(22)-Re(1)-C(23)	88.4(3)	**N(2)-Re(1)-N(3)**	83.80(17)

Table 2.4. Complex 2.13, selected bond lengths (Å) and angles (°).

2.7 The "Self Destruction" Experiment.

After the successful synthesis of the desired target **2.13**, the concept of the *linker self-destruction* mechanism proposed in **Scheme 2.4, Section 2.2.5** was studied. This experiment was designed to test if, after deprotection of the alcohol, the reaction proceeds to lactone formation, indicating that the cyclisation reaction (*linker self-destruction)* has taken place successfully. This study could also point towards an explanation as to why, in the synthesis of complex **2.10**, no cyclisation process was observed, **Scheme 2.23**.

Following the same conditions found in the literature for the desesterification reaction when SOB is used as esterification agent, tetrabutylammoniumfluoride, TBAF, was used as a fluoride source, and THF as solvent.[3] The reaction was carried out on a ^{1}H-NMR spectroscopic scale and was monitored by this technique. Typical experimental conditions used 4.5 mM of **2.13** and 38 mM of TBAF.

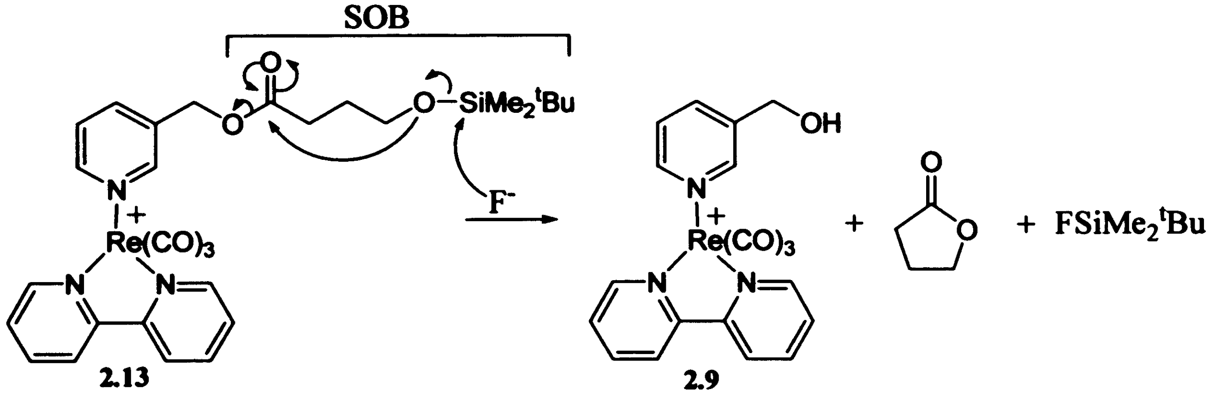

Scheme 2.27. Proposed *chain self-destruction* mechanism.

^{1}H-NMR spectra in THF-d_8 are shown in **Figure 2.6**. After the addition of TBAF, the peaks from the protons A, B and C of the butyryl chain attached to the 3-hydroxymethylpyridine disappear and three new peaks (A', B' and C') from the butyrolactone appear indicating that not only has the desilylation taken place, but also the *chain self-destruction* that leads to the butyrolactone formation has been a success.

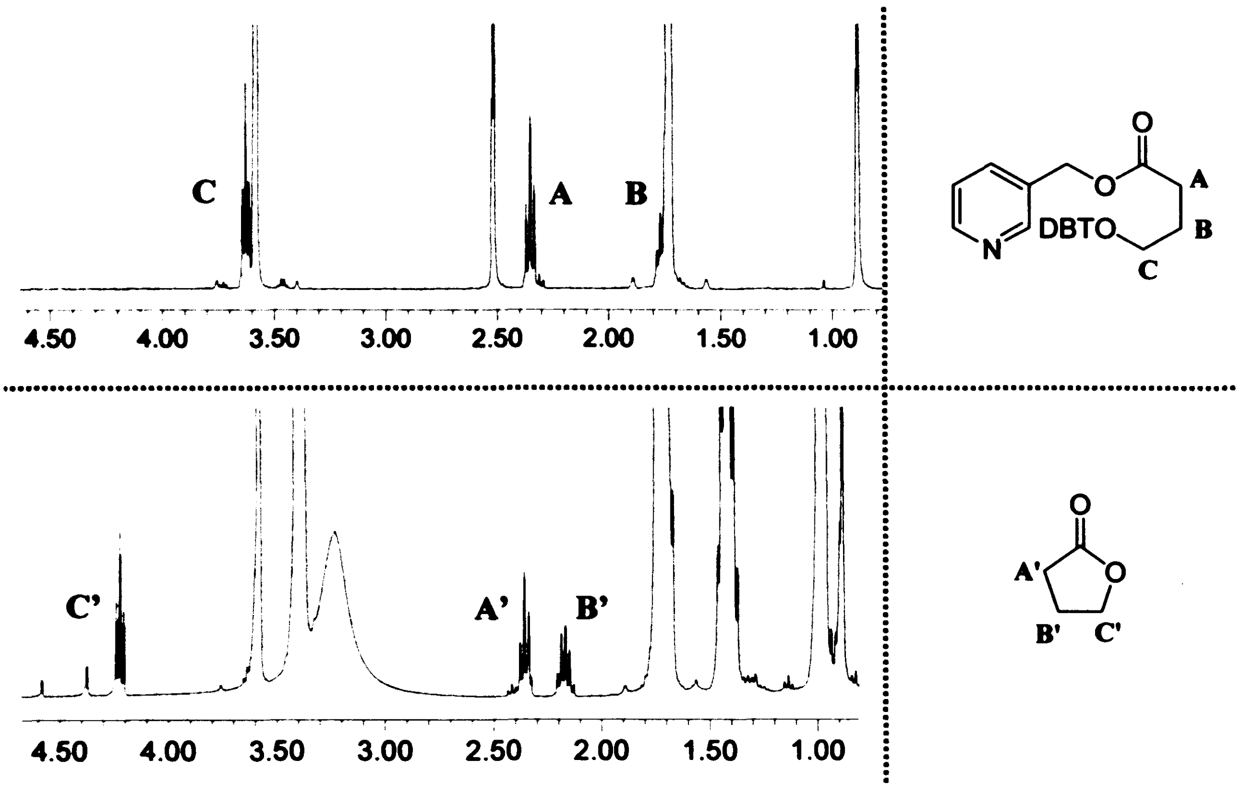

Figure 2.7. ^{1}H-NMR spectra (aliphatic region) of the pre and post-cyclisation species of the *chain self-destruction* experiment.

The reaction was also explored in different solvents in order to optimize the process and assess its suitability for use under physiological conditions. A summary of the results obtained are listed in **Table 2.5.**

	THF	$CDCl_3$	MeOD
Deprotection Reaction	Immediate (<5 min)	Slow (>12 h)	Slow (>12 h)
Desilylated product	Not observable	Not observable	Observable (15 days)
Cyclisation Reaction	Immediate (<5 min)	Immediate (<5 min)	Slow

Table 2.5. Summary.

The deprotection reaction and desilylated product are shown in **Scheme 2.28**, and the cyclisation reaction is shown in **Scheme 2.29**.

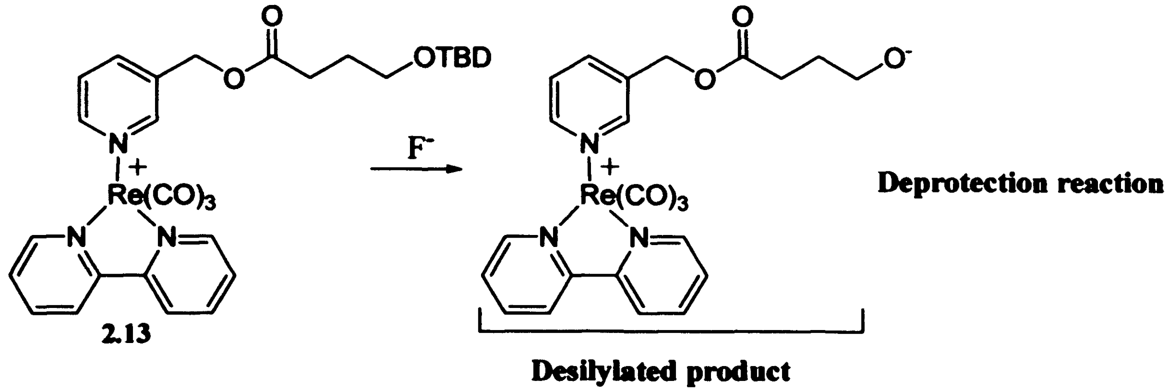

Scheme 2.28. Deprotection reaction and desilylated product.

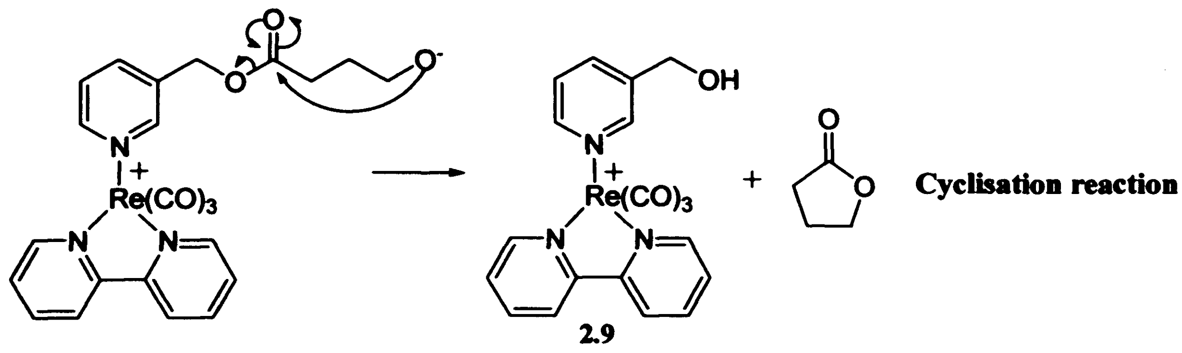

Scheme 2.29. Cyclisation reaction.

To understand these results some physical properties related to the solvent and the tetrabutylammonium salt, TBAF, should be considered. Depending on the polarity of the solvent, the ion pair, TBAF, is going to be more or less dissociated, facilitating the attack of fluoride at the silyl group. A compromise is needed in order not to exceed a particular polarity as not only is it responsible for the ion pair dissociation but also solvation of fluoride. Therefore, TBAF in a very polar solvent will be highly solvated which can slow down the desilylation reaction. According to these principles, a solvent like MeOH makes the deprotection reaction slower. Moreover, as MeOH is a protic solvent it slows down the cyclisation reaction, due to the protonation of the alkoxide, leaving only a small equilibrium concentration of alkoxide, which is the rapidly cyclising species in aprotic solvents.

Among the different conditions used, THF was found to be the most convenient solvent for the *self-destruction* reaction. Probably its high polarity, 4.1 P', and dipole moment, 1.63 Debye, facilitates dissociation of TBAF to give the free fluoride ion and its consequent attack at the silyl group. Moreover, the fact that THF is a non-protic solvent makes the final cyclisation easier as there are no proton sources that can protonate the alkoxide. In fact, when a protic solvent like MeOH is used instead of THF, the desilylated product is observed for up to 15 days until the final cyclisation is concluded, see **Scheme 2.29**.

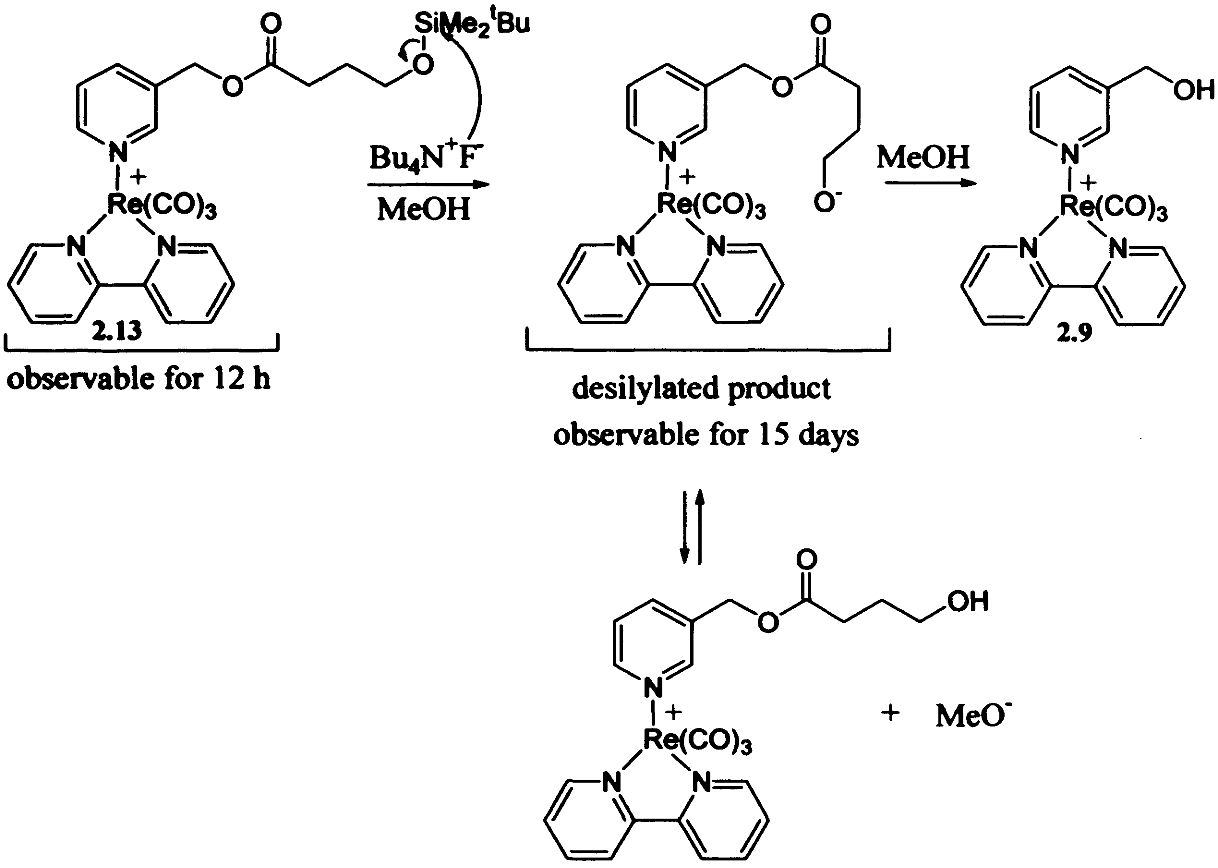

Scheme 2.30. *Chain self-destruction* experiment in MeOH.

Further studies were performed in $CDCl_3$ where, once again, its polarity and dipole moment, 4.1 Debyes and 1.04 P' respectively, can be used to explain the reaction rate differences from the other two solvents, MeOH and THF. In this case the deprotection reaction is slower than when THF is used as a solvent, probably because its low dipole moment does not allow easy TBAF ionisation. In comparison to MeOH, the cyclisation reaction is faster as chloroform is a non-protic solvent which will not interfere with the cyclisation process, **Scheme 2.31**.

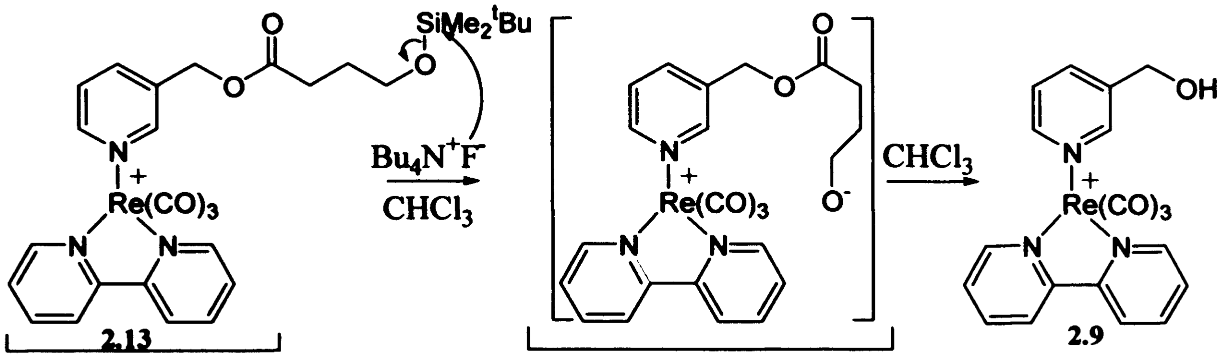

2.13

observable for 12 h

desilylated product
not observable

2.9

Scheme 2.31. *Chain self-destruction* experiment in CHCl$_3$.

A possible explanation for the lack of cyclisation observed in **Scheme 2.23** (Synthesis of the desilylated rhenium complex, **2.10**) could be because no TBAF was used during the reaction. Hence, the basicity of the system is insufficient for the cyclisation reaction to take place (F$^-$ is quite basic in water and TBAF always contains some water as anhydrous TBAF is not stable).[25] It is worth remembering that Ganem[2] showed that, on ester deprotection using BOB as a protecting group, a non-nucleophilic base is needed to cyclise the butyrate fragment, **Scheme 2.32.** The assumed desilylation conditions for complex **2.10** (*i.e.* F$^-$ from BF$_4^-$) are likely, via hydrolysis, to lead to an acidic environment through boric acid formation.

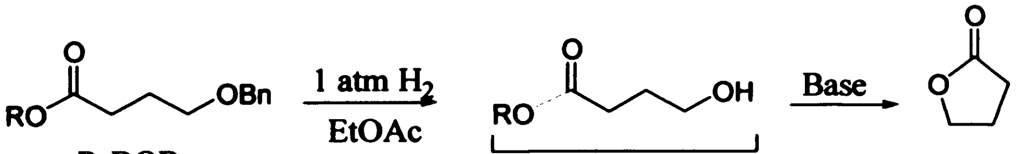

R-BOB

Does not cyclise
unless the medium is
basic enough

R: generic hydrocarbon chain

Scheme 2.32. Cyclisation conditions of R-BOB.

2.8 Photophysical Studies.

Photophysical studies of complexes **2.9** and **2.13** were carried out in order to assess their viability as biological probes. The electronic absorption spectra of both complexes were measured at room temperature and in acetonitrile solution; their spectral data are summarized in **Table 2.6.** With reference to previous studies of related rhenium (I) polypyridine complexes,[26] the intense absorption bands at *ca.* 246-318 nm have been assigned to spin-allowed intraligand (^{1}IL) ($\pi \rightarrow \pi^*$) (N-N and pyridine ligand) transitions. Additionally, the absorptions at *ca.* 340-342 nm has been assigned to spin-allowed metal-to-ligand charge-transfer (^{1}MLCT) ($d\pi(Re) \rightarrow \pi^*(N\text{-}N)$), transitions. An example of a UV spectrum of **2.9** is shown in **Figure 2.6**.

Complex	^{1}IL, λ_{abs}/nm (ε/dm^{3}mol^{-1}cm^{-1})	^{1}MLCT, λ_{abs}/nm, (ε/dm^{3}mol^{-1}cm^{-1})
2.9[a]	248 (4590), 264 (4605), 306 (2862), 318 (2240)	342 (980)
2.13[a]	246 (2917), 257 (2808), 306 (1962), 317 (1423)	340 (642)

a CH_3CN as solvent.

Table 2.6. Absorption band assignments.

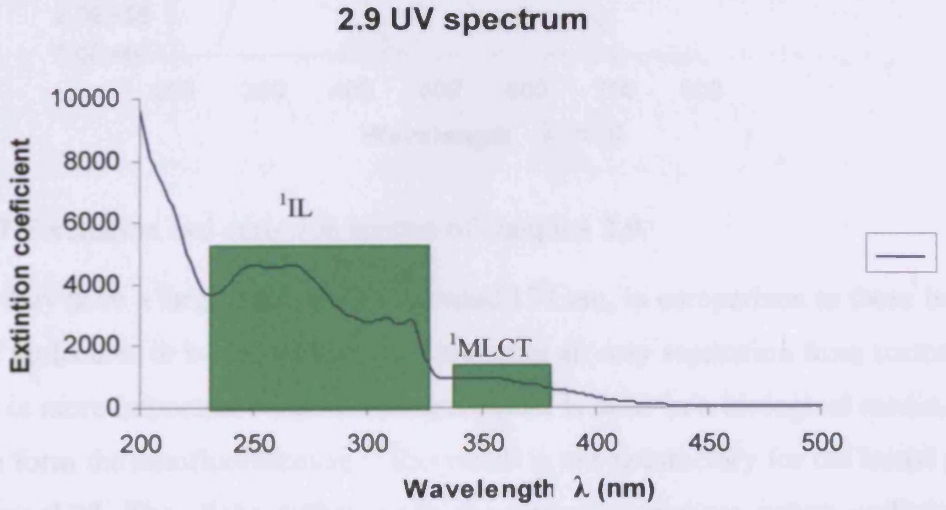

Figure 2.6. UV spectrum example of complex **2.9**.

The excitation and emission spectra were also recorded. These types of complex show an emission originating from the lowest energy ^{3}MLCT, ($d\pi(Re) \rightarrow \pi^*(N\text{-}N)$) excited state, *i.e.* phosphorescence. The luminescent properties of both complexes, **2.9** and **2.13**, do not differ from those that have previously been observed for ^{3}MLCT based emission from related rhenium bis(imide) complexes.[27] Both complexes presented broad excitation maxima at around 390 nm and also broad emission maxima, specifically 555 nm in the case of complex **2.13** and 556 nm for complex **2.9**, see emission and excitation spectra in **Figure 2.7**. In addition, the value of the lifetimes for both species do not differ significantly, 117 ns in the case of complex **2.9** and 127 ns for complex **2.13**, see **Table 2.7**. An example of the typical excitation and emission spectra can be seen in **Figure 2.7**.

Complex	Excitation$_{max}$ (λ/nm)	Emission$_{max}$ (λ/nm)	Lifetimes (τ/ns)
2.9$_a$	392	556	117
2.13$_a$	385	555	127

a CH_3CN as solvent.

Table 2.7. Excitation and emission maxima for **2.9** and **2.13**.

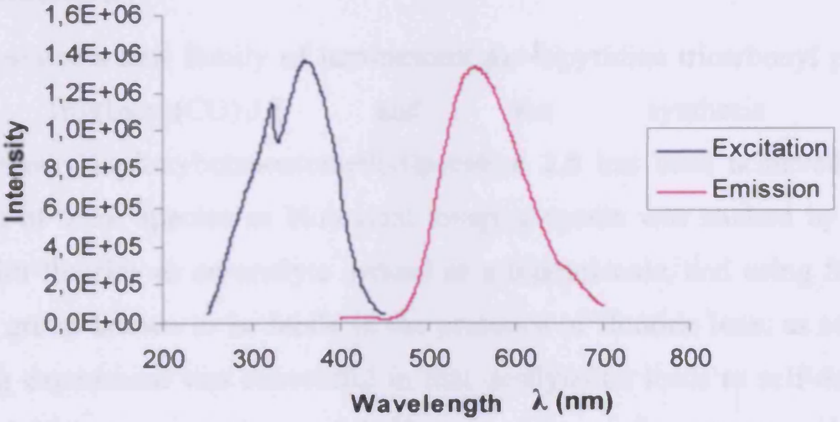

Figure 2.7. Excitation and emission spectra of complex **2.9**.

Although they have a large Stokes' shift, around 177 nm, in comparison to those belonging to organic molecules or biomolecules, thus allowing an easy separation from scattered light and, what is more important when the measurement is done in a biological media, an easy separation form the autofluorescence,[28] this result is not satisfactory for the initial purpose, see **Scheme 2.33**. The slight difference in the emission maxima values and also in the intensity of the bands between the initial imaging agent, **2.13**, and the self destructed complex, **2.9**, is probably due to the small electronic effect that changes in the pyridine susbtituent induce at the metal centre. This makes it difficult to calculate the exact concentration of analyte that has reacted with the initial complex and therefore the concentration of the analyte in the studied medium.

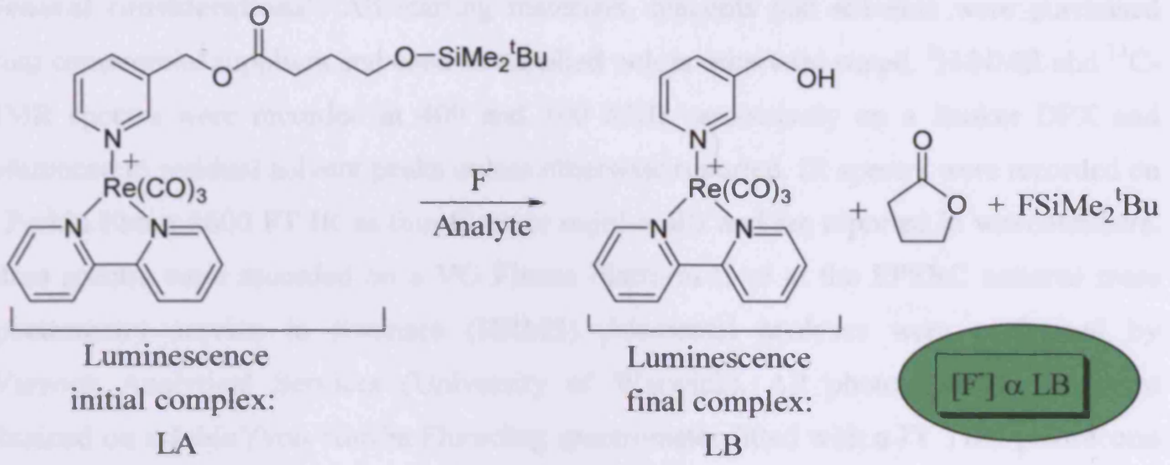

Scheme 2.33. Sensing experiment.

2.9 Conclusions

The synthesis of a new family of luminescent *fac*-bipyridine tricarbonyl pyridyl rhenium cations $[Re(bipy)(CO)_3L]$ and the synthesis of 3-(4-tertbutyldimethylsilyloxybutanoatomethyl)pyridine **2.5** has been achieved. The potential application of these species as biological imaging agents was studied by mimicking the process with fluoride as an analyte instead of a biomolecule, and using SOB, an alcohol protecting group known to be labile in the presence of fluoride ions, as sensor. Although the sensing experiment was successful in that desilylation leads to self-destruction, there are some problems to overcome, mainly the rate of the sensing process and the insolubility of the complexes in physiological conditions (*i.e.* aqueous systems).

The promising photophysical properties of **2.9** and **2.13** need to be tuned in order to enlarge the difference between the maxima of the emission peaks f the iornitial target, **2.13**, and the product **2.9,** in order to facilitate determination of the analyte concentration. Introduction of water solubilising groups such as sulphonates in the chelate ligand or the axial pyridine derivative could be the answer to the solubility issues. Modification to the axial ligand is crucial in order to increase the rate of cyclisation by, for example, improving the leaving group. All these changes would alter the electronic properties of the imaging agent and therefore their luminescent properties, thereby allowing easier differentiation of the pre- and post-cyclisation species.

2.10 Experimental

General considerations[e]: All starting materials, reagents and solvents were purchased from commercial suppliers and used as supplied unless otherwise stated. ^{1}H-NMR and ^{13}C-NMR spectra were recorded at 400 and 100 MHz respectively on a Bruker DPX and referenced to residual solvent peaks unless otherwise reported. IR spectra were recorded on a Perkin Elmer 1600 FT IR as thin films or nujol mulls and are reported in wavenumbers. Mass spectra were recorded on a VG Fisons Platform II or at the EPSRC national mass spectrometry service in Swansea (HRMS). Elemental analyses were performed by Warwick Analytical Services (University of Warwick). All photophysical data were obtained on a JobinYvon-Horiba Fluorolog spectrometer fitted with a JY TBX picosecond photodetection module and a Hamamatsu R5509-73 detector (cooled to –80 °C using a C9940 housing). The pulsed laser source was a Continuum Minilite Nd:YAG configured for 355 nm output. Lifetimes were obtained using the JY-Horiba FluorHub single photon counting module. Estimated errors are τ_{em} ± 10% and excitation and emission maxima are limited in accuracy to the monochromator slit width of 5 nm.

Sodium 4-hydroxybutylacetate (2.1).[12]

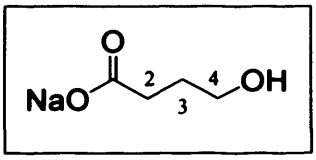

To a solution of γ-butyrolactone (11.2 g, 0.13 mol) in methanol (10 ml) was added sodium hydroxide (5.2 g, 0.13 mol). The solution was heated at reflux for 2 hours. Finally the methanol was removed on a rotary evaporator and the product was recovered as a white solid. (14.4 g, 88 % yield). δH (D_2O) 3.45 (2H, t, J = 6.6 Hz, CH_2(4)), 2.08 (2H, t, J = 7.6 Hz, CH_2(2)), 1.65 (2H, m, CH_2(3)).

4-terbutyldimethylsilyloxybutanoic acid (2.2).[15]

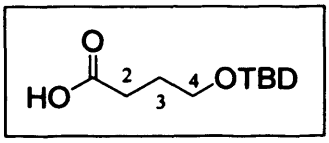

To a solution of sodium 4-hydroxybutylacetate (2.5 g, 19.8 mmol) in pyridine (25 ml) was added *tert*-butyldimethylsilyl chloride (3.0 g, 19.8 mmol). The reaction was stirred at room temperature for 72 hours. After this, ammonium chloride solution (saturated, 25 ml) was added and the mixture was neutralized with hydrochloric acid 0.5 M. Then it was extracted with ether (3 × 25ml) and finally the organic phase was extracted with copper sulphate solution (20 ml)

---

[e] *NB*. These general considerations are applicable to all the experimental sections throughout this thesis.

and dried with magnesium sulphate. Distillation gave the product as colourless oil. (1.2 g, 28 % yield). δH ($CDCl_3$) 3.56 (2H, t, J = 3.3 Hz, CH_2(4)), 2.30 (2H, t, J = 6.5 Hz, CH_2(2)), 1.81 (2H, m, CH_2(3)), 0.89 (9H, m, ($SiC(CH_3)_3$)), 0.01 (6H, m, ($Si(CH_3)_2$)). ν_{max} (Nujol) 1714 (CO).

Potassium 4-*tert*-butyldimethylsilyloxybutanoate (2.3).

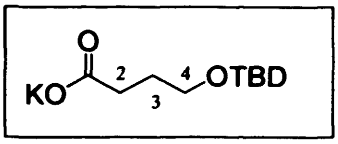

4-*tert*-butyldimethylsilyloxybutanoic acid (1.8 g, 1.2 mol) and potassium tert-butoxide (0.9 g, 1.2 mol) were stirred in solution in methanol (20 ml) under a nitrogen atmosphere at reflux for 3 hour. After removing the solvent on a rotary evaporator, 10 ml of toluene was added and subsequently evaporated. This process was repeated 4 times. Finally the product, **2.3**, was obtained as a yellow solid. (1.6 g, 76 % yield). δH (D_2O) 3.58 (2H, t, J = 6.6 Hz, CH_2(4)), 2.10 (2H, t, J = 7.2 Hz, CH_2(2)), 1.68 (2H, m, CH_2(3)), 0.80 (9H, m, $SiC(CH_3)_3$), 0.01 (6H, m, $Si(CH_3)_2$). δC ($CDCl_3$) 184 (*C*(1)), 64 (*C*(2)), 34 (*C*(4)), 28 (*C*(3)), 25 (SiC(*C*H$_3$)$_3$), 18 ((Si*C*)). ν_{max} ($CHCl_3$) 1564 (CO).

- Attempts towards the synthesis of 3-(4-*tert*-butyldimethylsilyloxybutanoatomethyl)pyridine (2.5).

A. *Via* an acyl chloride adduct (successful reaction but low yield).

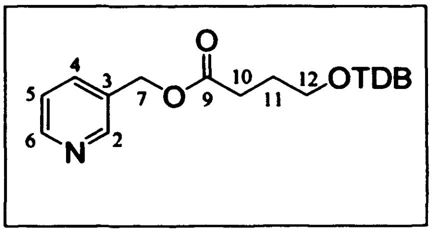

To a solution of potassium 4-*tert*-butyldimethylsilyloxybutanoate, **2.3**, (1.0 g, 4.0 mmol) in chloroform (10 ml) was added dropwise oxalyl chloride (0.36 ml, 4.0 mmol). The mixture was stirred at room temperature and under a nitrogen atmosphere for ½ hour. Then a solution of 3-(hydroxymethyl)pyridine (0.38 ml, 4.0 mmol) and triethylamine (0.38 ml, 4.0 mmol) in chloroform was added dropwise. After 16 hours stirring, 10 ml of dichloromethane was added and it was extracted with an aqueous solution of saturated sodium hydrogen carbonate (10 ml) and dried with magnesium sulphate. The product, **2.5** was purified by chromatography on silica using petroleum ether and ethyl acetate (7:3), R_f = 0.7, as eluent to give the product as a clear oil (0.1 g, 10 % yield). δH ($CDCl_3$) 8.60 (1H, s, C*H*(2)), 8.54 (1H, m, C*H*(6)), 7.68 (1H, m, C*H*(4)), 7.30 (1H, m, C*H*(5)), 5.10 (2H, s, CH_2(7)), 3.62 (2H t, J = 6.1 Hz, CH_2(12)), 2.42 (2H, t, J = 7.4 Hz, CH_2(10)), 1.82 (2H, m, CH_2(11)), 0.85 (9H, s, $SiC(CH_3)_3$), 0.0 (6H, s, $Si(CH_3)_2$). δC ($CDCl_3$) 172.3 (C(9)), 148.6 (C(6)), 148.5 (C(2)), 134.9 (C(4)), 130.6 (C(3)), 122.4 (C(5)), 62.5 (C(7)), 60.8 (C(12)), 29.6 (C(10)), 26.7 (C(11)), 24.8 (SiC(CH_3)$_3$), 17.3 (SiC). ν_{max} ($CHCl_3$) 1740 (CO). *m/z* EI/CI 310.2 $[MH]^+$, 252.1 $[M-{}^tBu]^+$. Accurate mass of ion $[M+H]^+ = 310.1833$, measured mass of ion $[M+H]^+ = 310.1833$.

B. Via a mixed anhydride (unsuccessful reaction).

To a solution of potassium 4-*tert*-butyldimethylsilyloxybutanoate, **2.3**, (890 mg, 4 mmol) in DCM (40 ml) was added toluene-4-sulfonyl chloride (660 mg, 4.0 mmol). The mixture was stirred at room temperature and under a nitrogen atmosphere for 1.5 hours. The solvent was removed on a high vacuum line to afford a white solid which was washed with petroleum ether in order to eliminate the impurities (452 mg, 35 % yield). δH ($CDCl_3$) 7.78 (2H, d, $J = 8.2$ Hz, C*H*(o)), 7.38 (2H, d, $J = 8.2$ Hz, C*H*(m)), 3.60 (2H, m, C*H*$_2$(4)), 2.50 (2H, t, $J = 7.3$ Hz, C*H*$_2$(2)), 2.46 (3H, s, C*H*$_3$), 1.80 (2H, m, C*H*$_2$(3)), 0.82 (9H, s, SiC(C*H*$_3$)$_3$), 0.00 (6H, s, Si(C*H*$_3$)$_2$). Due to its moisture sensitivity, **2.6** was stirred straight away with one equivalent of 3-hydroxymethylpyridine (0.09 ml, 0.9 mmol) in presence of triethylamine (0.12 ml, 0.9 mmol) in dry chloroform (15 ml) for 12 h at room temperature. The mixture was washed with an aqueous $NaHCO_3$ solution (3 × 10 ml). The organic layer was dried over $MgSO_4$, filtered, and concentrated *in vacuo*. The brown gel was a mixture of decomposition products.

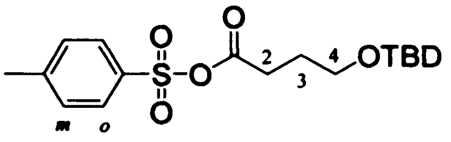

Intermediate compound:
Toluene-4-sulfonil-4-tertbutyldimethylsilyloxibutanoate
(2.6)

C. *Via* a coupling reaction (successful reaction in a good yield).

To a mixture of EDCI (440 mg, 2.2 mmol) and DMAP (139 mg, 1.1 mmol) in DCM (1.5 ml) was added a solution of 4-*tert*-butyldimethylsilyloxybutanoic acid, **2.2**, (250 mg, 1.1 mmol) in DCM (0.8 ml) at 0 °C. After 15 min, a solution of 3-(hydroxymethyl)pyridine (0.11 ml, 1.1 mmol) in DCM (1mL) was added to the reaction mixture, and stirring was continued at room temperature for 3 h. The mixture was diluted with an aqueous NH_4PF_6 solution (5 ml), and the aqueous layer was extracted with Et_2O (4 × 5 ml). The combined organic extracts were dried over $MgSO_4$, filtered, and concentrated *in vacuo*. The residue was purified by chromatography column

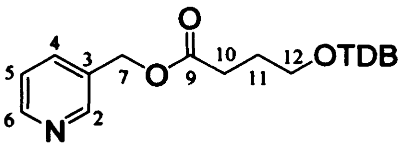

(hexane-EtOAc, 5:2), R_f = 0.7, to give compound **2.5** (161 mg, 47 %) as a white oil. δH ($CDCl_3$) 8.60 (1H, s, C*H*(2)), 8.54 (1H, m, C*H*(6)), 7.68 (1H, m, C*H*(4)), 7.30 (1H, m, C*H* (5)), 5.10 (s, 2H, C*H*$_2$(7)), 3.62 (2H, t, *J* = 6.1 Hz, C*H*$_2$ (12)), 2.42 (2H, t, *J* = 7.4 Hz, C*H*$_2$ (10), 1.82 (2H, m, C*H*$_2$(11)), 0.85 (9H, s, SiC(C*H*$_3$)$_3$), 0.0 (6H, s, Si(C*H*$_3$)$_2$). δC (CD_3Cl) 172.3 (*C*(9)), 148.6 (*C*(6)), 148.5 (*C*(2)), 134.9 (*C*(4)), 130.6 (*C*(3)), 122.4 (*C*(5)), 62.5 (*C*(7)), 60.8 (*C*(12)), 29.6 (*C*(10)), 26.7 (*C*(11)), 24.8 (SiC(*C*H$_3$)$_3$), 17.3 (Si*C*). *m/z* EI/CI 310.2 $[MH]^+$, 252.1 $[M\text{-}^tBu]^+$. Accurate mass of ion $[M+H]^+$ = 310.1833, measured mass of ion $[M+H]^+$ = 310.1833.

-Synthesis of the rhenium complexes: Chloride adduct, A, activated complexes, B, and final targets, C.

A: *fac*-Re(bipy)(CO)$_3$Cl (2.7).[7]

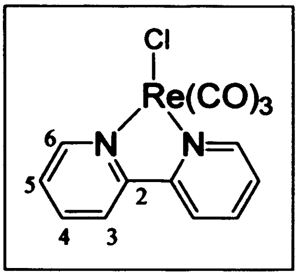

Re(bipy)(CO)$_3$Cl was prepared by heating equimolar quantities of Re(CO)$_5$Cl (211 mg, 0.6 mmol) and 2,2'-bipyridine (91 mg, 0.6 mmol) in dry toluene (2 ml) at reflux for 1 hour. The yellow product precipitated from solution and was filtered and used without further purification (262 mg, 98 % yield). δH ($CDCl_3$) 9.0 (2H, d, *J* = 5.6 Hz, C*H*(6)), 8.15 (2H, d, *J* = 7.10 Hz, C(3)), 8.0 (2H, m, C(4)), 7.50 (2H, m, C(5)). ν_{max} (Nujol) 2020, 1895, 1880 (CO).

B: *fac*-[Re(bipy)(CO)$_3$CH$_3$CN](BF$_4$) (2.8).[7]

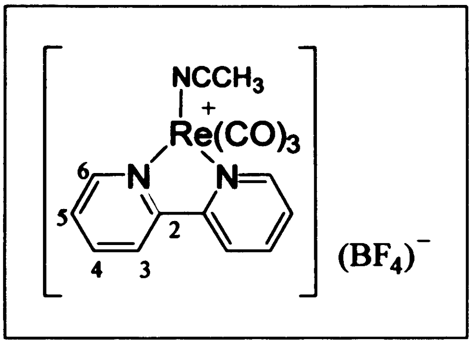

To a solution of Re(bipy)(CO)$_3$Cl (243 mg, 0.5 mmol) in acetonitrile (100 ml) was added one equivalent of silver tetrafluoroborate (105 mg, 0.5 mmol). It was heated at reflux under a nitrogen atmosphere in the dark for 5 hours. After filtering the solution through Celite, the solvent was removed at high vacuum. Then the dark yellow solid was dissolved in a smaller amount of acetonitrile and it was filtered again through Celite to remove the possible silver chloride remaining. Once again the solvent was removed at high vacuum affording a yellow solid (255 mg, 88 % yield). δH ($CDCl_3$) 8.85 (2H, d, *J* = 5.4 Hz, C*H*(6)), 8.49 (2H, d, *J* = 8.3 Hz, C*H*(3)), 8.19 (2H, m, C*H*(4)), 7.57 (2H, m, C*H*(5)) 2.13 (s, 3H, C*H*$_3$). ν_{max} (Nujol), 2035, 1918 (CO).

B: *fac*-[Re(bpy)(CO)$_3$CH$_3$CN](CF$_3$SO$_3$) (2.12).[7]

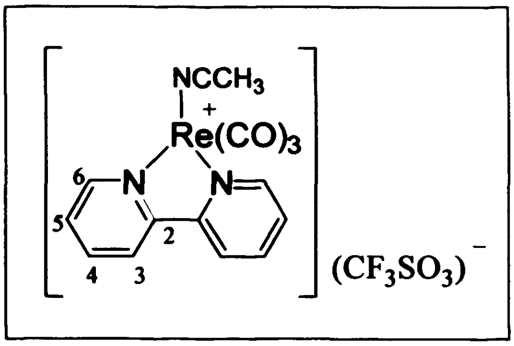

To a solution of Re(bpy)(CO)$_3$Cl (109 mg, 0.2 mmol) in acetonitrile (50 ml) was added one equivalent of silver triflate (60 mg, 0.2 mmol). It was heated at reflux under a nitrogen atmosphere in the dark for 6.5 hours. After filtering the solution through Celite, the solvent was removed at high vacuum. Then the dark yellow solid was dissolved in a smaller amount of acetonitrile and it was filtered again through Celite to removed the possible silver chloride remaining. Once again the solvent was removed at high vacuum affording a yellow solid (100 mg, 74 % yield). δH (CDCl$_3$) 8.88 (2H, d, *J* = 5.1 Hz, C*H*(6)), 8.61 (2H, d, *J* = 8.2 Hz, C*H*(3)), 8.20 (2H, m, C*H*(4)), 7.59 (2H, m, C*H*(5)), 2.20 (3H, s, C*H*$_3$). ν_{max} (Nujol) 2040, 1932, 1910 (CO).

C: *fac*-[Re(bipy)(CO)$_3$PyCH$_2$OH](BF$_4$) (2.9).

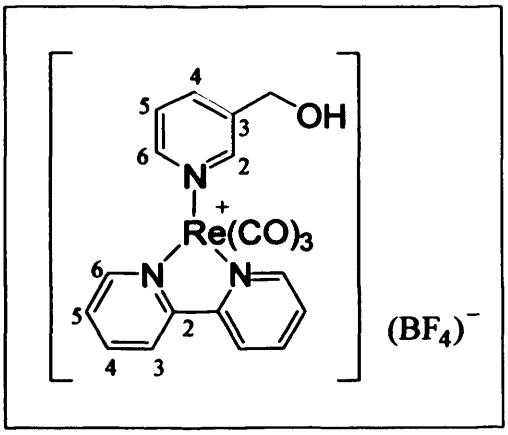

Complex Re(bipy)(CO)$_3$CH$_3$CN](BF$_4$) (255 mg, 0.4 mmol) and 3-(hydroxymethyl)pyridine (0.45 ml, 4 mmol) were heated at reflux in 175 ml of THF under a nitrogen atmosphere for 1.5 hour. After the solution had cooled, petroleum ether was added dropwise to crystallize the product as a yellow solid (178 mg, 62 % yield), m.p. 200 °C. δH (CD$_3$CN) 9.18 (2H, d, *J* = 5.5 Hz, C*H*(6) bipy), 8.30 (2H, d, *J* = 8.1 Hz, C*H*(3) bipy), 8.2 (2H, m, C*H*(4) bipy), 8.12 (1H, s, C*H*(2) Py), 8.04 (1H, d, *J* = 5.5 Hz, C*H*(6) Py), 7.68-7.78 (m, 3H, C*H*(4) Py, C*H*(5) bipy), 7.18 (1H, m, C*H*(5) Py), 4.38 (2H, s, C*H*$_2$), 3.33 (1H, s, O*H*). δC (CD$_3$CN) 195.4 (*C*O$_{eq.}$), 191.3 (*C*O$_{ap.}$), 155.4 (*C*(3), py), 153.5 (*C*(6), bipy), 150.0 (*C*(6), py), 149.5 (*C*(2), py), 140.8 (*C*(3), bipy), 140.6 (*C*(2), bipy), 137 (*C*(5), py), 127.8 (*C*(4), bipy), 125.8 (*C*(4), py), 124.3 (*C*(5), bipy), 59.6 (*C*H$_2$). ν_{max} (Nujol) 2032s, 1915sb υ (CO). *m/z* (ESI) 536.1 [MH]$^+$, 427 [M-BF$_4$-PyCH$_2$OH]$^+$. Elemental analysis, found C, 36.68; H, 2.30; N, 6.56. ReC$_{19}$H$_{15}$O$_4$N$_3$BF$_4$ requires C, 36.65; H, 2.41; N, 6.75. X-ray: C$_{19}$H$_{15}$BF$_4$N$_3$O$_4$ Re, *M* = 622.35, yellow block, 0.15 × 0.15 × 0.08 mm, monoclinic, space group P 2$_1$/c, *a* = 10.2550 Å, *b* = 12.5820 Å, *c* = 15.6370 Å, *β* = 94.006°, *V* = 2012.69 Å^3, *Z* = 4, D_c = 2.054 mg cm^{-3}, *F(000)* = 1192, 14713 Reflections collected, 4614 Reflections unique, R(int) = 0.0620; Goodness-of-fit on F2 = 1.030, *R1* = 0.0375, *wR2* = 0.0834.

C: *fac*-$[Re(bipy)(CO)_3PyCH_2OCO(CH_2)_3OH](BF_4)$ (2.10).

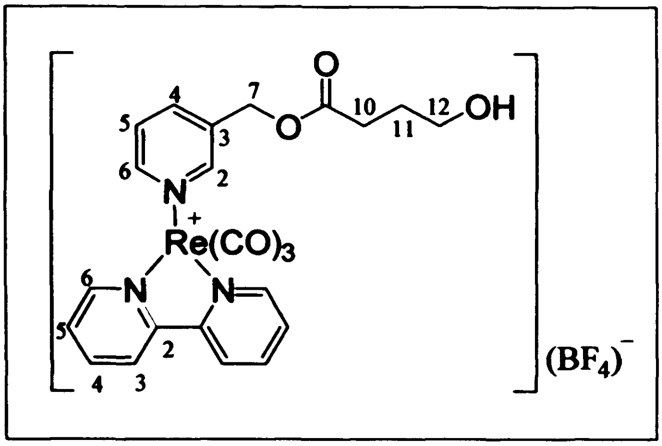

To a solution of $[Re(bipy)(CO)_3CH_3CN](BF_4)$ (219 mg, 0.4 mmol) in THF (100 ml) was added one equivalent of 3-(4-*tert*-butyldimethylsilyloxybutanoatomethyl)-pyridine (134 mg, 0.4 mmol) dissolved in 40 ml of the same solvent. It was heated at reflux under a nitrogen atmosphere for 9 hours and then stirred at room temperature. Finally it was filtered by gravity and the solvent was removed at the rotary evaporator. By recrystallisation from ethyl acetate a dark yellow solid was obtained, m.p. 72 °C. δH (CD_3CN) 9.21 (2H, m C*H*(6) bipy), 8.38 (2H, m, C*H*(3) bipy), 8.3-8.1(4H, m, C*H*(4) bipy, C*H*(2,6) Py), 7.87-7.79 (3H, m, C*H*(4) Py, C*H*(5) bipy), 7.29 (1H, m, C*H*(5) Py), 4.92 (2H, s, CH_2), 3.48 (2H, m, CH_2(12)), 2.38 (2H, t, J = 7.4 Hz, CH_2(10)), 1.68 (2H, m, CH_2(11)). ν_{max} (CH_3CN) 2031, 1920, 1734 (CO). *m/z* (ESI) 622.1 $[MH]^+$, 536.1 $[M\text{-}CO(CH_2)_3O]^+$ 427.0 $[M\text{-}BF_4\text{-}PyCH_2OCO(CH_2)OH]^+$. Theoretical isotope pattern 620.1 (58%), 621.1 (17%), 622.1 (100%), 623.1 (28%), 624.1 (3%). Actual isotope pattern 620.1 (57%), 621.1 (15%), 622.1 (100%), 623.1 (24%), 624.1 (5%).

C: *fac*-$[Re(bipy)(CO)_3PyCH_2OCO(CH_2)_3OSiMe_2{}^tBu]$(CF_3SO_3) (2.13).

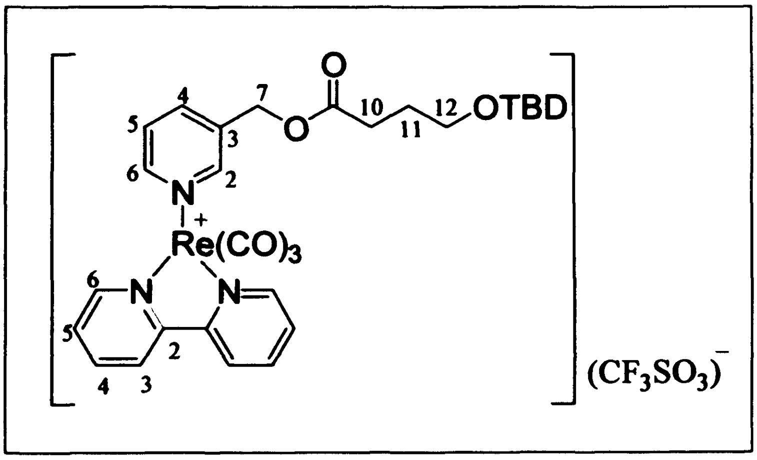

The reaction was carried out in THF (25 ml). The complex $Re(bipy)(CO)_3CH_3CN](CF_3SO_3)$ (100 mg, 0.16 mmol) and compound **2.5** (55 mg, 0.18 mmol) were heated at reflux under a nitrogen atmosphere for 10 h. After 2 days stirring at room temperatrure, petroleum ether was added dropwise to crystallize the product as a yellow solid (37 mg, 26 %), m.p. 145 °C. δH (CD_3CN) 9.08 (2H, d, J = 5.3 Hz, C*H*(6) bipy), 8.79 (2H, d, J = 8.9 Hz, C*H*(3) bipy), 8.35-8.28 (3H, m, C*H*(4) bipy), C*H*(2) Py), 7.97 (1H, d, J = 8.9 Hz, C*H*(6) Py), 7.80-7.71 (3H, m, C*H*(4) Py, C*H*(5) bipy), 7.35 (1H, m, C*H*(5) Py), 4.90 (2H, s, CH_2), 3.60 (2H, t, J = 6.3 Hz, CH_2(12)), 2.37 (2H, t, J = 7.4 Hz, CH_2(10)), 1.79 (2H, m, CH_2(11)), 0.88 (9H, s, SiC(CH_3)$_3$), 0.0 (6H, s, Si(CH_3)$_2$). δC (CD$_3$CN) 194.4 (*C*O$_{eq.}$), 191.0 (*C*O$_{ap.}$), 172.05 (*C*O(9)), 154.9 (*C*(2), bipy), 151.4 (*C*(6), bipy), 150.7 (*C*(2), py), 149.7 (*C*(6), py), 140.8 (*C*(4), bipy), 138.8 (*C*(4), py), 134.6 (*C*(3), py), 127.8 (*C*(3), bipy), 126.2 (*C*(5), py), 125.4 (*C*(5), bipy), 61.1 (*C*(7)), 60.8 (*C*(12)), 29.4 (*C*(10)), 26.7 (*C*(11)), 24.9 (SiC(*C*H$_3$)$_3$), 17.3 ((Si*C*)). ν_{max} (Nujol): 2035, 1935, 1925, 1722, υ (CO). *m/z* (ESI) 736.4 $[MH]^+$, 622.3 $[M\text{-}CF_3SO_3\text{-}Si(CH_3)_2C(CH_3)_3]^+$, 427.2 $[M\text{-}CF_3SO_3\text{-}PyCH_2OCO(CH_2)_2OSi(CH_3)_2C(CH_3)_3)]^+$. Theoretical isotope pattern 734.2 (56%), 735.2 (23%), 736.2 (100%), 737.2 (39%), 738.2 (11%). Actual isotope pattern 734.4 (60%), 735.4 (22%), 736.4 (100%), 737.4 (36%), 738.4 (11%). X-ray: $C_{30}H_{35}F_3N_3O_9ReSSi$, M = 884.96, yellow block, 0.10 × 0.05 × 0.05 mm, monoclinic, space group, a = 11.1847(8) Å, b = 13.3116(10) Å, c = 24.0160(18) Å, β = 95.5780(10)°, V = 3558.7(5) Å^3, Z = 4, D_c = 1.211 mg cm^{-3}, *F(000)* = 1264, Reflections collected = 45252, 12616 Reflections unique, R(int) = 0.0449; Goodness-of-fit on F2 = 1.579, *R1* = 0.0719, *wR2* = 0.2237.

2.11 References

[1] R. Y. Tsien, *Nature* **1981**, 290, 527.

[2] M. A. Clack, B. Ganom, *Tetrahedron Letters,* **2000**, 41, 9523.

[3] P. Renton, D. Gala, G. M. Lee, *Tetrahedron Letters,* **2001**, 42, 7141.

[4] A. Vogler, H. Kunkely, *Coord. Chem. Rev.*, **2000**, 991, 200.

[5] D. J. Stufkens, A. Vlcek, *Coord. Chem. Rev.*, **1998**, 177, 127.

[6] K. K.-W. Lo, K. H.-K. Tsang, W.-K. Hui, N. Zhu, *Inorg. Chem.*, **2005**, 44, 6100.

[7] J. V. Caspar, T. J. Meyer, *J. Phys. Chem.*, **1983**, 87, 952.

[8] L. Sacksteder, A. P. Zipp, E. A. Brown, J. Streich, J. N. Demas, B. A. DeGraff, *Inorg. Chem.*, **1990**, 29, 4335.

[9] E. Ioachim, E. A. Medlycott, G. S. Hanan, *Inorg. Chim. Act.*, **2006**, 359, 9, 2599.

[10] G. Tarzania, A. Duranti, A. Tontini, G. Spadoni, M. Mor, S. Rivara, V. P. Plazzi, S. Kthuria, D. Piomelli, *Bioorg. Med. Chem.*, **2003**, 11, 3965.

[11] Y.-H. Song, S. Hong, J. Lim, S. Chung, I. No, K. Lee, M. Yoon, *Chem. Pharm. Bull.*, **2004**, 52, 5, 567.

[12] C. S. Marvel, E. R. Birkhimer, *J. Am. Chem. Soc.*, **1929**, 51, 260.

[13] H. Friebolin (Ed.), *Basic One and Two Dimensional NMR Spectroscopy*, 4th ed., Wiley-VCH, New York, **2005**.

[14] M. Hesse, H. Meier, B. Zeeh (Eds.), *Métodos Espectroscópicos en Química Orgánica*, 5th ed. Síntesis, Madrid, **1995**.

[15] P. Renton, L. Shen, J. Eckert, G. M. Lee, D. Gala, G. Chen, B. Pramanik, D. Schumacher, *Org. Process Res. Dev.*, **2002**, 6, 1, 36.

[16] H. Günzler, H.-U. Gremlich (Eds.), *IR Spectroscopy An Introduction*, 1st ed., Wiley-VCH, Weinheim, **2002**.

[17] E. Haslam, *Tetrahedron,* **1980**, 36, 17, 2409.

[18] W. R. Roush, T. A. Blizzard, *J. Org. Chem.*, **1984**, 49, 10, 1772.

[19] N. Zhang, M. Tomizawa, J. E. Casida, *J. Org. Chem.*, **2004**, 69, 3, 876.

[20] B. Nieses, W. Steglich, *Angew. Chem. Int. Ed.*, **1978**, 17, 522.

[21] K. Nakamoto (Ed.), *Infrared And Raman Spectra Of Inorganic And Coordination Compounds*, 4th ed., J. Wiley & Sons, New York, **1986**.

[22] A. Albertino, C. Garino, S. Ghiani, R. Gobetto, C. Nervi, L. Salassa, E. Rosenberg, A. Sharmin, G. Viscardi, R. Buscaino, G. Croce, M. Milanesio, *J. Organomet. Chem.*, **2007**, 6, 1377.

[23] J. V. Smith, *Analyst,* **1995**, 120, 1231.

[24] E. Wolcan, G. Torchia, J. Tocho, O. E. Piro, P. Juliarena, G. Ruiz, M. R. Feliz, *Dalton Trans.*, **2002**, 2194.

[25] R. K. Sharma, J. L. Fry, *J. Org. Chem.*, **1983**, 48, 2112.

[26] B. J. Coe, N. R. M. Curati, E. C. Fitzgerald, S. J. Coles, P. N. Horton, M. E. Light, M. B. Hursthouse, *Organometallics,* **2007**, 26, 2318.

[27] J. A. Baiano, Jr. W. R. Murphy, *Inorg. Chem.,* **1991**, 30, 4594.

[28] R. R. Alfano, Y. Yuanlong, *IEEE J. Sel. Top. Quant.,* **2003**, 2, 148.

Chapter 3

Structural Modifications Directed Towards Improved Modulation Of Emission, Rate Of Cyclisation And Tuning Solubility In Re(I) Complexes.

3.1 Aims.

This chapter focusses on the synthesis of improved luminescent rhenium complexes for specific cell imaging. Tuning of luminescent properties and solubility as well as improvement in the cyclisation rates for the *self-destruction* device are investigated.

3.2 Introduction

3.2.1 Tuning of photophysical and photochemical properties.

The photophysical and photochemical properties of luminescent complexes of d^6 transition metal such as Re(I), Ru(II) or Ir(III) are influenced by the nature of the ligands and their environment. Therefore varying of one or more of these factors can tune the luminescent properties of complexes.

In particular, complexes of the type *fac*-$Re(NN)(CO)_3L$, where NN is an α-diimine ligand and L a pyridine derivative, can have their luminescence properties tuned by modifying the spectator ligand, L, and/or the chromophoric α-diimine. Modifications in the latter have been found to be more effective as they directly affect states implicated in the luminescent process (MLCT states). Variations in the pyridine derivative only affect the energy of these states by a secondary alteration of electron density on the central metal. Groups headed by Thomas J. Meyer[1] and B.A. DeGraff,[2] among other researchers, have studied how different electron-donating or electron-withdrawing character of the substituents on the α-diimine and/or on the pyridine derivative can tune the luminescent properties. **Figure 3.1** and **Figure 3.2** respectively.

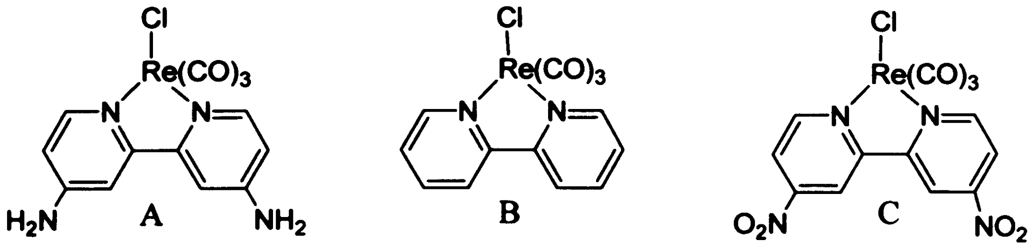

	A	B	C
Ex λ_{max} (nm)	350	370	448
Em λ_{max} (nm)	573	642	780

Figure 3.1. Rhenium complexes bearing a bipyridine or a derivatised bipyridine.

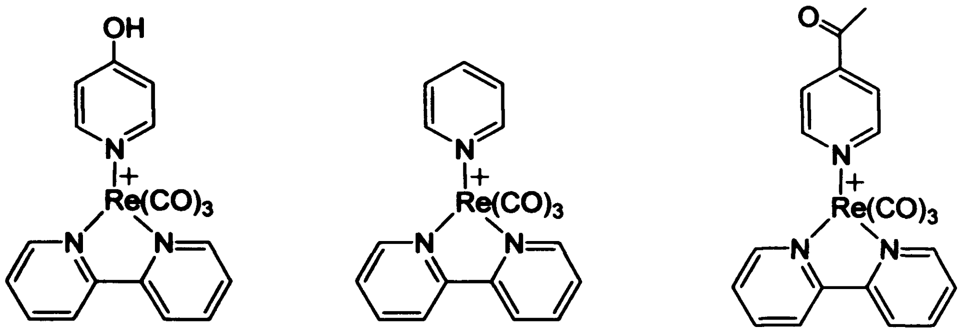

	A	B	C
Ex λ_{max} (nm)	402	366	340
Em λ_{max} (nm)	582	558	552

Figure 3.2. Rhenium complexes bearing a pyridine or a derivatised pyridine.

Extended π conjugation in the spectator ligand and in the α-diimine can also result in changes in the luminescent properties as this stabilises the π^*(α-diimine) and π^*(L) orbitals, promoting a red shift in the emission.

3.2.2 4'- Substituted-terpyridine complexes.

4'-Substituted-terpyridine complexes of Ru(II), Os(II) and Ir(III) have been widely studied[3,4] due to their important applications in biosensors, solar cells and molecular and electronic devices, *etc.* Functionalisation of terpyridine can not only be helpful in tuning the luminescent properties, but also in the design of novel probes. Recently, Williams *et al.* synthesised bis-terpyridine iridium complexes bearing pH-sensitive groups (phenol and pyridine, **Figure 3.3**) where changes in the pH modify the luminescent properties of the compounds drastically.

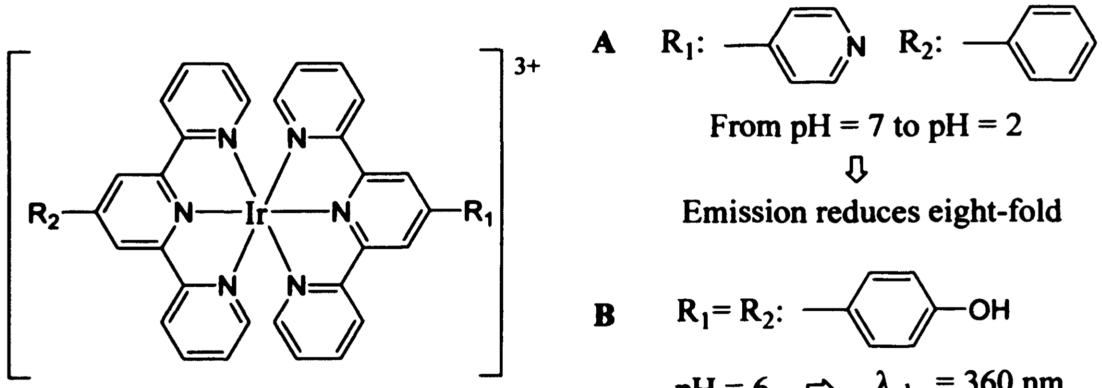

From pH = 7 to pH = 2

⇩

Emission reduces eight-fold

pH = 6 ⇨ λ_{abs} = 360 nm

pH = 10 ⇨ λ_{abs} = 468 nm

Figure 3.3. Examples of bis-terpyridine iridium complexes reported by Williams *et al.*[5]

3.2.3 Dicarbonyl rhenium complexes.

Only a few examples of dicarbonyl rhenium complexes[6,7] were found in the literature, **Figure 3.4,** in comparison to the numerous tricarbonyl analogues. The photophysical properties of the dicarbonyl complexes are also suitable for their use as fluorescent probes as they have increased emission, lifetimes, quantum yields and the MLCT absorption band shifts to longer wavelength than for the analogous tricarbonyl rhenium complexes. On the other hand, they may potentially work as macromolecular building blocks with a "linear shape" in contrast to the L-shaped geometry of the tricarbonyl rhenium complexes.

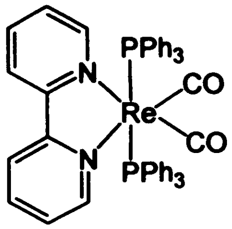

Figure 3.4. Example of a dicarbonyl rhenium complex reported by Ishitani.[7]

3.3 Premises.

Studies performed in the past 20 years have shown that changes in the luminescent properties of complexes can be generated by modifying directly conjugated substituents on the α-diimine and/ or the axial ligand. Therefore, a similar approach was considered in this work in order to produce detectable changes in emission caused by the *self-destruction* mechanism. This approach can also be used to increase the cyclisation rate *(i.e.* the *linker self-destruction* mechanism), as the direct conjugation of the *self-destruction* device to an aromatic system affords a better leaving group, which will accelerate the cyclisation reaction once the sensor has been removed. **Scheme 3.1** and **3.2** show a diagrammatic depiction of the improved target. The concept of the *linker self destruction* reaction was described in detail in **Chapter 2, Scheme 2.2.**

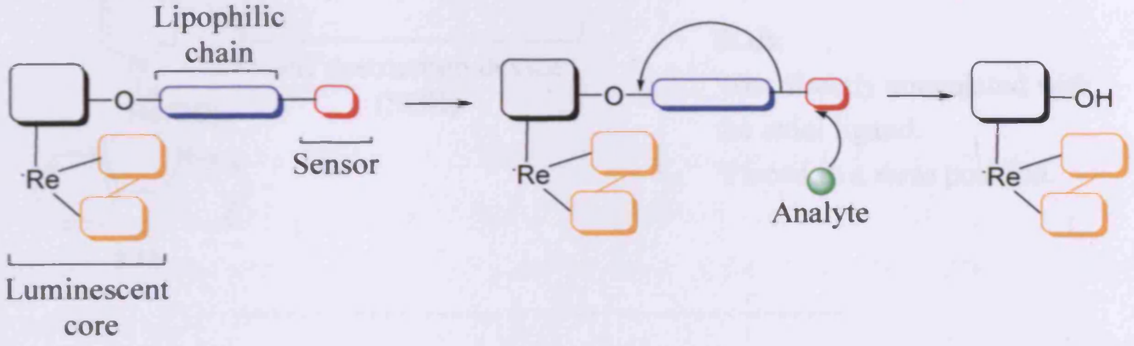

Scheme 3.1. Directly conjugated substituents in the axial ligand and its *linker self-destruction* reaction.

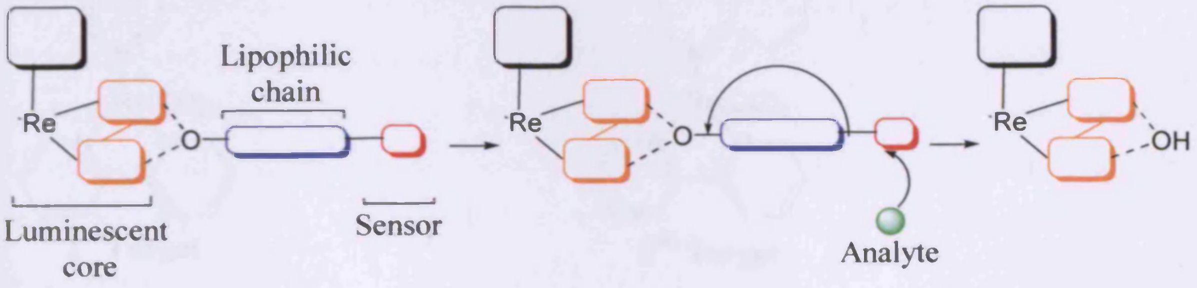

Scheme 3.2. Directly conjugated substituents in the α-diimine and its *linker self-destruction* reaction.

Further derivatisation is also needed in order to render the complexes more water soluble. Therefore, sulphonate groups or similarly charged, polar units can be introduced as substituents on either the α-diimine or in the axial ligand.

3.3.1 Luminescent properties and cyclisation rate.

Two molecules based on complex **2.13** have been designed to comply with the requirement for both an improved *linker self-destruction* mechanism and a greater difference in luminescent properties between the pre- and post-cyclisation species, as shown in **Figure 3.5**. The first imaging agent bears the self destruction device directly attached to the axial ligand in the *para* position (with respect to the nitrogen). This will directly affect the electronic properties of the N-Re bond, and consequently, the luminescence, by additional electron donation into the MLCT excited state. The second model also has the *self-destruction* device directly conjugated with the axial ligand, which in this case, is a quinoline – containing a more extended π-system than the pyridine.

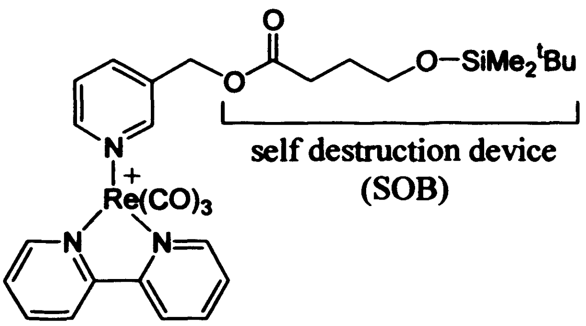

2.13

SOB:
·Not directly congujated with the axial ligand.
·Placed in a *meta* position.

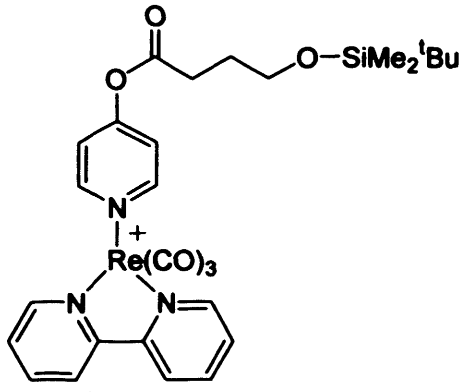

1st Target

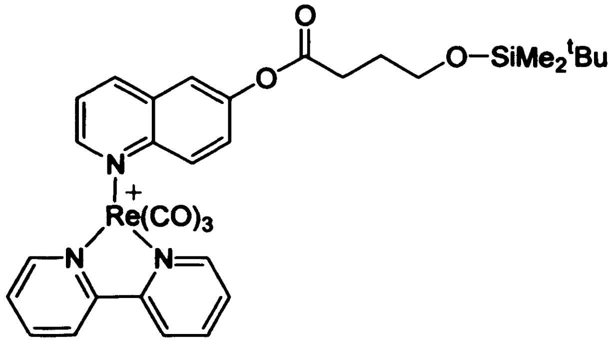

2nd Target

SOB:
·Directly congujated with the axial ligand.
·Placed in a *para* position.

Figure 3.5. Specific targets for improving the luminescence and cyclisation rate of species **2.13**.

A further target complex is shown in **Figure 3.6**. This complex is based on studies reported by several research groups such as those of Sullivan,[6] and Koike,[7] concerning the favourable photochemical features of dicarbonyl diimine rhenium complexes and on the reported synthesis of the rhenium biscarbonyl complex, [Re(terpy)$(CO)_2$Cl], made by Sebastiano Campagna *et al.*[8]

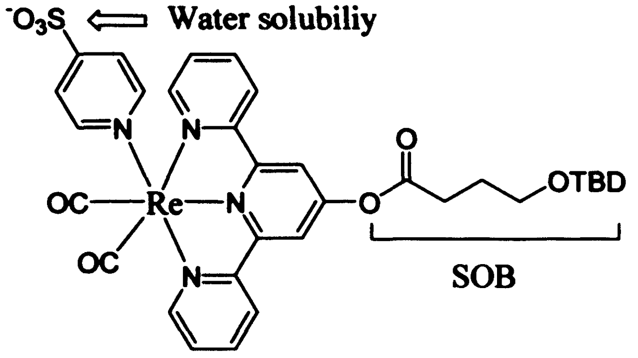

SOB:
- Directly conjugated
- Placed in para position

3rd Target

Figure 3.6. Specific model of a water soluble dicarbonyl rhenium complex.

This third model also bears the *self-destruction* device, SOB, directly conjugated with an aromatic ring. In this case, it is attached to the α-diimine ligand, and there is an axial water soluble pyridine present as well, in order to enhance the solubility of the compound in polar solvents.

Finally, in order to progress towards the synthesis of a luminescent rhenium complex with biologically relevant applications, two new complexes were designed whose *self-destruction* device has been modified so that it can be triggered by nitro-reductase[a]. The nitro-reductase enzyme is derived from bacteria and is also used as a marker gene in genetic engineering. Therefore, detection of nitro-reductase is important both for detecting the presence of bacteria and for showing that genetic modification has occurred. Both structures are shown in **Scheme 3.3** together with the proposed *self-destruction mechanism*.

---

[a] Nitro reductase is an enzyme that catalyses the reduction of nitro groups in a wide range of substrates to produce the corresponding hydroxylamine.

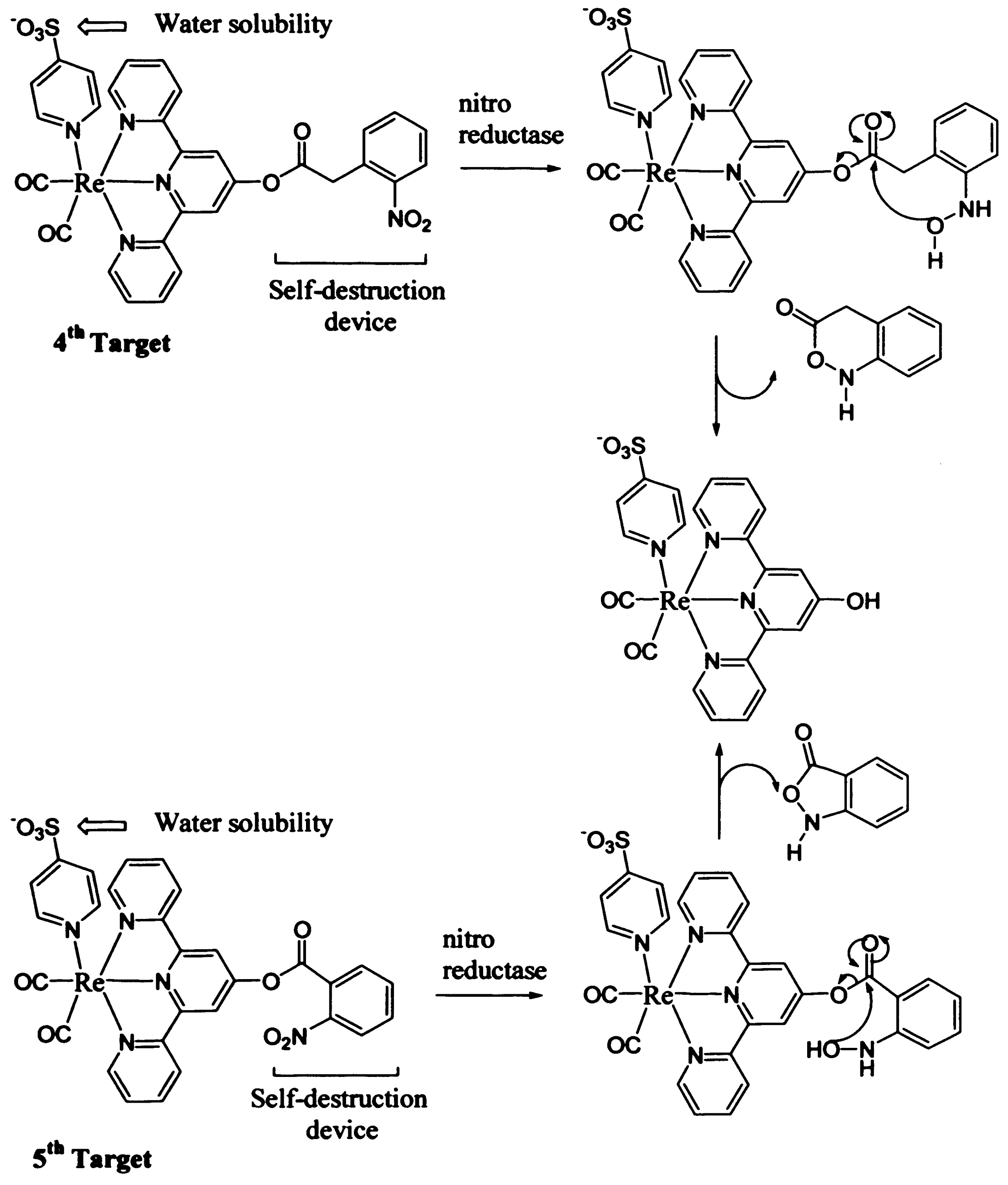

Scheme 3.3. Specific models with nitro groups as the trigger.

3.3.2 Solubility in biological media.

The sixth and final challenge described in this chapter will deal with the problem of low solubility in polar solvents. Water solubilising substituents are needed in order to modulate the solubility of new complexes towards a practical application in biological systems.

Figure 3.7 represents a rhenium complex with a water soluble diimine ligand with an extended π-system and the already reported ligand, **2.5**.

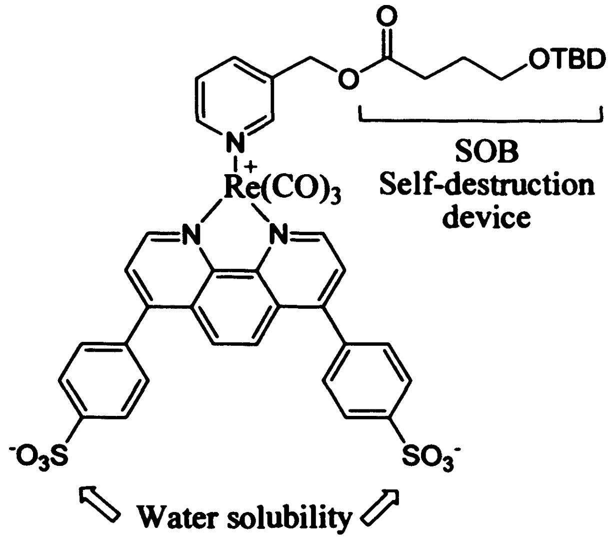

6th Target

Figure 3.7. Target water soluble rhenium complex.

3.3.3 Retrosynthetic analysis.

The synthetic pathway that was followed to synthesise the six proposed imaging agents is the same as that followed in the synthesis of complexes **2.9** and **2.13** in **Chapter 2** (*vide supra* **Scheme 2.5**). In addition, based on the excellent results also obtained and discussed in the previous chapter concerning the synthesis of the axial ligand, compound **2.5**, the same retrosynthetic analysis (coupling reaction) is considered when it comes to synthesising the five new *self-destruction* ligands, **Scheme 3.4** and **Scheme 3.5**.

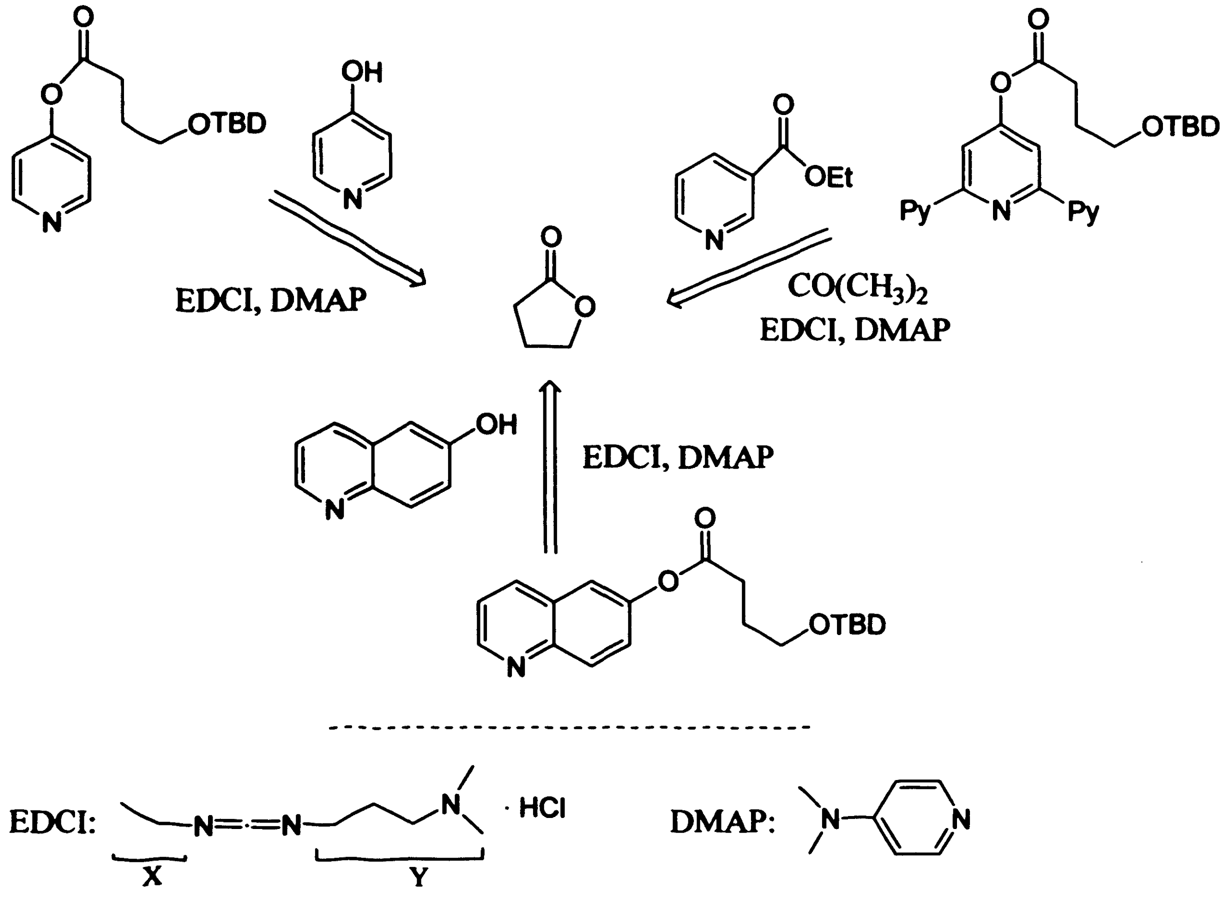

Scheme 3.4. Retrosynthetic analysis of ligands bearing SOB as *self-destructing* device.

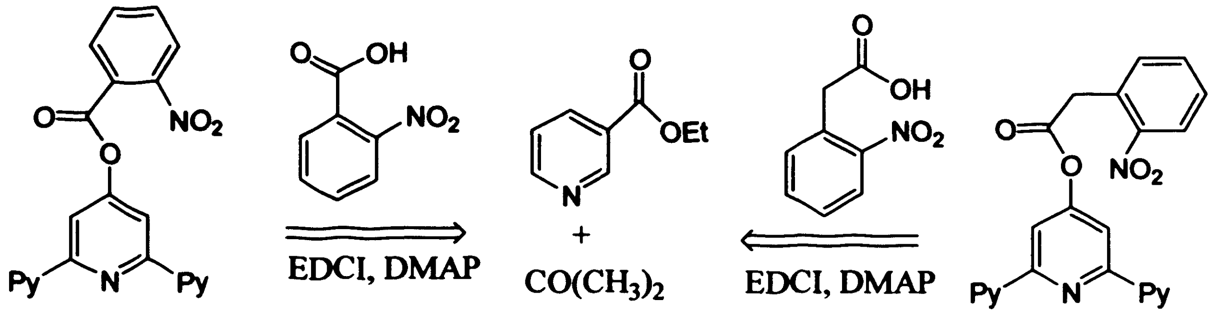

EDCI, DMAP see **Scheme 3.4**

Scheme 3.5. Retrosynthetic analysis of ligands bearing a nitro group as the trigger for the *self-destruction* mechanism.

3.4 Results And Discussion.

3.4.1 Attempted synthesis of a Re complex with a *para* substituted pyridyl axial ligand.

Several attempts to synthesise the functionalised 4-hydroxypyridine using the established coupling method (EDCI and DMAP, **Scheme 3.4**) were not successful, giving a mixture of starting material and unidentified decomposition products. Possibly, the equilibrium between the hydroxyl and ketone forms reduces the nucleophilicity of the hydroxyl group, preventing the coupling reaction from taking place, **Scheme 3.6.**

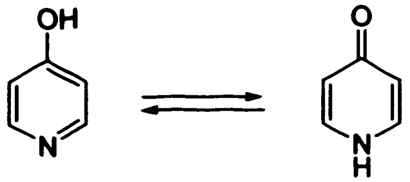

Scheme 3.6. Pyridone-hydroxypyridine equilibrium.

Coordination of 4-hydroxypyridine to the rhenium core followed by the coupling reaction to attach the *self-destruction* device to the hydroxyl group could overcome this problem. The same procedure as reported by DeGraff *et al.*[2] was used to synthesise [Re(CO)$_3$(bipy)(4-HO-py)](ClO$_4$), **Scheme 3.7.** The synthesis entails the direct reaction of the Re(CO)$_3$(bipy)Cl with an excess of the axial ligand, 4-hydroxypyridine, in presence of the silver perchlorate. ^{1}H-NMR spectroscopy confirmed the success of the reaction, with the axial ligand proton signals shifting to low field upon coordination.

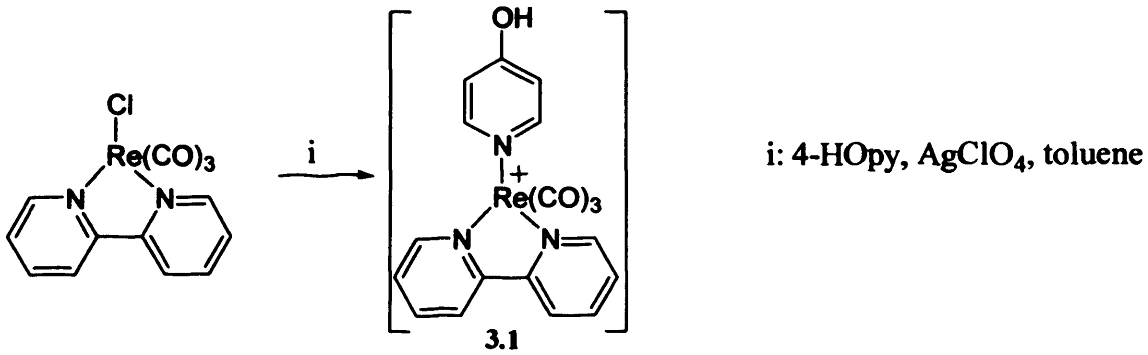

Scheme 3.7. DeGraff's procedure for coordination of 4-hydroxypyridine to a rhenium centre.

The coupling reaction was then attempted using the same conditions as before but using chloroform instead of DCM due to the poor solubility of complex **3.1** in DCM, **Scheme 3.8.** After stirring for 3 days, no product formation was observed. This can be rationalised by the hydroxyl group having lowered electron density, and thus, lower nucleophilicity. The electron density of the hydroxyl group can be donated to the metal centre quite efficiently as the donor and acceptor are placed in *para* to each other.

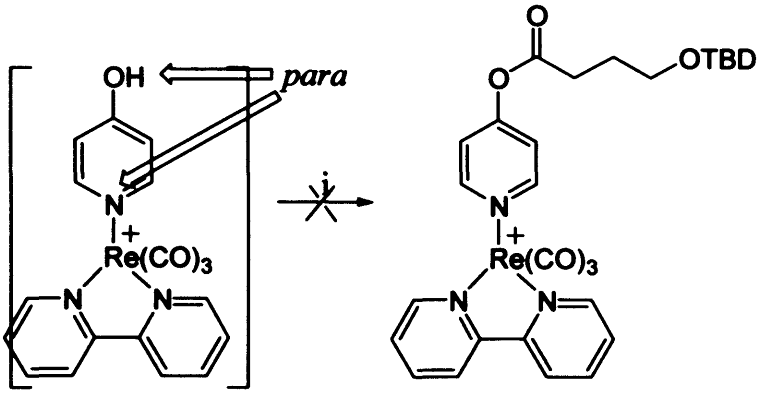

Scheme 3.8. Lack of reactivity of complex **3.1** towards coupling with SOB.

3.4.2 Synthesis of a Re complex with a more conjugated axial ligand.

6-SOB-Quinoline, **3.2**, was synthesised successfully by the coupling reaction between the 6-HO-quinoline and 4-*tert*-butyldimethylsilyloxybutanoic acid, **2.2**, **Scheme 3.9.** The low yield of the reaction can be rationalised by the low solubility of the starting material, 6-hydroxyquinoline and its low nucleophilicity (the direct conjugation of the hydroxyl with the aromatic system increases the electron delocalisation within the molecule). The structure of the white crystalline solid that was isolated from the reaction was confirmed by ^{1}H-NMR spectroscopy, as the protons belonging to the acid fragment were shifted to low field; further characterization by IR and mass spectrometry corroborated the result.

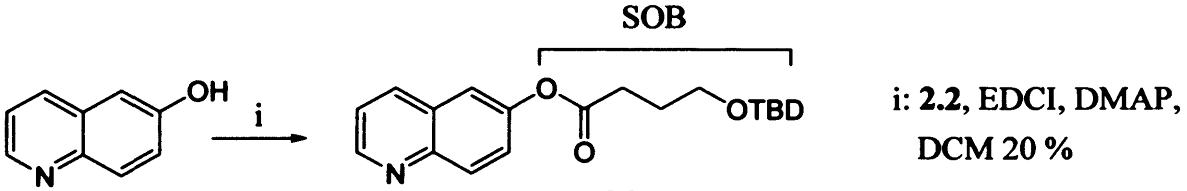

3.2

Scheme 3.9. Coupling reaction between 6-hydroxyquinoline and **2.2.**

Next, the reaction of the quinoline derivative **3.2**, with the activated rhenium species [Re(CO)$_3$(bipy)(CH$_3$CN)](CF$_3$SO$_3$), **2.12**, was attempted, **Scheme 3.10** (*N.B.* Synthesis of the activated rhenium species has been discussed in **Chapter 2**). Unfortunately, no displacement of acetonitrile by the new ligand was observed under normal reaction conditions (THF, reflux, N$_2$), with both starting materials being recovered from the reaction mixture. A higher boiling solvent, toluene, was then tried in an attempt to force the reaction with a higher temperature but with the same negative result. In this case, however, the products recovered from the reaction were the activated rhenium complex and unidentified decomposition products derived from the ligand.

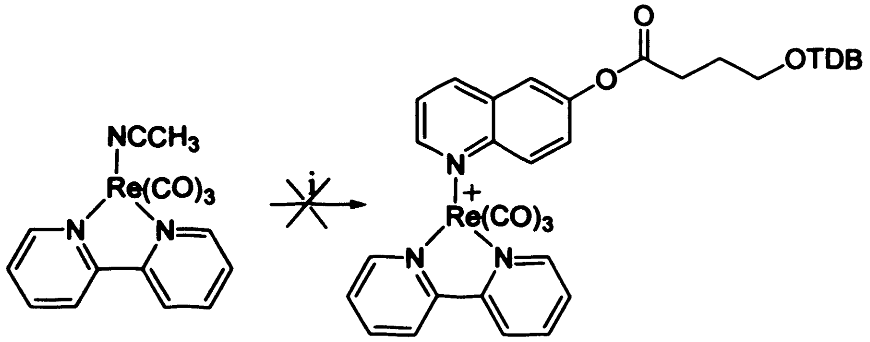

i: **3.2**, THF
i: **3.2**, toluene

Scheme 3.10. Reaction of **3.2** with the activated rhenium species.

Given the difficulty in synthesising the desired target, attention turned to the synthesis of a rhenium adduct with two quinoline derivatives instead of the chelate ligand, bipy, as rhenium complexes with a similar structure, $[Re(CO)_3(N)_2L]$, where N is a highly conjugated monodentate pyridine, also have good photophysical properties to use as fluorescent probes.[9]

Chloro pentacarbonyl rhenium was heated with either two equivalents of ligand **3.2** in toluene, or with 6-hydroxyquinoline, **Scheme 3.11**. However, neither of these reactions led to the desired product; ester hydrolysis was observed in the case of ligand **3.2** and no reaction occurredwhen 6-hydroxyquinoline was used. Therefore, the idea of using a quinoline derivative as an anchor for the linker chain and sensor was dropped.

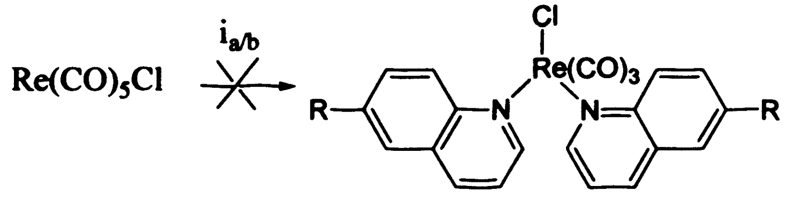

R, -OH, -SOB
i_a: 3.2, Toluene
i_b: 6-OH-Quinoline, Toluene

Scheme 3.11. Attempted synthesis of rhenium quinoline complexes.

3.4.3 Attempted synthesis of Re complexes with *tert*-pyridine derivatives as the α-diimine.

The synthesis of 4'-hydroxyterpyridine was published by Edwin C. Constable and Michael D. Ward in 1990.[10] It entails a two step synthesis starting with the reaction of ethyl 2-

pyridine carboxylate, acetone and sodium hydride to afford 1,5-bis(2'-pyridyl)pentane-1,3,5-trione. Subsequently, addition of ammonium acetate to an ethanol solution of this intermediate gives the desired product, **Scheme 3.12**. The product was successfully obtained following the described procedure, and as its ^{1}H-NMR spectrum correlated with the reported data, no further characterization was carried out.

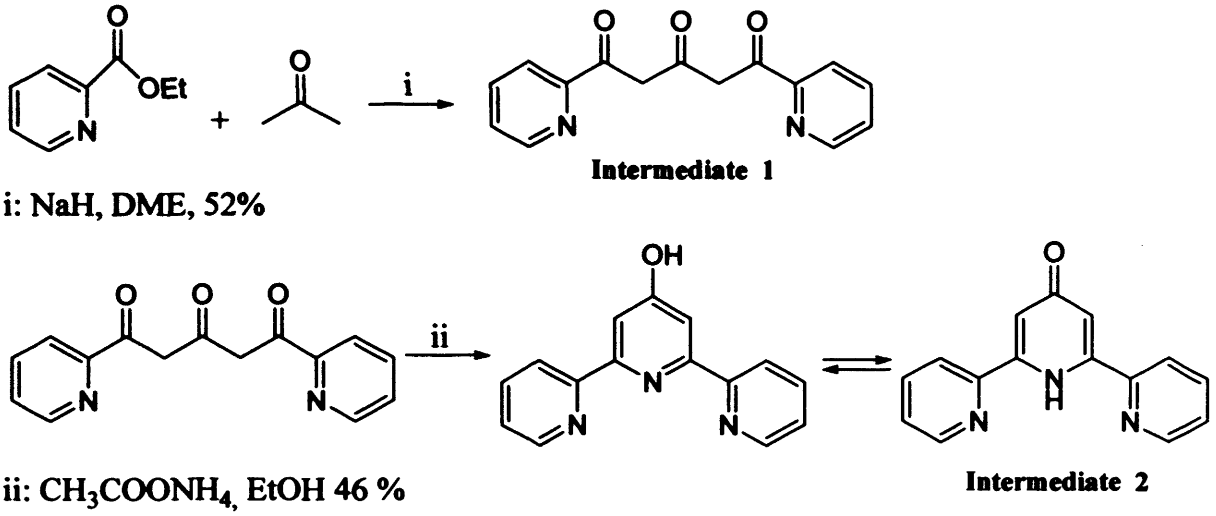

Scheme 3.12. Synthesis of 4'-hydroxyterpyridine by Constable and Ward's procedure.

Additional ligand functionalisation was carried out using the coupling reagents, EDCI and DMAP. Compounds **3.3**, **3.4**, and **3.5** were synthesised following a general procedure whereby the corresponding carboxylic acid was added to a mixture of DMAP and EDCI in dry DCM at 0 °C. After stirring a solution of the alcohol adduct for 15 min, 4'hydroxyterpyridine was added in the same solvent to the reaction mixture and stirring was continued for the required time at room temperature under a nitrogen atmosphere, **Scheme 3.13.**

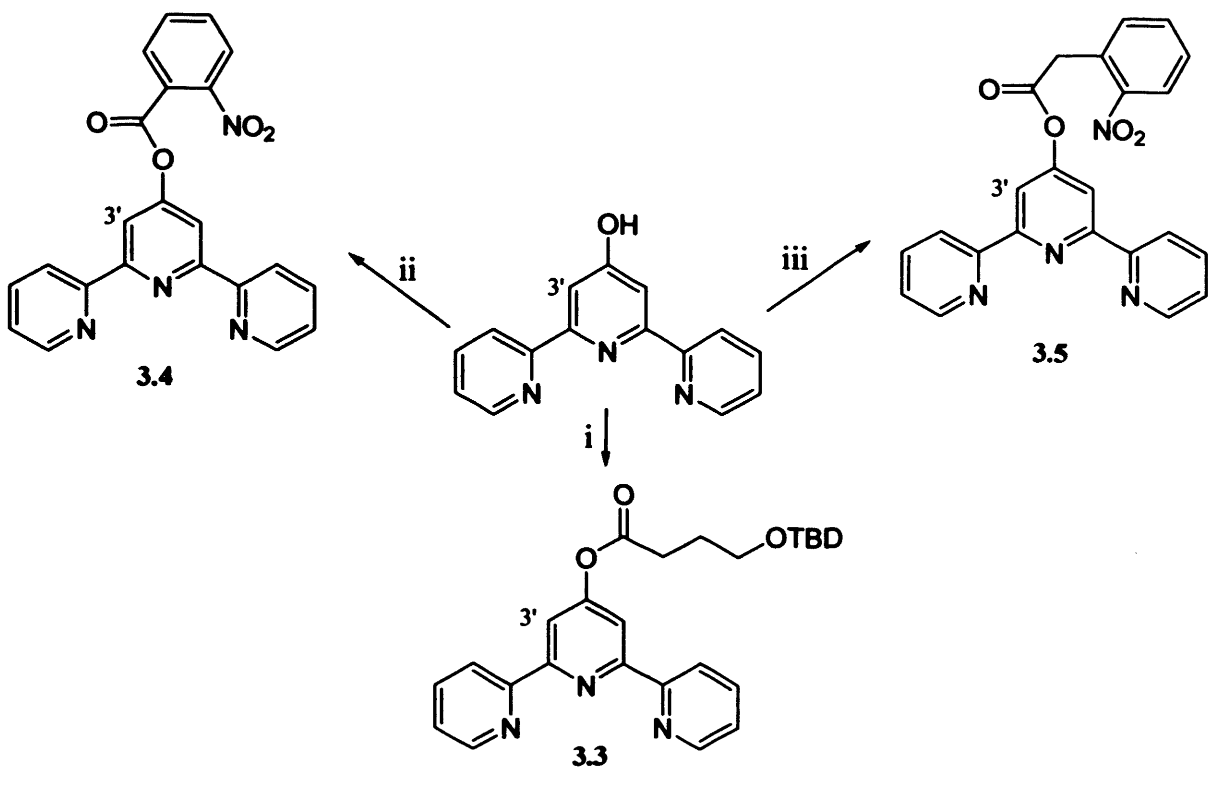

i: **2.5**, EDCI, DMAP, DCM, 3 h, 20 %

ii: 2-$NO_2C_6H_4COOH$, EDCI, DMAP, DCM, 3 days, 47 %

iii:2-$NO_2C_6H_4CH_2COOH$, EDCI, DMAP, DCM, 3 days, 36 %

Scheme 3.13. Synthesis of **3.3**, **3.4**, and **3.5**.

The three reactions were monitored by ^{1}H-NMR spectroscopy whereby the shift of the 3′ protons from 7.00 ppm in the starting material to 8.32, 8.18, and 8.20 ppm in the new compounds **3.3**, **3.4**, and **3.5**, respectively, indicated the reaction was complete. Moreover, the double integration of each peak in the regions of the ^{1}H-NMR spectrum relating to the terpyridine fragment, together with the ^{13}C-NMR spectrum, in which only half the number of carbons belonging to the terpyridine fragment appeared, showed that the new compounds were symmetrical. Further characterisation (IR and mass spectrometry) confirmed their structures.

Coordination of these three species and 4-hydroxyterpyridine to chloropentacarbonyl rhenium was performed using standard conditions, see **Scheme 3.14**. However, the product obtained from each reaction turned out to be the bidentate terpyridine derivative complex, *i.e.* a facial tricarbonyl rhenium system, which disagrees with the data reported in 1988 by Sebastiano Campagna *et al.*[8] for a similar complex [$Re(CO)_2$(terpy)Cl]. ^{1}H and ^{13}C- NMR spectroscopy showed the loss of ligand symmetry upon coordination, suggesting a bidentate coordination. Moreover, the appearance of three carbonyl stretching bands, one symmetric and two asymmetric, in IR experiments indicated the existence of three carbonyls within the complex (if there were only two carbonyls in the complex then only two bands would have been visible, υ_{sym} and υ_{asym}). Mass spectrometry, additional crystallographic data from complex **3.6** and further reports found in the literature[11] corroborated these results, see **Section 3.7**.

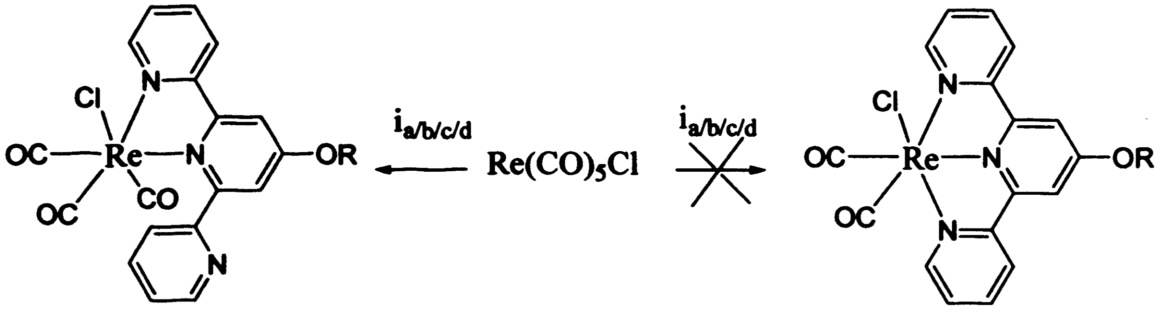

R: -H ⇨ i_a: 4'-HO-terpy, toluene, 89 % ⇨ 3.6
-$CO(CH_2)_3OTBD$ ⇨ i_b: 3.3, toluene, 80 % ⇨ 3.7
-$CO(2\text{-}NO_2C_6H_4)$ ⇨ i_c: 3.4, toluene, 60 % ⇨ 3.8
-$COCH_2(2\text{-}NO_2C_6H_4)$ ⇨ i_d: 3.5, toluene, 57 % ⇨ 3.9

Scheme 3.14. Coordination of terpyridine derivatives to $Re(CO)_5Cl$.

3.4.3.1 Reactivity of complex 3.6.

The activation reaction of these terpyridine derivative complexes was then attempted, starting with complex **3.6**. The yellow solid, **3.6**, was dissolved in acetonitrile affording a bright yellow solution which changed to pale yellow after addition of an excess of silver tetrafluoroborate. After heating at reflux under nitrogen atmosphere in the dark overnight, the ^{1}H-NMR spectrum showed marked changes, which could not be explained by a simple halide abstraction reaction as a less complicated spectrum was observed suggesting the formation of a more highly coordinated species, **Figure 3.8**.

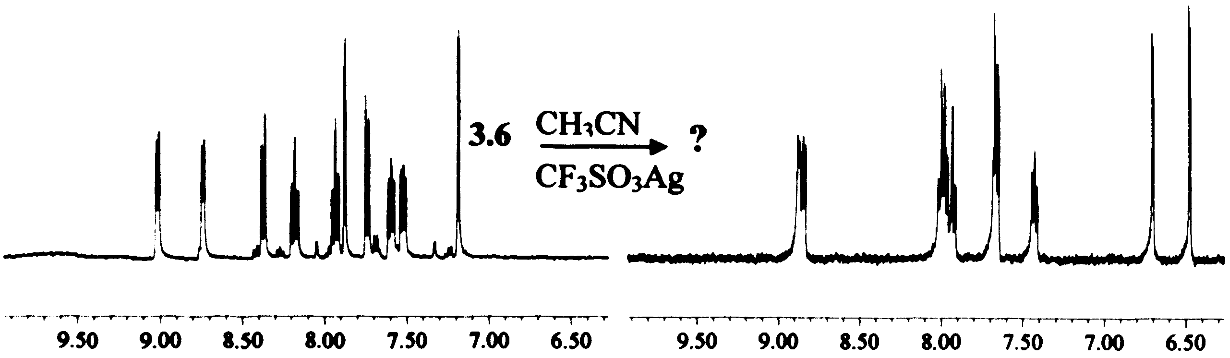

Figure 3.8. The ^{1}H-NMR spectra of the starting material **3.6** and the final product **3.10**.

Slow evaporation of an acetonitrile solution of this complex afforded yellow crystals suitable for X-ray diffraction studies, revealing the reason for the highly symmetric ^{1}H-NMR spectrum. The solid state structure contains three rhenium units, [Re(CO)$_3$(Oterpy)], bonded to each other through the oxygen atom in a triangular geometry. The three non-coordinated pyridyl units are bound to a single silver atom which is located in the central position of the triangle but in a different plane, mimicking a cup shape, **Scheme 3.15**. The crystal structure of this compound will be discussed in detail in **Section 3.7.2**.

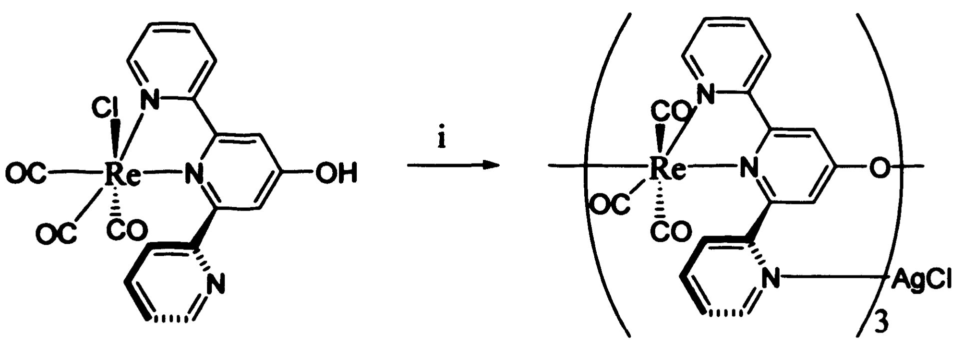

3.10

i: CF_3SO_3Ag, CH_3CN

Scheme 3.15. Unexpected tetrametallic species **3.10**.

In order not to use a silver compound to synthesise the activated species, which might template the formation of the tetrametallic complex, two different approaches were then considered. Complex **3.6** was reacted with sodium tetrafluoroborate in acetonitrile for 16 hours affording the acetonitrile adduct, **3.11**. Complex **3.6** was also reacted with trifluoromethylsulfonic acid (triflic acid) affording the triflate adduct, **3.12**, after stirring for 1 hour at room temperature, **Scheme 3.16**.

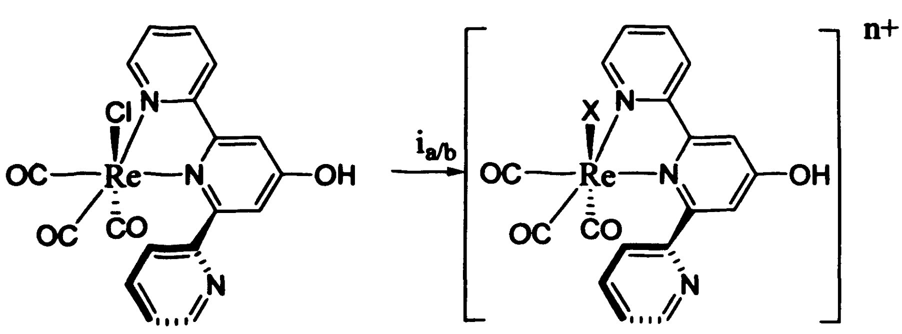

i_a: $NaBF_4$, CH_3CN, 70% i_a:X=CH_3CN, n = 1: **3.11**

i_b: CF_3SO_3H, DCM, 90% i_b: X= F_3CSO_3 n = 0: **3.12**

Scheme 3.16. Synthesis of activated complexes using triflic acid and $NaBF_4$.

Substitution of the labile triflate and acetonitrile ligands for pyridine was then attempted by heating both reagents at reflux, in a 1:1.5 ratio in THF. The reactions were monitored by ^{1}H-NMR spectroscopy, which suggested, by the shift of the hydroxy-terpy protons and the appearance of a new set of peaks belonging to the coordinated pyridine, completion of the reaction in less than one hour. The pyridine excess was the only impurity observed. Different attempts to isolate the product from the reaction, *e.g.* by precipitation and/ or washing with different solvents, were completely unsuccessful, ending up with the starting rhenium complex. Therefore, this observation suggests that the starting material, complex **3.6**, and the pyridine are in a dynamic equilibrium with the desired product. Once the excess of ligand is removed the reaction is displaced toward the reactants leading to complex **3.6** as the only product in the reaction.[b]

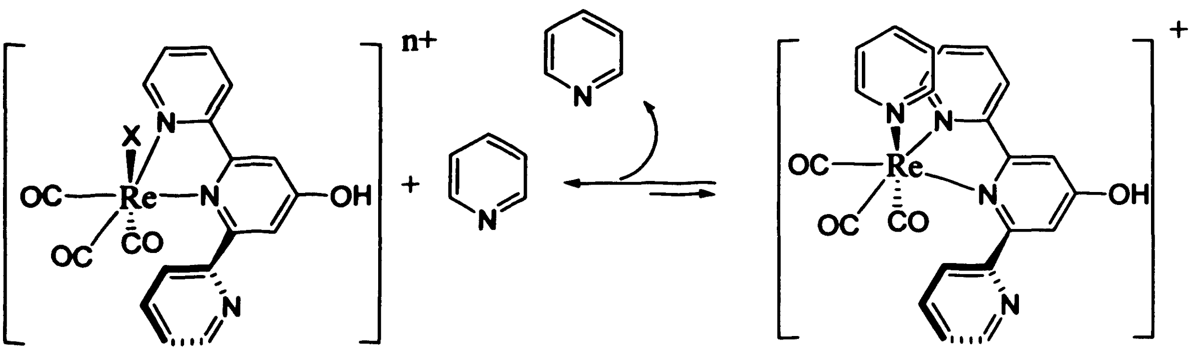

X: CH_3CN (n = 1) or CF_3SO_3 (n = 0)

Scheme 3.17. Equilibrium displacement when pyridine is removed from complexes **3.11** and **3.12**.

---

[b] Le Châtelier principle: If a dynamic equilibrium is disturbed by changing the conditions, the position of the equilibrium moves to counteract the change.

These results, plus a report published by Orrel and co-workers,[12] suggest that terpyridines behave as fluxional bidentate ligands in rhenium complexes. This inspired an investigation into the fluxional behaviour of the 4-hydroxy terpyridine complex and to determine whether this ligand fluxionality led to increased lability of the axial ligands, possibly *via* a seven-coordinate intermediate, **Figure 3.9**

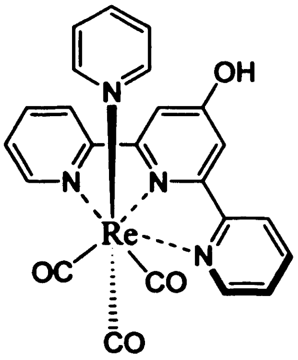

Figure 3.9. Proposed seven-coordinate intermediate of 4-hydroxyterpyridine rhenium complex with pyridine in the axial position.

The chloro-rhenium complex **3.6**, and 5 equivalents of pyridine were dissolved in CD_3CN. Triethylamine was also added in order to prevent protonation of the pyridine by the phenol of **3.6** that could lead to the reaction failure. ^{1}H-NMR spectroscopy demonstrated complete conversion of the chloro-complex to the pyridine complex (*N.B.* the reactivity of the unactivated chloro-complex is itself unusual and suggests a labilising effect by terpy). Then, 10 equivalents of 3-hydroxymethylpyridine was added to the NMR sample and once again ^{1}H-NMR spectra were recorded in which almost complete displacement of the original pyridine ligand was observed after heating for 5 hours at 80 °C. These observations demonstrate beyond doubt that complexes of the bidentate hydroxyterpyridine ligand are many times more labile than simple bipyridine analogues, **Figure 3.10**.

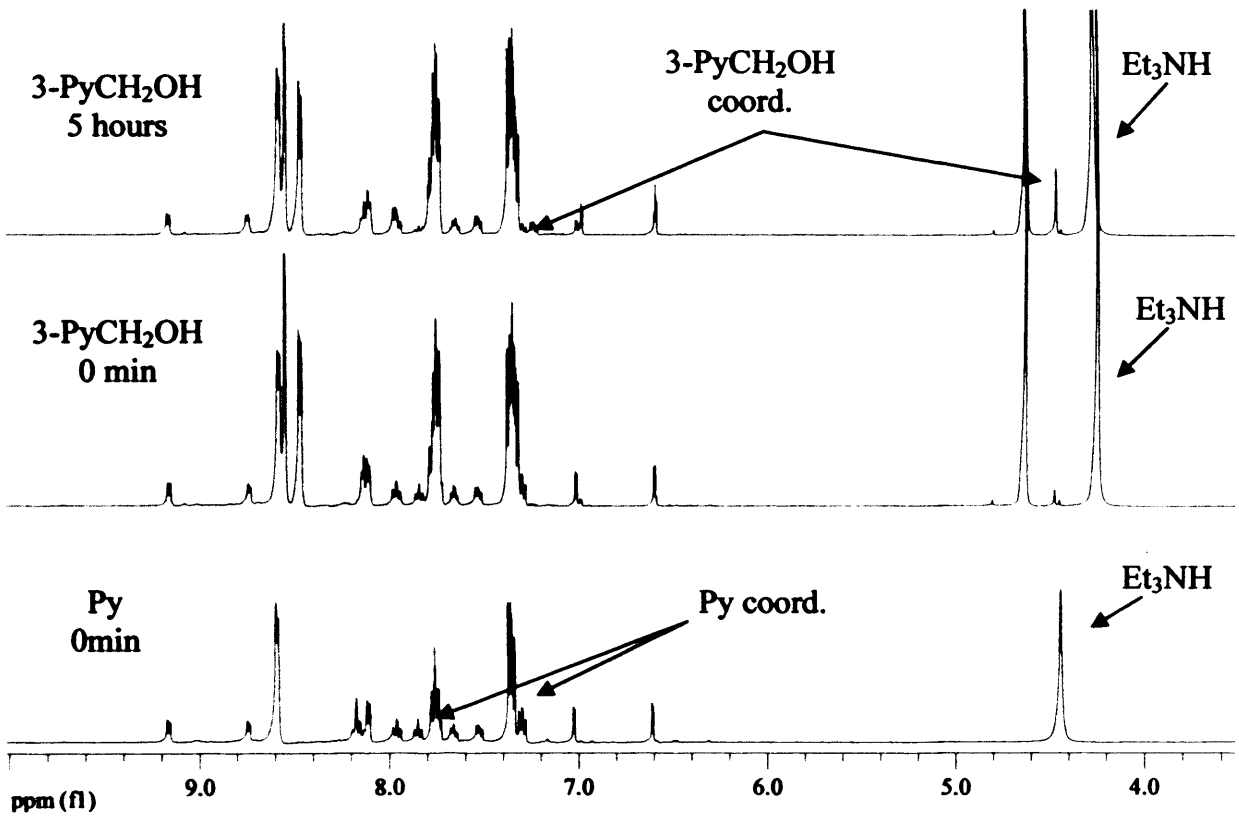

Figure 3.10. ^{1}H-NMR studies of the fluxional behaviour of terpyridine ligands.

Further investigations into the fluxionality of the 4'-hydroxyterpyridine rhenium complex were carried out. A series of variable temperature ^{1}H-NMR spectra of complex **3.6**, [Re(CO)$_3$(4'-OHterpy)Cl] were recorded in acetonitrile, ranging from 20 to 80 °C at 10 °C intervals. In the first three experiments, below a temperature of 40 °C, multiplets due to ten non-equivalent protons from the 4'-hydroxyterpyridine that are associated with a bidentate chelate complex are observed. At 50 °C the peaks start to broaden and at 80 °C the two signals belonging to the protons 5 and 5'' coalesced, indicating rapid exchange of environments in the complex and hence, fluxionality of the 4'-hydroxyterpyridine complex, **Scheme 3.18** and **Figure 3.11**.

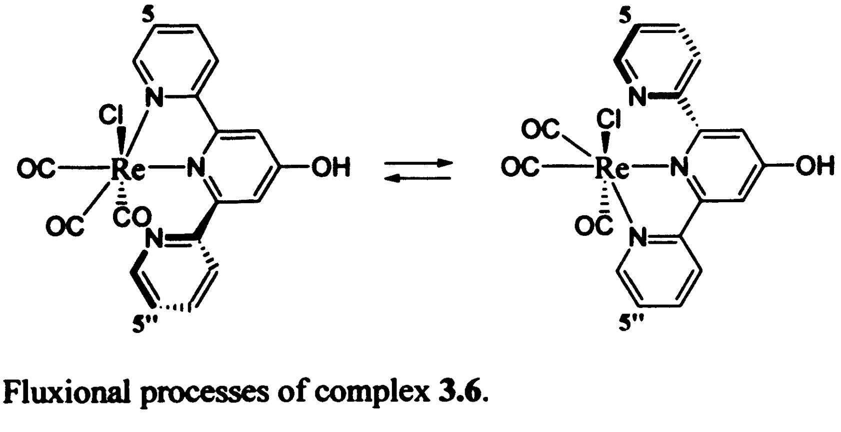

Scheme 3.18. Fluxional processes of complex **3.6**.

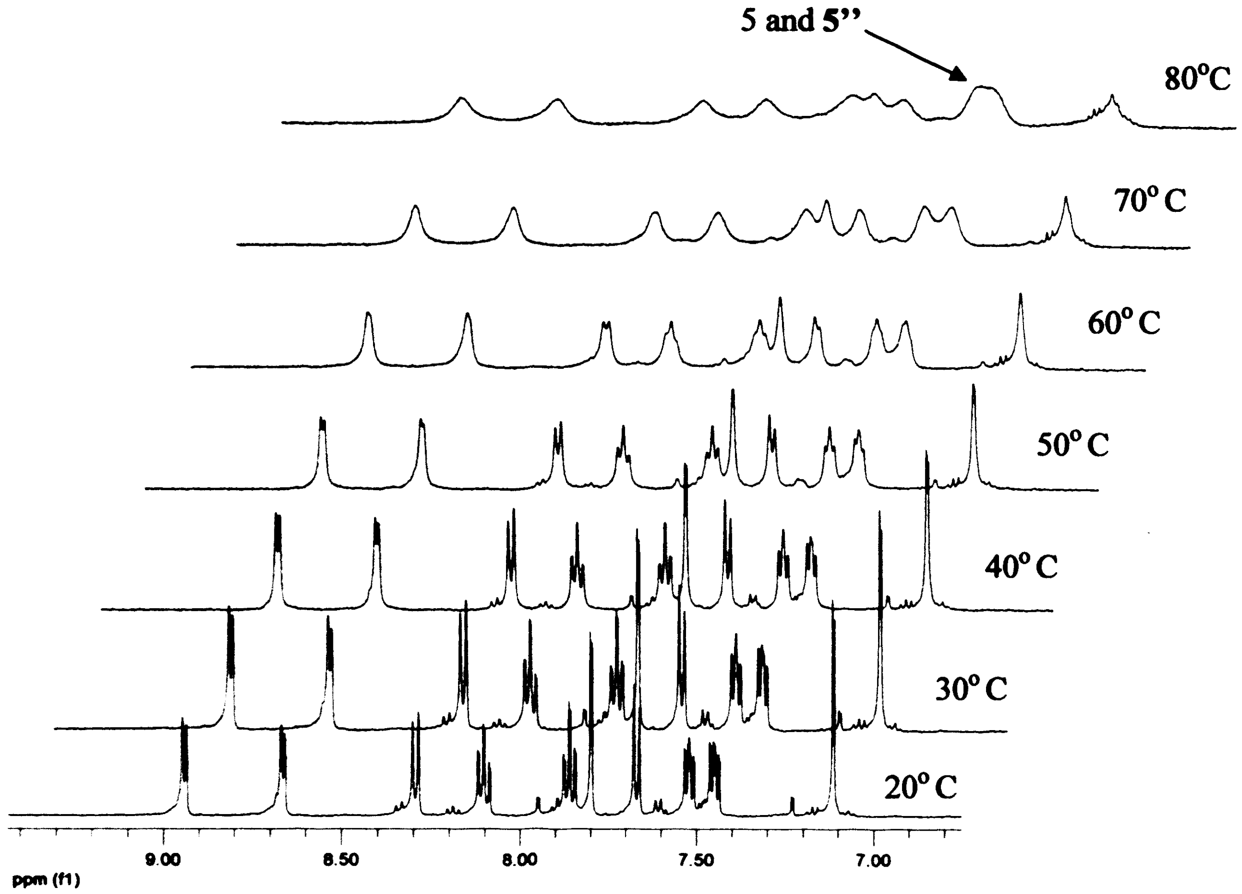

Figure 3.11. VT ^{1}H-NMR spectra of complex **3.6**.

Although no higher temperature experiments were carried out in order to see coalescence of any other peaks, the coalescence of 5, 5'' was used to calculate an approximate energy barrier for the process using the Eyring equation (eq 5.1).[13]

$$k = \chi \frac{k_B\, T}{h} e^{-\Delta G^{\ddagger}/RT} \quad \text{(eq. 5.1)}$$

$$\Delta G^{\ddagger}_{C} = 4.58\, T_C \left(10.32 + \log \frac{T_C}{k_C}\right) \quad \text{cal mol}^{-1}\ \text{(eq. 5.2)}$$

$$\Delta G^{\ddagger}_{C} = 19.14\, T_C \left(10.32 + \log \frac{T_C}{k_C}\right) \quad \text{J mol}^{-1}\ \text{(eq. 5.3)}$$

χ: Transmision coefficient
(usually assumed to be exactly 1)

k_B: Boltzman constant
($3.2995 \cdot 10^{-34}$ cal K^{-1})
($1.3805 \cdot 10^{-23}$ J K^{-1})

h: Planck constant
($1.5836 \cdot 10^{-34}$ cal s)
($6.6256 \cdot 10^{-34}$ J s)

Figure 3.12 Free energy of activation ($\Delta G^{\ddagger}$) from Eyring equation.

For a coalescence temperature T_C the rate constant k_C of the fluxional process is given by the equation shown below, (**eq. 5.4**).

$$k_C = \frac{\pi \Delta \nu}{(2)^{1/2}} \qquad \textbf{(eq. 5.4)}$$

$\Delta\nu$: Separation in Hz between two signals in absence of exchange.

Figure 3.13. Formula for the rate constant at the coalescence temperature.

$\Delta\nu$ is determined experimentally from the spectra recorded at temperatures which are far below the coalescence temperature and whose sharp peaks indicated slow (on the NMR time scale) exchange between the species. Specifically for complex **3.6**, the spectrum recorded at 293 K was taken as the example of slow exchange. The separation between the signals of the protons 5 and 5'' ($\Delta\nu$) has a value of 34.03 Hz and hence, k_C has a value of 75.59 s^{-1} (**eq. 5.4**). Finally the energy barrier is calculated by substitution of T_C (353 K) and k_C in **eq. 5.3**, affording a value of 74.24 kJ mol^{-1}, see **Figure 3.14**

$$\Delta G^{\ddagger}_{C} = 19.14 \cdot 353 \left(10.32 + \log \frac{353}{75.59}\right) \text{ J mol}^{-1} \quad \textbf{(eq. 5.3)}$$

$$\Delta G^{\ddagger}_{C} = 74.24 \text{ kJ mol}^{-1}$$

Figure 3.14. Result of the energy barrier calculation.

By using the equation **5.1**, the rate of the exchange process at room temperature can also be calculated. Therefore, k is 0.59 s^{-1} at 298 K

Importantly, this rate for the fluxional process at room temperature indicates that while the exchange is slow on the NMR timescale, the rate of exchange is high in real terms, happening 0.59 times per second. Thus, if the exchange process is involved with the displacement of axial ligands then this too would be a rapid process.

3.4.3.2 Reactivity of complexes 3.7, 3.8, 3.9.

Complexes **3.7**, **3.8** and **3.9** differ from complex **3.6** through functionalisation of the hydroxyl group on the terpyridine ligand. This would not only avoid the formation of the trinuclear species **3.10** when the complexes are reacted with silver, but also might stop the fluxional process occurring as the functionalised terpyridines are less electron rich in comparison with complex **3.6**.

The activation reaction of these terpyridine complexes was then attempted, starting with the reaction of complex **3.8** and $AgBF_4$ in dry acetonitrile. Unfortunately, ^{1}H-NMR spectroscopic experiments showed formation of species **3.10**, indicative of an ester hydrolysis reaction. Possibly, the coordination of the terpyridine derivative to the rhenium makes the ester less stable due to the lower electron density in the terpyridine fragment, therefore making the oxygen a better leaving group. This observation agrees with a previous investigation carried out by Williams *et al.* that demonstrated a big shift of pK_a values of 4'-hydroxyterpyridine upon coordination to Ir(III) (from pK_a(HOterpy) = 10 to pK_a(HOterpy-Ir) = 8, *i.e.* after coordination, the negative charge is more delocalized and hence, the R-OH acidity increases).[5]

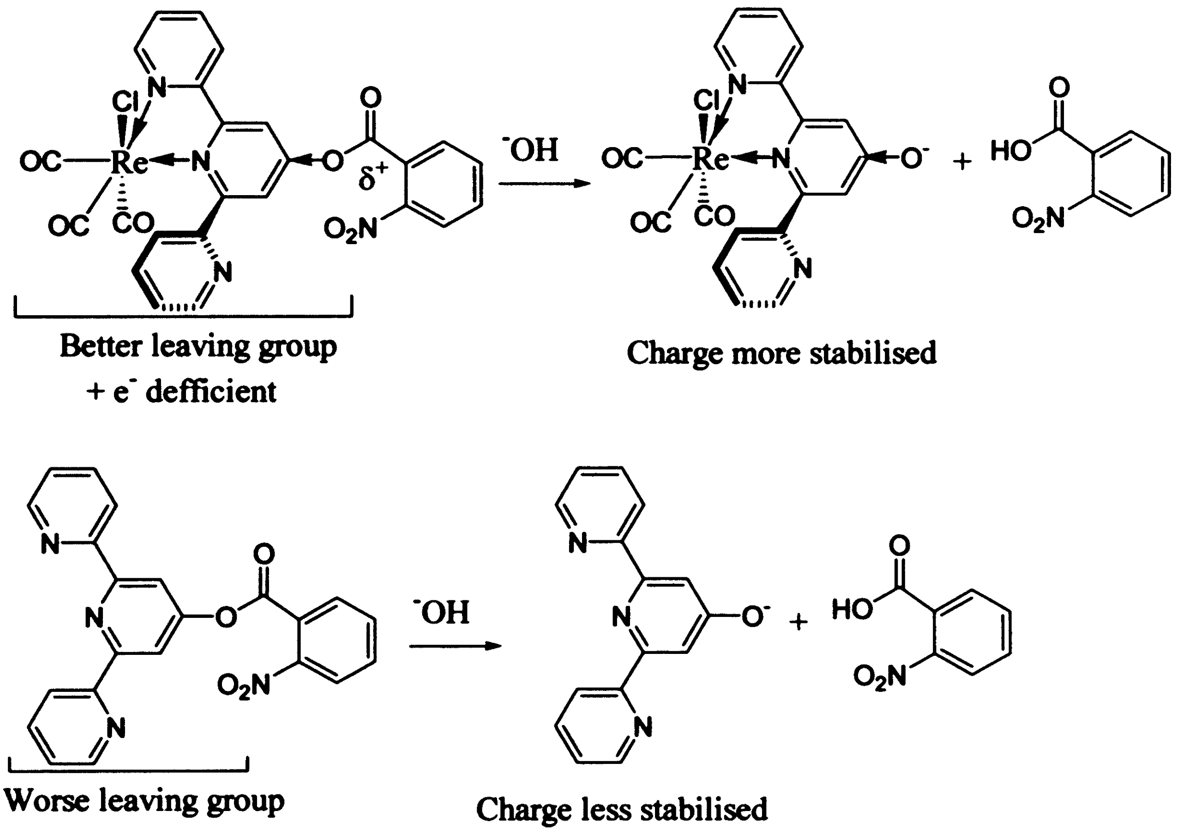

Scheme 3.19. Possible hydrolysis process of terpyridine derivative complexes.

The relative rate of ester hydrolysis of these complexes and of the corresponding ligands was studied (10 mg of studied species, 3 μl D_2O, 1.5 ml CD_3CN). The experiment was carried out on a NMR scale and monitored by this technique. Hydrolysis of the ester of complexes **3.7**, **3.8**, **3.9** occurred in less than 30 minutes, whereas the corresponding ligands did not show any ester hydrolysis for more than 12 hours. Complex **3.9** was the most rapidly hydrolysed, in line with the principle that it does not have the extra resonance stabilisation between the terpyridine and the aromatic ring which is present in complex **3.8**.

Complex **3.7** turned out to be the most stable which can be explained on the basis of stabilisation of the intermediate water adduct by the NO_2 group in complexes **3.8** and **3.9**, see **Scheme 3.20**.

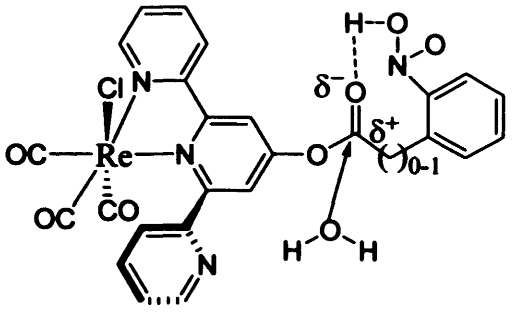

Scheme 3.20. Possible activation of the terpyridine derivative complexes.

Since these complexes undergo facile hydrolysis reactions, they are not suitable to be used as imaging agents for biological issues due to their instability in aqueous biological media. Therefore, no further studies of their properties were undertaken and attention turned to the next aim, the development of water soluble imaging probes.

3.4.4 Approach towards a Re complex bearing water soluble α-diimine with an extended π-system.

As was discussed in **Section 3.3.2**, the water solubility required for fluorescent probes for applications in biological systems will be provided by using a commercially available water soluble α-diimine, 1,10-bathophenanthroline sulphate disodium salt. This chelating ligand would replace the conventional bipyridine used in previous complexes.

Due to the low solubility of all complexes derived from this ligand in non-aqueous solvents, it was not possible to access the final target using the traditional reaction conditions.[14] For this reason a counterion exchange process was performed prior to reaction with $Re(CO)_5Cl$, **Scheme 3.21**. The commercial disodium salt was treated with two equivalents of tetrabutylammonium hydrogen sulphate in water. After an extraction with DCM, the product was isolated from the organic phase as an easily handleable pink anhydrous solid.

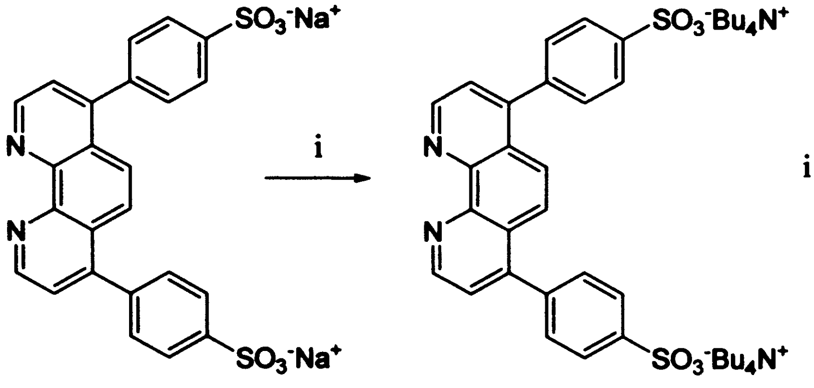

3.13

i: Bu_4NSO_4H, H_2O, DCM

Scheme 3.21. Counterion exchange process.

The tetrabutylammonium salt **3.13**, was reacted with cloro pentacarbonyl rhenium in toluene for 2 hours affording the desired complex, **3.14**, as an orange solid in 84 % yield, **Scheme 3.22.** The similarity of the frequencies of the carbonyl stretching bands (2018, 1910 and 1883 cm^{-1}) to those reported for analogous complexes[14] indicated the success of the reaction. Further complex characterisation (^{1}H-NMR and ^{13}C-NMR spectroscopy and mass spectrometry) corroborated this result. The activated rhenium complex was then synthesised by stirring complex **3.14** with trifluoromethylsulfonic acid as previous work with similar species demonstrated that this was a fast and clean method to obtain the activated species.

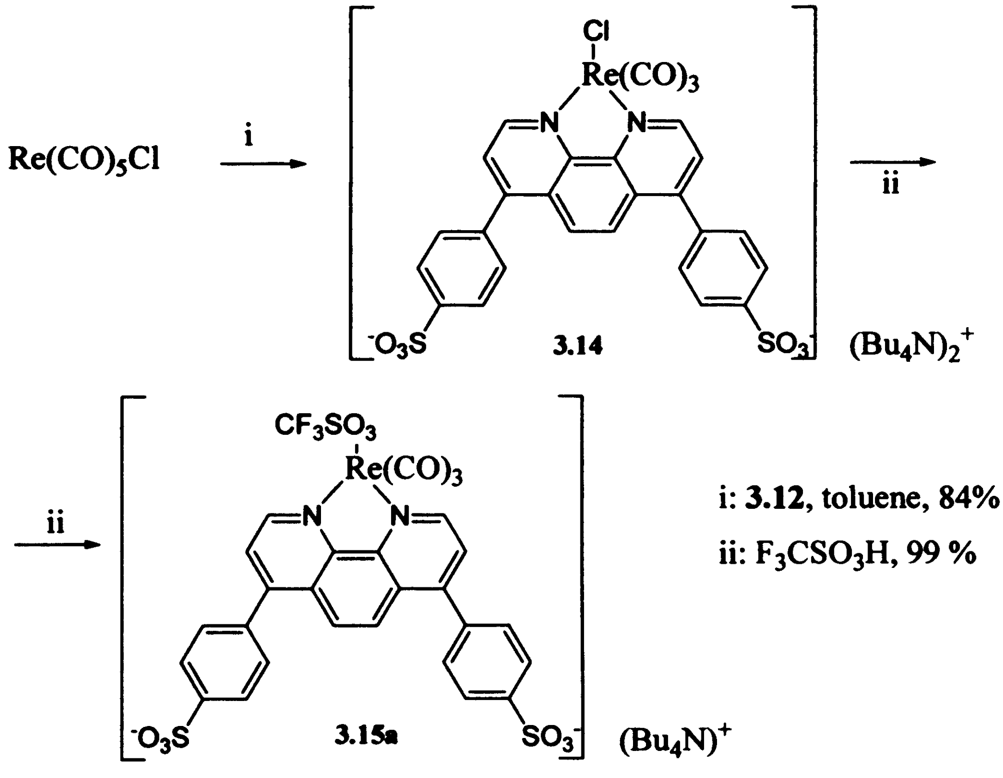

i: **3.12**, toluene, 84%

ii: F_3CSO_3H, 99 %

Scheme 3.22. Synthesis of the activated water soluble rhenium complex, **3.15**.

The activated rhenium complex was heated to reflux with pyridine in acetonitrile and with 3-hydroxymethylpyridine in THF. The desired product, in each case, was obtained successfully after 5 and 7 days respectively, **Scheme 3.23**.

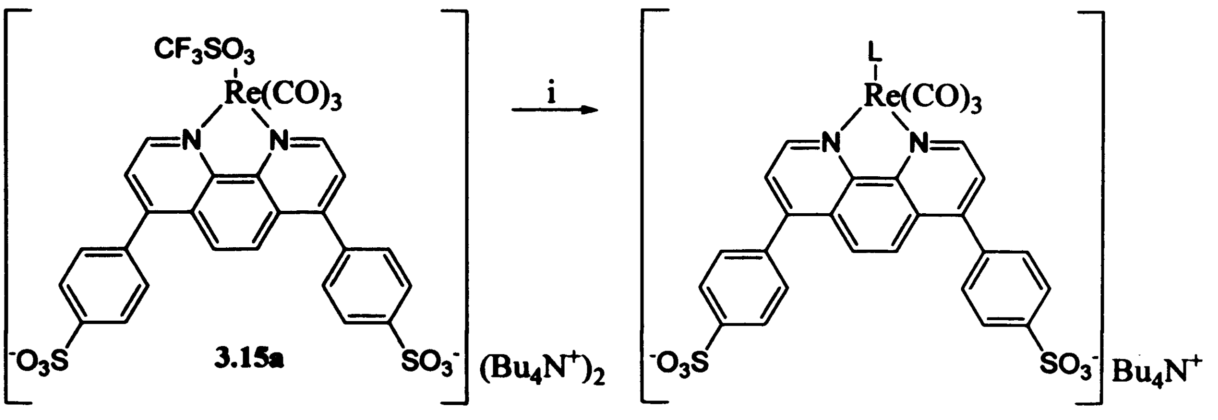

3.15a

i: Py, CH_3CN, 43 % ⇨ **3.16**

i: 3-$HOCH_2Py$, THF, 46 % ⇨ **3.17**

Scheme 3.23. Substitution of the triflate for the desired pyridine derivative.

A new approach was considered in order to diminish these protracted reaction times. Another activated species was synthesised by heating **3.14** with $AgCF_3SO_3$ to reflux in an acetonitrile solution in order to abstract the chloride and insert a more labile ligand (CH_3CN). Then, the new activated rhenium complex **3.15b** was reacted with a range of pyridine derivatives in methanol, which was found to be a more suitable solvent for these reactions than THF as the reaction time decreased from *ca.* 5 days to between 5 and 10 hours. This result might be explained by the better solubility of the starting material, **3.15b**, in polar solvents, which were not used in an initial stage due to their coordinating character, **Scheme 3.24.** The reactions were monitored by ^{1}H-NMR spectroscopy where the shift of protons (6) in bathophenanthroline to lower field and the new set of peaks belonging to the coordinated axial pyridine derivative indicated that the reaction was complete.

Unfortunately, when compound **2.5** (3-TBDO$(CH_2)_3OCOCH_2$Py) was used as an axial ligand, a mixture of complexes was obtained, including the expected product. Mass spectrometry confirmed its formation: (ESI) 1070.3 $[M]^+$, 870.1 $[M\text{-}CO(CH_2)_3OTBD]^+$, 761.1 $[M\text{-}PyCH_2OCO(CH_2)_3OTBD]^+$ with a good match to the expected isotope pattern. However, further attempts to purify the product by precipitation or washing with a variety of solvents were unsuccessful.

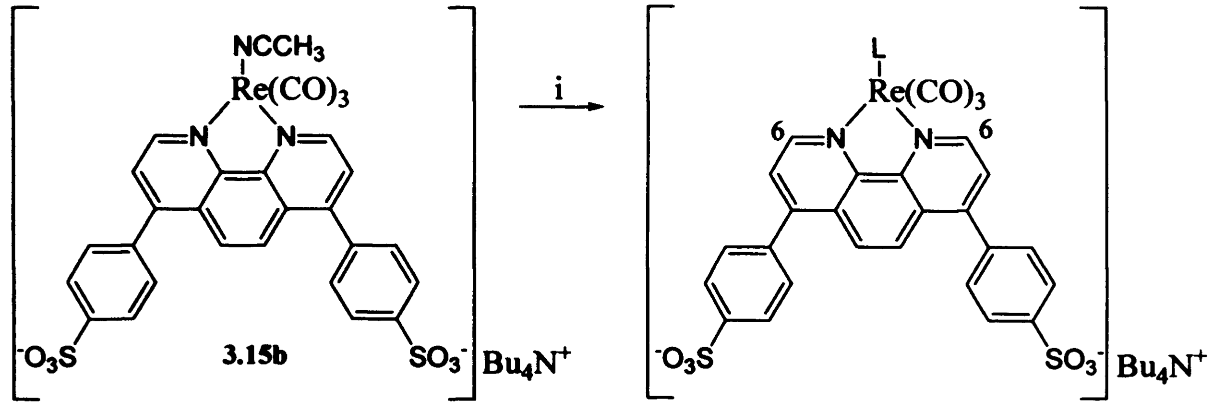

i: Py, MeOH 45 % ⇨ 3.16
i: 3-HOCH$_2$Py, MeOH 43 % ⇨ 3.17
i: 3-TBDO(CH$_2$)$_3$OCOCH$_2$Py (2.5), MeOH ⇨ 3.18

Scheme 3.24. Synthesis of complexes 3.16, 3.17 and 3.18.

In order to demonstrate the possibility of further functionalisation of the complexes once a pyridine derivative was coordinated, compound 3.17 was reacted with mystiric acid in the presence of EDCI and DMAP in DCM, giving a much more lipophilic complex than the three previously synthesised analogues, **Scheme 3.23.** In the ^{1}H-NMR spectrum, the observed shift of the methylene protons (7) from 4.38 to 4.83 ppm was indicative of the success of the reaction; further characterisation corroborated this result.

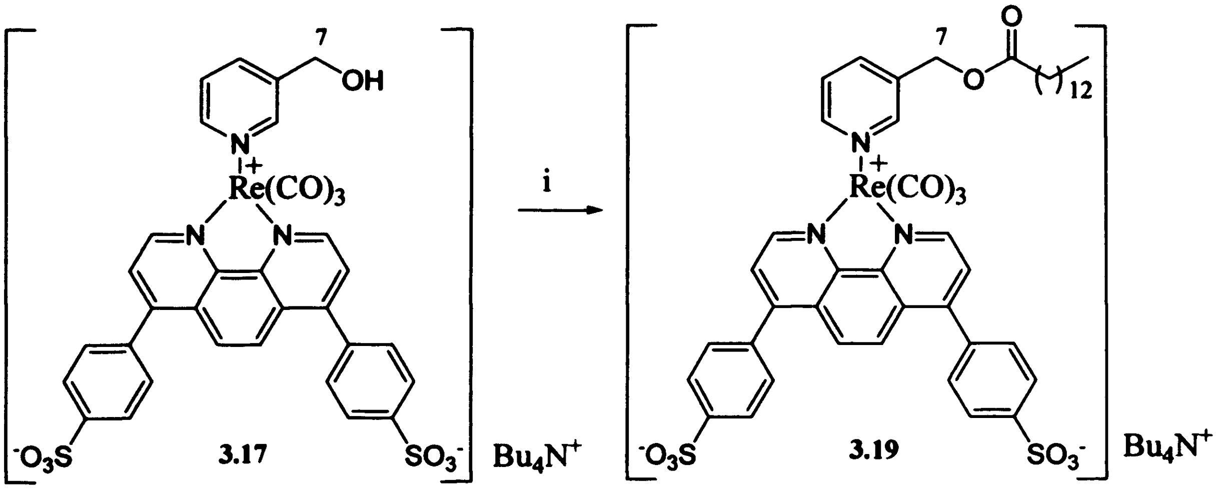

i: Mystiric acid, EDCI, DMAP, DCM, 62 %

Scheme 3.25. Coupling reaction of the preformed complex 3.17.

After having synthesised a variety of sulphonated rhenium complexes as tetrabutylammonium salts, the recovery of the water solubility was then achieved using ion exchange chromatography with Amberlite IR 120-H, as the ammonium form. Therefore final complexes were obtained as the water-soluble ammonium salts.

3.5 The "Self Destruction" Experiment.

3.5.1 SOB: self destructing device.

Due to the lack of success in synthesising the rhenium complex bearing ligand **3.2** and also the ease of the ester hydrolysis reaction observed for complex **3.7** (a functionalised terpyridine), no attempts to measure the cyclisation rate were undertaken for these complexes.

3.5.2 NO_2-derivatives: self-destructing device.

The procedure followed to study the self destruction mechanism of the NO_2 derivatives entails the use of NADPH[c] in stoichiometric amounts to provide the hydride needed for the reduction of the nitro group and the enzyme nitroreductase as a catalyst. Changes of NADPH absorption bands in the UV spectrum would indicate the reduction of the nitro groups but it would not confirm whether the cyclisation reaction has taken place or not, **Scheme 3.26.** ^{1}H-NMR spectroscopy is needed to demonstrate the presence of species **a,** therefore the experiments need to be done on a considerably larger scale than if using UV techniques. Unfortunately, high concentrations of substrates inhibit the enzyme, nitroreductase, and in addition, complexes **3.8** and **3.9** undergo easy hydrolysis, a reaction indicating their unsuitability for use in biological media, so no *"self destruction"* experiments were carried out with these targets either.

---

[c] NADPH: Nicotinamide adenine dinucleotide phosphate, the reduced from of NADP$^+$, provides the reducing equivalents for oxidation-reduction reactions. Both forms absorb strongly in the ultraviolet due to the adenine base. The difference in the ultraviolet absorption spectra between the oxidized and reduced forms makes it simple to measure the conversion of one to another, and therefore the percentage of reaction conversion.

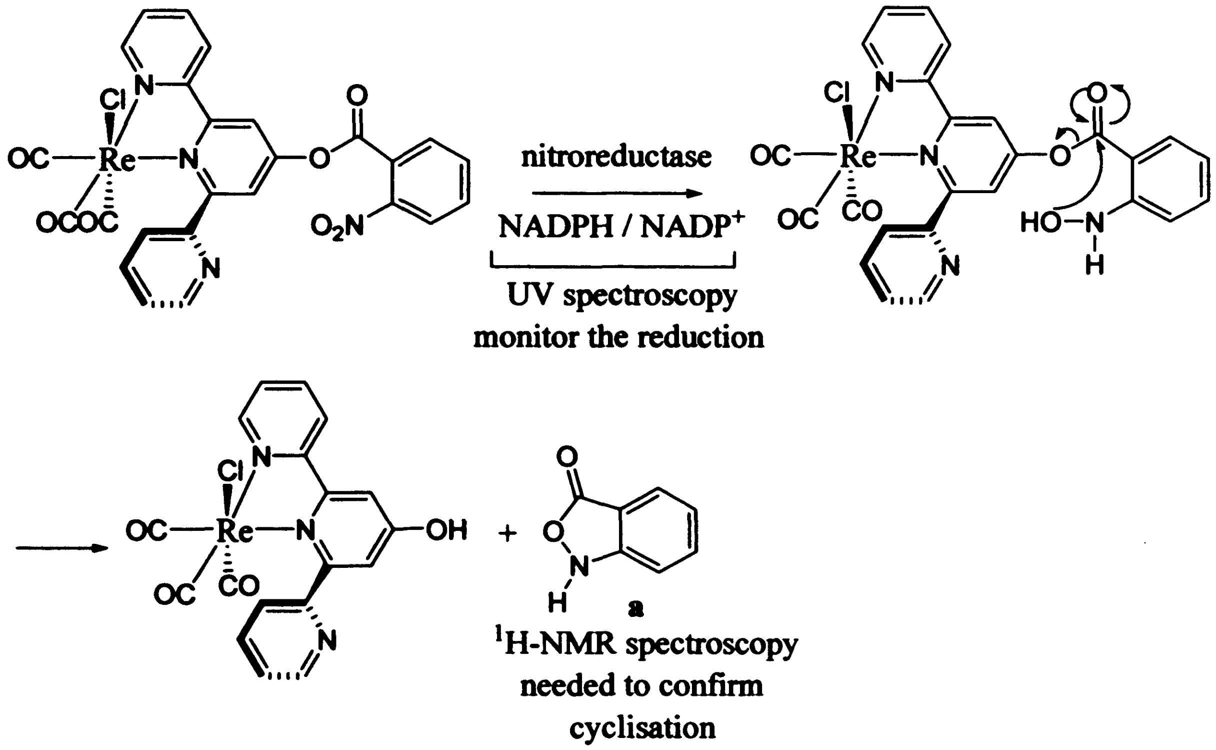

Scheme 3.26. Sensing processes for complexes whose sensor is a nitro group.

3.6 Photophysical Studies.

The fluorescence behaviour of the complexes **3.6** - **3.9** and **3.16**, **3.17**, **3.19** was examined to assay their suitability for cell microscopy applications. **Table 3.1** records the bands observed by UV spectroscopy, which correlate with the data reported in the literature for similar complexes.[15] Two distinct absorption bands are observed for the two types of complexes, ligand $\pi \rightarrow \pi^*$ and MLCT ($d\pi(Re) \rightarrow \pi^*(N\text{-}N)$) transitions. The IL transitions occur between 213 nm and 336 nm for all the complexes, while the MLCT transitions occur at *ca.* 371 nm for the complexes bearing the terpyridine as the chromophore, red-shifted by around 10 nm for those complexes bearing the more conjugated bathophenanthroline system.

Complex	^{1}IL λ_{abs}/nm, (ε/dm^{3}mol^{-1}cm^{-1})	^{1}MLCT, λ_{abs}/nm, (ε/dm^{3}mol^{-1}cm^{-1})
3.6$_a$	243 (9282), 292(8093)	358 (1687)
3.7$_a$	205 (8391), 264 (4095), 295 (3579)	375 (453)
3.8$_a$	240 (11977), 254 (9911) 299 (9911)	376 (1830)
3.9$_a$	235 (22557), 260 (14839) 295 (11405)	374 (1546)
3.16$_b$	231 (11325), 260 (11325), 285 (12297)	381 (3205)
3.17$_b$	235 (7888), 282 (7765)	382 (4196)
3.19$_b$	213 (30584), 292 (19711), 336 (6958)	391 (3430)

a. CH_3CN as solvent.
b. MeOH as solvent.

Table 3.1. Absorption bands of complexes **3.6-3.9** and **3.16**, **3.17**, **3.19**.

The excitation and emission spectra for the same complexes were recorded in CH_3CN for the terpyridine complexes and in MeOH or water for the bathophenanthroline derivatives. **Table 3.2** summarises the values recorded for the excitation and emission maxima, which do not differ from those that are expected for complexes of the type, *fac*-Re(NN)$(CO)_3$L. All showed broad excitation maxima ranging from 360 to 396 nm and emission maxima ranging from 543 to 585 nm, originating from the lowest energy ^{3}MLCT ($d\pi(Re) \rightarrow \pi^*(N\text{-}N)$) excited state.

An important conclusion can be drawn comparing the emission and excitation values given by both types of complexes, the hydroxyterpyridine derivative complexes **3.6** - **3.9**, and the water soluble extended π α-diimine complexes, **3.16**, **3.17** and **3.19**. The *self-destruction* device is more effective when placed on the α-diimine than when on the axial ligand, *i.e.* the luminescence of the complexes is significantly more affected after the *self-destruction* has taken place (compare the values of the destructed species **3.6**, and complexes bearing the self destruction devise on the α-diimine **3.7**, **3.8**, and **3.9**, with the destructed species **3.17** and **3.19**, complex analogue to a species bearing a self destruction device in the axial ligand). This difference is presumably due to the modification of the electronic properties on the α-diimine which is directly implicated in the ^{3}MLCT [dπ(Re) → π*(diimine)] transition.

Complex	Excitation λ/nm	Emission λ/nm	Lifetimes τ/ns
3.6$_a^*$	385	585	--
3.7$_a$**	393	563	--
3.8$_a$**	360	543	--
3.9$_b$**	370	559	--
3.16$_b$	375	566	756$_c$
3.17$_b^*$	378	563	764$_c$
3.19$_b$	393	558	2590$_c$

a CH_3CN as solvent.
b MeOH as solvent.
c Water as solvent.
*** Complex bearing self destruction device.*
** Complex after self destruction.*

Table 3.2. Excitation, emission maxima and lifetimes for complexes **3.6** - **3.9** and **3.16**, **3.17** and **3.19**.

In addition, the lifetimes of the water soluble complexes **3.16**, **3.17** and **3.19** were measured, see **Table 3.2**. The latter, which not only has the bathophenanthroline α-diimine, but also a C_{13} lipophilic chain, has a lifetime of 2.59 μs which is considerably larger than the lifetimes of species **3.16** and **3.17** (756 and 764 ns respectively). It is speculated that the lipophilic chain in the axial ligand is interacting with the α-diimine and thus affecting the relaxation and/or quenching processes of the complex, thus increasing the lifetime of the unit. This interaction could be driven by hydrophobic forces, making an interaction between the lipophilic chain and the bathophenanthroline unit favourable and thus protecting the excited state from solvent interactions.[16] However, whether this interaction involves aggregation, micelle formation or unimolecular conformations has not been determined.

Only a few examples of quantum yields of compounds of the general formula [Re(bisim)(CO)$_3$X] are available in the literature. Their values range from 0.7 in the case of isonitrile complexes of the type [Re(bisim)(CO)$_3$CNR]$^+$ where R is a *t*-butyl or n-alkyl group[16] to 0.0001 in [Re(4,4'-(NO$_2$)$_2$bipy)(CO)$_3$Cl].[1] A general trend is observed that an increase in the level of conjugation in the bisimide ligand increases the value of the quantum yield, as does as the introduction of electron donating groups. However, to arrive at a general estimate for these kinds of complexes based on the literature is not straight forward, as reported data shows great variations in quantum yield for apparently minor structural variations (Φ([Re(bipy)(CO)$_3$NCMe]$^+$) = 0.015, Φ([Re(phen)(CO)$_3$NCPr]$^+$) = 0.069).[17] These variations imply either a very complex set of parameters which determine the overall value, or unreliability in the literature data. Unfortunately, it was not possible to carry out any quantum yield analysis of the novel rhenium complexes due to technical problems. Nevertheless, in an attempt to estimate some likely values for the range and variations in the quantum yields of these complexes, the data reported by Meyer[1] in 1991 were considered as the most useful and reliable guideline. These suggest that those cationic rhenium complexes bearing a pyridine derivative in the axial position would have greater quantum yields than the neutral analogous chloride complexes (Φ([Re(bipy)(CO)$_3$(4-EtPy)]$^+$) = 0.18, Φ([Re(bipy)(CO)$_3$Cl]) = 0.0045). In addition, complexes with an extended conjugated chelate ligand, such as the bathophenanthroline sulphonates, would also be expected to have greater quantum yield values than the less conjugated bipyridine complexes (Φ([Re(bipy)(CO)$_3$Cl]) = 0.0045, Φ([Re(phen)(CO)$_3$Cl]) = 0.036).

3.7 Discussion Of Crystal Structures

3.7.1 Crystalline structure of complex 3.6.[d]

Single crystals of complex [Re(OH-terpy)$(CO)_3$Cl] suitable for X-ray crystallography were grown by the slow evaporation of an acetonitrile solution of the complex. Crystallographic refinement data are given in **Table 3.3**. The perspective ORTEP drawing of the complex **3.6**, with selected atomic numbering is shown in **Figure 3.15** and selected bond lengths and angles are summarised in **Table 3.4.**

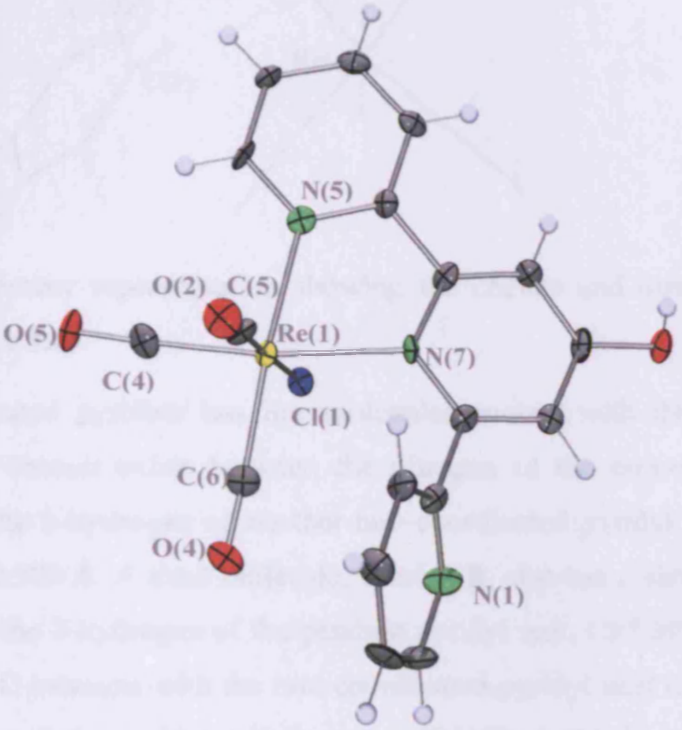

Figure 3.15. ORTEP representations of the structure of **3.10** with thermal ellipsoids drawn at the 50% level.

The rhenium coordination sphere can be described as a slightly distorted octahedron where the three carbonyl ligands are arranged in a *facial* geometry. The 4-hydroxyterpyridine and the two carbonyls *trans* to it describe the equatorial plane. The third carbonyl and the chloride ligand are placed in the apical plane. Deviation from an ideal octahedron mostly originates from geometric restraints imposed by the chelate ligand with a chelate angle of N(5)Re(1)N(7): 74.9(3)° instead of the ideal angle of 90°. It is worth noting that the non-coordinated pyridine has a torsion angle of 58.48° with respect to the two, almost coplanar,

---

[d] Crystal structure measured and solved by Richard Arthur at Cardiff University.

coordinated pyridyl fragments, with the nitrogen pointing in the same direction as the Re-Cl bond.

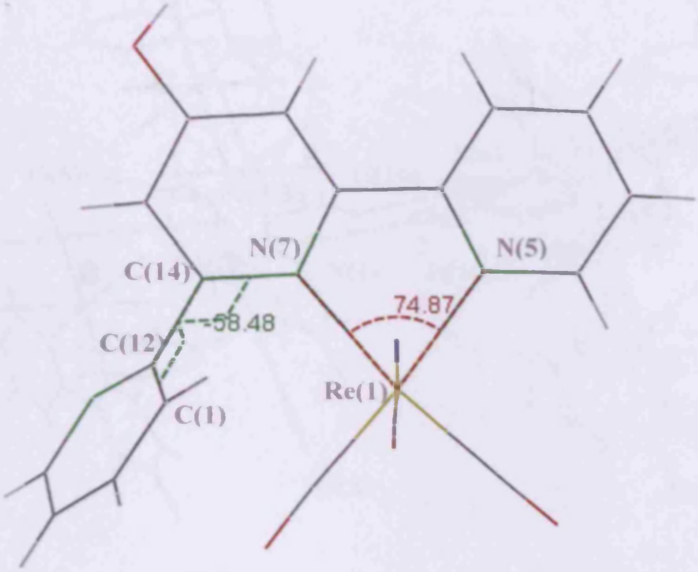

Figure 3.16. Mercury representation showing the chelate and torsion (pendant pyridyl) angles of complex **3.6**.

The non-coordinated pyridine has intermolecular contact with three other species, see **Figure 3.17.** A contact exists between the nitrogen of the non-coordinated pyridyl in species **A** with the 6-hydrogen of another non-coordinated pyridyl from adjacent species **A'**, N(1)H(16): 2.599 Å. A third molecule, species **B**, also has a short interaction between the chlorine and the 3-hydrogen of the pendant pyridyl unit, Cl(1)H(1A): 2.847 Å. Finally a fourth species **C** interacts with the non-coordinated pyridyl unit *via* a contact between a carbonyl oxygen and the pyridyl 4-hydrogen, O(5)H(7): 2.683 Å. All of these interactions are presumably predominantly electrostatic as they are too long to be considered as conventional strong hydrogen bonds.[18]

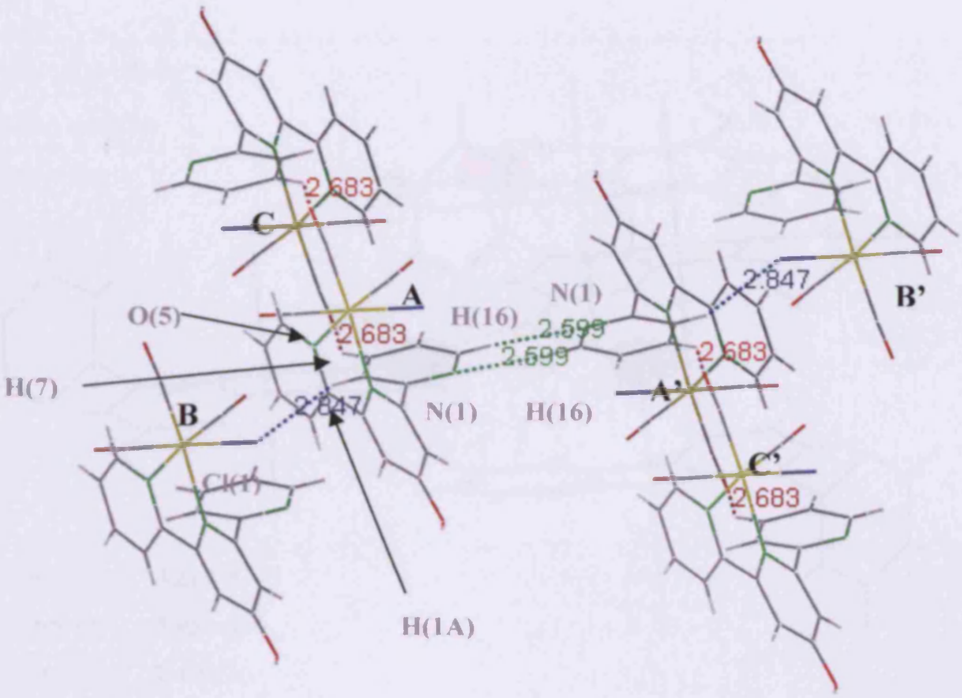

Figure 3.17. Line drawing of complex **3.6** showing non-coordinated pyridyl intermolecular contacts with three surrounded species.

The distortion from planarity displayed by the chelate ligand between the two coordinated pyridyl rings (torsion angle N(7)-C(17)-C(9)-N(5): 7.34 °) can be rationalized as a packing effect. The environment and interaction of each of the coordinated pyridyl unit is different, presumably due to the hydroxyl substituents placed at the 4' position. The hydroxyl moiety interacts with a chlorine atom from an adjacent molecule (blue highlight 3.050 Å) as well as with a hydrogen from a second molecule (green highlight, 2.499 Å) and finally with a pyridyl carbon from a third molecule which was omitted for clarity (red highlight, 3.217 Å), **Figure 3.18.**

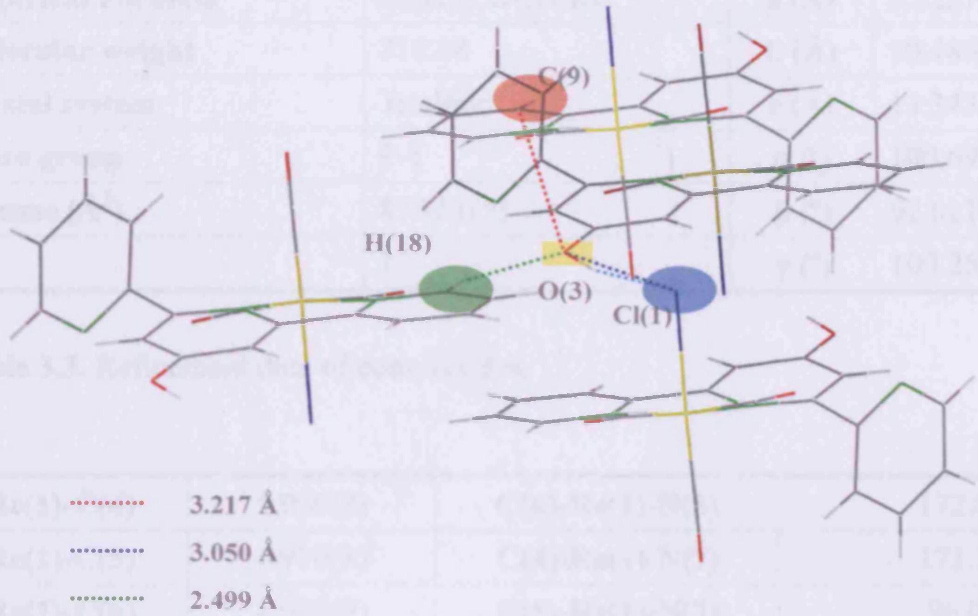

Figure 3.18. Mercury representation of complex **3.6** showing the intermolecular contacts of the hydroxyl group with the surrounding species: green-blue highlight shows interaction O(3)-Cl(1), green-grey highlight shows interaction O(3)-H(18), green-red highlight shows interaction O(3)-C(19).

The carbonyl bond distances at *ca.* 1.909 Å and Re-Cl bond length at 2.517(2) Å are consistent with those found for similar rhenium (I) tricarbonyl complexes. Selected bond lengths and angles are given in **Table 3.4**.

Empirical Formula	$C_{26}H_{16}ClN_4O_7Re$	**a (Å)**	6.5227(2)
Molecular weight	718.08	**b (Å)**	10.4890(3)
Crystal system	Triclinic	**c (Å)**	13.3433(4) A
Space group	P-1	**α (°)**	100.6910(10)
Volume (Å^3)	879.81(5)	**β (°)**	92.6110(10)
Z	1	**γ (°)**	100.2530(10)

Table 3.3. Refinement data of complex **3.6**.

Re(1)-C(4)	1.906(8)	**C(6)-Re(1)-N(5)**	172.8(3)
Re(1)-C(5)	1.910(8)	**C(4)-Re(1)-N(7)**	171.2(3)
Re(1)-C(6)	1.929(9)	**C(5)-Re(1)-N(7)**	96.0(3)
Re(1)-N(5)	2.152(7)	**C(6)-Re(1)-N(7)**	101.4(3)
Re(1)-N(7)	2.216(6)	**N(5)-Re(1)-N(7)**	74.9(3)
Re(1)-Cl(1)	2.5187(19)	**C(4)-Re(1)-Cl(1)**	94.6(2)
C(4)-Re(1)-C(5)	87.1(3)	**C(5)-Re(1)-Cl(1)**	178.2(2)
C(4)-Re(1)-C(6)	86.8(4)	**C(6)-Re(1)-Cl(1)**	90.5(3)
C(5)-Re(1)-C(6)	89.2(3)	**N(5)-Re(1)-Cl(1)**	82.95(18)
C(4)-Re(1)-N(5)	96.6(3)	**N(7)-Re(1)-Cl(1)**	82.35(18)
C(5)-Re(1)-N(5)	97.3(3)		

Table 3.4. Selected bond lengths (Å) and angles (°) of complex **3.6**.

3.7.2 Crystalline structure of complex 3.10.[e]

Slow evaporation of an acetonitrile solution of complex **3.10** afforded crystals suitable for analysis by X-ray diffraction techniques. Crystallographic refinement, selected bond length and angle data, and perspective ORTEP drawings of the complex, **3.6**, with atomic numbering are given in **Table 3.5**, **Table 3.6**, **Figure 3.19** and **Figure 3.20** respectively. Complex **3.10** is formed by three distorted octahedral units, *fac*-[Re(Oterpy)$(CO)_3$], where

---

[e] Crystal structure measured and solved by Richard Arthur at Cardiff University.

the terpyridine molecules are acting as both bidentate ligands coordinated through nitrogen to one rhenium atom and as bridging molecule to form a triangular shape, see **Figure 3.19.**

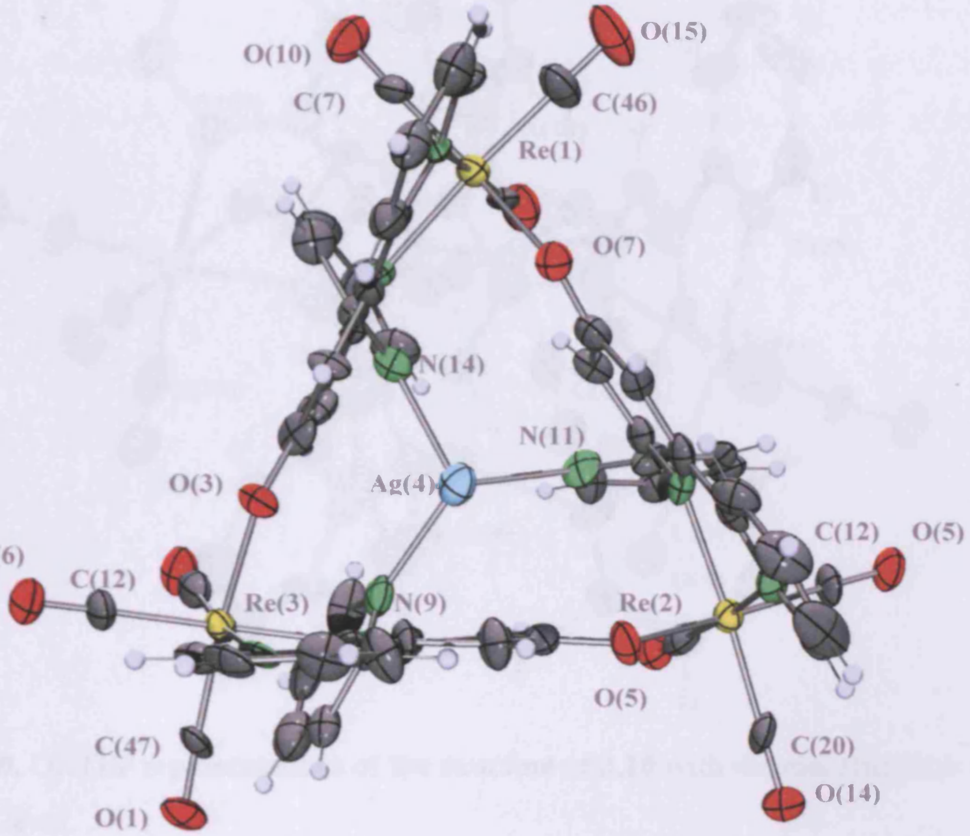

Figure 3.19. ORTEP representations of the structure of **3.10** with thermal ellipsoids drawn at the 50% level.

In addition, the three pendant pyridyl units are attached to a silver atom located in the central position of the triangle formed by the rhenium units, see **Figure 3.20**. Its position is displaced by 0.516 Å, from the plane formed by the three nitrogen atoms bound to it (**Figure 2.21**).

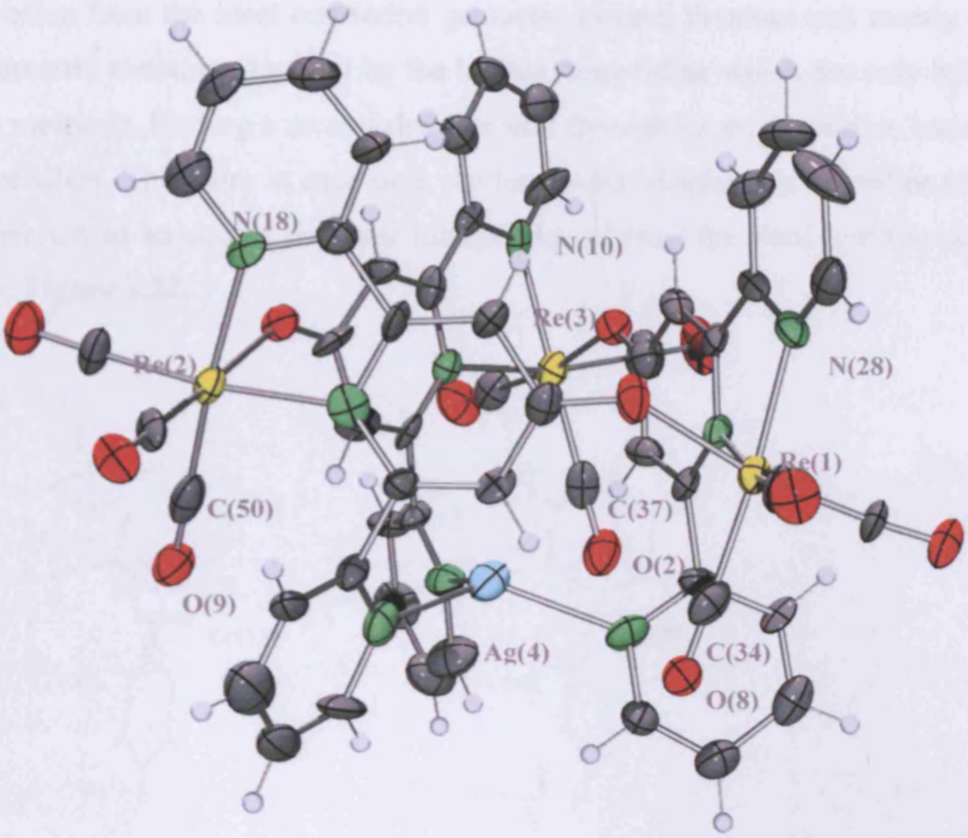

Figure 3.20. ORTEP representations of the structure of **3.10** with thermal ellipsoids drawn at the 50% level.

Figure 3.21. Mercury representations of the structure of **3.10.** presenting the different distances along the cavity.

The deviation from the ideal octahedral geometry in each rhenium unit mostly originates from geometric restraints imposed by the hydroxyterpyridine which not only behaves as a bridging molecule, binding a second rhenium unit through its axial position, but also as the ligand for silver. Therefore in each unit, the terpyridine displays two pyridine units bound to the rhenium in an almost coplanar relationship whereas the third pyridine is bound to Ag(I) see **Figure 3.22.**

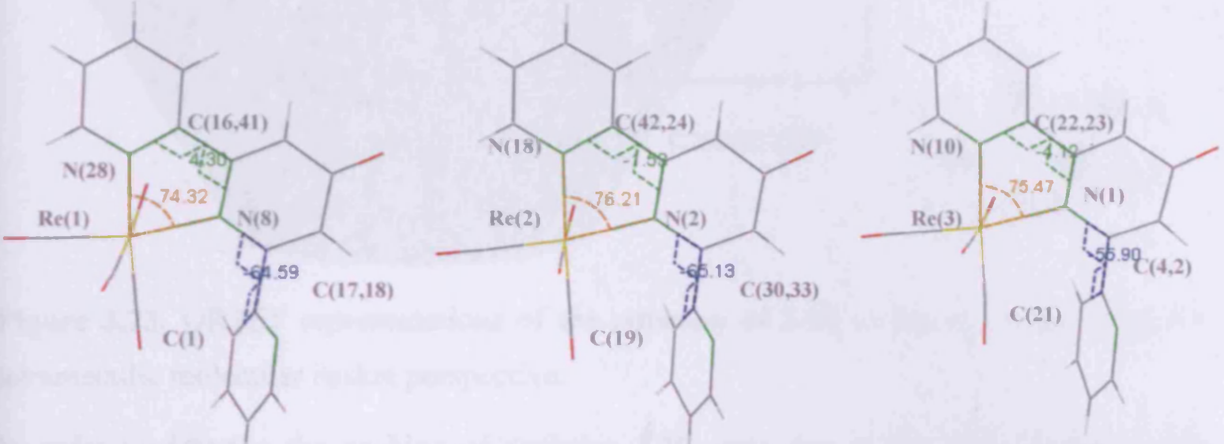

Figure 3.22. Three rhenium units.

This combination of coordination geometries presents a cone shape that is *ca.* 7.3 Å deep and 7.0 Å wide, measured from the three nitrogen atoms at the top and bottom of the "cone" respectively, **Figure 3.23.** The silver atom defines the bottom of the cone and one of the chelated pyridyl units of each rhenium unit defines the base. Thus, overall the three triangular rhenium containing units are connected to form a conical vessel which is closed at one end by the AgPy$_3$ unit to give a tetrametallic molecular basket.

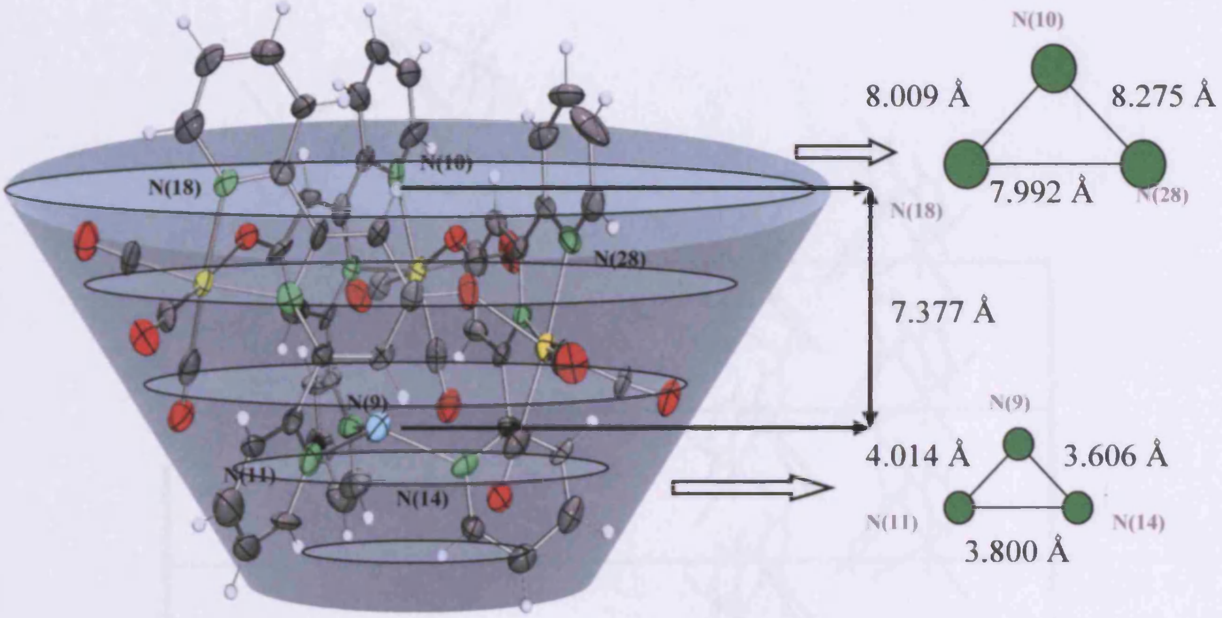

Figure 3.23. ORTEP representations of the structure of **3.10** inside of a cone to give a tetrametallic molecular basket perspective.

In order to describe the packing of complex **3.10**, only one of the three rhenium units (Re(1)) is displayed to simplify the view of the structure and also to help understanding. The unit cell is formed by four complexes (AB-CD) where each pair is a mirror image and they are flipped 180° as indicated by the space group of the system (P_21/c), see **Figure 3.24**.

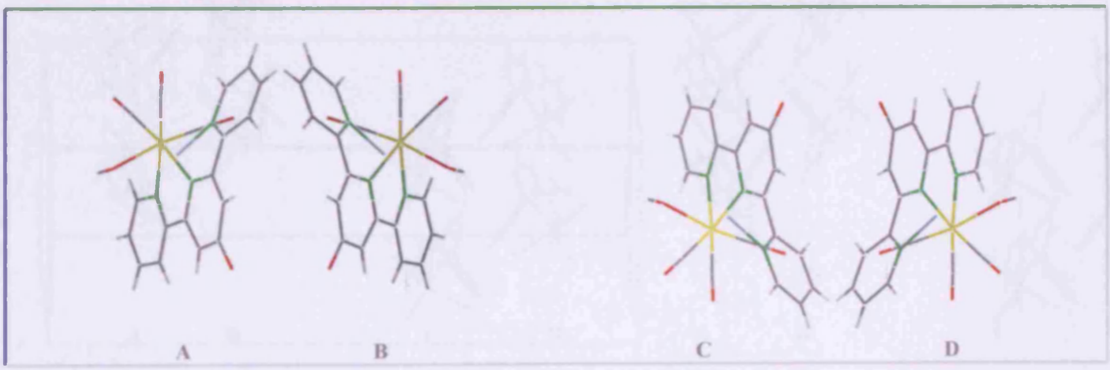

Figure 3.24. Packing of complex **3.10**, viewed along a axis

The four units (AB-CD) are not aligned; they are placed in a zig-zag shape. **Figure 3.25** shows the packing of complex **3.10** with an increment in the number of units, 3 × (AB-CD), along the a axis.

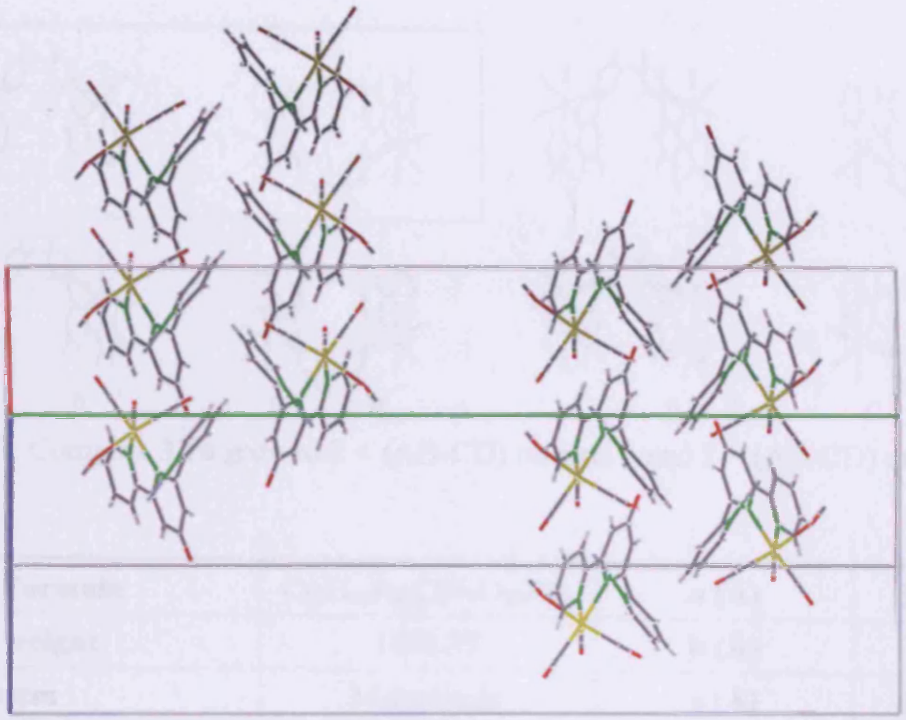

Figure 3.25. 3 × (AB-CD) units of complex **3.10.**

The growth of units along the b axis shows the same pattern as in the previous case, *i.e.* four units (AB-CD) where each pair is a mirror image and they are flipped 180°. It can be seen easily when fragments are grown along axis b as in **Figure 3.26**.

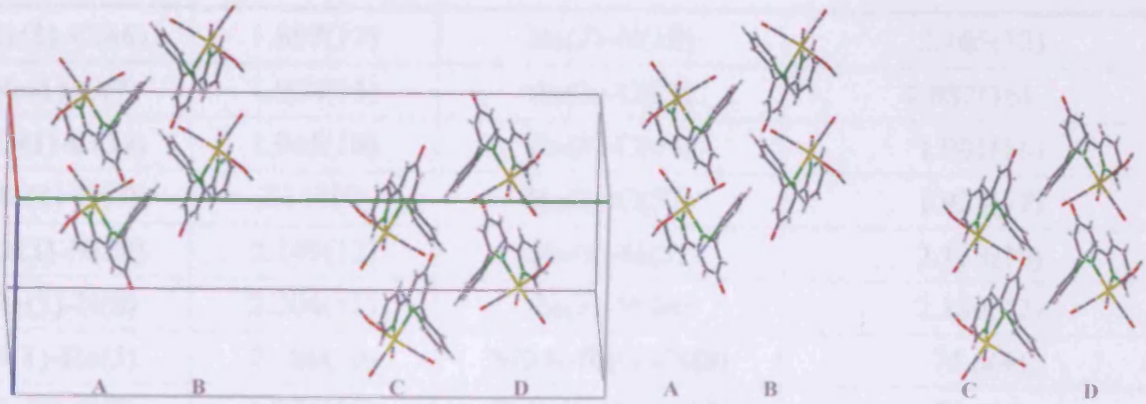

Figure 3.26. Complex **3.10** grown 2 × (AB-CD) on axis a and 2 × (AB-CD) on axis b.

Finally the growth of fragments along the c axis shows a pattern that does not differ from that observed in the a axis, *i.e.* the four units in the unit cell (AB-CD) are placed just over/below another four (AB-CD). **Figure 3.27** shows the view along the axis a where there is a fragment growth of 2 × (AB-CD) on axis b and 2 × (AB-CD) on axis c.

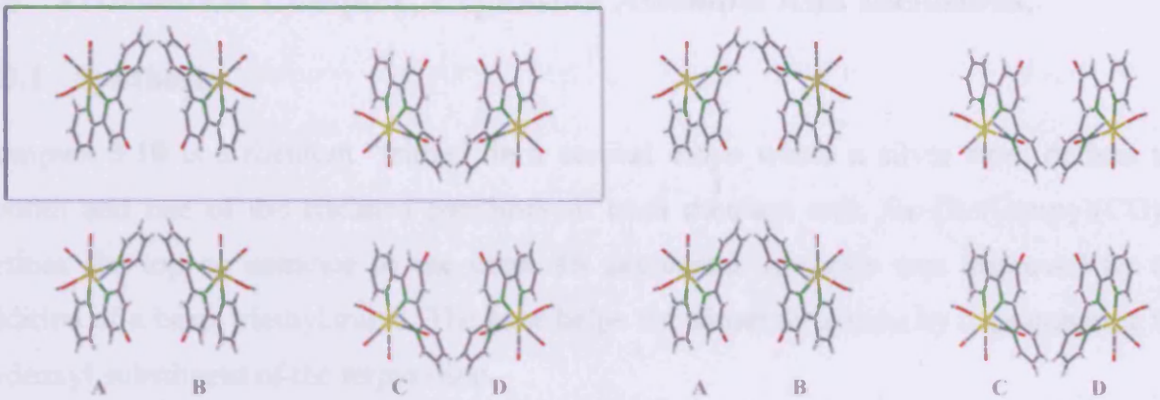

Figure 3.27. Complex **3.10** growed 2 × (AB-CD) on axis b and 2 × (AB-CD) on axis c.

Empirical Formula	$C_{54}H_{30}AgClN_9O_{12}Re_3$	**a (Å)**	13.468(3)
Molecular weight	1698.79	**b (Å)**	38.005(8)
Crystal system	Monoclinic	**c (Å)**	13.015(3)
Space group	P 2_1/c	**α (°)**	90
Volume (Å^3)	6277.55	**β (°)**	109.55(3)
Z	4	**γ (°)**	90

Table 3.5. Refinement data of complex **3.10**.

Re(1)-C(46)	1.897(17)	**Re(2)-N(18)**	2.165(12)
Re(1)-C(7)	1.924(13)	**Re(3)-C(12)**	1.882(16)
Re(1)-C(34)	1.945(18)	**Re(3)-C(47)**	1.901(16)
Re(1)-O(7)	2.114(9)	**Re(3)-C(37)**	1.928(17)
Re(1)-N(28)	2.149(12)	**Re(3)-O(3)**	2.138(10)
Re(1)-N(8)	2.204(11)	**Re(3)-N(10)**	2.186(12)
N(1)-Re(3)	2.186(10)	**N(28)-Re(1)-N(8)**	74.6(4)
Re(2)-C(5)	1.876(15)	**N(2)-Re(2)-N(18)**	76.0(4)
Re(2)-C(20)	1.897(16)	**N(10)-Re(3)-N(1)**	75.7(4)
Re(2)-C(50)	1.96(2)	**N(11)-Ag(4)-N(14)**	125.7(4)
Re(2)-O(5)	2.115(9)	**N(11)-Ag(4)-N(9)**	113.5(4)
Re(2)-N(2)	2.159(11)	**N(14)-Ag(4)-N(9)**	105.5(5)

Table 3.6. Selected bond lengths and angles of complex **3.10**.

3.8 Trirhenium Complex, Expansion Attempts And Inclusions.

3.8.1 Synthesis.

Complex **3.10** is a rhenium "trimer" in a conical shape where a silver atom defines the bottom and one of the chelated pyridines of each rhenium unit, *fac*-[Re(Oterpy)(CO)$_3$], defines the top or entrance to the cone. Its accidental synthesis was improved by the addition of a base, triethylamine. The base helps the trimer formation by deprotonating the hydroxyl substituent of the terpyridine.

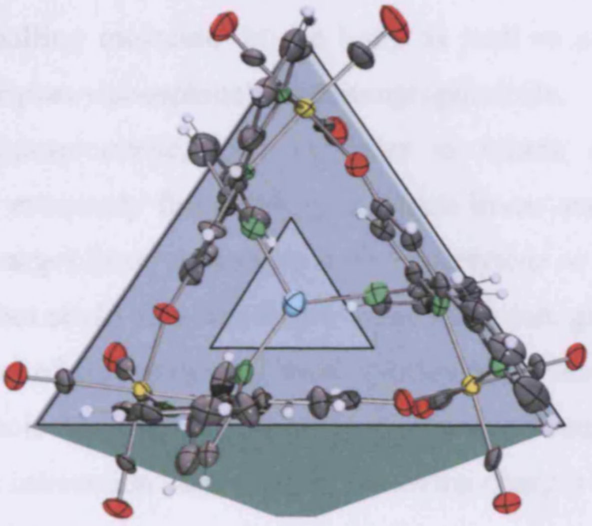

Figure 3.28. Complex **3.10** modified with a cartoon to help visualise the cavity in the tetrametallic basket.

3.8.2 Expansion attempts.

The silver atom potentially acts as a template, preorganising the monomeric units in a favourable arrangement for formation of the complex. Therefore, several attempts were made to synthesise new polynuclear rhenium complexes using other metals besides silver. Selection of the possible template metals was made based on their preferred coordination geometries, *i.e.* only metals that could lead to an approximately planar geometry at the base of the cup, possible if the metal allows a trigonal planar or distorted tetrahedral coordination were chosen. Unfortunately, even though a range of metals (CuI, ZnCl$_2$, NaBH$_4$) was used, none of the solids isolated from those reactions was the desired product. Their poor solubility and complicated ^{1}H-NMR spectra, suggest a mixture of products, possibly polymers, which were impossible to characterize by standard methods.

3.8.3 Inclusions.

As the crystallographic data had demonstrated, complex **3.10** has a conical shape around 7.4 Å deep and 8 Å wide which may allow the inclusion of small linear molecules and more interestingly, given that **3.10** is luminescent, their sensing, if after the inclusion process there is a change in the photophysical properties of the whole unit. Therefore, this novel luminescent trirhenium complex could have important applications as a small molecules sensor, an important issue in safety and environmental chemistry, *e.g.* CN^-, F^- *etc*. Three different substrates were chosen for the inclusion experiment: nitric oxide, known as being a signalling molecule[f] in the body as well as a toxic air pollutant, 3-(cyclopentadienyl-bis(triphenylphosphine)rutheniumpropionitrile, L(1) and 3-(4-(dimethylamino)phenyl)propionitrile, L(2) in order to mimic acetylene, which is a colorless, odorless and extremely flammable gas. These linear acetonitrile analogues not only should mimic the target linear molecules such as acetylene or cyanide and fit into the cavity of the complex, but could also coordinate to the silver ion, giving enhanced binding. Moreover, the high level of conjugation of these species might lead to a bigger change in luminescence of the whole unit upon inclusion of the guest molecule. Such an effect could arise from an electronic interaction (accepting or removing charge) with the emission states of the tetrametallic species.

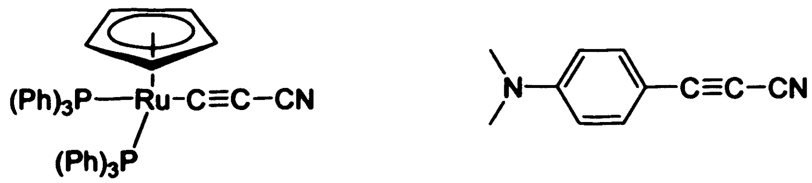

3-[(cyclopentadienylbis-
(triphenylphosphine)ruthenium]
propionitrile
L(1)

3-(4-(dimethylamino)phenyl)
propionitrile
L(2)

Figure 3.29. Chemical structure of **L(1)** and **L(2)**.

After combining the two reagents, luminescence measurements were carried out to assess any change in the photophysical properties of the trimer, which could indicate the inclusion of the guest molecule. The experiments were carried out in neat acetonitrile in the first instance, then increasing the amount of water present up to a ratio of 1: 7 (acetonitrile:

---

[f] Species that transmit information between cells and regulate a diverse range of physiological and cellular processes.

water) in order to enhance the inclusion of the guest in the cavity by hydrophobic forces. In the case of NO, the experiment was performed in a sealed cuvette due to the toxicity and air-sensitivity of the gas. **Table 3.7** and **Table 3.8** summarise the photophysical properties of the isolated and combined host and guests before and after the addition of water.

Complex	Ex. λ/nm	Em. λ/nm	Host-guest	Ex. λ/nm	Em. λ/nm
3.10$_a$	371	571			
3.10$_{(1:1)}$	372	571			
3.10$_{(1:3)}$	369	541			
3.10$_{(1:7)}$	370	541			
L(1)$_a$	346	366, 386$_{sh}$	**3.10+ L(1)**$_a$	371	573
				344	569
L(1)$_{(1:1)}$	345	391, 412$_{sh}$	**3.10+ L(1)**$_{(1:1)}$	371	564
L(1)$_{(1:3)}$	345	391, 414$_{sh}$	**3.10+ L(1)**$_{(1:3)}$	371	544
			3.10+ L(1)$_{(1:7)}$	371	544
L(2)$_a$	275	384, 454	**3.10+ L(2)**$_a$	279	553
	381	432, 453		356	432, 553$_{sh}$
				381	453, 557$_{sh}$
L(2)$_{(1:1)}$	381	430, 454	**3.10+ L(2)**$_{(1:1)}$	275	430$_{sh}$, 514
				396	455, 467$_{sh}$, 577$_{sh}$
			3.10+ L(2)$_{(1:3)}$	275	413
				396	491

a CH_3CN *as solvent.*
(X:X): $(CH_3CN:H_2O)$
sh: shoulder

Table 3.7. Emission and excitation maxima of complex **3.10** when **L(1)** or **L(2)** are used as guest.

Complex	IL	MLCT	Host-guest	IL	MLCT
3.10$_{a}$	260	354			
3.10$_{(1:1)}$ **3.10**$_{(1:3)}$ **3.10**$_{(1:7)}$	258	352			
L(1)$_{a}$	214, 291		**3.10+ L(1)**$_{a}$	214sh, 240, 287sh,	356
L(1)$_{(1:1)}$ **L(1)**$_{(1:3)}$	206, 229		**3.10+ L(1)**$_{(1:1)}$	212, 234sh, 250sh, 299sh	360
L(2)$_{a}$	210, 230, 317, 359		**3.10+ L(2)**$_{a}$	237, 314, 359	
L(2)$_{(1:1)}$	204, 230, 332, 359				

a CH_3CN *as solvent.*

(X:X):(CH_3CN:H_2O)

sh: shoulder

Table 3.8. Absorption bands of complex **3.10** when **L(1)** or **L(2)** is used as guests.

The excitation spectra of the trirhenium complex **3.10** showed a broad excitation band ranging from 280 to 395 nm with its excitation and emission maxima at 371 nm and 570 nm respectively. Addition of the ruthenium complex does not lead to any significant change in the luminescent properties, and even the addition of water did not modify the luminescence as the observed blue shift of the emission to 544 nm is the same as observed for the complex **3.10** alone in water. On the other hand, the emission maximum from the ruthenium complex at 366 nm seems to disappear after mixing with complex **3.10.** While this loss of emission from the guest could indicate inclusion, this was not taken as conclusive proof, and in any case the useful luminescence of the proposed sensor (complex **3.10**) could not be used to sense any such inclusion.

In the case of applying an organic compound (**L2**) as the guest, the maximum Re(I) ^{3}MLCT emission is shifted from 571 to 553 nm *i.e.* 18 nm blue-shift, immediately upon addition of the guest to an acetonitrile solution of complex **3.10**. Addition of water to the mixture does not displace the maximum peak to 544 nm as in the previous experiments, indicating that, in this case, the complex has undergone a modification that affects its energetic levels. Moreover it is worth noticing that upon excitation at 279 nm, where both species absorb, the emission observed came only from complex **3.10**, at 553 nm, which means that there had been a loss of emission from the guest, presumably due to an energy transfer from the organic ligand to the complex and therefore demonstrating a connection between both species.

Complex	**Excitation λ/nm**	**Emission λ/nm**	**Lifetimes τ/ns**
3.10$_a$	371	571	21
3.10+NO	352, 365, 379, 396	542	10
3.10+NO (degassed)	352, 365, 379, 395	530	
3.10+NO (areated)	353, 365, 379, 392	529	

Table 3.9. Emission and excitation maxima of complex **3.10** when NO is used as guest.

The luminescent properties of the complex **3.10** are altered to a greater degree after the addition of NO to an acetonitrile solution. A blue shift of the emission maximum (from 571 nm to 542 nm) as well as a more structured excitation spectrum[8] is observed upon bubbling NO through an acetonitrile solution of the complex. Further degassing of the mixture, in order to get rid of the excess NO remaining in solution and allowing only the NO strongly encapsulated in the trimer cavity to remain, led to an even further blue shift in the emission maximum, 542 nm to 530 nm. On the other hand, a structured excitation spectrum was observed upon NO addition, whose intensity increased after degassing of the sample. These preliminary results could be interpreted as an indication of NO inclusion, which would provide a useful method of NO sensing. In an attempt to test the reversibility of the sensing process, *i.e.* if the removal of the guest molecule would lead to the recovering the initial luminescent properties of the complex, the sample was aerated. Unfortunately, neither a red shift in the emission maximum, nor a less structured excitation spectrum was observed, only a loss in emission intensity, therefore suggesting the process is irreversible, see **Figure 3.30.**

---

[8] A structured excitation spectrum indicates population of higher vibrational levels of the electronically excited state of the molecule and such transitions are vibronic.

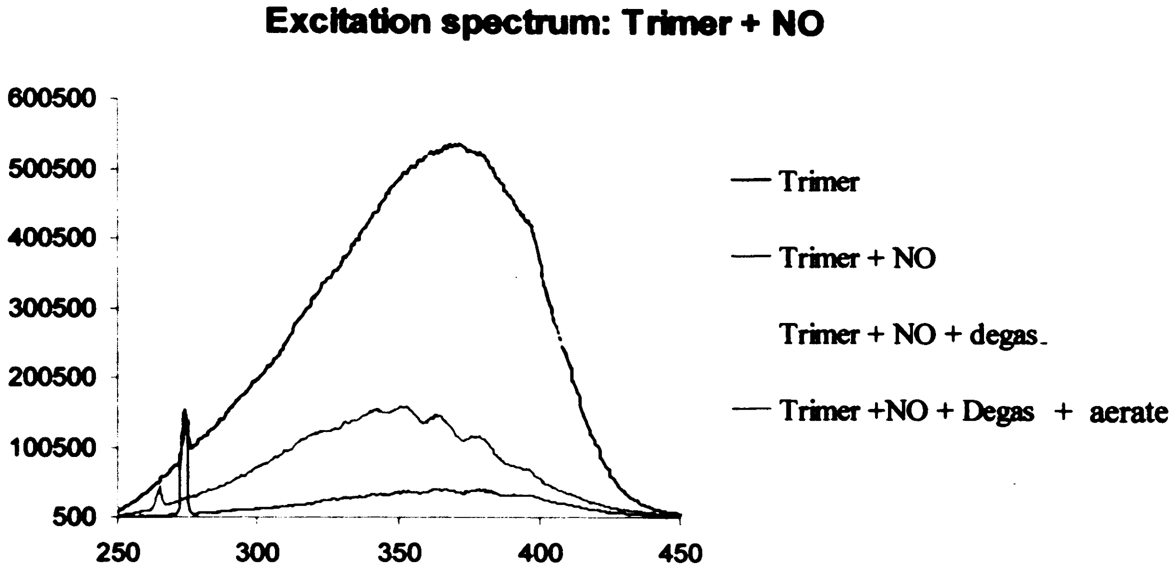

Figure 3.30. Excitation spectrum of complex **3.10** ("trimer") when NO is used as guest.

An additional study of the lifetime of complex **3.10** in the presence and absence of NO was carried out in order to further investigate the sensing process. However, due to the similarity of the values obtained, 21 ns for the complex alone and less than 10 ns in the case of the inclusion experiment, no conclusion could be drawn from this experiment.

3.9 Conclusions.

Investigations into the modulation of the *self-destruction* rate of cyclisation, the luminescent properties and solubility of complexes of the type $[Re(bisim)(CO)_3L]^{n+}$, where L is a pyridine derivative (n = 1) or a chloride (n = 0), were discussed in this chapter.

i. Modulation of the *self-destruction* cyclisation rate led to the successful synthesis of a quinoline derivative which, unfortunately, did not coordinate to Re(I) and to a new range of terpyridine derivatives and their corresponding *fac*-tricarbonylrhenium chloro-complexes. Unfortunately, the ease of hydrolysis upon coordination to the transition metal prevented these novel complexes from being used as biological fluorescent probes. Moreover, the fluxional behaviour of the terpyridine derivative in these complexes prevents successful inclusion of axial pyridine derivatives. But when a silver salt is used to abstract the chloride placed in the axial position, an unpredicted tetrametallic molecular basket is synthesised instead.

Attempts to increase the size of the cavity in the tetrametallic species by changing the central metal (Ag) were unsuccessful since a mixture of highly insoluble solids was obtained which were impossible to separate and characterize by standard methods. On the other hand, this tetrametallic species might be useful as a luminescent sensor for linear molecules, but the inclusion of molecules such as NO, 3-(cyclopentadienyl-bis(triphenylphoposphine)rutheniumpropionitrile, and 3-(4-(dimethylamino)phenyl)propionitrile promoted no reversible changes in its luminescent properties.

ii. Modulation of solubility was achieved by using bathophenanthroline sulphonate as a diimine ligand. Therefore, the synthesis of a range of novel water soluble rhenium complex of the type $[Re(bisim)(CO)_3L]^+$, where L are pyridine derivatives with different lipophilicities, was accomplished.

These results indicate the viability of tuning the solubility of this kind of rhenium complex. However, it highlights the difficulty in increasing the cyclisation rate by conjugating the *self-destruction* device directly to an aromatic system, as this increases secondary processes such as ester hydrolysis, making the whole system unusable in biological media.

A possible solution might be to consider the insertion of a quencher in the chain of the self destruction device, which would not only accelerate the *self-destruction* mechanism by the

Thorpe-Ingold effect but would also function as an switch on/off switch, making the recognition process easier, **Scheme 3.27**.

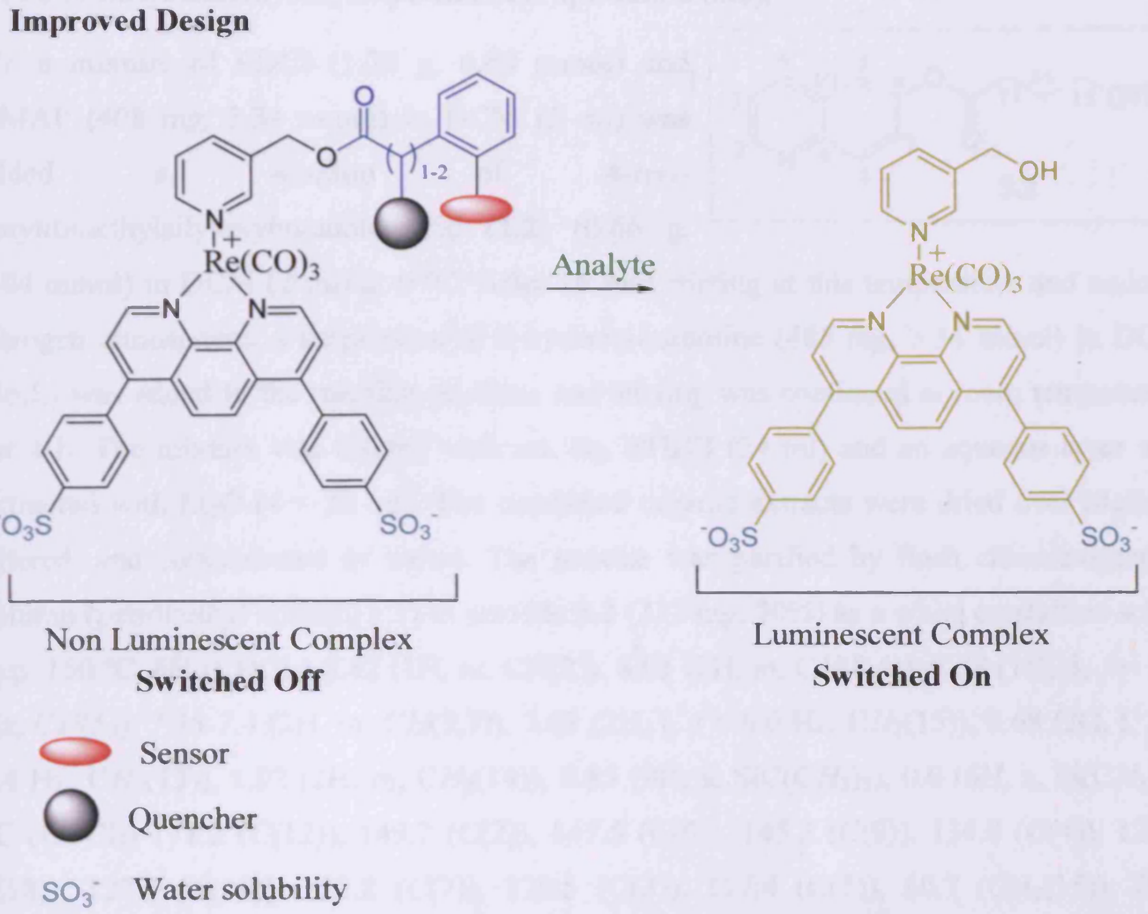

Scheme 3.27. An improved target designed following the results obtained in this chapter.

3.10 Experimental.

6-(4-*tert*-butyldimethylsilyloxybutanoate)quinoline (3.2).

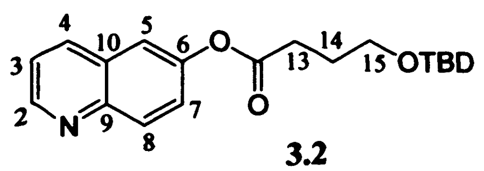

3.2

To a mixture of EDCI (1.28 g, 6.68 mmol) and DMAP (408 mg, 3.34 mmol) in DCM (6 ml) was added a solution of 4-*tert*-butyldimethylsilyloxybutanoic acid (**2.2**) (0.66 g, 3.04 mmol) in DCM (2 ml) at 0 °C. After 15 min stirring at this temperature and under a nitrogen atmosphere, a suspension of 6-hydroxyquinoline (485 mg, 3.34 mmol) in DCM (4mL) was added to the reaction mixture, and stirring was continued at room temperature for 4 h. The mixture was diluted with sat. aq. NH_4Cl (24 ml) and an aqueous layer was extracted with Et_2O (4 × 20 ml). The combined organic extracts were dried over $MgSO_4$, filtered, and concentrated *in vacuo*. The residue was purified by flash chromatography column (petrol:ethyl acetate, 1:1) to provide **3.2** (232 mg, 20%) as a white crystalline solid, m.p. 150 °C. δH ($CDCl_3$) 8.82 (1H, m, C*H*(2)), 8.01 (2H, m, C*H*(8,4)), 7.58 (1H, d, *J* = 2.5 Hz, C*H*(5)), 7.35-7.4 (2H, m, C*H*(3,7)), 3.68 (2H, t, *J* = 6.0 Hz, C*H*$_2$(15)), 2.68 (2H, t, *J* = 7.4 Hz, C*H*$_2$(13)), 1.92 (2H, m, C*H*$_2$(14)), 0.85 (9H, s, SiC(C*H*$_3$)$_3$), 0.0 (6H, s, Si(C*H*$_3$)$_2$); δC ($CDCl_3$) 171.2 (*C*(12)), 149.2 (*C*(2)), 147.5 (*C*(6)), 145.2 (*C*(9)), 134.8 (*C*(4)), 129.9 (*C*(8)), 127.5 (*C*(10)), 123.8 (*C*(7)), 120.5 (*C*(3)), 117.4 (*C*(5)), 60.7 (*C*H$_2$(15)), 29.8 (*C*H$_2$(13)), 26.8 (*C*H$_2$(14)), 24.9 (SiC(*C*H$_3$)$_3$), 17.3 (Si*C*). ν_{max} ($CDCl_3$) 1772 (CO); APCI 346.2 $[MH]^+$.

1,5-bis(2'-pyridyl)pentane-1,3,5-trione (int.1). [10]

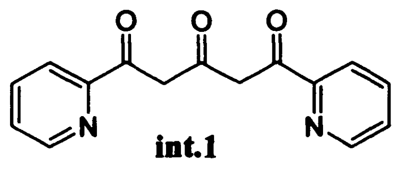

int.1

A solution of acetone (0.36 ml, 5.30 mmol) and ethyl 2-pyridine carboxylate (2.02 ml, 13.2 mol) in dry 1, 2 dimethoxymethane (10 ml) was added very slowly and via syringe to a suspension of sodium hydride (0.83 g, 34.6 mol) in dry DME (10 ml) maintained under a nitrogen atmosphere. It was stirred for 30 minutes while the colour of the suspension changes from grey to orange. Then it was heated to reflux for 6 hours. The solvent was removed *in vacuo* using an external trap. The orange paste was carefully treated with 20 ml of cold water. The orange solution was filtered through Celite and the filtrate was adjusted to pH 7 using diluted hydrochloric acid. The yellow solid so obtained was collected by filtration and washed with water. Then it was dissolved in diethyl ether and dried over magnesium sulphate as this solid retains water tenaciously, (1.1 g, 52 % yield). Characterization already reported by Constable *et al.*[10]

2,6-Bis(2’-pyridyl)4-pyridone (int.2).[10]

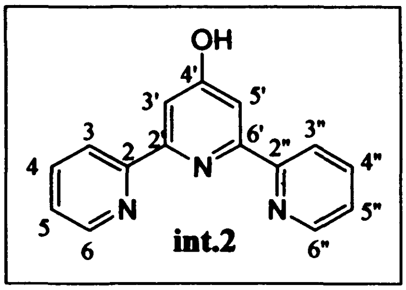

int.2

A solution of 1,5-bis(2’-pyridyl)pentane-1,3,5-trione (0.85 g, 3.13 mmol) and ammonium acetate (1.70 g, excess) in ethanol (25 ml) was heated to reflux for 6 hours. After this time the dark solution was concentrated to half volume. It was cooled and the yellow precipitate formed was washed with diethyl ether to afford a white solid which was recrystallised as white needles from ethanol. Occasionally other products may contaminate the crystals, and in these cases further purification by Kugelrohr is required (0.403 g, 46 % yield). δH ($CDCl_3$) 12.0 (1H, bs, O*H*), 8.75 (2H, d, *J* = 4.3 Hz, C*H*(6, 6’’)), 7.9-7.8 (4H, m, C*H*(3, 4, 3’’, 4’’)), 7.4 (2H, m, C*H*(5, 5’’)), 7.12 (d, 2H, *J* = 1.7 Hz, C*H*(3’, 5’)). Characterization already reported by Constable *et al.*[10]

N.B. In complexes **3.3** – **3.9** the slight broadening of the signal for C*H*(6,6’’) leads to an apparent doublet, while the multiplicity of C*H*(4.4’’) indicates a ^4J coupling of *ca.* 1.6 Hz should be observed.

4-(4-*tert*-butyldimethylsilyloxybutanoate)-2,6-bis(2’-pyridyl)-pyridine (3.3).

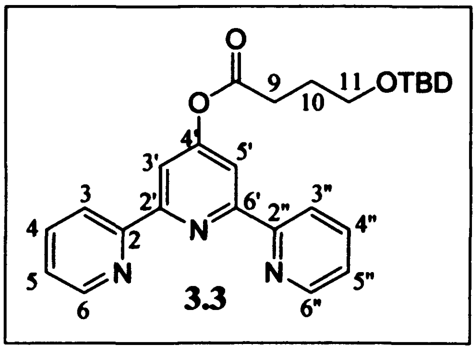

3.3

To a mixture of EDCI (0.13 g, 0.66 mmol) and DMAP (0.04 g, 0.31 mmol) in DCM (5 ml) was added a solution of 4-tert-butyldimethylsilyloxybutanoic acid (**2.2**) (0.16 g, 0.31 mmol) in DCM (3 ml) at 0 °C. After 15 min stirring at this temperature and a under nitrogen atmosphere, a solution of 2,6-bis(2’-pyridyl)-4-pyridone (75 mg, 0.31 mmol) in DCM (3 ml) was added to the reaction mixture, and stirring was continued at room temperature for 1 h. The mixture was diluted with sat. aq. NH_4Cl (10 ml) and an aqueous layer was extracted with Et_2O (4 × 15 ml). The combined organic extracts were dried over $MgSO_4$, filtered, and concentrated *in vacuo*. The residue was purified by flash chromatography column (ethanol: ethyl acetate, 1:3) obtaining **3.3** as a white solid, 26 mg, 20 % yield, m.p. 104 °C; δH ($CDCl_3$) 8.60 (2H, d, J = 4.1 Hz, C*H*(6, 6")), 8.54 (2H, d, J = 7.8 Hz, C*H*(3, 3")), 8.18 (2H, s, C*H*(3', 5')), 7.79 (2H, t, J = 7.8, C*H*(4, 4")), 7.26 (2H, m, C*H*(5, 5")), 3.62 (2H, t, J = 5.9 Hz, CH_2(11)), 2.65 (2H, t, J = 7.4 Hz, CH_2 (9)), 1.92 (2H, m, CH_2(10)), 0.82 (9H, s, $SiC(CH_3)_3$), 0.00 (6H, s, $Si(CH_3)_2$); δC ($CDCl_3$), 170.0 (*C*O), 158.8 (*C*(4')), 156.6 (*C*(2', 6')), 154.5 (*C*(2, 2")), 148.1 (*C*(6, 6")), 135.9 (*C*(4, 4")), 123.0 (*C*(3, 3")), 120.3 (*C*(5, 5")), 113.4 (*C*(3', 5')), 60.8 (*C*(11)), 29.9 (CH_2(9)), 26.9 (CH_2(10)), 25.0 ($SiC(CH_3)_3$), 17.3 (Si*C*), -6.3 ($Si(CH_3)_2$); ν_{max} ($CHCl_3$): 1766 (CO); APCI 450.2 $[MH]^+$.

4-(2-nitrobenzoate-2,6-bis(2'-pyridyl)-pyridine (3.4).

2-nitrobenzoic acid (67 mg, 0.40 mmol) was added to a mixture of EDCI (168 mg, 0.8 mmol) and DMAP (54 mg, 0.40 mmol) in dry DCM (5 ml) at 0 °C. After 15 min stirring under a nitrogen atmosphere, a solution of 2,6-bis(2'-pyridyl)-4-pyridone (100 mg, 0.40 mmol) in dry DCM (3 ml) was added to a reaction mixture, and stirring was continued at room temperature for 12 h. The mixture was diluted with sat. aq. NH_4Cl (10 ml) and an aqueous layer was extracted with Et_2O (4 × 20 ml). The organic layer was dried over $MgSO_4$, and concentrated *in vacuo*. The residue was purified by washing with ethanol affording the product as a white solid (75 mg, 47 %), m.p. 160 °C. δH, ($CDCl_3$) 8.65 (2H, d, J = 4.7 Hz, C*H*(6, 6")), 8.57 (2H, d, J = 7.8 Hz, C*H*(3, 3")), 8.32 (2H, s, CH(3', 5')), 8.02 (1H, d, J = 7.9 Hz, C*H*(11)), 7.87 (2H, d, J = 7.4 Hz C*H*(14)), 7.81 (2H, td, J = 7.8, 1.7 Hz, C*H*(4, 4"), 7.75-7.65 (2H, m, C*H*(12,13)), 7.35-7.26 (2H, m, C*H*(5, 5")). δC ($CDCl_3$) 162.0 (*C*O), 158.4 (*C*(4')), 156.6 (*C*(2', 6')), 153.8 (*C*(2, 2")), 147.9 (*C*(6, 6")), 147.0 (*C*(10)), 136.2, 133.4, 131.4, 129.2, 125.9, 123.3 (*C*(3, 3"), *C*(9)), 120.6 (*C*(5, 5")), 113.2 (*C*(3', 5')). ν_{max} ($CHCl_3$): 1761 (CO); APCI 399.1 $[MH]^+$.

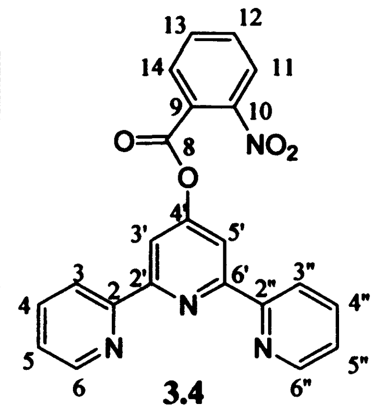

3.4

4-(2-Nitrophenylethanoate-2,6-bis(2’-pyridyl)-pyridine (3.5).

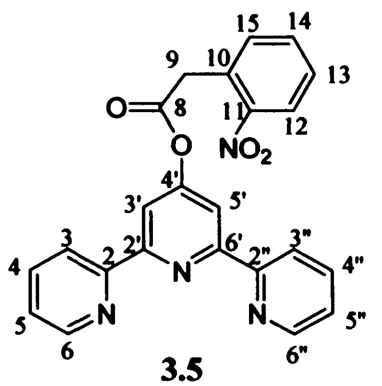

3.5

2-Nitrophenylethanoic acid (76 mg, 0.4 mmol) was added to a mixture of EDCI (168 mg, 0.8 mmol) and DMAP (54 g, 0.4 mmol) in DCM (5 ml) at 0 °C affording a reddish solution. After 15 min stirring at this temperature and under a nitrogen atmosphere, a solution of 2,6-bis(2’-pyridyl)-4-pyridone (100 mg, 0.4 mmol) in DCM (3 ml) was added to a reaction mixture, and stirring was continued at room temperature for 3 h. The mixture was diluted with sat. NH$_4$Cl (15 ml) and an aqueous layer was extracted with Et$_2$O (4 × 20 ml). The combined organic extracts were dried over MgSO$_4$ and concentrated *in vacuo*. The light brown solid was purified by washing with methanol affording the product as a white solid (60 mg, 36 %), m.p. 119 °C. δH (CDCl$_3$) 8.63 (2H, d, *J* = 4.5 Hz, C*H*(6, 6”)), 8.53 (2H, d, *J* = 7.8 Hz, C*H*(3, 3”)), 8.19 (2H, s, CH(3’, 5’)), 8.14 (1H, d, *J* = 8.1 Hz, C*H*(11)), 7.78 (2H, td, *J* = 7.8, 1.7 Hz, C*H*(4, 4”)) 7.60 (1H, m, C*H*(14)), 7.51-7.41 (2H, m, C*H*(13, 15)) 7.30 (2H, m, C*H*(5, 5”)), 4.25 (2H, s, C*H*(9)); δC (CDCl$_3$) 166.4 (*C*O), 159.8 (*C*(4’)), 156.5 (*C*(2’, 6’)), 154.1 (*C*(2, 2”)), 148.0 (*C*(6, 6”)), 147.6 (*C*(11)), 136.0 (*C*(4, 4”)), 132.9, 132.5, 128.1, 127.9, 124.4(*C*(12)), 123.1 (*C*(3, 3”)), 120.4 (*C*(5, 5”)), 113.3 (*C*(3’, 5’)). ν_{max} (CHCl$_3$): 1771 (CO); APCI 413.1 [MH]$^+$.

fac-[Re(2,6-Bis(2’-pyridyl)-4-pyridine)(CO)$_3$Cl] (3.6).

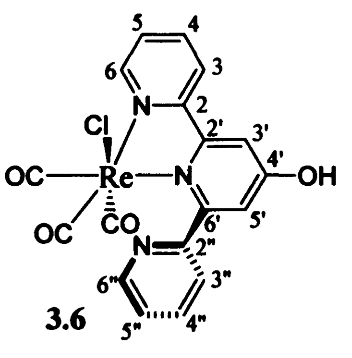

3.6

Re(CO)$_5$Cl (50 mg, 0.14 mmol) and 2,6-bis(2’-pyridyl)-4-pyridone (26 mg, 0.14 mmol) were heated at reflux in dry toluene (2.5 ml) for 1 hour. The yellow product precipitated from solution and was collected by filtration and washed with toluene (70 mg, 89 % yield), m.p. 160°C (decomposition). δ(H) (CD$_3$CN) 8.98 (1H, d, *J* = 5.5 Hz, C*H*(6)), 8.69 (1H, d, *J* = 4.6 Hz, C*H*(6”)), 8.30 (1H, d, *J* = 7.8 Hz, C*H*(3)), 8.11 (1H, td, *J* =, 7.8, 1.2 Hz, C*H*(4)), 7.85 (1H, td, *J* = 7.8, 1.6 Hz, C*H*(4”)), 7.82 (1H, d, *J* = 2.4 Hz, C*H*(3’)), 7.68 (1H, d, *J* = 7.8 Hz, C*H*(3”)), 7.52 (1H, m, C*H*(5)), 7.46 (1H, m, C(5”)), 7.12 (1H, d, *J* = 2.4 Hz, C*H*(5’)); δC, (CD$_3$CN) 166.2, 162.9, 158.3, 157.9, 156.4, 152.4, 149.0, 139.4, 136.4, 126.7, 124.8, 124.4, 124.0, 114.5, 111.1, ν_{max} (CH$_3$CN): 2020, 1915, 1892 (CO), ν_{max} (Nujol): 2019, 1888 (CO); *m/z* (ESI) 560.9. $[M\text{-}Cl\text{+}CH_3CN]^+$, 556.0 $[MH]^+$, 520.0 $[M\text{-}Cl]^+$, 492.0 $[M\text{-}Cl\text{-}CO]^+$, 464.0 $[M\text{-}Cl\text{-}2CO]^+$, 436.0 $[M\text{-}Cl\text{-}3CO]^+$. Theoretical isotope pattern $[M\text{-}Cl\text{+}CH_3CN]^+$ 559.1 (58%), 560.1 (12%), 561.1 (100%), 562.1 (21%), 563.1 (3%), [M-Cl] 518.0 (58%), 519.0 (11%), 520.0 (100%), 521.0 (20%), 522.0 (2%). Actual isotope pattern $[M\text{-}Cl\text{+}CH_3CN]^+$ 559.0 (57%), 560.0 (11%), 560.9 (98%), 561.9 (20%), 563.1 (5%), [M-Cl] 518.0 (60%), 519.0 (10%), 520.0 (100%), 520.9 (20%), 522.0 (3%). HRMS (ESI) calculated $[M\text{-}Cl\text{+}CH_3CN]^+$ = 559.0539, measured $[M\text{-}Cl\text{+}CH_3CN]^+$ = 559.0545. X-ray: $C_{26}H_{16}ClN_4O_7Re$, M = 718.08, yellow block, 0.2 × 0.2 × 0.2 mm^3, space group P-1, a = 6.5227(2) Å, b = 10.4890(3) Å, c = 13.3433(4) Å, α = 100.6910(10)°, β = 92.6110(10)°, γ = 100.2530(10)°, V = 879.81(5) $Å^3$, Z = 1, D_c = 1.3551 mg cm^{-3}, *F(000)* = 348, Reflections collected = 13815, 4013 Reflections unique, R(int) = 0.1758; Goodness-of-fit on F2 = 0.989, Final R indices [I>2sigma(I)]: *R1* = 0.0566, *wR2* = 0.1439.

***fac*-[Re(4-(4-*tert*-butyldimethylsilyloxybutanoate)-2,6-bis(2'-pyridyl)pyridine)(CO)$_3$Cl] (3.7).**

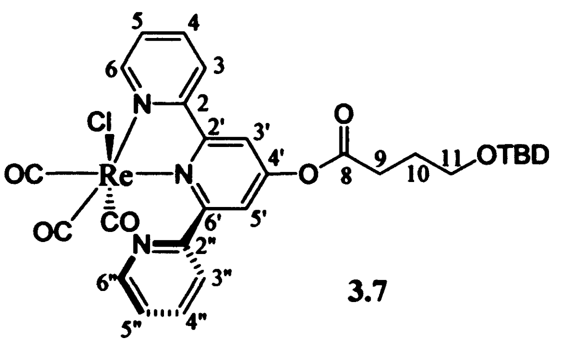

3.7

$Re(CO)_5Cl$ (21 mg, 0.06 mmol) and **3.3** (26 mg, 0.06 mmol) were heated at reflux in dry toluene (1 ml) for 4 hours. The yellow solution was cooled in an ice bath and a yellow precipitate formed which was collected by filtration, then purified by recrystallisation from hot toluene to give the title compound as a yellow solid (35 mg, 80 % yield), m.p. 170 °C. δ(H) ($CDCl_3$) 9.05 (1H, bd, J = 4.4 Hz C*H*(6)), 8.76 (1H, bs, C*H*(6")), 8.13-7.88 (5H, m, C*H*(3, 4, 3', 3", 4")), 7.58 (1H, bs, C*H*(5')), 7.40 (2H, m, C*H*(5, 5")), 3.68 (2H, t, J = 5.8 Hz, C*H*$_2$(11)), 2.69 (2H, t, J = 7.2 Hz C*H*$_2$(9)), 1.91 (2H, m, C*H*$_2$(10)), 0.85 (s, 9H, SiC(C*H*$_3$)$_3$), 0.00 (6H, s, Si(C*H*$_3$)$_2$); δ(C) ($CDCl_3$) 195.6 (*C*O), 192.6 (*C*O), 189.0 (*C*O), 169.2, 162.7, 158.5, 157.7, 156.0, 155.3, 152.2, 148.4, 137.9, 136.3, 125.9, 124.6, 124.1, 122.9, 119.1, 114.5, 60.5 (*C*(11)), 30.1 (*C*H$_2$(9)), 26.4 (*C*H$_2$(10)), 24.9 (SiC(*C*H$_3$)$_3$), 17.3 (Si*C*), -6.0 (Si(*C*H$_3$)$_2$); ν_{max} ($CHCl_3$): 2019, 1910, 1895, 1777, (CO); *m/z* (ESI) 720.1 $[M\text{-}Cl]^+$, 520.0 $[M\text{-}Cl\text{-}CO(CH_2)_3OTBD]^+$, 592.0 $[M\text{-}Cl\text{-}CO(CH_2)_3OTBD\text{-}CO]^+$. Theoretical isotope pattern $[M\text{-}Cl]^+$ 718.2 (55%), 719.2 (22%), 720.2 (100%), 721.2 (38%), 722.2 (12%). Actual isotope pattern [M-Cl]

718.1 (54%), 719.1 (21%), 720.1 (100%), 721.1 (32%), 722.1 (10%). HRMS (ESI) calculated $[M\text{-}Cl]^+$ = 720.1534, measured $[M\text{-}Cl]^+$ = 720.1541.

***fac*-[Re(4-(2-nitrobenzoate)-2,6-bis(2’-pyridyl)pyridine)(CO)$_3$Cl] (3.8).**

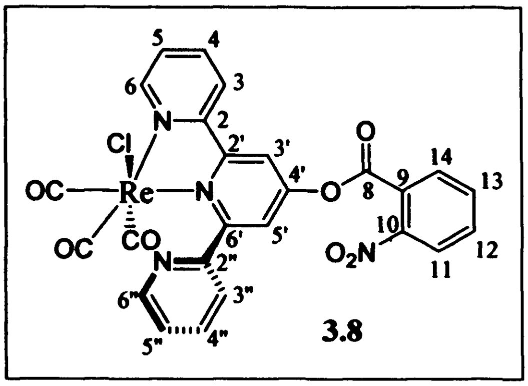

3.8

$ReCO_5Cl$ (58mg, 0.16mmol) and one equivalent of **3.4** (64 mg, 0.16 mmol) were dissolved in toluene (4 ml) and heated to 100 °C for 2 hours. The yellow solid precipitated from the solution was separated by filtration and washed with toluene, (68 mg, 60 % yield), m.p. 160 decompose. δ(H) ($CDCl_3$) 9.05 (1H, d, *J* = 5.0 Hz, C*H*(6)), 8.77 (1 H, d, *J* = 4.5 Hz, C*H*(6”)), 8.21-8.10 (4H, m, C*H*(3, 3”, 11, 14)), 7.94-7.72 (5H, m, C*H*(3,’4, 4”12, 13)), 7.67 (1H, d, *J* = 2.03 Hz, C*H*(5’)), 7.49 (2 H, m, C*H*(5, 5”)), δ(C) ($CDCl_3$) 164.8(*C*O), 162.7(*C*(4)), 159.5, 159.4, 157.4, 156.5, 153.5 (2C), 150.1, 139.4, 137.5, 134.5, 133.4, 130.6, 127.5, 126.3, 125.8, 125.6, 124.9, 124.7, 120.58, 116.17 ν_{max} (Nujol): 2024, 1928, 1917 (CO); *m/z* (ESI) 710.1 $[MH]^+$, 562.1 $[M\text{-}COC_6H_4(NO_2)]^+$, 520.1 $[M\text{-}CH_3CN\text{-}COC_6H_4(NO_2)]^+$, 491.1 $[M\text{-}CH_3CN\text{-}COC_6H_4(NO_2)\text{-}CO]^+$. Theoretical isotope pattern $[M\text{-}BF_4]^+$ 708.1 (60%), 709.1 (20%), 710.1 (100%), 711.1 (32%), 712.1 (7%). Actual isotope pattern $[M\text{-}BF_4]^+$ 708.1 (60%), 709.1 (19%), 710.1 (100%), 711.1 (33%), 712.1 (5%). HRMS (ESI) calculated $[MH]^+$ = 708.0652, measured $[MH]^+$ = 708.0656.

***fac*-[Re(4-(2-Nitrophenylethanoate)-2,6-bis(2’-pyridyl)pyridine)CO)$_3$Cl] (3.9).**

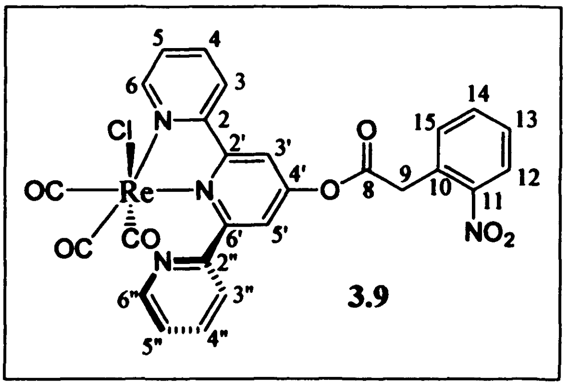

3.9

A solution of $Re(CO)_5Cl$ (44 mg, 0.12 mmol) and **3.5** (50 mg, 0.12 mmol) in 3 ml of dry toluene was heated at 70 °C for 2 hours. The yellow solid precipitate was collected by filtration, washed with toluene and dried under vacuum (50 mg, 57% yield). δ(H) (CD_3CN) 9.04 (1H, d, *J* = 5.4 Hz, C*H*(6)), 8.76 (1H, d, *J* = 4.4 Hz, C*H*(6”)), 8.41 (1H, d, *J* = 8.1 Hz, C*H*(3)), 8.29 (1H, d, *J* = 2.3 Hz, C*H*(3’)), 8.19 (2H, m, C*H*(12, 3”)), 7.95 (1H, m, C*H*(14)), 7.80-7.55 (7H, m, C*H*(4, 5, 5’, 4”, 5”, 12, 13)), 4.37 (1H, s, C*H*(10)). δ(C) (CD_3CN) 177.7(*C*O), 167.5(*C*(4)), 159.5, 152.6, 152.4, 149.3, 139.6, 136.5, 136.3, 136.1, 134.6, 133.7, 129.1, 128.3, 127.9, 127.1, 125.0, 124.8, 120.0, 119.4, 116.3, 111.13, 39.1(CH_2). ν_{max} (Nujol): 2021, 1911, 1886, 1766 (CO); *m/z* (ESI) 719.1[MH]$^+$, 683.1 [M-Cl]$^+$, 520.1 [M-Cl-$COCH_2C_6H_4(NO_2)$]$^+$, 492.1 [M-Cl-$COCH_2C_6H_4(NO_2$-CO]$^+$, 436.2 [M-Cl-$COCH_2C_6H_4(NO_2$-3CO]$^+$. Theoretical isotope pattern [M+H]$^+$ 717.0 (50%), 718.0 (17%), 719.0 (100%), 720.0 (34%), 721.0 (35%), 722.0 (10%). Actual isotope pattern [M+H]$^+$ 717.1 (29%), 718.1 (9%), 719.1 (68%), 720.1 (20%), 721.1 (21%), 722.1 (11%). HRMS (ESI) calculated [M+H]$^+$ = 717.0310, measured [M+H]$^+$ = 717.0316.

fac-[Re(2,6-Bis(2'-pyridyl)-4-oxypyridine)(CO)$_3$]$_3$AgCl, (3.10).

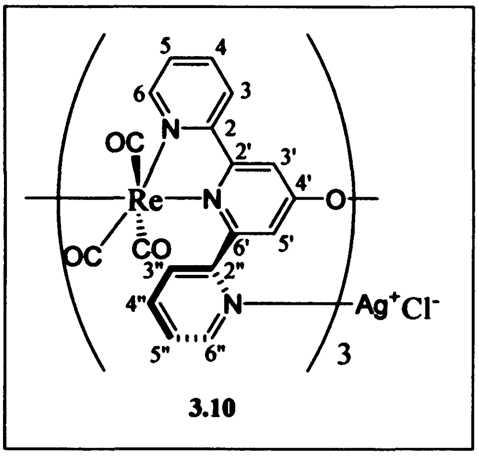

3.10

Silver tetrafluoroborate (63 mg, 0.3 mmol) was added to an acetonitrile (20 ml) solution of complex **3.6** (60 mg, 0.1 mmol) and triethylamine (14 µl, 0.1 mmol). After heating for two hours at 80 °C, the yellow solution was filtered through Celite. The solvent was then removed at high vacuum to give a yellow gel which was purified by washing with diethyl ether. Finally the product was obtained as yellow crystals by slow evaporation of an acetonitrile solution (110 mg, 65 % yield). δ(H) (CD_3CN) 8.89-8.83 (2H, m, C*H*(6, 6")), 8.03-7.71 (3H, m, C*H*(3, 4, 3")), 7.69-7.91 (2H, m, C*H*(4", 5")), 7.41 (1H, m, C*H*(5)), 6.70 (2H, d, *J* = 2.4 Hz C*H*(3')), 6.47 (1H, d, *J* = 2.4 Hz C*H*(5')). δ(C) (CD_3CN) 196.1 (CO_{eq}), 195.9 (CO_{ap}), 194.9 (*C*O), 176.6(*C*(4')O), 162.9, 157.7, 157.0, 156.5, 153.1, 152.2, 150.1, 149.5, 140.2, 139.8, 137.7, 126.9, 126.1, 125.8, 124.9, 124.6, 123.9, 123.4, 115.8, 112.2. ν_{max} (Nujol): 2016, 1888 (CO); *m/z* (ESI) 1664.8 [M-Cl+H]$^+$, 1145.5 [M-Cl-(Re(OterPy)$(CO)_3$)]$^+$, 597.8 [M-Cl-2(Re(OterPy)$(CO)_3$)-CO]$^+$. Theoretical isotope pattern [M-Cl+H]$^+$, 1659.0 (8%), 1660.0 (3%), 1661.0 (43%), 1662.0 (25%), 1663.0 (95%), 1664.0 (58%), 1665.0 (100%) 1666.0 (59%), 1667.0 (48%), 1668.0 (24%), 1669.0 (9%). Actual isotope pattern [M-Cl+H]$^+$, 1658.8 (7%), 1659.8 (5%), 1660.8 (42%), 1661.8 (26%), 1662.8 (90%), 1663.8 (55%), 1664.8 (100%), 1665.8 (57%) 1666.8 (50%), 1667.8 (23%), 1668.8 (17%), 1669.8 (3%). X-ray: $C_{54}H_{30}AgClN_9O_{12}Re_3$, *M* = 1698.79, yellow block, 0.2 × 0.2 × 0.2 mm^3, space group P2$_1$/c, *a* = 13.468(3) Å, *b* = 38.005(8)Å, *c* = 13.015(3) Å, *β* = 109.55(3)°, *V* = 6277.55 Å^3, *Z* = 4, *D*$_c$ = 1.797 mg cm^{-3}, *F(000)* = 3208, 40145 Reflections collected, 12833 Reflections unique, R(int) = 0.0977; Goodness-of-fit on F2 = 1.161, Final R indices [I>2sigma(I)]: *R1* = 0.0751, *wR2* = 0.1870.

[1,10-Bathophenanthroline sulphonate tetrabutylammonium salt] (3.13). [19]

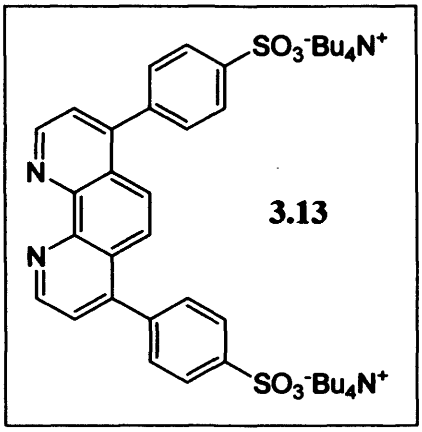

3.13

An aqueous solution (1 ml) of tetrabutylammonium hydrogen sulfate (0.14 g, 0.42 mmol) was added to a solution of bathophenanthroline disulfonic acid disodium salt hydrate (0.10 g, 0.18 mmol) in the same solvent (1 ml). The resulting pink solution was extracted with DCM (4 × 2 ml) and then dried with $MgSO_4$. The removal of the solvent at high vacuum afforded **3.13** as a pink solid (0.172 g, 95 % yield), m.p. 58 °C. *m/z* (ESI) 732 $[M+Bu_4N]^-$, 491 $[MH]^-$, 245 $[Bu_4N]^+$ Theoretical isotope pattern $[M+Bu_4N]^-$ 732.3 (100%), 733.3 (50%), 734.3 (30%), 735.5 (7%). Actual isotope $[M+Bu_4N]^-$ 732.3 (100%), 733.3 (49%), 734.3 (31%), 735.5 (8%).

fac-[Re(1,10-bathophenanthroline sulphonate)(CO)$_3$Cl](Bu$_4$N)$_2$ (3.14).

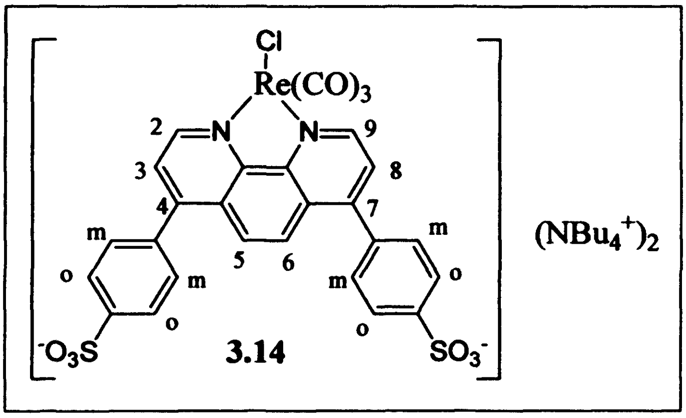

3.14

To a suspension of $Re(CO)_5Cl$ (31 mg, 0.085 mmol) in dry toluene (2 ml) was added **3.13** (88 mg, 0.085 mmol). The mixture was heated for 2 h under N_2 atmosphere to afford an orange gel. The solvent was decanted and the gel formed was washed several times with diethyl ether until it became a solid which was then dried under vacuum to give **3.14** as a yellow solid (92 mg, 84 % yield), m.p. 105 °C. δH (CD_3CN) 9.40 (2H, m, C*H*(2,9)), 8.02-7.85 (6H, m, 4C*H*(o), C*H*(5,6)), 7.62 (4H, m, 4C*H*(m)), 7.25 (2H, m, C*H*(3,8)), 3.09 (16H, m, 8 × NCH_2), 1.60 (16H, m, 8 × NCH_2CH_2) 1.35 (16H, m, 8 × CH_2CH_3), 0.98 (24H, m, 8 × CH_3). δC (CD_3CN) 197.5 (CO_{eq}), 190.0 (CO_{ap}), 152.4 , 150.1 (2C), 147.0, 146.0 (2C), 136.1, 135.1, 130.7, 130.6, 129.4 (2C), 128.7, 128.5, 128.4, 128.3, 127.8, 126.8 (2C), 126.7, 126.1 (2C), 125.2 (2C) 57.9, 22.9, 18.9, 12.5. ν_{max} (Nujol) 2018, 1910, 1883 (CO);. *m/z* (ESI) 1038.3 $[M-Bu_4N]^-$.Theoretical isotope pattern $[M-Bu_4N]^-$ 1036.2 (47%), 1037.2

(25%), 1038.2 (100%), 1039.2 (52%), 1040.2 (50%), 1041.2 (30%), 1042.2 (8%). Actual isotope [M-Bu_4N^+]$^-$ 1036.3 (50%), 1037.3 (37%), 1038.3 (100%), 1039.3 (49%), 1040.3 (50%), 1041.3 (20%), 1042.3 (10%).

***fac*-[Re(1,10-bathophenanthroline sulphonate)(CO)$_3$CF$_3$SO$_3$](Bu$_4$N) (3.15a).**

To a solution of **3.14** (100 mg, 0.07 mmol) in DCM (3 ml) was added 10.45 equivalents of trifluoromethylsulfonic acid (0.07 ml, 0.8 mmol) and the mixture was stirred for one hour under nitrogen atmosphere, then n-hexane was added using a pressure funnel until a yellow precipitate was formed. The solvent was removed *via* cannula and this operation was repeated twice in order to eliminate residual triflic acid. Finally, the solid was dried under vacuum to give **3.15a** as a yellow powder (0.123 mg, 99 %). δH (CD_3OD) 9.52 (2H, d, *J* = 5.4 Hz, C*H*(2,9)), 8.15 - 7.63 (12H, m, C*H*(3,5,6,8), 4 × C*H*(*o,m*)), 3.13 (16H, m, 8 × NC*H*$_2$), 1.56 (m, 16H, 8 × NCH$_2$C*H*$_2$) 1.32 (16H, m, 8 × C*H*$_2$CH$_3$), 0.95 (24H, m, 8 × C*H*$_3$). ν_{max} (Nujol) 2030, 1926, 1902 (CO).

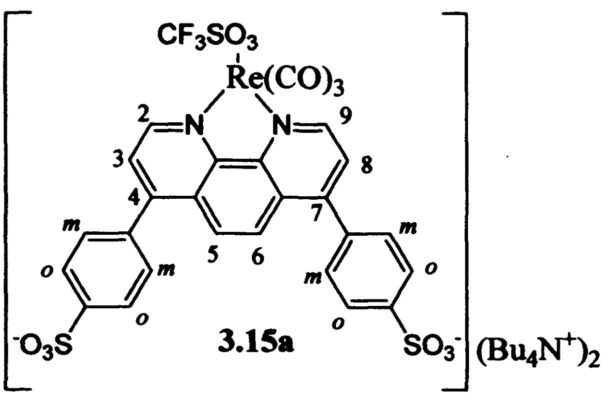

3.15a

***fac*-[Re(1,10-bathophenanthroline sulphonate)(CO)$_3$(CH$_3$CN)](NH$_4$) (3.15b).**

3.14 (0.90 g, 0.70 mmol) and AgCF$_3$SO$_3$ (0.20 g, 0.74 mmol) were heated to reflux in CH$_3$CN (30 ml) for 4 hours. After 12 hours of further stirring at room temperature the white solid formed during the reaction was removed by filtration through Celite. Then the solvent was removed at high vacuum, and the yellow slurry was dissolved in a small amount of methanol to precipitate the excess of AgCF$_3$SO$_3$ and/or AgCl formed during the reaction. The white solid was separated by filtration through Celite; this process was repeated twice. Finally a yellow solid was obtained after removing the solvent under a high vacuum, (0.70 g, 95 %), m.p. 163 °C. δH

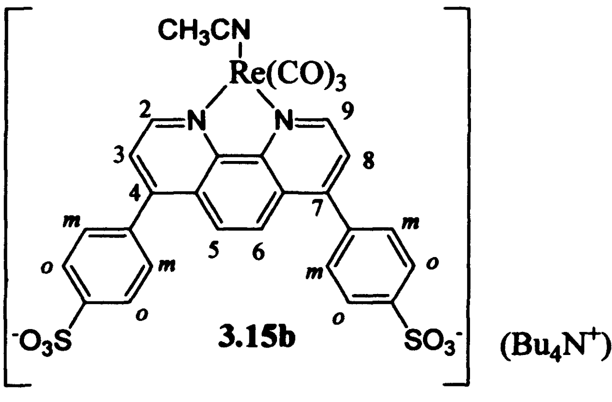

3.15b

(CD$_3$OD) 9.54-946 (2H, m, C*H*(2,9)), 8.6 (2H, s, C*H*(5,6)) 8.04-7.62 (10H, m, C*H*(3,8), 4 × C*H*(*o,m*)), 3.13 (16H, m, 8 × NC*H*$_2$), 2.07 (2H, s, C*H*$_3$)), 1.94 (1H, s, C*H*$_3$), 1.54 (m, 16H, 8 × NCH$_2$C*H*$_2$), 1.32 (16H, m, 8 × C*H*$_2$CH$_3$), 0.93 (24H, m, 8 × C*H*$_3$). ν_{max} (MeOH) 2039, 1944 (CO).

fac-[Re(1,10-bathophenanthroline sulphonate)(CO)$_3$Py](NH$_4$) (3.16).

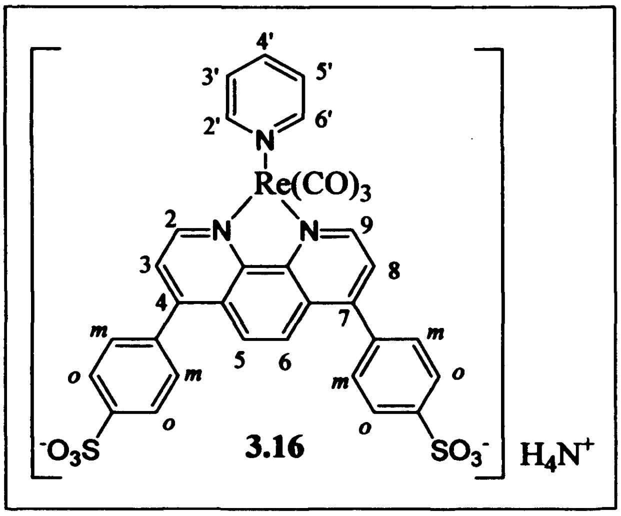

3.16

To a solution of **3.15a** (0.1g, 0.07 mmol) in CH$_3$CN (7 ml) was added diisopropylethylamine (0.7 ml, 0.4 mmol) and pyridine (0.06 ml, 0.7 mmol). After refluxing for five days under a nitrogen atmosphere the solvent was removed and the yellow solid was redissolved in the smallest possible volume of methanol. Dry diethyl ether was added until a precipitate formed then the supernatant liquid was removed *via* cannula and the remaining yellow solid was dried under high vacuum. The yellow solid was dissolved in the smallest possible volume of methanol and it was passed through an ion exchange column (Amberlite IR120 H resin as NH$_4^+$ form) which had been previously washed with aqueous ammonia eluting with methanol/water. The yellow coloured fraction which eluted immediately was collected and evaporated and dried under vacuum to give **3.16** as a yellow solid (26 mg, 43 %) m.p. > 150 °C. δH (CD$_3$OD) 9.72 (2H, m, CH(2,9)), 8.47 (2H, dd, J=3.62, 3.18, C*H*(2',6')) 8.09-7.92 (8H, m, 4 × C*H*(*o,m*)) 7.73 (1H, m, C*H*(4')), 7.69-7.55 (4H, m, C*H*(3, 5, 6, 8)) 7.25 (2H, m, C*H*(3',5')). δC (CD$_3$OD) 197.1 (*C*O$_{eq}$), 193.3 (*C*O$_{ap}$), 155.0, 153.7, 153.6 (2C), 148.9, 148.5 (2C), 147.1 (2C), 141.6 (2C), 138.8, 137.2, 133.1 (2C), 131.5 (2C), 130.9 (3C), 130.8 (2C), 129.1, 129.0, 128.7, 128.4, 128.2, 127.6 (2C). ν_{max} (Nujol) 3401, 2026, 1893 (CO); *m/z* (FAB) 840.1 [MH$_2$-NH$_4$]$^+$, 761.0 [MH$_2$-Py-NH$_4$]$^+$ Theoretical isotope pattern [M]$^-$ 838.0 (57%), 839.0 (30%), 840.0 (100%), 841.0 (48%), 842.0 (16%), 843.0 (5%). Actual isotope [M]$^-$ 838.1 (47%), 839.1 (37%), 840.1 (100%), 841.1 (40%), 842.1 (17%), 843.1 (5%). HRMS (ESI$^-$) calculated [M]$^-$ = 838.0098, measured [M]$^-$ = 838.0093.

fac-[Re(1,10-bathophenanthroline sulphonate)(CO)$_3$PyCH$_2$OH] [H$_4$N] (3.17).

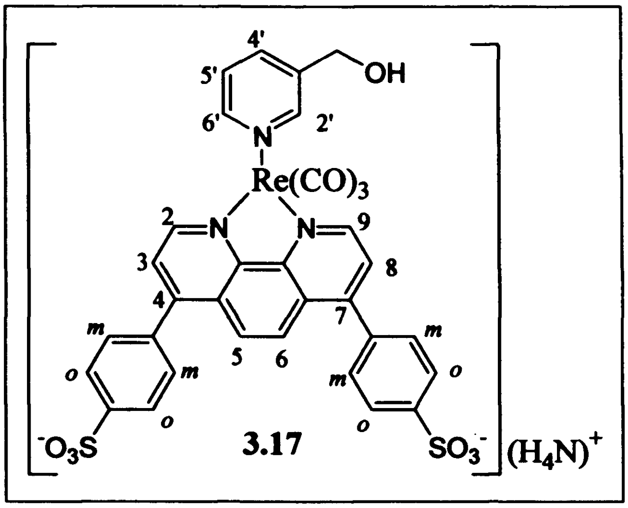

3.17

3-(Hydroxymethyl)pyridine (0.02 ml, 0.195 mmol) and **3.15a** (40 mg, 0.03 mmol) were heated at reflux in THF (5 ml) under a nitrogen atmosphere for a week followed by stirring for 2 more days. The solvent was removed under vacuum and the residue dissolved in the smallest volume possible of methanol to give a yellow solution. Dry diethyl ether was added until a precipitate formed then the supernatant liquid was removed *via* cannula and the remaining yellow solid was dried under high vacuum. The yellow solid was dissolved in the smallest possible volume of methanol and it was passed through an ion exchange column (Amberlite IR120 H resin as NH_4^+ form) which had been previously washed with aqueous ammonia eluting with methanol. The yellow coloured fraction which eluted immediately was collected and evaporated and dried under vacuum to give **3.17** as a yellow solid (20 mg, 46%), m.p. > 150 °C. δH (CD$_3$OD) 9.71 (2H, d, J = 4.83 Hz, C*H*(2,9)), 8.38 (1H, s, C*H*(2')), 8.32 (1H, d, J = 4.95 Hz, C*H*(6')), 8.05 (2H, d, J = 5.1 Hz, 2 × C*H*(o)) 7.95-8.01 (3H, m, C*H*(4'), C*H*(5,6)), 7.93 (2H, d, J = 6.7 Hz Hz, 2 × C*H*(o)) 7.55-7.7 (6H, m, C*H*(3,8) 4 × C*H*(m)), 7.18 (1H, m, C*H*(5')), 4.38 (2H, s, PyC*H*$_2$O). δC (CD$_3$OD) 195.6 (*C*O$_{eq}$), 191.4 (*C*O$_{ap}$), 154.4, 150.0 (2C), 150.7, 150.0, 147.4 (2C),, 146.8, 146.4 (2C), 141.2, 138.2 137.2, 135.7, 131.6, 130.0 (2C), 129.3 (3C), 129.2 (2C), 127.5, 127.4, 127.1, 126.6, 126.2, 126.1 (2C), 60.2. ν_{max} (Nujol) 3414, 2028, 1906 (CO); m/z (FAB) 870.2 [MH$_2$-NH$_4$]$^+$, 761.1 [MH$_2$-PyCH$_2$O-NH$_4$]$^+$. Theoretical isotope pattern [M]$^-$ 868.0 (55%), 869.0 (20%), 870.0 (100%), 871.0 (40%), 872.0 (18%), 873.0 (8%). Actual isotope [M]$^-$ 868.2 (60%), 869.2 (23%), 870.2 (100%), 871.2 (40%), 872.2 (18%), 873.2 (4%). HRMS calculated [M]$^-$ = 868.0203, measured [M]$^-$ = 868.0204.

fac-[Re(1,10-bathophenanthroline sulphonate)$(CO)_3PyCH_2OCO(CH_2)_{12}CH_3$] [$H_4N$] (3.19).

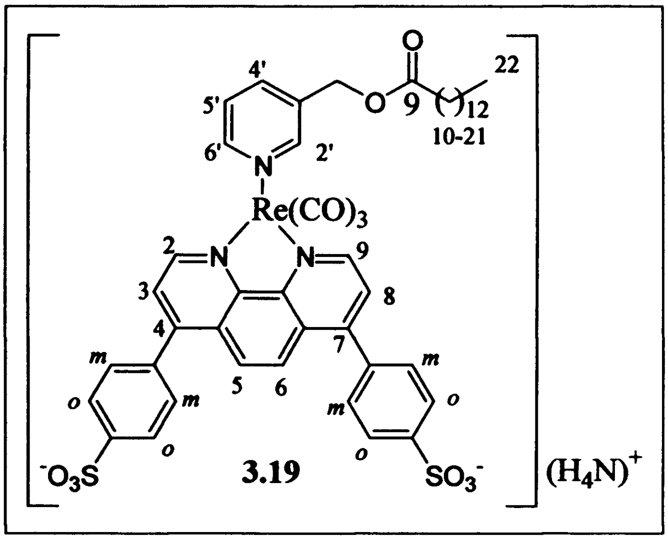

3.19

Mystiric acid (18 mg, 0.08 mmol) was added to a mixture of EDCI (26 mg, 0.1 mmol) and DMAP (4 mg, 0.03 mmol) in dry DCM (5 ml) at 0 °C. After 15 min stirring under a nitrogen atmosphere, a solution of complex **3.17** (50 mg, 0.04 mmol) in dry DCM (3 ml) was added to the reaction mixture, and stirring was continued at room temperature for 2 h. The solvent was evaporated to dryness and the residue was washed with ethyl acetate to remove the excess of EDCI and DMAP. The yellow solid was dissolved in the smallest possible amount of methanol and it was passed through an ion exchange column (Amberlite IR120 H resin as NH_4^+ form) which had been previously washed with aqueous ammonia eluting with methanol/water (1:1). The yellow coloured fraction which eluted immediately was collected and evaporated and dried under vacuum to give **3.18** as a yellow solid (27 mg, 62 %), m.p. 167 °C δH (CD_3OD) 9.71 (2H, m C*H*(2,9)), 8.45 (1H, m, C*H*(6')), 8.32 (1H, s, C*H*(2')), 8.10-7.97 (8H, m, 4 x C*H*(o), C*H*(3,5,6,8)) 7.78 (1H, dd, *J* = 1.5, 7.8 Hz C*H*(4')), 7.69-7.70 (4H, m, 4 × C*H*(m)) 7.25 (1H, t, *J* = 7.8, 5.7 Hz, C*H*(5')), 4.83 (2H, s, $PyCH_2O$), 2.03 (2H, t, *J* = 7.4 Hz, C*H*(10')), 1.25-0.85 (22H, m, C*H*(11'-21')), 0.79 (2H, m, CH_3(22)). δC (CD_3OD) 197.1 (CO_{eq}), 192.9 (CO_{ap}), 174.9 (*C*O(9)), 154.1, 152.6, 152.5 (2C), 152.2, 147.0, 145.0, 143.7, 140.4, 138.1, 131.9, 130.9, 130.6, 130.3, 129.8, 129.6, 128.1, 127.9, 127.6 (2C), 127.4 (3C), 127.2, 127.1, 126.8 (2C), 126.6, 126.2, 62.6 ($PyCH_2O$), 33.9 (*C*(10)), 32.4 (*C*(11)), 30.0, 29.9 (2C), 29.7 (2C), 29.4, 29.1 (2C), 25.1 (*C*(20)), 23.0 (*C*(21)), 13.7 (*C*(22)). ν_{max} (CH_3CN) 2030, 1826, 1738 (CO); *m/z* (ESI) 1080.3 $[MH_2\text{-}NH_4]^+$, 761.1 $[MH_2\text{-}PyCH_2OCO(CH_2)_{12}CH_3\text{-}NH_4]^+$. Theoretical isotope pattern $[M]^-$ 1078.2 (55%), 1079.2 (30%), 1080.2 (100%), 1081.2 (58%), 1082.2 (38%), 1083.2 (6%). Actual isotope pattern $[M]^-$ 1078.4 (42%), 1079.4 (45%), 1080.3 (100%), 1081.3 (60%), 1082.4 (21%), 1083.3 (2%).

3.11 References.

[1] L. A. Worl, R. Duesing, P. Chen, L. D. Ciana, T. J. Meyer, *Dalton Trans.*, **1991**, 849.

[2] L. A. Sacksteder, A. P. Zipp, E. A. Brown, J. Streich, J. N. Demas, B. A. DeGraff, *Inorg. Chem.*, **1990**, 29, 4335.

[3] E. C. Constable, A. M. W. C. Thompson, *Dalton Trans.*, **1994**, 1409.

[4] J. G. Vosa, J. M. Kelly, *Dalton Trans.*, **2006**, 4869.

[5] M. Licini, J. A. G. Williams, *Chem. Commun.* **1999**, 1943.

[6] J. L. Smithback, J. B. Helms, E. Schutte, S. M. Woessner, B. P. Sullivan, *Inorg. Chem.*, **2006**, 45, 2163.

[7] K. Kioke, J. Tanabe, S. Toyama, H. Tsubaki, K. Sakamoto, J. R. Wetwell, F. P. A. Johnson, H. Hori, H. Saitoh, O. Ishitani, *Inorg. Chem.*, **2000**, 39, 2777.

[8] A. Juris, S. Campagna, I. Bidd, J. M. Lehn, R. Ziessel, *Inorg. Chem.*, **1988**, 27, 4007.

[9] P. J. Giordano, M. S. Wrighton, *J. Am. Chem. Soc.*, **1979**, 2888.

[10] E. C. Constable, M. D. Ward, *Dalton Trans.*, **1990**, 1405.

[11] **(a)** E. W. Abel, N. J. Long, K. G. Orrell, A. G. Osborne, H. M. Pain, V. Sik, *Chem. Commun.* **1992**, 303. **(b)** E. R. Civitello, P. S. Dragovich, T. B. Karpishin, S. G. Novick, G. Bierach, J. F. O'Connell, T. D. Westmoreland, *Inorg. Chem.*, **1993**, *32*, 237.

[12] E. W. Abel, N. J. Long, K. G. Orrel, A. G. Osborne, H. M. Pain, V. Šik, *Chem. Commun.*, **1992**, 303.

[13] H. Friebolin (Ed.), *Basic One and Two Dimensional NMR Spectroscopy*, 4th ed., Wiley-VCH, New York, **2005**.

[14] J. V. Caspar, T. J. Meyer, *J. Phys. Chem.*, **1983**, 87, 952.

[15] M. S. Wrighton, D. L. Morse, L. Pdungsap, *J. Am. Chem. Soc.*, **1975**, 97, 2073.

[16] L. Sackslesder, M. Lee, J. N. Demas, B. A. DeGraff, *J. Am. Chem. Soc.*, **1993**, 115, 8230.

[17] G. A. Reitz, J. N. Demas, B. A. DeGraff, E. M. Stephens, *J. Am. Chem. Soc.*, **1988**, 110, 5051.

[18] J. Emsley, *Chem. Soc. Rev.*, **1980**, 9, 91.

[19] A. J. Amoroso, M. P. Coogan, J. E. Dunne, V. Fernández-Moreira, J. B. Hess, A. J. Hayes, D. Lloyd, C. Millet, S. J. A. Pope, C. Williams, *Chem. Commun.*, **2007**, 3066.

Chapter 4

Thiol-selective Rhenium(I) Luminescent Agent

4.1 Introduction.

4.1.1 Thiol-reactive transition metal complexes.

Thiol-selective compounds allow specific labelling of proteins due to the low number of free sulfhydryl groups present in proteins in comparison to an abundance of amino groups. Fluorophores such as maleimide derivatives of fluorescein, rhodamine and pyrene are traditionally used for this purpose; however these compounds have several drawbacks in their use as they are photochemically unstable, require UV excitation and have short lifetimes (less than 100 ns). In 1997, Lakowicz and co-workers[1] synthesised the first sulfhydryl reactive metal complex [Ru(2,2'-bipyridine)$_2$(1,10-phenanthroline-5-maleimide)](PF$_6$)$_2$, which had far more suitable photophysical properties for use as a probe for biological molecules, *i.e.* a long lifetime (1.1 μs) and a large Stokes' shift (145 nm) as well as being photochemically stable. **Scheme 4.1** depicts the use of the ruthenium complex to label a variety of proteins such as Human Serum Albumin (HSA)[a], β-galactosidase[b] or Immunoglobin G (IgG)[c].

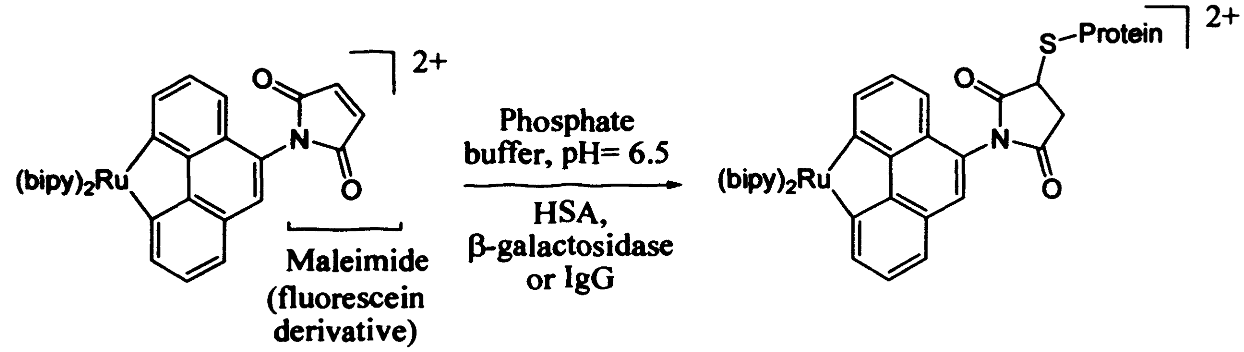

HSA: Human serum albumin
IgG: Immunoglobulin G

Scheme 4.1. First example of a thiol reactive transition metal complex.

The photophysical features of the metal complexes allow an increase in the sensitivity of detection and measurement. This then permits time gating, a technique that removes the autofluorescence of biological samples which typically have a lifetime of less than 10 ns, interfering with the fluorescence from the metal complex. Studies of the microsecond

---

[a] Blood protein produced by the liver whose function is to maintain the osmotic pressure.

[b] Enzyme that catalyses the hydrolysis of β-galactosides to monosaccharide.

[c] Protein with four subunits (immunoglobulin) distributed equally in blood and tissues whose function is to protect the body against phatogens.

dynamics of proteins can be carried out using these probes as they display high fluorescence anisotropy in the absence of rotational diffusion. Anisotropy decay data are used to determine rotational correlation times of the proteins, which show local probe motions in addition to overall rotational diffusion.

Chemically, the reaction described in **Scheme 4.1** between the sulfhydryl reactive metal complex and the protein fragment is known as a Michael addition or 1,4-nucleophilic addition, involving nucleophilic attack at an α,β-unsaturated carbonyl group. Thiol and amine groups are both able to react with α,β-unsaturated systems but in different ways defined by the ***hard-soft acid-base theory*** which classifies RNH_2 as a hard base and RSH as a soft base. Therefore, RNH_2 will react with hard electrophiles, such as the carbonyl carbon, whereas RSH will react with soft electrophiles, such as the C_β. Moreover, thiol groups tend to react more quickly as they are better nucleophiles due to the softer character that facilitates polarization, **Figure 4.1.**

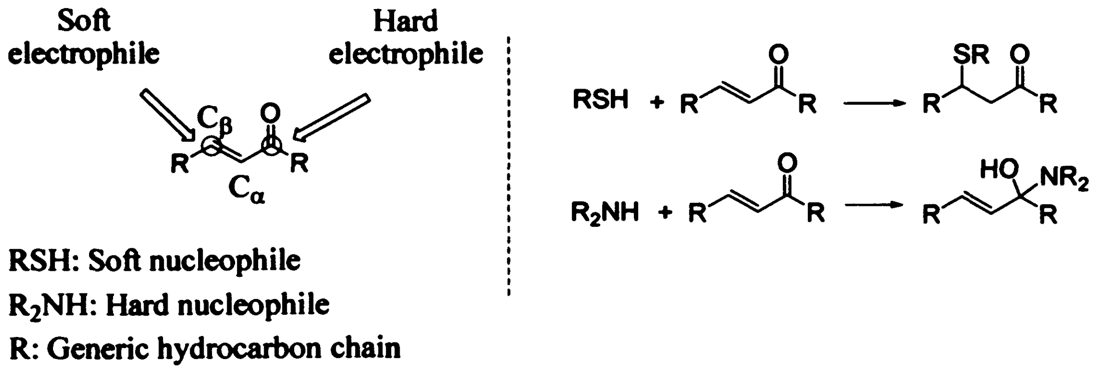

Figure 4.1. The relative reactivities of RSH and R_2NH in Michael additions.

4.1.2 Chloro and iodo derivatives as sulfhydryl reactive groups.

A further series of thiol-reactive metal complex probes was described by Lakowicz and co-workers.[2] Known thiol reactive groups such as chloro- and iodo-methyl groups on the ligand were used as triggers instead of relying on organic fluorophores already in use for this purpose. Two examples of these complexes are shown in **Figure 4.2.**

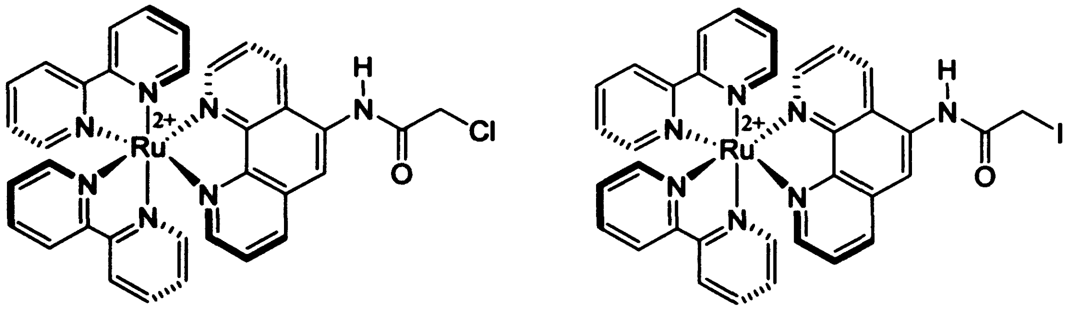

$[Ru(bipy)_2(phen\text{-}ClA)]^{2+}$ $[Ru(bipy)_2(phen\text{-}IA)]^{2+}$

Figure 4.2. Thiol selective Ru(II) complexes.

Not only Ru(II) complexes were found to be suitable for this purpose, but also $[Re(CO)_3(\alpha\text{-diimide})]^+$ complexes (**Figure 4.3**)[3] which, based on physical properties such as luminescence lifetime, Stokes' shift, quantum yield and anisotropy data, were found to be suitable compounds for labelling free thiol groups in proteins. It is worth noting that the thiol reactive groups are also able to react with amine groups. However, the rate of the reaction for amine derivatives is much slower than for the thiol analogues as the amine moieties become more strongly solvated due to their smaller size and higher charge concentration thereby inhibiting the reaction path.

The work carried out on both the rhenium and ruthenium complexes has opened a new door for the use of transition metal complexes in biophysics and clinical chemistry.

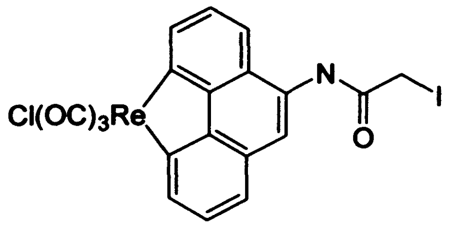

$Re(CO)_3(phen\text{-}IA)Cl$

Figure 4.3. A thiol selective Re(I) complex.

4.2 Design Of A New Rhenium Thiol-Reactive Fluorophore.

While numerous luminescent metal complexes have been synthesised and characterised, only a few have been prepared with suitable reactive groups present that would allow selective binding to proteins. Thus, the aim of the work described in this chapter is to investigate novel approaches to the synthesis of a rhenium complex which can react selectively with sulfhydryl residues.

4.2.1 The target structure of the thiol-reactive fluorophore.

Following the guidelines established by Lakowicz the design of the thiol selective luminescent metal complex bearing a thiol-reactive group such as a halogen on a ligand was made. In particular, this work will describe such a compound comprised of a luminescent rhenium complex bearing a chloromethyl group susceptible to attack by free thiols. The specific target is shown in **Scheme 4.2.**

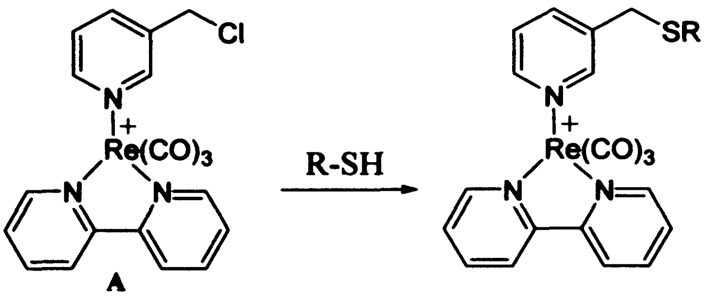

A

R: Generic hydrocarbon chain, or biological entity

Scheme 4.2. Designed target (A) to comply with the thiol selectivity.

4.2.2 Retrosynthetic analysis.

Using the same retrosynthetic analysis[4] presented in **Chapter 2** (see **Scheme 2.4**) the rhenium metal complex depicted in **Scheme 4.2** was designed. For the axial ligand, two options were considered: introduce the preformed chloromethylated axial ligand, which is commercially available as a hydrochloride salt, to the metal centre (**Option A, Scheme 4.3**); or chlorinate a reactive fragment on the ligand already coordinated to the metal, typically an alcohol group (**Option B, Scheme 4.3**).

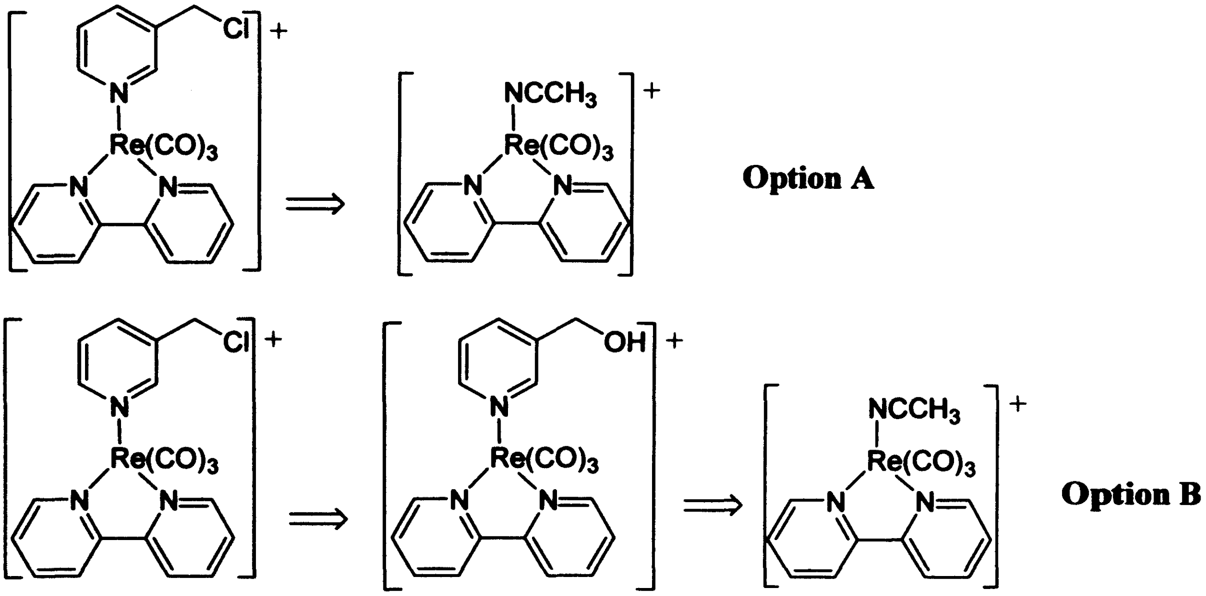

Scheme 4.3. Retosynthetic analysis of two possible routes for the axial ligand.

4.3 Results And Discussion.

4.3.1 Approach towards a thiol-reactive Re complex using a prefabricated chlorinated ligand.

After carefully analysing the two options to reach the final target, a direct substitution reaction using the prefabricated chlorinated ligand was chosen for the first attempt, as the conditions for chlorination of alcohols are often harsh. The initial steps of the synthesis have been recorded in **Chapter 2**. A brief scheme of the reactions performed can be seen below.

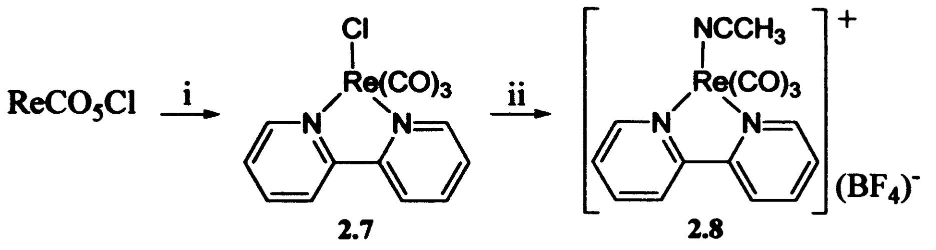

i: bipy, toluene, 98 %

ii: $AgBF_4$, CH_3CN, 88 %

Scheme 4.4. Brief scheme of the reactions performed to synthesise the activated rhenium complex, **2.8** (i: formation of rhenium chelated adduct (**2.7**), ii: chloride abstraction).

Substitution of the labile axial acetonitrile ligand using the commercially available picolyl chloride was attempted using standard conditions, **Scheme 4.5.** However, the reaction of the activated species, **2.8**, with the prefabricated chloride ligand, $PyCH_2Cl{\cdot}HCl$, in presence of a base, Et_3N, did not lead to the desired target, but instead, it gave an unexpected product, the precursor $[Re(bipy)(CO)_3Cl]$, **2.7.** Faced with this surprising result, the structure of the product obtained was carefully analysed using ^{1}H-NMR and IR spectroscopy by comparison with that of an authentic rhenium chloride adduct, $[Re(bipy)(CO)_3Cl]$, **Figure 4.4.**

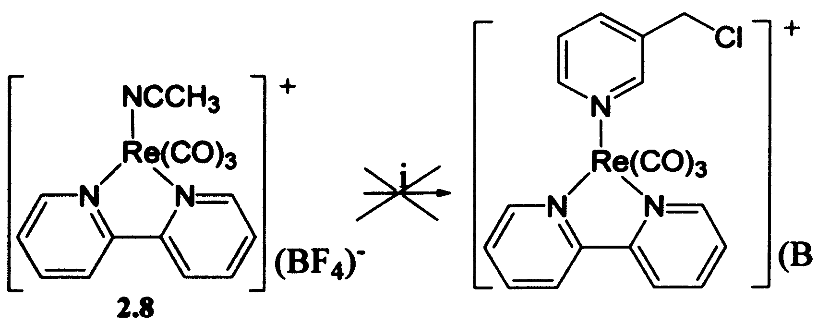

i: $PyCH_2Cl{\cdot}HCl$, Et_3N, THF

Scheme 4.5. Unsuccessful acetonitrile substitution.

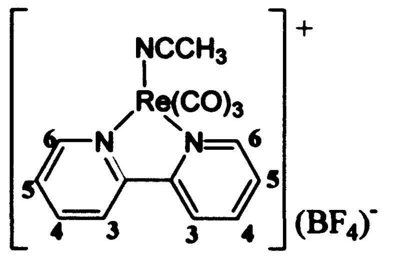

2.8

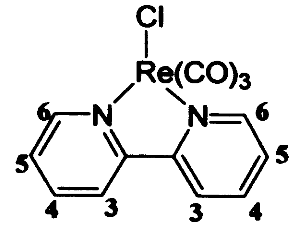

2.7

Reported data for 2.7 ^{1}H-NMR
δ (ppm): $CDCl_3$
9.0 (2H, d, C(6))
8.15 (2H, d, C(3))
8.0 (2H, t, C(4))
7.50 (2H, m, C(5))

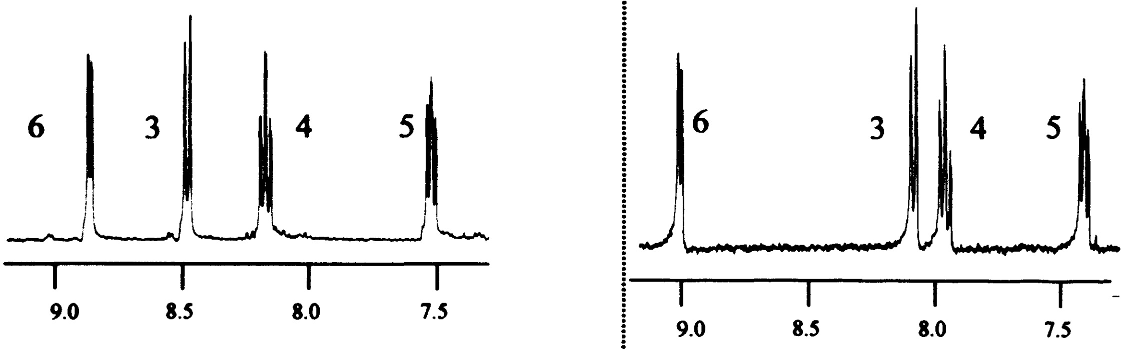

^{1}H-NMR spectrum of complex 2.8, the starting material of the reaction

^{1}H-NMR spectrum of final product from the reaction of 2.8 and $PyCH_2Cl{\cdot}HCl$

Figure 4.4. ^{1}H-NMR spectra of the starting material and product from the reaction of 2.8 and $PyCH_2Cl{\cdot}HCl$. Spectroscopic data of complex 2.7, [Re(bipy)(CO)$_3$Cl].

This unexpected reactivity can be explained by the small steric demand of the chloride ion as a nucleophile in comparison with the bulky pyridine derivative. In order to overcome this problem, silver tetrafluoroborate was introduced into the reaction mixture to precipitate the chloride ion as the silver salt. However, once again, the same product, [Re(bipy)(CO)$_3$Cl], was recovered from the reaction mixture. It is probable that the excess pyridine coordinates to the silver, solubilising the cation, leaving the chloride ions in solution and therefore available to react with the rhenium complex to form complex **2.7**.

In a final attempt to eliminate any possible chloride ions form the reaction mixture, the picolyl chloride was pre-treated with silver tetrafluoroborate. Both reagents were dissolved in dry IPA and after precipitation of a white solid, assumed to be AgCl, the colourless solution was transferred, via cannula, into a second IPA solution of [Re(bipy)(CO)3CH3CN]BF_4, **2.8**, and triethylamine (Et_3N), **Scheme 4.6.**

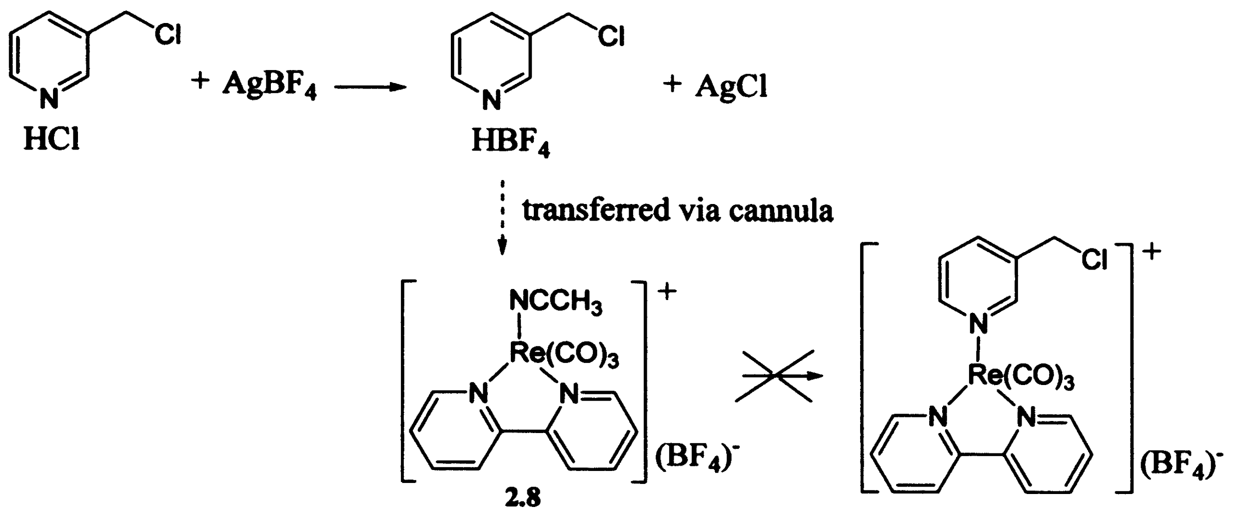

Scheme 4.6. Attempted substitution of the acetonitrile ligand in complex **2.9**.

Unfortunately, [Re(bipy)(CO)$_3$Cl], **2.7**, was, once again, the main product recovered from this reaction. The only explanation found for this unexpected result is the displacement of the chloride ion from the chloromethyl group. The coordination reaction of this chloride to the metal centre might be faster than the coordination of the desired pyridine derivative due to its smaller size, *i.e.* removing any electronic considerations.

4.3.2 Approach towards a thiol-reactive Re complex via a chlorination reaction.

Faced with the difficulty of displacing the acetonitrile with the pre-formed ligand, PyCH$_2$Cl·HCl, a second option was considered, entailing the synthesis of a complex bearing a reactive unit, an alcohol, and its subsequent tosylation, with tosyl chloride. The hydroxymethyl pyridine complex, **2.9**, discussed in **Chapter 2**, was treated with tosyl chloride in the presence of a base, Et$_3$N. After heating at reflux in DCM for 4 hours, surprisingly, the same result was obtained as in **Section 4.3.1**, that is, the formation of [Re(bipy)(CO)$_3$Cl], **2.7**, along with decomposition products. Attempts to avoid the formation of complex **2.7**, by addition of silver tetraflouroborate were unsuccessful, leading to a mixture of decomposition products, **Scheme 4.7.**

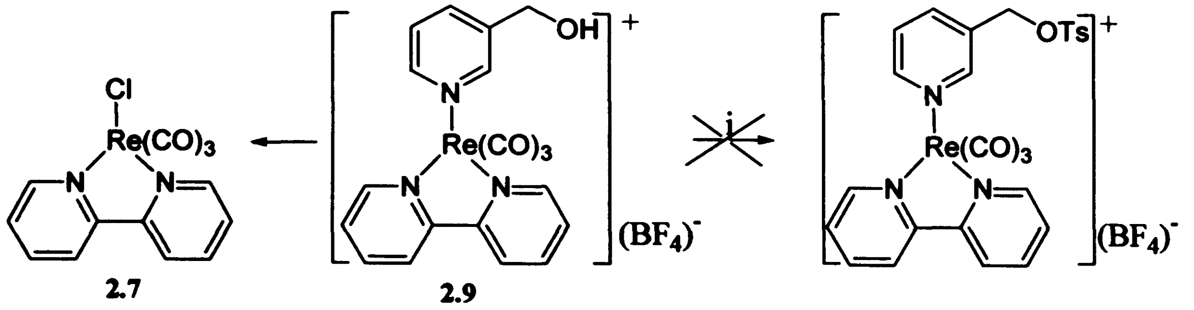

i: TsCl, Et_3N, $AgBF_4$, DCM

Scheme 4.7. Attempted tosylation of **2.9**.

This result can only be rationalized by activation of the pyridine ligand towards displacement during the reaction with the tosyl chloride. This reaction pathway is unusual and the mechanism is not clear. It is possible that the donor properties of the pyridine group decrease upon tosylation, making substitution for the chloride ion easier, **Scheme 4.8.**

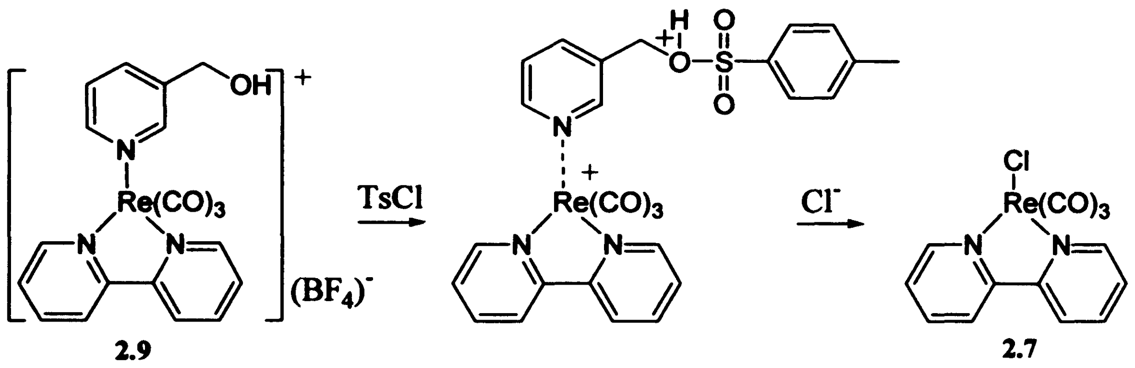

Scheme 4.8. Proposed mechanism of the displacement of the pyridine derivative for the chloride ion.

4.3.3 Approach towards a thiol reactive Re complex using thionyl chloride.

A recent report published by Coe *et al.* in 2007 prompted a revision of the proposed synthesis.[5] In this report, by using thionyl bromide, a well know brominating reagent, the successful bromination of a similar system in 68 % yield was achieved, **Scheme 4.9.**

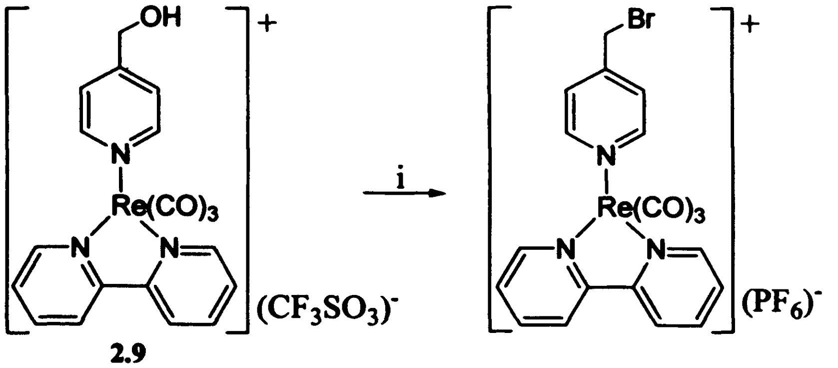

i: $SOBr_2$, NH_4PF_6 $_{(aq)}$,
24h, rt, 68 %

2.9

Scheme 4.9. Bromination reaction.

Suprisingly, the harsher conditions described were the key to the synthesis of [Re(bipy)(CO)$_3$PyCH$_2$Cl]PF$_6$, **4.1**. Complex **4.1** was obtained in 78 % yield after stirring overnight at room temperature in neat thionyl choride followed by subsequent dropwise addition of a saturated aqueous solution of ammonium hexafluorophospate, NH_4PF_6. **Scheme 4.10.**

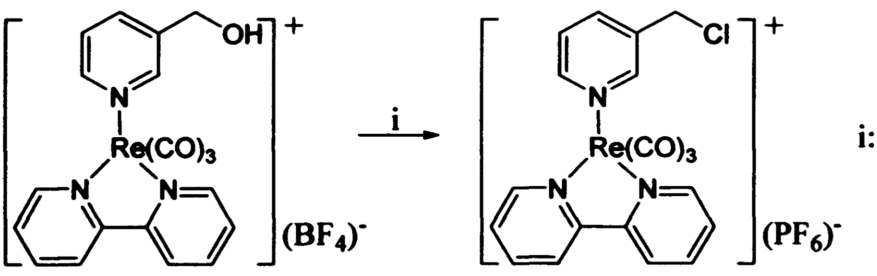

i: $SOCl_2$, NH_4PF_6 $_{(aq)}$, 78 %

2.9

4.1

Scheme 4.10. The synthesis of [Re(bipy)(CO)$_3$PyCH$_2$Cl]PF$_6$, **4.1.**[6]

^{1}H-NMR spectroscopy showed a shift of the methylene proton from 4.38 ppm to 4.58 ppm upon chlorination. These data agreed with those obtained by ^{13}C-NMR, where a shift of the methylene carbon was observed from 59.6 to 41.1 ppm, a value typical for a chloromethyl group.[7] Moreover, crystallographic studies corroborated the structure of complex **4.1**, [Re(bipy)(CO)$_3$PyCH$_2$Cl]PF$_6$.

4.3.4 Crystal structure dicussion.[d]

Single crystals of complex [Re(bipy)(CO)$_3$PyCH$_2$Cl]PF$_6$ were grown by the slow evaporation of a solution of the complex in chloroform. Crystallographic refinement data

---

[d] [d] Crystal structure measured and solved by Richard Arthur at Cardiff University.

are given in **Table 4.1**. The perspective ORTEP drawing of the studied complex, **4.1**, with atomic numbering is shown in **Figure 4.5.**

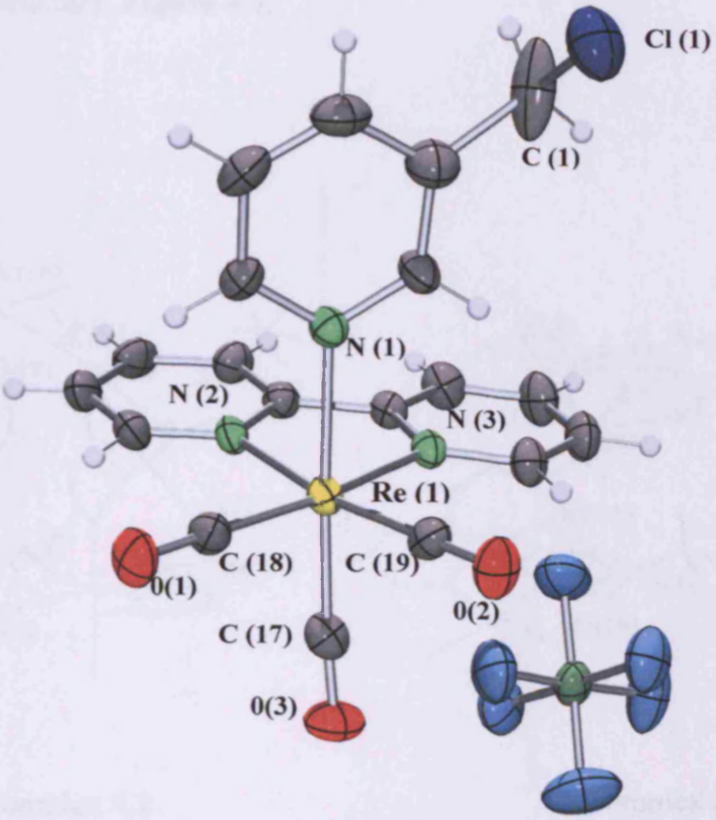

Figure 4.5. ORTEP representations of the structure of **4.1** with thermal ellipsoids drawn at the 30 % level.

The three carbonyl ligands are arranged in a *facial* geometry and the rhenium coordination sphere can be described as a slightly distorted octahedron, where the chelate ligand, bipyridine, and two of the carbonyls *trans* to it form the equatorial plane. The third carbonyl and the chloromethylated pyridine ligand are placed in the apical plane. Deviation from ideal octahedral geometry (N(2)ReN(3): 75.01(2) instead of 90^{o}) originates from the geometric restraints imposed by the chelate ligand,.

Selected bond lengths and angles are given in **Table 4.2**. The Re-C and Re-N bond distances are close to those reported for analogous rhenium structures [Re(bipy)(CO)$_3$L], with L being a pyridine derivative. Only small differences in bond lengths were found on comparing complex **4.1** with its hydroxyl analogue, **2.9**, probably because of the bulkier chloromethyl substituent. For example, the Re-N(3) bond length is 2.160(6) Å in complex **4.1**, whereas the distances between the same atoms in its analogue, **2.9**, is 2.172 (4) Å, perhaps due to the arrangement different interactions of the pyridine substituents that lead to a totally different packing. In particular, an intermolecular contact between the chlorine of one complex and the two equatorial carbonyl carbons of an adjacent complex was observed in the structure, **Figure 4.7.**

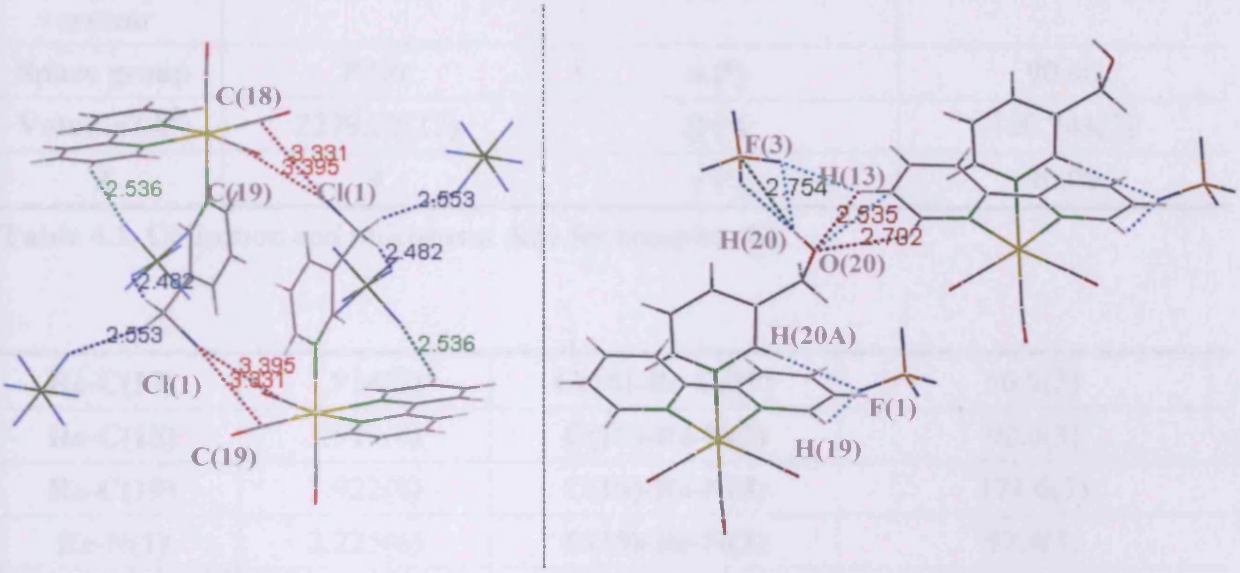

Complex **4.1** Complex **2.9**

Figure 4.6. Short interactions of pyridine substituents in complex **2.9** and complex **4.1.**

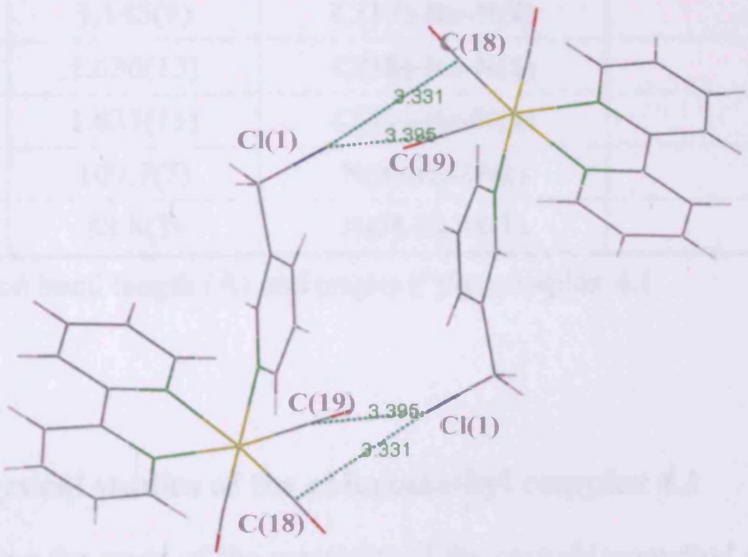

Figure 4.7. Short interactions of pyridine substituent in complex **4.1.**

Empirical Formula	$C_{19}H_{14}ClF_6N_3O_3PRe$	**a (Å)**	13.7391(4)
Molecular weight	698.95	**b (Å)**	11.5590(4)
Crystal system	Monoclinic	**c (Å)**	14.6082(5)
Space group	$P2_1/c$	**α (°)**	90.00
Volume ($Å^3$)	2279.27(13)	**β (°)**	100.743(2)
Z	4	**γ (°)**	90.00

Table 4.1. Collection and refinement data for complex **4.1**.

Re-C(17)	1.914(9)	**C(18)-Re-C(19)**	90.9(3)
Re-C(18)	1.918(8)	**C(17)-Re-N(3)**	92.0(3)
Re-C(19)	1.922(8)	**C(18)-Re-N(3)**	171.6(3)
Re-N(1)	2.225(6)	**C(19)-Re-N(3)**	97.4(3)
Re-N(2)	2.172(6)	**C(17)-Re-N(2)**	97.4(3)
Re-N(3)	2.160(6)	**C(18)-Re-N(2)**	96.6(3)
C(17)-O(3)	1.156(10)	**C(19)-Re-N(2)**	171.4(3)
C(18)-O(1)	1.152(9)	**N(3)-Re-N(2)**	75.0(2)
C(19)-O(2)	1.145(9)	**C(17)-Re-N(1)**	177.7(3)
C(3)-C(1)	1.636(13)	**C(18)-Re-N(1)**	93.0(3)
C(1)-Cl(1)	1.637(11)	**C(19)-Re-N(1)**	91.6(3)
C(3)-C(1)-Cl(1)	109.7(7)	**N(3)-Re-N(1)**	86.4(2)
C(18)-Re-C(17)	88.8(3)	**N(2)-Re-N(1)**	83.8(2)

Table 4.2. Selected bond length (Å) and angles (°)for complex **4.1**.

4.3.5 Photophysical studies of the chloromethyl complex 4.1

Prior to undertaking the study of the reactivity of the new chloromethyl rhenium complex, **4.1**, its photophysical properties were analysed to confirm its suitability for biological imaging applications. The absorption properties of **4.1** do not differ from those expected of a cationic rhenium tricarbonyl bisimine, showing the typical MLCT as a broad band centred at 354 nm, with the maximum excitation at 364 nm and the emission maximum at 551 nm. The large Stokes' shift, 187 nm, will eliminate any self-quenching problems often found with commercially available probes such as Fluorescein, as well as allowing differentiation from interfering autofluorescence. The fluorescence lifetime of 131 ns is long in comparison with those of organic molecules, allowing the off-gating of any interfering autofluorescence from biological samples which typically display lifetimes in the order of 10 ns.

4.4 Study Of The Reactivity Of Chloromethyl Complex 4.1.

Having successfully synthesised a choromethylpyridine substituted rhenium complex, whose photophysical properties make it suitable to be used as a biological probe, a variety of reactions with biologically relevant potential nucleophiles was then undertaken to test whether the desired thiol specificity had been replicated.

4.4.1 Reactivity with simple amino groups.

No reaction occurred between complex **4.1** and the esterified amino acid, leucine methyl ester hydrochloride, in the presence of a base after stirring for 2 days at room temperature in acetonitrile. Even heating at 50 °C for 5 days led to no formation of the expected product, **Scheme 4.11.**

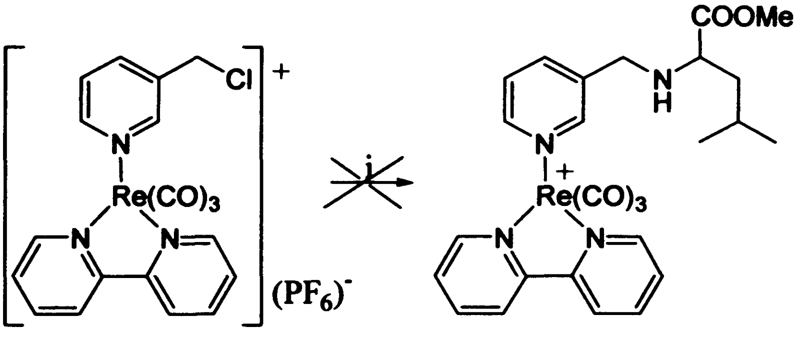

i: Leucine methyl ester hydrochloride, Et_3N, CH_3CN

Scheme 4.11. Attempted reaction of **4.1** with a leucine derivative.

On the contrary, when complex **4.1** was treated with two equivalents of isopropyl amine in acetonitrile, the reaction was complete after 4 days stirring at room temperature giving the amine adduct in an isolated yield of 77 %, **Scheme 4.12.** ^{1}H-NMR and ^{13}C-NMR spectroscopy confirmed the new structure in solution by the shift from 4.58 to 3.58 ppm and 41.1 to 45.3 ppm of the methylene group protons and carbon respectively. It is worth noting that the large chemical shift of the methylene group is probably due to anisotropy effects, *i.e.* even thought the methylene carbon has free rotation it may has as a preferred orientation with the proton pointing towards the bipyridine ligand because of steric effects.

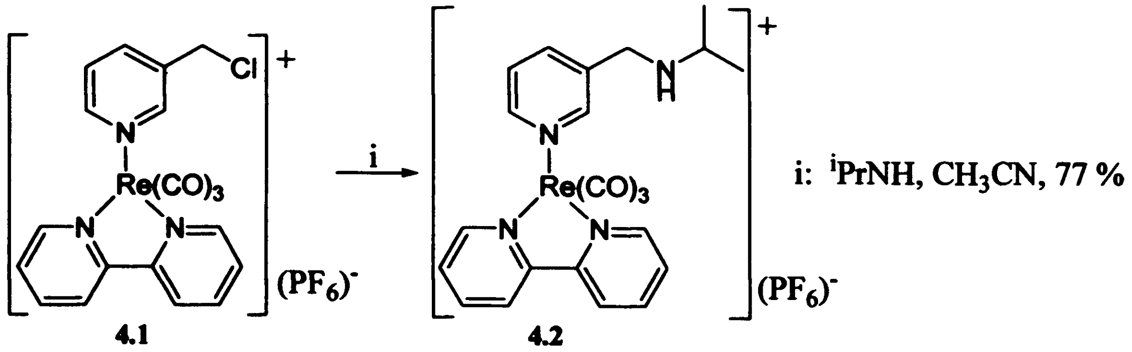

Scheme 4.12. Reaction of **4.1** with isopropyl amine.

A more sterically hindered amine, cyclohexylamine, was then reacted with the chloromethylene complex, **4.1**. Using the same conditions as in the synthesis of the isopropyl amine complex, the new product, **4.3**, was synthesised successfully in 64 % yield. ^{1}H-NMR and ^{13}C-NMR spectroscopic studies showed the same trend in chemical shifts for the methylene constituents as observed for those in complex **4.2**, *i.e.* a shift from 4.58 to 3.38 ppm and 41.1 to 46.4 ppm respectively.

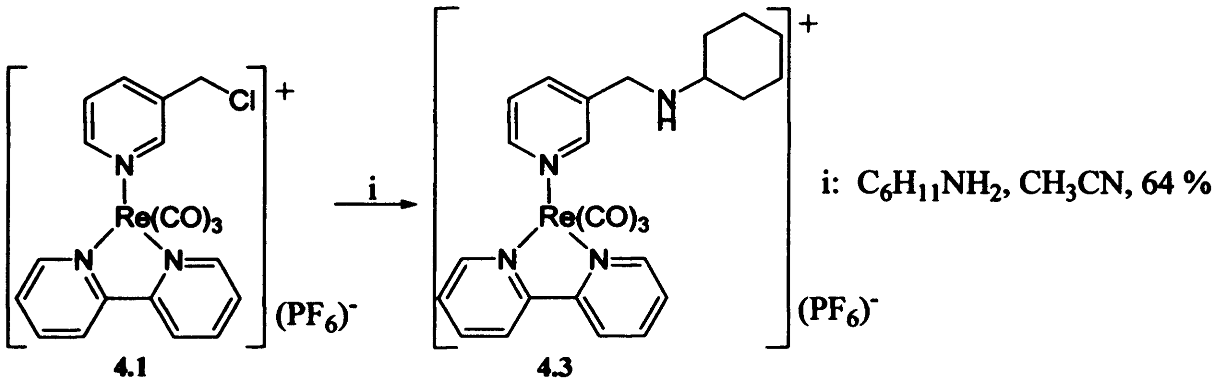

Scheme 4.13. Reactivity of **4.1** with cyclohexylamine.

4.4.2 Reactivity of complex 4.1 with mixed N, S groups.

Having studied the reactivity of the chloromethyl complex, **4.1**, with amino groups, the required thiol selectivity was tested using biologically relevant species containing both N and S moieties as potential nucleophiles. Cysteine methyl ester, a methylated amino acid with a thiol group, was chosen as the first mixed species to be tested with the studied complex, **4.1**. Prior to the reaction, the amino acid was liberated from its hydrochloride salt as the free amine, then stirred with the chloromethyl complex, **4.1**, in the presence of a base (Et_3N) at room temperature for 1 hour until ^{1}H-NMR spectroscopy showed no starting material was left in the reaction mixture. A dark yellow solid was obtained after removing the solvent and washing the residue with water, **Scheme 4.14.**

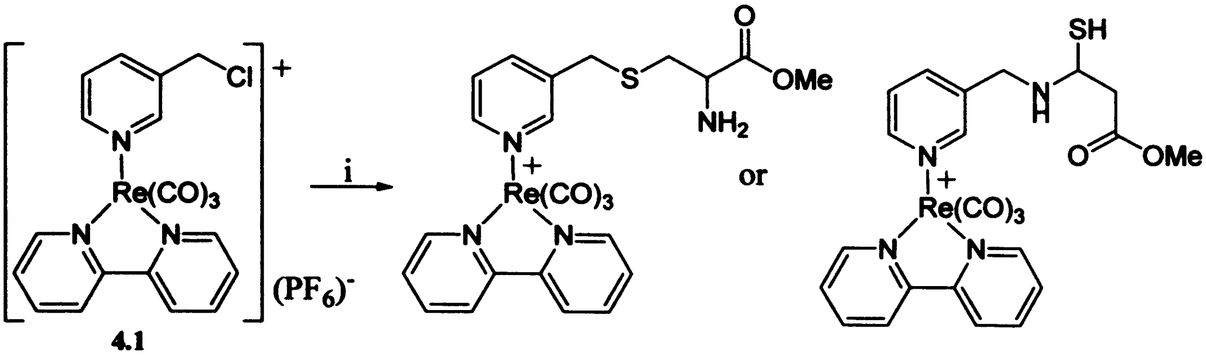

i: Cys-methyl-ester, Et_3N, CH_3CN, 65 %

Scheme 4.14. Reactivity with Cys-methyl-ester.

A ^{1}H-NMR spectroscopic study showed a clear shift of the methylene protons from 4.58 to 3.50 ppm indicating the reaction had occurred. However, it is not certain which of the two possible nucleophiles, S or N, had reacted from ^{1}H-NMR spectroscopy alone, as a similar methylene shift was observed in the case of complexes **4.2** and **4.3** where N was the nucleophile. ^{13}C-NMR spectral data revealed that S was, in this case, the only nucleophile that had undergone a S_N2 reaction, as the methylene carbon resonated at 32.0 ppm in the final product, typical of the C_α of a thioester,[8] in contrast to a signal at 41.1 ppm for the starting material. In the case of complexes **4.2** and **4.3**, the methylene carbon appears at 45.3 and 46.4 ppm respectively. Further characterization data are reported in the experimental section.

The fact that complex **4.1** had reacted selectively with a thiol group in the presence of both a thiol and an amine group represents a preliminary success in the search for a selective-thiol reactive complex. In order to confirm this result, a more complex biologically relevant thiol, reduced glutathione (GSH), was chosen in order to further demonstrate the selectivity of the chloromethyl complex **4.1**. **Figure 4.8.**

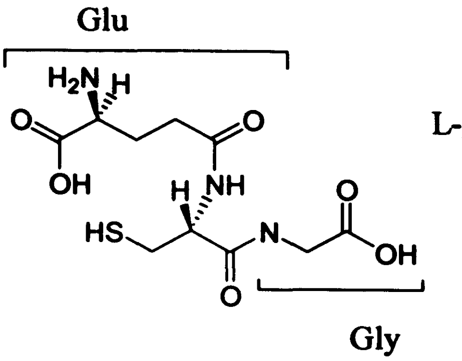

Figure 4.8. Structure of reduced glutathione.

L-Glutathione was treated with the chloromethyl complex **4.1** in the presence of a base, Et_3N, in a mixture of degassed solvents (methanol, water). The desired glutathione complex was obtained as a yellow solid in 44 % yield.

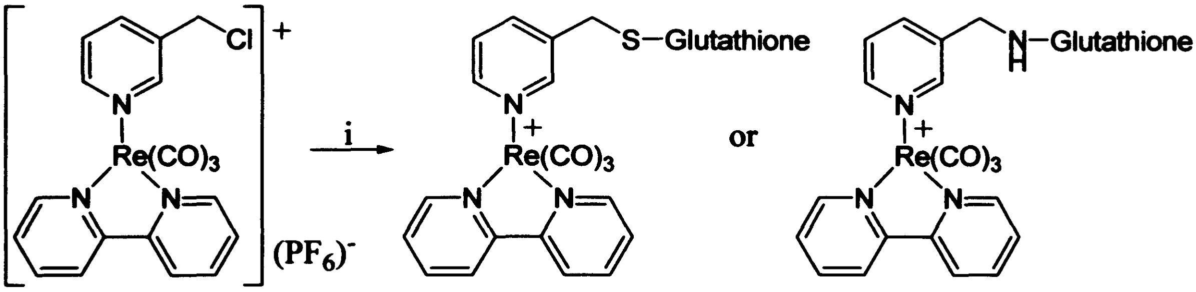
4.1

i: reduced glutathione, Et_3N, $MeOH:H_2O$, 44 %

Scheme 4.15. Reactivity with L-glutathione.

Data from ^{1}H-NMR and ^{13}C-NMR spectroscopy agreed with those reported for the cysteine complex **4.4**, where the protons and carbon from the methylene group are observed at 3.62 and 38.9 ppm respectively, indicating once again selective nucleophilic attack of the thiol, **Figure 4.9.** Further characterization corroborating the structure of the new thiol complex **4.5** can be seen in detail in the experimental section, **Section 4.7.**

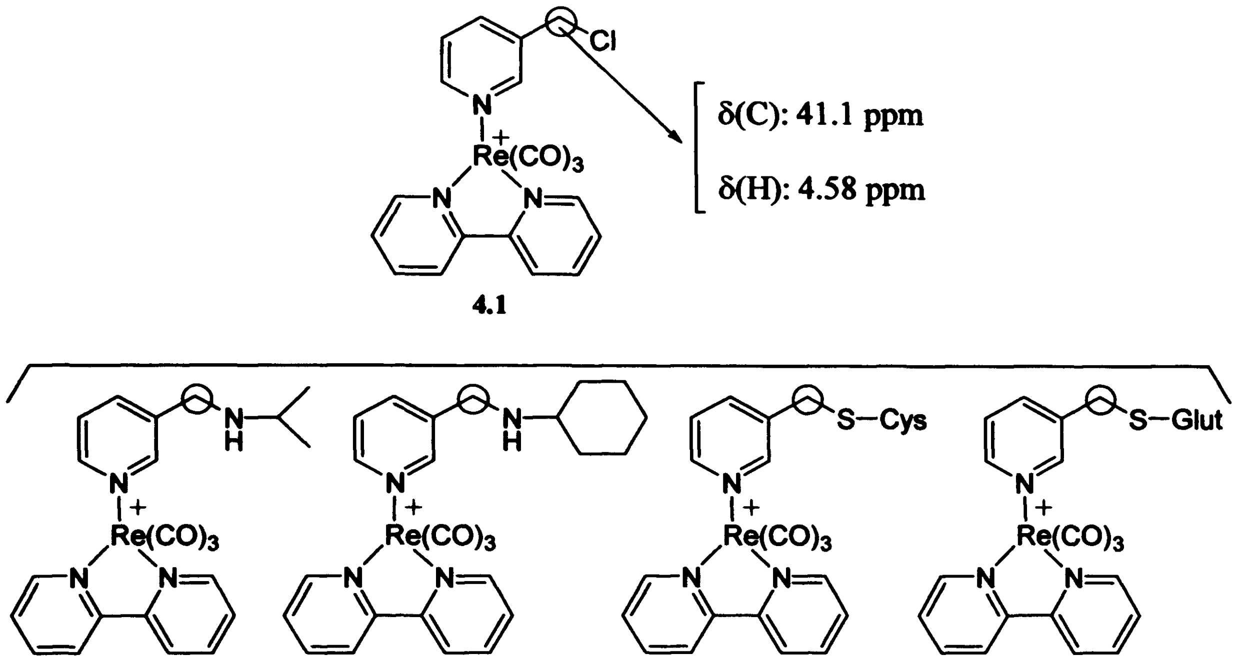

4.1

δ(C): 41.1 ppm
δ(H): 4.58 ppm

4.2
δ(C): 45.3 ppm
δ(H): 3.38 ppm

4.3
δ(C): 46.4 ppm
δ(H): 3.65 ppm

4.4
δ(C): 35.2 ppm
δ(H): 3.50 ppm

4.5
δ(C): 38.9 ppm
δ(H): 3.62 ppm

Figure 4.9. A summary of the ^{1}H-NMR and ^{13}C-NMR spectroscopic data for the CH_2 unit in **4.1** to **4.5**.

These results show that not only has a new fluorescent thiol-reactive metal complex been synthesised, but also thiol selectivity has been demonstrated as in the presence of two nucleophiles, N and S, only S-alkylation is observed. This result is in concordance with the reactivity expected for these two species, where thiol compounds afford faster nucleophilic substitution reactions, S_N2, than amino derivatives as they are better nucleophiles.

4.5 Photophysical Studies Of Chloromethyl Complex 4.1 And Its Derivatives, Complexes 4.2-4.5.

The UV-visible absorption spectra of complexes **4.1** - **4.5** in CH_3CN or MeOH, **Table 4.3**, exhibit an absorption band at *ca.* 350 nm. This band is assigned to metal-to-ligand charge-transfer (MLCT) d(ReI) → π*(bipy) transitions, by analogy with previous studies on related complexes.[9] Additionally, absorption bands between 247-319 nm have been assigned to spin-allowed intraligand (^{1}IL) ($\pi \rightarrow \pi^*$) (N-N and pyridine ligands) transitions.

Complex	^{1}IL (λ_{abs}/nm)	^{1}MLCT (λ_{abs}/nm)
4.1$_a$	248, 268, 314	358
4.2$_a$	260, 318	350
4.3$_a$	260, 318	349
4.4$_b$	247, 319	352
4.5$_b$	246, 269, 309, 320	356

a. CH_3CN as solvent.

b. MeOH as solvent.

Table 4.3. Electronic absorption spectral data for complexes **4.1** – **4.5**.

The excitation and emission spectra were also recorded at room temperature in MeOH or CH_3CN solutions. The excitation and emission maxima are placed at *ca.* 395 and 555 nm in the case of the amine adducts and at *ca.* 360 and 550 nm for the thiol adducts (**Table 4.4**). In addition, luminescent lifetimes of complexes **4.4** and **4.5** were determined, showing values of 122 ns and 116 ns respectively. These excitation and emission properties, typical of a cationic rhenium tricarbonyl bisimine, together with their large Stokes' shifts and the 100 nanosecond luminescent lifetimes suggest the phosphorescent nature of the emission, a ^{3}MLCT [dπ(Re) → π*(diimine)] transition.

Complex	Excitation λ/nm	Emission λ/nm	Lifetimes τ/ns
4.2_a	395	555	-
4.3_a	396	556	-
4.4_b	360	550	122
4.5_b	361	551	116

a CH_3CN as solvent.
b MeOH as solvent.

Table 4.4. Excitation, emission wavelengths and lifetimes for complexes **4.2** – **4.5**.

4.6 Conclusions.

A thiol reactive rhenium complex, **4.1**, has been synthesised and its thiol selectivity demonstrated by reacting the new probe with biologically relevant mixed nucleophilic species. Not only does it have a reasonably long fluorescence lifetime and large Stokes' shift, but also affords derivatives with the same characteristics. This makes it a promising fluorescent probe for proteins *in vivo*: given the high concentration of reduced thiols in cells, the thiol adducts would be the major species present.

4.7 Experimental.

fac-[Re(bipy)(CO)$_3$PyCH$_2$Cl](PF$_6$), 4.1

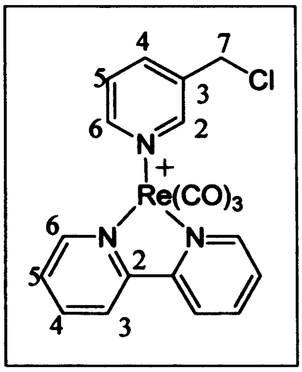

A solution of *fac*-[Re(bipy)(CO)$_3$PyCH$_2$OH](BF$_4$), **2.5** (150 mg, 0.2 mmol) in 3 ml of thionyl chloride was stirred under a nitrogen atmosphere overnight. The mixture was cooled in an ice bath and a saturated aqueous NH$_4$PF$_6$ solution was added very slowly, dropwise, with extremely rapid stirring until a yellow solid precipitate formed. The precipitate was separated from the mixture of solvents by filtration and washed several times with water to give **4.1** as a yellow solid (132 mg, 78 % yield), m.p. 180 °C. δH (CD$_3$CN) 9.18 (2H, d, *J* = 5.4 Hz, C*H*(6) bipy), 8.42 (2H, d, *J* = 6.4 Hz, C*H*(3) bipy) 8.32 (3H, m, C*H*(2) Py, C*H*(4) bipy), 8.20 (1H, d, *J* = 5.5 Hz, C*H*(6) Py), 7.91 (1H, d, *J* = 4.5 Hz, C*H*(4) Py), 7.82 (2H, m, C*H*(5) bipy), 7.33 (1H, m, C*H*(5) Py), 4.58 (2H, s, C*H*$_2$). δC (CD$_3$CN) 195.0 (*C*O$_{eq.}$), 191.2 (*C*O$_{ap.}$) 155.2 (*C*(2), bipy), 153.4 (*C*(6), bipy),151.0, 151.1 (*C*(2), Py, *C*(6), Py), 140.7 (*C*(4), bipy), 139.0 (*C*(4), Py), 136.6 (*C*(3), Py), 128.3 (*C*(3), bipy), 126.1 (*C*(5), Py), 124.2 (2*C*(5), bipy), 41.1 (*C*H$_2$). ν_{max} (Nujol): 2027, 1922, 1895 (CO). *m/z* (ESI) 553.9 [MH]$^+$ and 427.0 [M–PF$_6$–PyCH$_2$Cl]$^+$. Theoretical isotope pattern 552.0 (52%), 553.0 (11%), 554.0 (100%), 550.0 (22%), 556.0 (31%) and 557.0 (8%); observed isotope pattern 551.9 (50%), 552.9 (11%), 553.9 (100%), 554.9 (22%), 556.0 (30%) and 557.0 (5%). HRMS (ESI) calculated [M–PF$_6$]$^+$ = 552.0248; measured [M–PF$_6$]$^+$ = 552.0252. ReC$_{19}$H$_{14}$O$_3$N$_3$ClPF$_6$ requires C, 32.65; H, 2.02; N, 6.01; found C, 32.46; H, 1.92; N, 5.93%. X-ray: *M* = 698.95, yellow block, 0.2 × 0.2 × 0.2 mm, monoclinic, space group: P2$_1$/c, *a* = 13.7391(4) Å, *b* = 11.5590(4) Å, *c* = 14.6082(5) Å, β = 100.743(2)°, *V* = 2279.27(13) Å^3, *Z* = 4, D_c = 1.934 mg cm^{-3}, *F(000)* = 1268, reflections collected = 33013, R(int) = 0.1529; Goodness-of-fit on F2 = 1.023, *R1* = 0.0503, *wR2* = 0.1094.

fac-[Re(bipy)(CO)$_3$PyCH$_2$NH^{i}Pr](PF$_6$), 4.2.

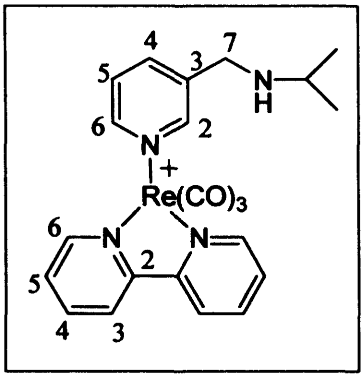

2.5 equivalents of ^{i}propylamine (17 ml, 0.17 mmol) was added to a solution of *fac*-[Re(bipy)(CO)$_3$PyCH$_2$Cl](PF$_6$), **4.1** (50 mg, 0.07 mmol) in acetonitrile (5 ml). The mixture was stirred for 3 days stirring at room temperature and then the solvent was removed on a high vacuum line to afford a dark yellow slurry which was dissolved in THF. Diethyl ether was added dropwise to precipitate the product as a yellow solid (40 mg, 77 %), m.p. 98 °C. δH (CD$_3$CN) (ppm) 9.31 (2H, d, J = 5.2 Hz, C*H*(6) bipy), 8.49 (1H, s, C*H*(2) Py), 8.40 (2H, d, J = 8.2 Hz, C*H*(3) bipy), 8.28 (2H, m, C*H*(4) bipy), 8.21 (1H, d, J = 7.1 Hz, C*H*(6) Py), 8.06 (1H, d, J = 7.1 Hz, C*H*(4) Py), 7.82 (3H, m, C*H*(5) bipy), 7.30 (1H, m, C*H*(5) Py), 3.82 (2H, s, CH_2), 3.82 (1H, q, J = 6.3 Hz, C*H*), 1.30 (6H, d, J = 6.3 Hz, CH_3). δC (CD$_3$CN) (ppm) 155.5 (*C*(3), Py), 153.8 (*C*(6), bipy), 152.2 (*C*(6), Py), 151.3 (*C*(2), Py), 141.0 (*C*(3), bipy), 140.5 (*C*(2), bipy), 139.6 (*C*(5), Py), 128.6 (*C*(4), bipy), 125.8 (*C*(4), Py), 124.5 (*C*(5), bipy), 45.4(*C*(7)), 44.3 (*C*(9)), 14.3 (*C*H$_3$). ν_{max} (CH$_3$CN): 2035, 1931 (CO). *m/z* (ESI) 577.2 [MH]$^+$, 427.1 [M–PF$_6$-PyCH$_2$NC(CH$_3$)$_2$]$^{++}$. Theoretical isotope pattern 575.1 (60%), 576.1 (15%), 577.1 (100%), 578.1 (25%), 579.1 (4%), Actual isotope pattern 575.2 (65%), 576.2 (18%), 577.2 (100%), 578.2 (28%), 579.2 (5%), HRMS (ESI) calculated [M+PF$_6$]$^+$ = 721.0936, measured [M+PF$_6$]$^+$ = 721.0935.

fac-[Re(bipy)(CO)$_3$PyCH$_2$NH(C$_6$H$_{11}$)](PF$_6$), 4.3.

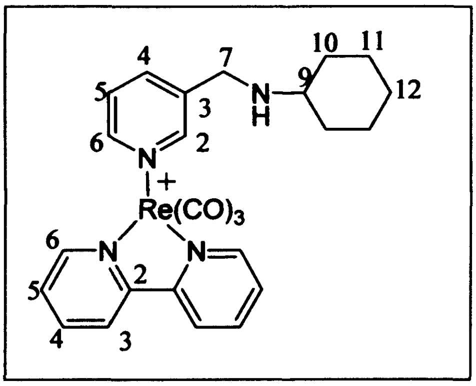

A mixture of *fac*-[Re(bipy)(CO)$_3$PyCH$_2$Cl](PF$_6$), **4.1** (50 mg, 0.07 mmol) and cyclohexylamine (20 ml, 0.17 mmol) in acetonitrile (5 ml) was stirred for 3 days at room temperature. Then the solvent was removed on a high vacuum line to afford a dark yellow slurry which was dissolved in THF. Petroleum ether was added dropwise to precipitate the product as a yellow solid (35 mg, 64 %). m.p. 95 °C. δH (CD$_3$CN) (ppm) 9.17 (2H, d, J = 4.9 Hz, C*H*(6) bipy,), 8.40 (2H, d, J = 8.1 Hz, C*H*(3) bipy), 8.30 (m, 2H, C*H*(4) bipy), 8.20 (s, 1H, C*H*(2) Py), 8.13 (d, 1H, J = 5.2 Hz, C*H*(6) Py), 7.82-7.78 (m, 3H, C*H*(4) py, C*H*(5) bipy), 7.22 (m, 1H, C(5) Py), 3.65 (s, 2H, CH_2), 2.17-0.91 (11H, m, Cy). δC (CD$_3$CN) (ppm) 155.5 (*C*(3), Py), 153.6 (*C*(6), bipy), 150.8 (*C*(6), Py), 149.8 (*C*(2), Py), 141.0 (*C*(3), bipy), 140.9 (*C*(2), bipy), 138.9 (*C*(5), Py), 128.5 (*C*(4), bipy), 125.7 (*C*(4), Py), 124.3 (*C*(5), bipy), 55.3 (*C*(9)), 46.4

(*C*(7)), 32.8 (*C*(10)), 25.6 (*C*(12)), 24.2 (*C*(11)). ν_{max} (CH_3CN): 2035, 1929 (CO). *m/z* (ESI) 617.3 $[MH]^+$, 427.2 $[M\text{-}PF_6\text{-}PyCH_2NH(C_6H_{11})]^+$. Theoretical isotope pattern 615.2 (60%), 616.2 (18%), 617.2 (100%), 618.2 (30%), 619.2 (4%), Actual isotope pattern 615.2 (62%), 616.3 (19%), 617.3 (100%), 618.3 (31%), 619.3 (4%), HRMS (ESI) calculated $[MH]^+ = 615.1528$, measured $[MH]^+ = 615.1529$.

***fac*-[Re(bipy)(CO)$_3$PyCH$_2$SCH$_2$CH(NH$_2$)COOMe](PF$_6$), 4.4.**

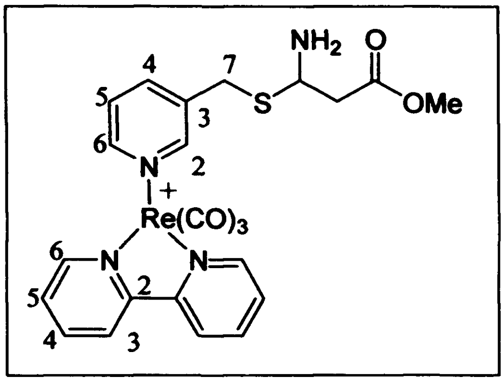

L-Cystine methyl ester (59 mg, 0.4 mmol) was added to a de-gassed solution of **5.1** (50 mg, 0.07 mmol) and triethylamine (0.04 ml, 0.3 mmol) in 10 ml of acetonitrile. After stirring for 1 h under a flow of nitrogen, the solvent was removed and the dark solid remaining was washed with water (2 × 2 ml) to afford **5.4** as a dark yellow solid (44 mg, 65.4 % yield), m.p. 185 °C. δH (CD_3CN) (ppm) 9.16 (2H, d, *J* = 5.3 Hz, C*H*(6) bipy), 8.28 (2H, d, *J* = 8.1 Hz, C*H*(3) bipy) 8.19 (2H, m, C*H*(4) bipy), 8.09 (1H, s, C*H*(2) Py), 8.03 (1H, d, *J* = 5.5 Hz, C*H*(6) Py), 7.70–7.75 (3H, m, C*H*(5) Py and C*H*(5) bipy), 7.18 (1H, m, C*H*(5) Py), 3.50 (2H, s, C*H2*), 3.39 (1H, m, C*H*), 2.22–2.39 (2H, m, C*H*$_2$(Cys)); δC ($CDCN_3$) (ppm) 195.3 (*C*O$_{eq.}$), 192.3 (*C*O$_{ap.}$) 155.6 (*C*(2), bipy), 153.8 (*C*(6), bipy), 151.6 (*C*(2), Py), 150.3 (*C*(6), Py), 141.0 (*C*(4), bipy), 140.1 (*C*(4), Py), 138.0 (*C*(3), Py), 128.7 (*C*(3), bipy), 126.2 (*C*(5), Py), 124.5 (*C*(5), bipy), 54.2 (*C*H), 51.5 (*C*H$_3$), 35.2 (*C*H$_2$), 32.0 (*C*H$_2$(Cys)). ν_{max} (CH_3CN): 2036, 1931 (CO). *m/z* (ESI) 653.1 $[MH]^+$ and 427.0 $[M\text{–}PF_6\text{–}PyCH_2SCH_2CH(NH_2)COOMe]^+$. Theoretical isotope pattern 651.1 (55%), 652.1 (18%), 653.1 (100%), 654.1 (29%) and 655.1 (10%), observed isotope pattern 651.1 (58%), 652.1 (16%), 653.1 (100%), 654.1 (27%) and 655.1 (9%). HRMS (ESI) calculated $[M\text{–}PF_6]^+ = 653.0863$; measured $[M - PF_6]^+ = 653.0868$.

fac-$[Re(bipy)(CO)_3PyCH_2SCH_2CH[NHCO(CH_2)_2CH(NH_2)COOH]CONHCH_2COOH]$ 4.5.

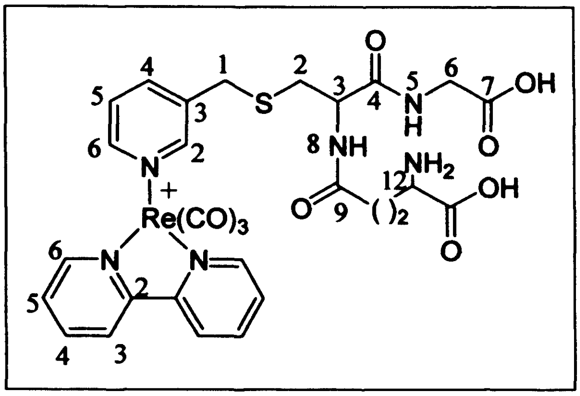

L-Glutathione (44 mg, 0.14 mmol) was added to a yellow suspension of **4.1** (50 mg, 0.07 mmol), and triethylamine (0.04 ml, 0.28 mmol) introduced in 15 ml of de-gassed methanol. Next, 3 ml of de-gassed water was added to the suspension, affording a dark solution, from which a dark precipitate appeared after a few minutes of stirring at 40 °C. The mixture of solvents was removed under vacuum and the dark solid remaining was dissolved in water, from which the impurities were filtered off. The solvent was then removed, and the residue was redissolved in the smallest possible volume of water and passed through an ion exchange column (Amberlite IR120 H resin, NH_4^+ form) that had previously been washed with aqueous ammonium chloride, eluting with water. The yellow coloured fraction that eluted immediately was collected, evaporated and dried under vacuum to give **4.5** as a yellow solid (26 mg, 44 % yield), m.p. 168 °C. δH (D_2O) (ppm) 9.17 (2H, d, *J* = 5.5 Hz, C*H*(6) bipy), 8.22 (2H, d, *J* = 8.2 Hz, C*H*(3) bipy) 8.08–8.10 (4H, m, C*H*(4) bipy, C*H*(6,2) Py), 7.62–7.69 (3H, m, C*H*(4) Py, C*H*(5) bipy), 7.08 (1H, t, *J* = 7.7 Hz, C*H*(5) Py), 4.10 (1H, m, C*H*(3)), 3.62 (5H, m, PyCH_2, CH_2(2), C*H*(12)), 2.23–2.32 (4H, m, CH_2(6), CH_2(10)), 1.98 (2H, m, CH_2(11)). δC (D_2O) (ppm) 196.0 (*C*$O_{eq.}$), 192.0 (*C*$O_{ap.}$), 176.4 (4C(2*C*OOH, 2*C*ON), 174.9, 174.2, 171.6, 157.0 (*C*(2), bipy), 153.9 (*C*(6), bipy), 151.7 (*C*(2), Py)), 150.9 (*C*(6), Py), 141.2 (*C*(4), bipy), 140.3 (*C*(4), Py), 137.6 (*C*(3), Py), 128.7 (*C*(3), bipy), 126.5 (*C*(5), Py), 124.6 (*C*(5), bipy), 54.3 (*C*(6)), 52.6 (*C*(12)), 43.5 (*C*(2)), 38.9 (CH_2(glu)), 32.0 (*C*(3)), 31.6 (*C*(11)), 26.4 (*C*(10)). ν_{max} (CH_3CN): 2022, 1915, 1897 (CO). *m*/*z* (ESI) 825.1 $[MH]^+$ and 427.0 $[M{-}PF_6{-}PyCH_2SCH_2CH[NHCO(CH_2)_2CH(NH_2)COOH]CONHCH_2COOH]^+$. Theoretical isotope pattern 823.1 (54%), 824.1 (21%), 825.1 (100%), 826.1 (36%) and 827.1 (11%). Actual isotope pattern 823.1 (58%), 824.1 (20%), 825.1 (100%), 826.1 (34%) and 827.1 (12%). HRMS (ESI) calculated $[M{-}PF_6]^+$ = 823.1319; measured $[M{-}PF_6]^+$ = 823.1333.

4.8 References.

[1] E. Terpetschnig, J. D. Datterlbaum, H. Szmacinski, J. R. Lakowicz, *Anal. Biochem.* **1997**, 251, 242.

[2] F. N. Castellano, J. D. Dattelbaum, J. R. Lakowicz, *Anal. Biochem.,* **1998**, 255, 165.

[3] J. D. Dattelbaum, O. O. Abugo, J. R. Lakowicz, *Bioconjugate Chem.,* **2000**, 11, 553.

[4] J. V. Caspar, T. J. Meyer, *J. Phys. Chem.* **1983**, 87, 952.

[5] B. J. Coe, N. R. M. Curati, E. C. Fitzgerald, S. J. Coles, P. N. Horton, M. E. Light, M. B. Hursthouse, *Organometallics,* **2007**, *26,* 2318.

[6] A. J. Amoroso, R. J. Arthur, M. P. Coogan, J. B. Court, V. Fernández-Moreira, A. J. Hayes, D. Lloyd, C. Millet, S. J. A. Pope, *New J. Chem.*, **2008**, 32, 1097.

[7] H. Friebolin (Ed.), *Basic One and Two Dimensional NMR Spectroscopy,* 4th ed., Wiley-VCH, New York, **2005**.

[8] M. Hesse, H. Meier, B. Zeeh (Eds.), *Métodos Espectroscópicos en Química Orgánica,* 5th ed. Síntesis, Madrid, **1995**.

[9] K. K.-W. Lo, D. C.-M. Ng, W.-K. Hui, K.-K. Cheung, *Dalton Trans.*, **2001**, 2634.

Chapter 5

Electrochemistry, Membrane Permeability and Confocal Fluorescence Microscopy Studies.

5.1 Introduction To Electrochemistry.

5.1.1 Relevance of redox potentials in cell biology: Cyclic voltammetry.

The knowledge of the electrochemical behaviour of a metal complex can be used to provide a measure of the complex's chemical reactivity associated with redox processes, and therefore it is a quantification of the stability of the complex core and ligands in the presence of redox agents. As the MLCT process involves oxidation of metal and reduction of ligand, a knowledge of these redox potentials can help to predict the photophysics of the complexes. Additionally, a metal complex which undergoes redox changes in the range of biological redox processes could act as a sensor for the redox state of a cell. For both these reasons, an important feature when it comes to synthesising complexes to be used as biological probes is the relative values of the redox potentials of processes for the complexes compared to the redox potentials of biological reducing and oxidising agents. [1,2] An electrochemical study of the novel rhenium complexes must be therefore carried out to know if the imaging agents are stable in biological media, and consequently, to confirm their suitability to be used as luminescent cell probes.

Cyclic voltammetry is a technique that studies the electrochemical behaviour of electro-active species over a wide potential range. The method consists of cycling the potential between two electrodes which are immersed in a degassed and unstirred solution of the analysed species and an electrolyte, and measuring the resulting current. A schematic drawing showing an electrochemical cell for voltammetry is below show.

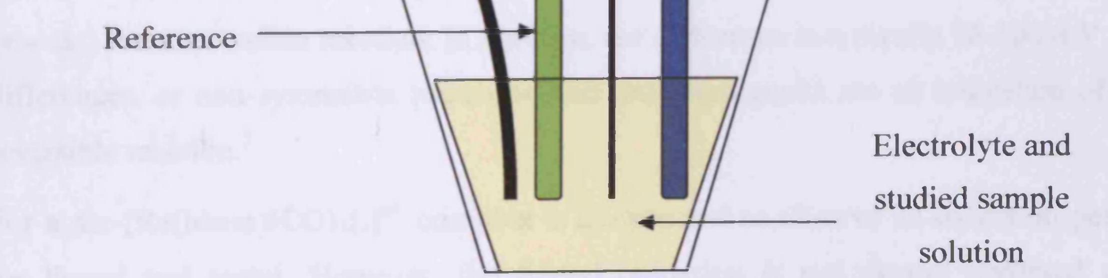

Figure 5.1. Cell for voltammetry.

· Inlet gas: inert gas to degas the solvent between each measurement.

· Reference electrode: provides a known reference potential which is insensitive to small variations of temperature or the passage of a small current within solution, *e.g.* Saturated Calomel Electrode (SCE).

· Working electrode: the electrode on which the investigated process takes place.

· Auxiliary electrode or counter electrode: completes the circuit with the working electrode.

Cyclic voltammetry is characterised by a smooth increase of a working electrode potential from one potential limit to the other and back. Both the potential limits and the potential sweep rate are the basic adjustable parameters. The current at the working electrode is then plotted versus the applied voltage to give the cyclic voltammogram trace, **Figure 5.2.**

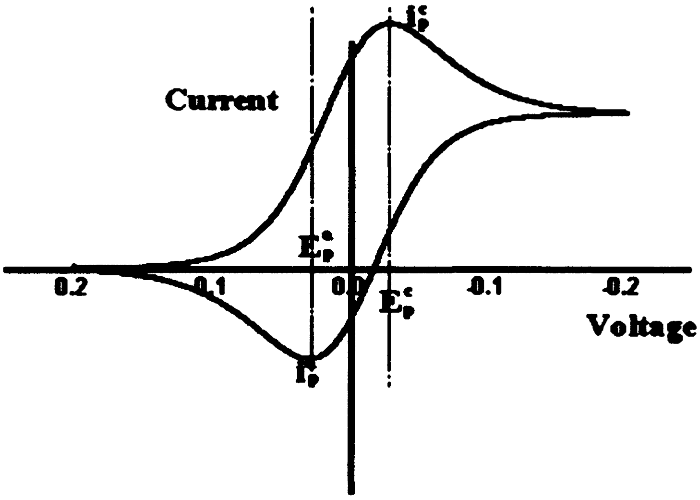

Figure 5.2. Typical cyclic voltammogram showing the important parameters: E_p^c reduction potential, E_p^a oxidation potential, I_p^c, I_p^a current intensity.

Generally there are two limiting cases for all systems, either a reversible electrode process or an irreversible electrode process. The potential difference between the reduction and oxidation peaks is theoretically 59/n mV (n: number of electron associated with the process) for a reversible reaction. In practice, the difference is typically 70-100 mV. Larger differences, or non-symmetric reduction and oxidation peaks are an indication of a non-reversible reaction.[3]

For a *fac*-$[Re(bisim)(CO)_3L]^{n+}$ complex it is expected to observe an oxidation peak both for ligand and metal. However, the ligand oxidation is not always observed as it is sometimes at too high a voltage. In the reduction wave the first peak is typically the reduction of the ligand, and sometimes reduction of the metal is also observed. The two easiest processes therefore, metal oxidation and ligand reduction, are associated with the MLCT process.

It is important to consider that in cyclic voltammetry experiments reduction gives a radical anion centred on the ligand, but the whole complex is reduced, while in the MLCT process, the ligand radical anion is formed at the same time as the metal is oxidised, so the energies of both processes are not exactly correlated. However, for a series of similar complexes a trend of variations in redox potentials should correlate with the energy of the MLCT as observed by the absorption and emission spectra.[4]

5.2 Electrochemistry Discussion

Electrochemical behaviour of the newly prepared complexes **2.9**, **3.6**, **3.10**, **3.12** and **4.1** depicted in **Figure 5.3**, as representatives of each family of compounds synthesised in this thesis, was studied.

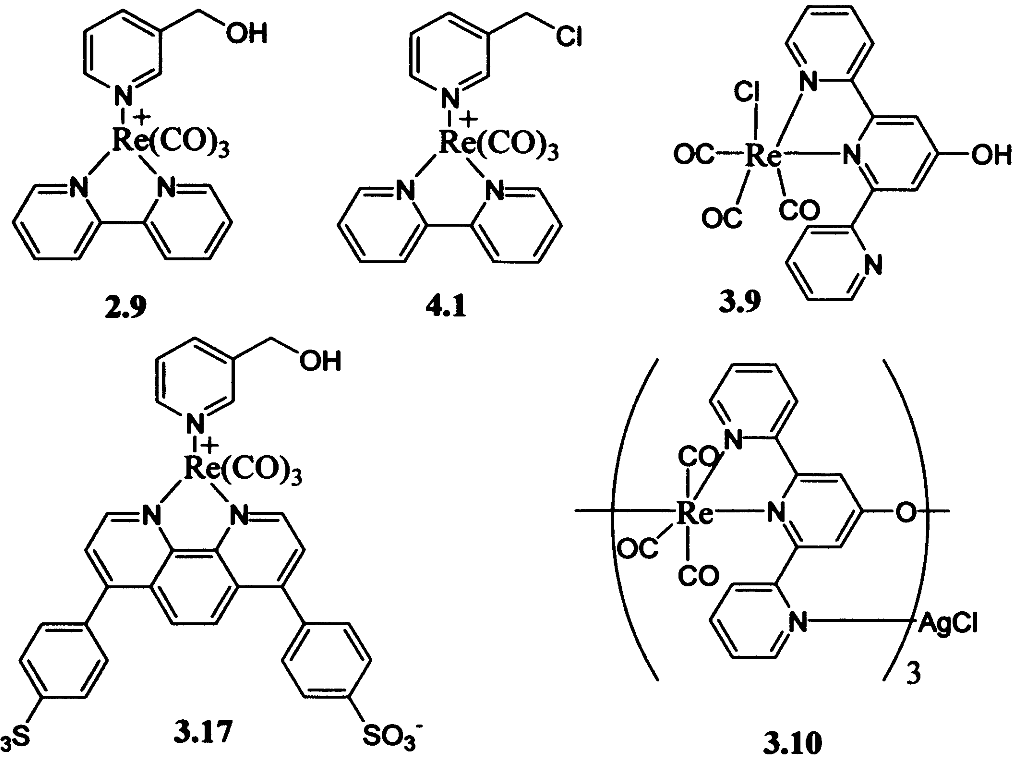

Figure 5.3. Complexes **2.9**, **3.6**, **3.10**, **3.12** and **4.1**

Each experiment was carried out in dry, deoxygenated acetonitrile solution under a nitrogen atmosphere, using tetrabutylammonium hexafluorophosphate 0.1 M as the supporting electrolyte. A glass cell with a platinum bead working electrode, a platinum wire counter electrode and a silver wire reference electrode was used as the electrochemical cell system. In addition, ferrocene was used as internal standard. The redox potentials are listed in **Table 5.1**.

Complex	Oxid. $E_{1/2}$ (V)	Red. $E_{1/2}$ (V)	Excitation λ/nm	Emission λ/nm
2.9[a,b]	0.66 1.42	-1.57 (65) -1.91	365	556
3.9[a]	0.74 1.09	-1.59	370	559
4.1[a]	1.40	-1.61 -1.95	364	551
3.17[a]	1.44	-1.44	378	563

a From cyclic voltammetry in acetonitrile/0.1 M in TBAP. Potentials are in volts vs. Fc/Fc^+ at a sweep rate of 100 mVs^{-1}. The difference between cathodic and anodic peak potentials (mV) is given in parentheses.

b Irreversible; potential is given for the cathodic wave.

Table 5.1. Redox potential values of complexes **2.9**, **3.9**, **3.17** and **4.1**.

All complexes present an irreversible oxidation between 1.09 and 1.44 V that can be associated with a metal centred oxidation, Re(I)/Re(II), as has been observed before for similar species.[5] It is worth noting that the complexes with either a bipyridine or a bathophenanthroline chelate ligand (**2.9**, **4.1** and **3.17**) have oxidation potentials at *ca.* 1.42 V, whereas for complex **3.9**, the oxidation value is 1.09 V. This is in concordance with the fact that the more extended conjugation in the chelate ligand renders the metal site less electron rich and hence decreases the ease of oxidation. The nature of the N-based axial ligand also affects the ease of metal oxidation *i.e.* the stronger the σ donor, the easier the metal oxidation. However, for the complexes **2.9** and **4.1** the oxidation potential remains practically the same (1.42 and 1.40 V respectively). Their structural difference is in the substituents on the axial ligand, 3-CH_2OH *vs.* 3-CH_2Cl respectively, with similar electronic effects over the pyridine-rhenium bond. In addition, irreversible oxidation potentials at *ca.* 0.70 V were observed in the cases of complexes **2.9** and **3.9** which might be connected to the axial ligand oxidation[6] in the case of complex **2.9**, and to the oxidation of the hydroxyl group in the chelate ligand in the case of complex **3.9**.

All the complexes studied showed a first reduction potential that could be related to the chelate ligand reduction, $NN^{0/-}$, ranging from -1.44 (in complex **3.17**) to -1.61 V (in complex **4.1**). The bathophenanthroline adduct, complex **3.17**, has the least negative reduction potentials as a consequence of greater conjugation which makes the ligand more easily reducible. A second irreversible reduction potential was observed in complexes **2.9** and **4.1**, which might be associated with the reduction of the metal, Re(I)/Re(0).[7]

It can seen from the trend of oxidation potentials in **Table 5.1** that **3.9** is the most readily oxidised, which is expected as this is a neutral complex, while the others are cations. Complexes **2.9** and **4.1** are essentially the same, which is expected as a different non-conjugated substituent in the axial position should have practically no effect. Complex **3.17** shows a slightly higher oxidation potential which can be explained as its increased conjugation lowers the unoccupied π^* levels to allow better back donation from the Re $d\pi$ orbital, and electron withdrawing $-SO_3^-$ groups also remove electron density from the metal.

The trend in reduction potentials can be explained in terms of the high conjugation and electron withdrawing effect of $-SO_3^-$ in **3.17**, giving the lowest reduction potential with the remaining complexes showing similar reduction behaviour. While complex **3.9** has a very different ligand structure to **2.9** and **4.1**, their reduction potentials are similar. Probably it is due to the fact that the extra pyridyl, which increases the resonance of the system and therefore should decrease the reduction potential, is compensated by the hydroxyl group in the chelate ligand, which is a donating group and hence should increase the reduction potential.

Doing a comparison of cyclic voltammetry with spectroscopic studies, complex **3.9** shows the lowest oxidation potential, indicating a high energy level for the metal d orbitals; as the ligand reduction potential is similar to that in the other complexes, therefore the energy gap should be smaller. Complexes **2.9** and **4.1** have practically identical oxidation and reduction potentials but **3.17** shows a slightly higher oxidation and considerably lower reduction potential, and should therefore have a lower energy MLCT band than **2.9** and **4.1.** These predictions agree qualitatively with the spectroscopic data (see **Table 5.1**) while a quantitative correlation is much more complex and would require more closely related examples.[4]

The electrochemistry of a more complex species, complex **3.10**, was also analysed, and the data are reported in **Table 5.2**. Cyclic voltammetry measurements of this species were carried out using the same conditions described before. A first irreversible oxidation is observed at 0.10 V possibly due to the silver oxidation followed by two more irreversible oxidation potentials at 1.51 and 1.89 V that might be associated with a two-step oxidation of two rhenium centres in sequence, *i.e.* Re(I, I, I)→ Re(II, I, I)→ Re(II, II, I). The fact that two oxidations are observed that might be associated with rhenium oxidation implies some kind of communication between them. If the three rhenium atoms were not communicating with each other, only one oxidation potential (the same E_{ox} value for all of them) should be observed, a three electron process. On the other hand, if they are interacting with each other, complex **3.10** should have three different oxidation potentials. Therefore a possible explanation for observing only two values, 1.27 and 1.65 V, could be that once the silver and two rheniums have been oxidised, a greater potential needs to be applied to oxidise the third rhenium atom. Since the experiment was performed using a window of -2.3 to 2.0 V, there was not sufficient potential to oxidise the third rhenium atom.

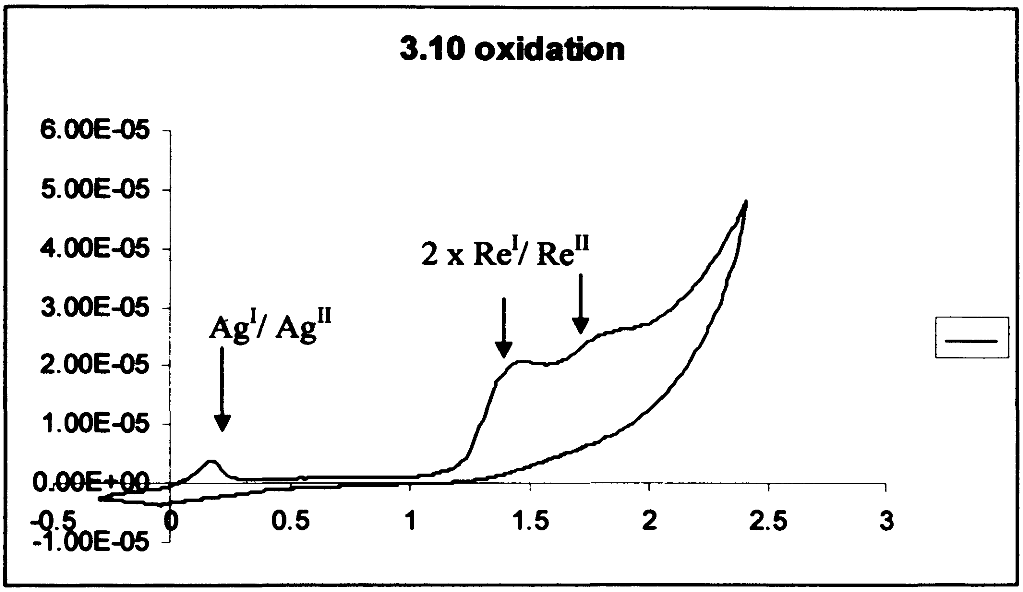

Figure 5.4. Representation of the oxidation window of complex **3.10**.

Only two values for the reduction potentials of complex **3.10** were recorded, occurring at -1.63 and -1.87 V. Comparison with the previous values obtained for complexes **2.9** and **4.1** (1.91 V and 1.95 V vs. Fc/Fc^+ respectively) suggests a possible metal-based character. The presence of two potentials might be associated with two rhenium step-wise reductions, *i.e.* Re(I, I, I)→ Re(0, I, I)→ Re(0, 0, I), again indicative of some kind of interaction between the three rhenium metal atoms in the complex. Unfortunately, only two reduction values were recorded, again probably due to the high potential needed to reduce the third metal. An alternative explanation for these two reduction potentials could be that they are just a ligand reduction and a metal reduction, *i.e.* the orbitals involved in the oxidation are better coupled than those orbitals involved in the reduction. These possible explanations need to be further analysed to reach a certain conclusion.

Complex	Oxid. $E_{1/2}$	Red. $E_{1/2}$
3.10$_a$	0.10	-1.63
	1.27	-1.87
	1.65	

a From cyclic voltammetry in acetonitrile/0.1 M in TBAP. Potentials are in volts vs. SCE at a sweep rate of 100 mV/s. The difference between cathodic and anodic peak potentials (mV) is given in parentheses.

Table 5.2. Redox potential values of complex **3.10.**

Mixed valence complexes can be divided into three classes depending on the degree of interaction between the metal centres (Robin and Day classification).[8] Class 1 are those complexes where there is no interaction between the metal centres. Class 3 are those where electronic charge is completely delocalised along the complex. Finally, Class 2 includes complexes where some communication between the metal centres is observed. This category contains the largest number of mixed valence complexes and is probably where complex **3.10** fits.

The comproportionation constant, a measure of the thermodynamic stability of the first oxidation product, indicates the nature of communication between the metal centres and is calculated from the equation shown below in **Equation 5.1**.

F: Faraday constant, $9.6584 \cdot 10^4 \mathrm{J\,mol^{-1}}$

R: $8.314\ \mathrm{J\,K^{-1}\,mol^{-1}}$

$$K_c = \exp \frac{(\Delta E)\,F}{R\,T}$$

T: 298 K

Equation 5.1. Equation of comproportionation constant.

If complex **3.10** does undergo step-wise oxidation and reduction processes, the calculated comproportionation constant using the equation presented in **Figure 5.5** would be $1.1 \cdot 10^4$ for the reduction and $2.7 \cdot 10^6$ for the oxidation. This would indicate that the mixed valence of the tetranuclear complex is more stable than the isovalent forms[a] and therefore there is communication between the metal centres. Comparing these values with those reported in the literature for similar rhenium complexes[9] or analogous ruthenium complexes,[10] emphasise the necessity of further studies to verify that such communication between the metal centres is taking place.

---

[a] The isovalent form in a statistical equilibrium would have a comproportionation constant of <4.

$\Delta E_{red} = 0.24$ V $\Rightarrow$ $K_c = 1.1 \cdot 10^4$

$\Delta E_{ox} = 0.38$ V $\Rightarrow$ $K_c = 2.7 \cdot 10^6$

5.3 Electrochemistry Conclusions.

The electrochemical properties of a variety of rhenium complexes of the type $[Re(bisim)(CO)_3L]^{n+}$, where bisim represents a bisimine derivative, *i.e.* bipyridine, phenanthroline or derivatives, and L is either a pyridine derivative (n = 1) or chloride (n = 0), were studied. All of them showed an irreversible oxidation as well as in the case of complex **2.9** and **4.1** an irreversible reduction of the metal centre. However, no redox trends were found in any redox processes associated with the ligand.

Examination of the tetrametallic species **3.10** showed possible two-step reduction and oxidation sequences. Its calculated high comproportionation constant (compared with those found in the literature)[9, 10] encourages further studies in order to examine the possible use of this tetrametallic species as a redox sensor or molecular wire.

5.4 Membrane Permeability

An obvious requisite for cellular imaging is that the luminescent probe must be membrane permeable unless it is to enter the cell by an active transport process. The lipophilicities of the complexes can be assayed by their interactions with liposomes, lipid bilayer vesicles which are often used as models for cell membranes.[11] A variety of different experiments can be performed to study the ability of luminescent probes to penetrate cell membranes. *Method 1* first encapsulates the complex to be studied, then, after chromatographic separation from the initial solution, a solution of a non-membrane permeable quencher is added to the liposomes. *Method 2* uses the opposite approach where the non-membrane permeable quencher is encapsulated in liposomes followed by addition of the luminescent probe, see **Figure 5.5.** In both cases, any interaction between the solutes will lead to differences in luminescence. This assesses the grade of permeability of the luminescent probe, as encapsulation ensures that only in membrane-permeable solutes will such an interaction occur.

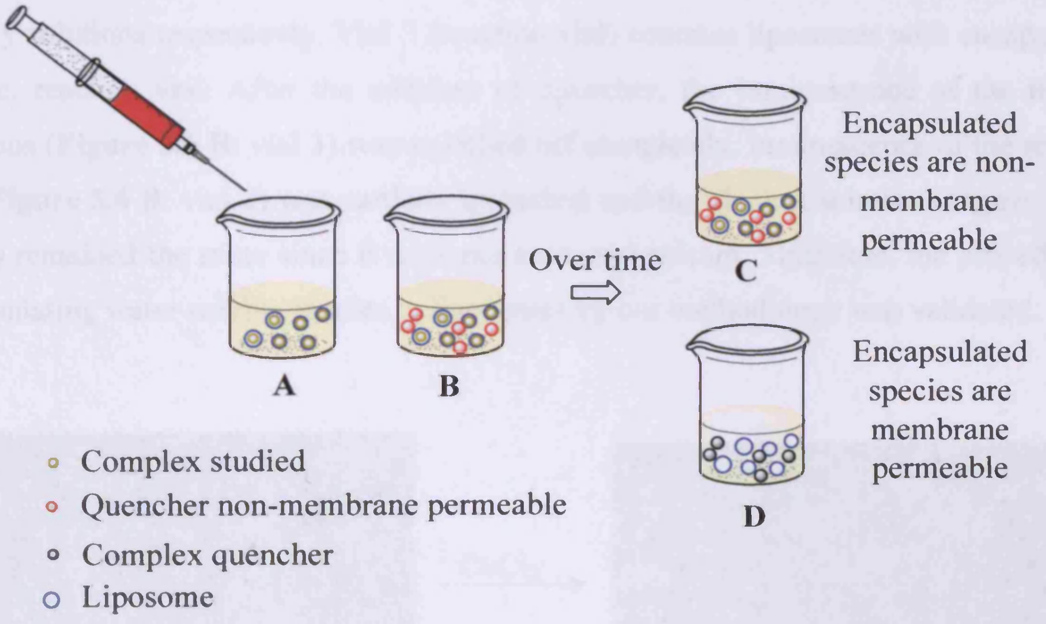

Figure 5.5. Illustration of a quenching experiment to test the permeability of the species encapsulated in the liposomes following *Method 1.*

5.4.1 Encapsulation of calceine.

Prior to the study of the cell permeability behaviour of the novel, water soluble, rhenium complexes, a test experiment was done in order to validate the formation of liposomes and the quenching experiments. Following a procedure from the literature,[12] an encapsulation experiment was performed using calcein (a well known fluorescent, non-membrane permeable species) as the encapsulated solute and cobalt (II) chloride as the quencher. The experiment consisted of forming liposomes with calcein encapsulated within the inner compartment (see **Section 5.5.1** for liposome generation), by adding a calcein solution at the lipid hydration stage. At this point, examination of the liposome sample under a UV lamp corroborated the presence of calcein in the sample. This, however did not indicate whether the liposome formation has been successful. Subsequent addition of a cobalt chloride solution only partially quenched the observed luminescence demonstrating the success of the encapsulation experiment and thus, the formation of liposomes. In the absence of liposomes, all of the luminescence would be quenched, as it is only by the physical separation of calcein and cobalt (II) ions by the liposome membrane that total quenching is avoided.

As can be seen in **Figure 5.6** solutions of liposomes without calcein (**Figure 5.6 A**: vial 1) and calcein in a liposome-free buffer (**Figure 5.6 A**: vial 3) were used as blank-x and blank-y solutions respectively. Vial 2 (reaction vial) contains liposomes with encapsulated calcine, reaction vial. After the addition of quencher, the luminescence of the blank-y solutions (**Figure 5.6 B**: vial 3) was switched off completely, luminescence of the reaction vial (**Figure 5.6 B**: vial 2) was partially quenched and the blank-x solution (**Figure 5.6 B**: vial 1) remained the same since it does not have any calcein. Therefore, the procedure of encapsulating water soluble species in liposomes by our methodology was validated.

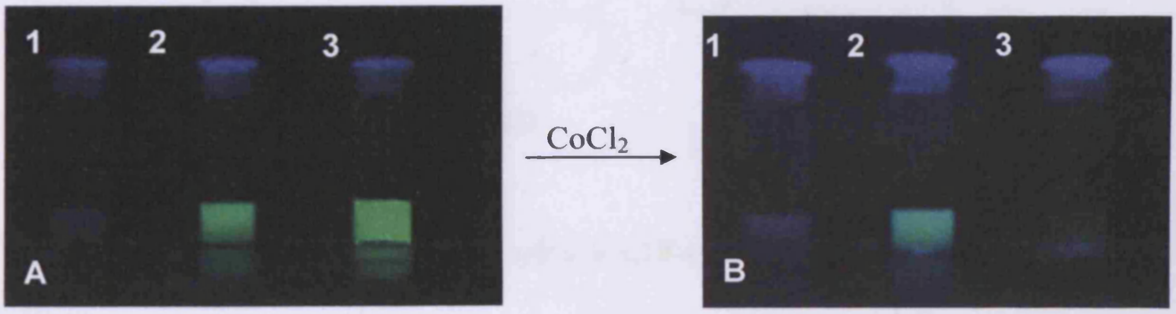

Figure 5.6 (**1**)-liposomes without calcein, (**2**)-liposomes with encapsulated calcein and (**3**)-buffer solution with calcein. Left picture (**A**): before addition of the quencher, right picture (**B**): after addition of the quencher.

5.4.2 Encapsulation of water soluble species with an internal standard.

Liposomes encapsulating the novel water soluble rhenium complexes **3.17** and **3.19** were generated in order to address the relative lipophilicity of these species, their affinity for lipid or aqueous phases (i.e. their partition behaviour between water and membrane) and their permeability through the lipid bilayer. An impermeable internal standard (bathophenanthroline) was also encapsulated in order to facilitate the recognition of changes in the observed luminescence after the addition of quencher, **Figure 5.7**. The procedure followed was similar to that already described (see **Section 5.4.1**) for the encapsulation of calcein, except for the fact that this time the liposomes were passed though a GPC column (Sepharose 4B, see liposome generation in **Section 5.5.2**) to ensure that all the luminescence observed comes from the encapsulated species. Unfortunately, luminescent measurements did not shown any emission from the MLCT states, suggesting that either all the species are membrane permeable, so that there is an extremely low concentration of the dye in the liposome, or that the luminescence of the internal standard obscured the MLCT emission, or possibly that it acted as a quencher.

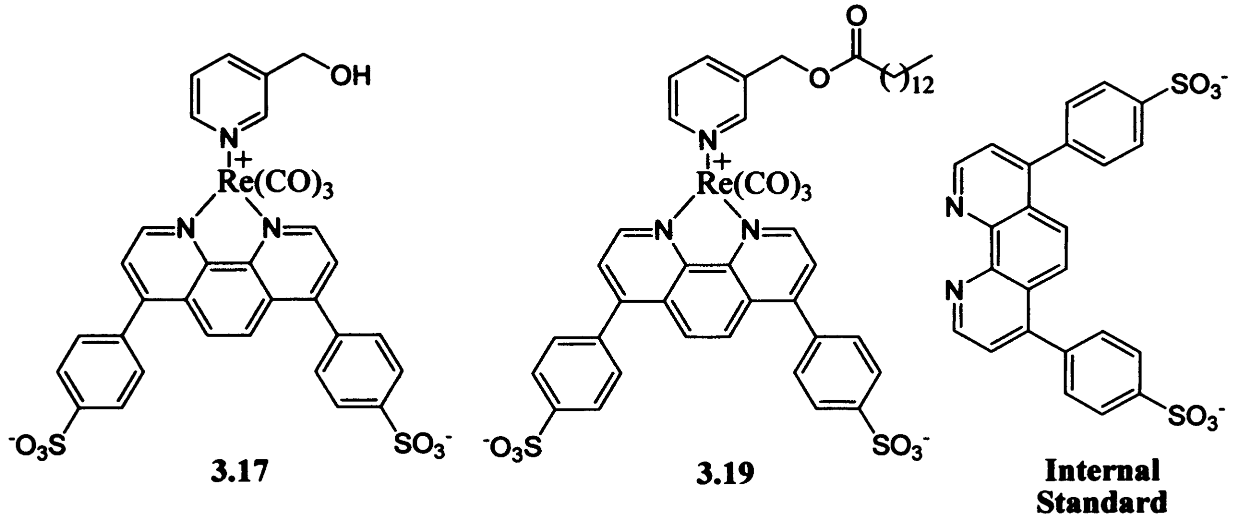

Figure 5.7. Chemical structure of complexes **3.17** and **3.19** and the internal standard.

5.4.3 Encapsulation of luminescent rhenium species and the study of their behaviour in the presence of quenchers.

The complexes examined were two anionic water soluble complexes, **3.17** and **3.19**, and a cationic lipophilic species, **2.9**, **Figure 5.8.** The same procedure was followed to generate the liposomes encapsulating these species (see experimental discussion in **Section 5.4.2**), except for the generation of liposomes with compound **2.9**. The non-water soluble species **2.9** was mixed with the phospholipids in chloroform at the solubilisation stage. In addition, the concentration of the different dyes in the bulk phospholipid solution as increased from $9{\cdot}10^{-9}$ to $2{\cdot}10^{-7}$ mM in order to avoid non-detectable luminescence. Also no internal standard was added.

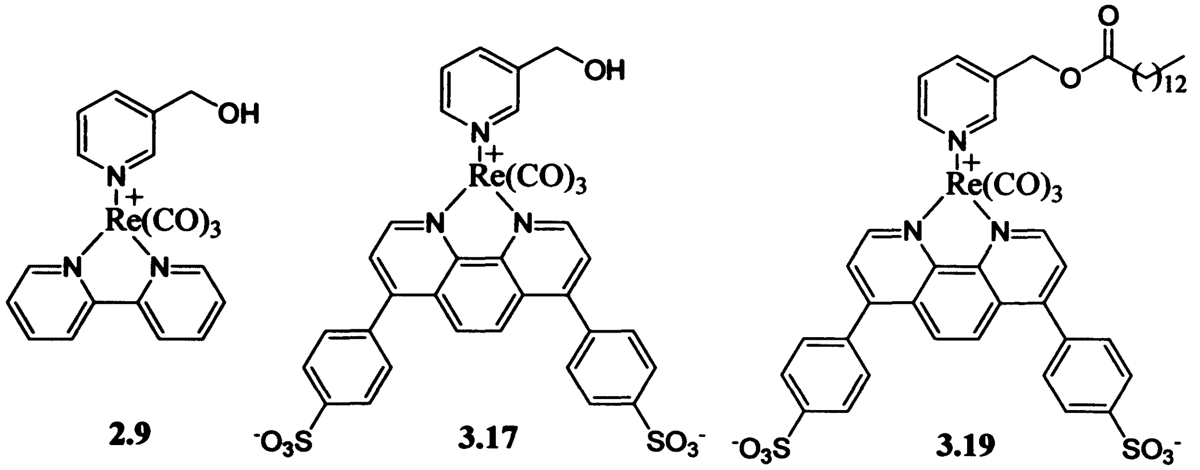

2.9 **3.17** **3.19**

Figure 5.8. Chemical structure of complexes **2.9**, **3.17** and **3.19**.

Examination of the emission of the 3 aliquots showed that the encapsulation experiment was successful, as the samples′ luminescence remained after the liposomes had been passed though a GPC column in order to wash the outside of the vesicle (see liposome generation in **Section 5.5.2** for understanding the vesicle cleaning process). Then, an aqueous solution of $CoCl_2$ (10 µl, 10 mM) as added to the liposomes encapsulating **3.19**. Measurement of the MLCT emission over time showed a strange trend especially at the first stages of the quenching process, **Figure 5.9**. Initially only small changes were observed which are assigned to experimental error; then only more than one hour after the addition of Co(II) a progressive quenching of the MLCT emission was observed. It would seem unlikely that a membrane permeability process would have an initial delay, and thus it is possible that processes other than permeation followed by quenching (maybe lipidic bilayer hydrolysis processes due to the presence of $CoCl_2$, a Lewis acid) are responsible for these results.

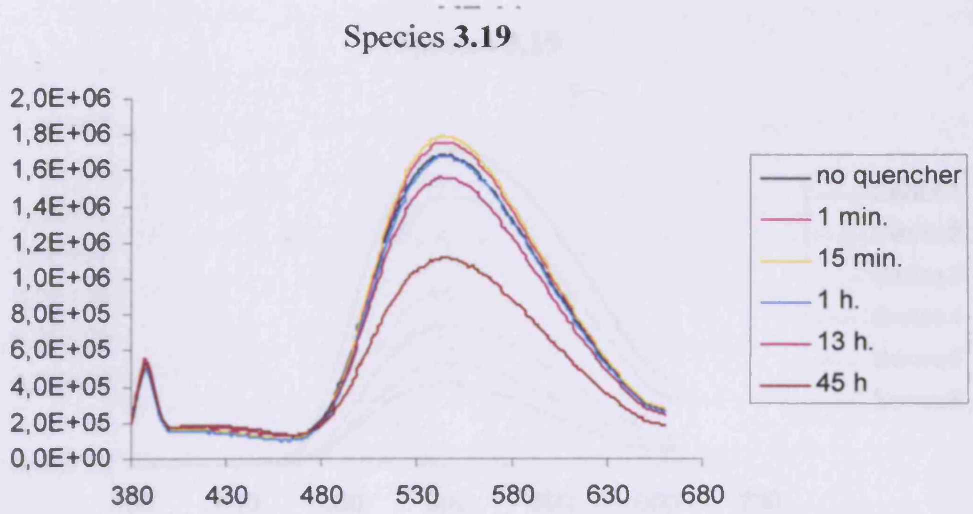

Figure 5.9. Variation with time of the emission spectra of liposomes encapsulating complex **3.19** before and after $CoCl_2$ addition.

These ambiguous results cast doubt on the effectiveness of using $CoCl_2$ as a quencher to switch off the MLCT emission of rhenium complexes, which had been anticipated by analogy with the similar $[Ru(bipy)_3]^{2+}$ MLCT process.[13,14] Therefore, 30 µl $CoCl_2$ 10 mM was added to a water solution of 0.18 mM of complex **3.19** or **3.17** and after demonstrating the low quenching behaviour, a range of other known water soluble quenchers of MLCT systems as tested against these complexes, such as $CoCl_2$, $CrCl_3$, $CuSO_4$, NaI (**Figure 5.10, 5.11**). Unfortunately none seemed to be an effective rhenium complex quencher since, even though a decrease in the luminescence intensity of the MLCT transition was observed, it could be due to a more diluted sample as the experiment entailed the addition of the quencher to the same liposome aliquot.

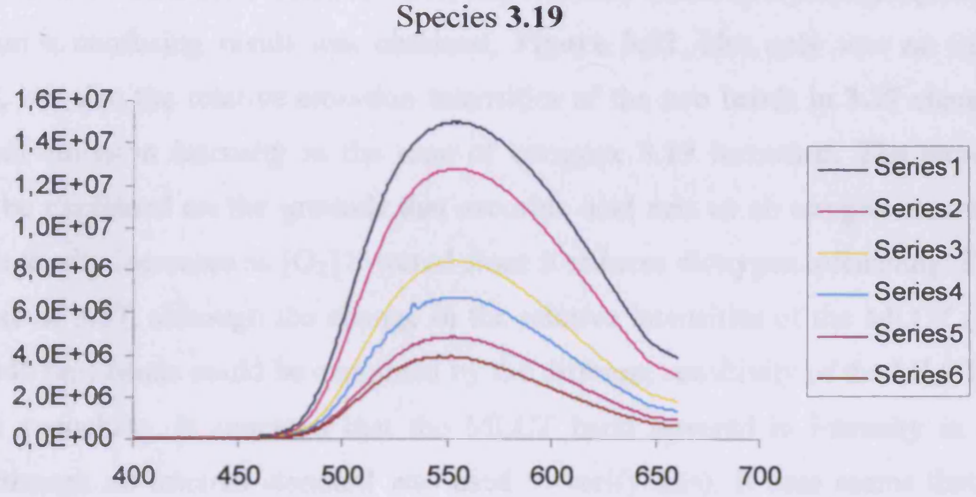

Series 1: No quencher; **Series 2**: 30 μl, 10 mM $CoCl_2$; **Series 3**: Several drops, 10 mM $CoCl_2$; **Series 4**: 30 μl, 10 mM $CrCl_3$; **Series 5**: Several drops, 10 mM $CrCl_3$; **Series 6**: Several drops, 10 mM $CuSO_4$.

Figure 5.10. Variation of the emission spectra of complex **3.19** in buffer after addition of common quenchers.

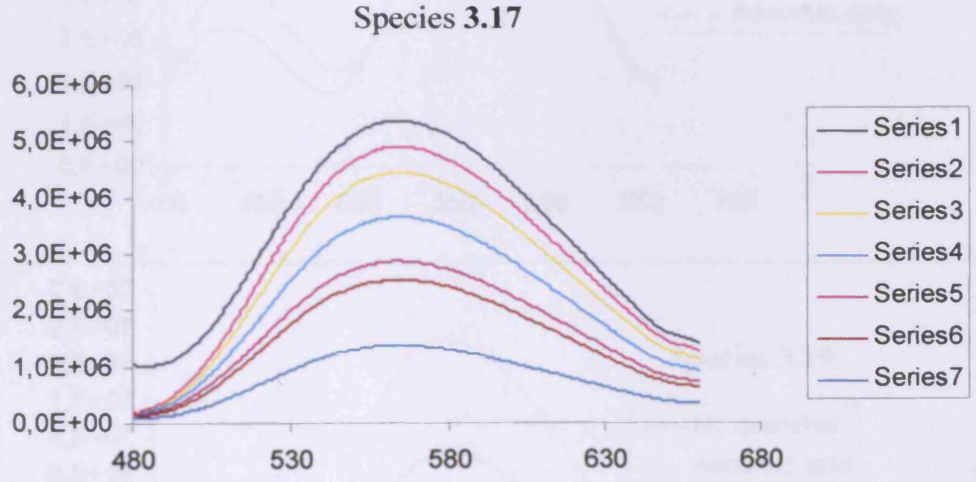

Series 1: No quencher; **Series 2**: 30 μl, 10 mM $CoCl_2$; **Series 3**: Several drops, 10 mM $CoCl_2$; **Series 4**: 100 μl, 10 mM $CrCl_3$; **Series 5**: 300 μl, 10 mM $CrCl_3$; **Series 6**: Several drops, 10 mM $CuSO_4$; **Series 7**: Several drops, 10 mM NaI.

Figure 5.11. Variation of the emission spectra of complex **3.17** in buffer after addition of common quenchers.

Ascorbic acid, a well known electron acceptor, was also tested as a possible quencher, but once again a confusing result was obtained, **Figure 5.12**. Not only was no quenching observed, but also the relative emission intensities of the two bands in **3.17** changed, and the overall emission intensity in the case of complex **3.19** increased. The increase can possibly be explained on the grounds that ascorbic acid acts as an oxygen scavenger and thus the intensity increases as [O_2] lowered since it reduces dioxygen quenching. However, in the case of **3.17**, although the change in the relative intensities of the MLCT (556 nm) and IL (440 nm) bands could be explained by the different sensitivity of the MLCT band to dioxygen quenching, it appeared that the MLCT band lowered in intensity in absolute terms (although no internal standard was used to verify this). It thus seems that there is some complex and interesting behaviour to be discovered concerning the interaction of ascorbate and Re complexes. However, for these purposes, ascorbate is not an effective quencher.

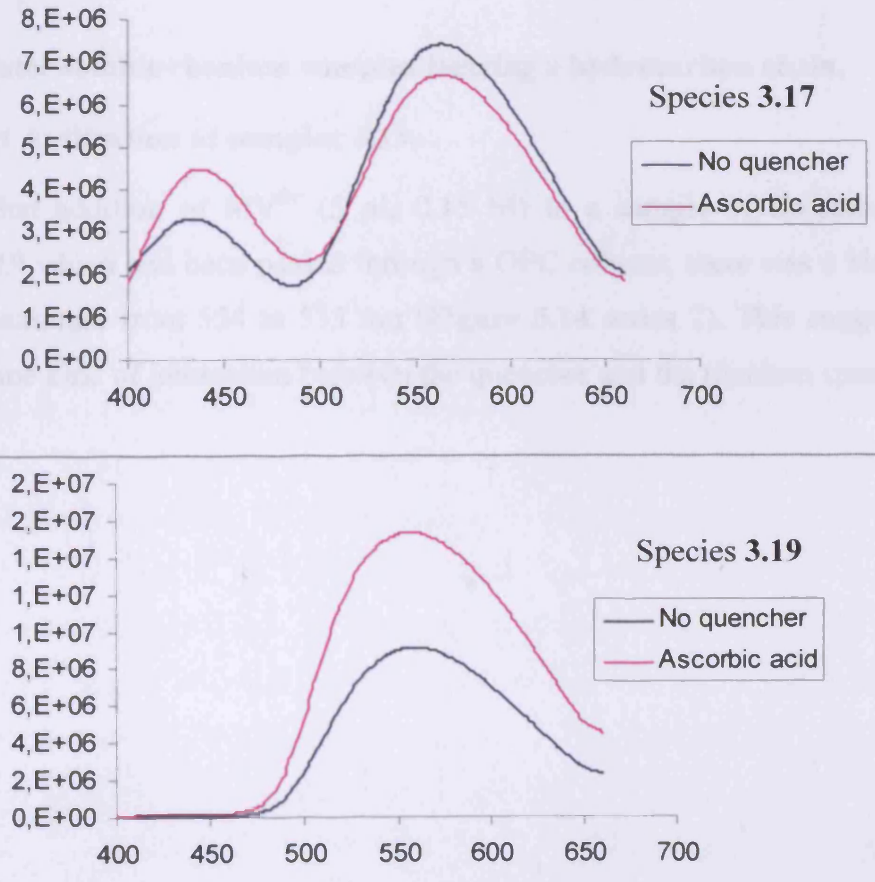

Figure 5.12. Emission spectra of complexes **3.19** and **3.17** in buffer before and after the addition of 30 µl of 10 mM solution of ascorbic acid.

5.4.4 Encapsulation of luminescent rhenium species using phospholipids: cholesterol (80:20) and the study of their behaviour in the presence of methyl viologen (MV^{2+})

After these negative results methyl viologen (MV^{2+}),[b] another potential MLCT quencher, which has been shown to efficiently quench a range of rhenium bisimine complexes, [13, 15] was tried. Although the procedures found in the literature assume methyl viologen to be a non-membrane permeable species, a mixture of cholesterol and phospholipid was used for preparation of the liposomes for these experiments. Cholesterol fills all the possible channels that form in the lipidic bilayer helping to block molecules that could fit in such channels. Cholesterol was only incorporated in a 20:80 ratio (cholesterol:phospholipid) due to the difficulty that higher percentanges of cholesterol can cause at the hydration stage. (see liposome generation in **Section 5.4.3.**)

5.4.4.1 Water soluble rhenium complex bearing a hydrocarbon chain.

Experiment A: titration of complex 3.19.

After the first addition of MV^{2+} (5 µl, 0.15 M) to a sample of liposomes containing complex **3.19** which had been passed through a GPC column, there was a blue shift of the emission maximum from 554 to 533 nm (**Figure 5.14** series 2). This suggests that there has been some kind of interaction between the quencher and the rhenium species.

---

[b] 1,1'-Dimethyl-4,4'-dipyridinium is an extensively studied molecule due to its electron acceptor properties, also known as paraquat and formerly used as herbicide.

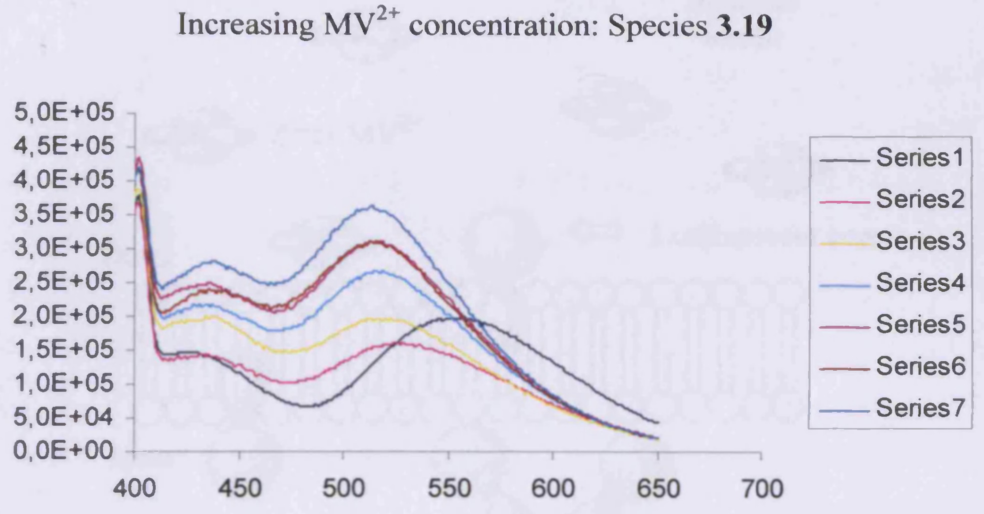

Series 1: No quencher; **Series 2**: 5 μl, MV^{2+}, 0.15 M; **Series 3**: 10 μl, MV^{2+}, 0.15 M; **Series 4**: 15 μl, MV^{2+}, 0.15 M; **Series 5**: 20 μl, MV^{2+}, 0.15 M; **Series 6:** 25 μl, MV^{2+}, 0.15 M; **Series 7**: 30 μl, MV^{2+}, 0.15 M.

Figure 5.13. Variation of the emission spectra of liposomes encapsulating complex **3.19** with an increasing concentration of MV^{2+}.

One possible explanation for this process could be that this complex, which is water soluble because of the sulphonate groups, but at the same time contains the most lipophilic unit of all the complexes studied (a C_{12} chain), might be forming part of the lipid membrane and therefore locating its luminescent core (ReBisimine) in an equal ratio either towards outside or the inner side of the liposome, allowing easy quenching of the luminescence. In addition, the species that are not part of the membrane might be distributed in the inside of the liposome close to the lipidic membrane, probably interacting with the polar heads (Me_3N^+) of the phospholipids, forming micelles in order to protect the hydrocarbon chain from the aqueous environment (**Figure 5.14**). Therefore, there might be a high concentration of rhenium complex concentrated along the lipidic membrane, and probably within the Főrster distance. As a result of this, the complex molecules might be susceptible to being quenched by the methyl viologen.

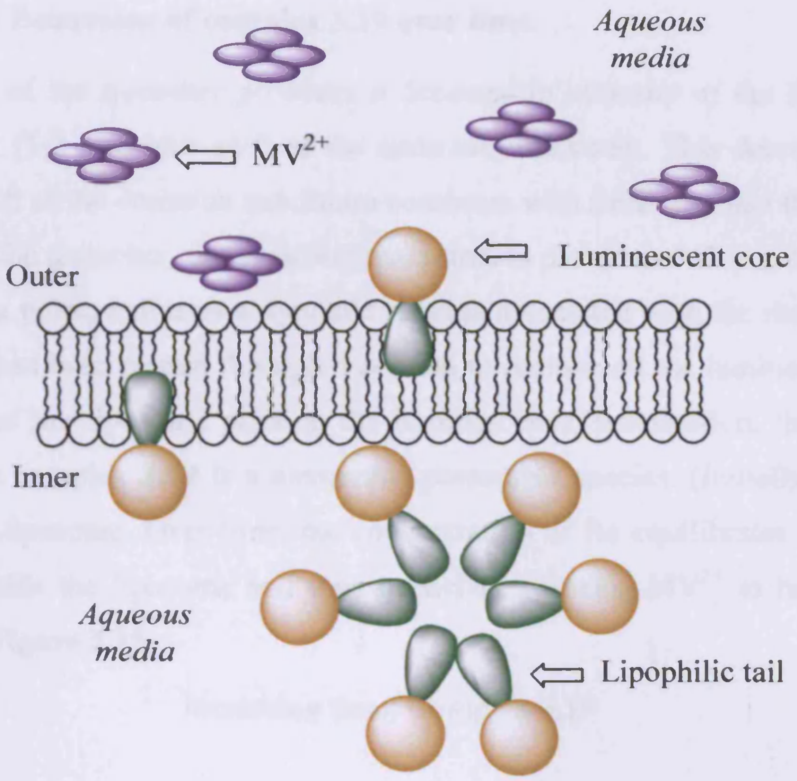

Figure 5.14. Assumed distribution of a water soluble rhenium complex bearing a long hydrocarbon chain in a liposome.

In consecutive additions of MV^{2+}, the maximum emission value reached 513 nm and it remained the same even with further addition of quencher. Since series 5, 6 and 7 (**Figure 5.15**) are essentially just the spectrum of MV^{2+}, only series 1, 2, 3 and 4 were analysed. A big but not total loss of emission was seen in the first addition, meaning that some but not all of the Re emission is quenched by MV^{2+}. Given that we know that this addition of MV^{2+} totally quenches this concentration of Re if there are no liposomes, or if the Re is rapidly membrane permeable, this indicates that some of the Re is encapsulated or not available for quenching as it is in the membrane with the luminescent core pointing toward the inner compartment. Furthermore, if no rhenium complexes were encapsulated not only would there be a total loss of emission observed, but also an immediate, not gradual, maximum emission shift to the MV^{2+} position.

It can be concluded that the lipophilic water soluble rhenium complex **3.19** might preferably be in the inner and outer membrane rather than exclusively encapsulated in the inner aqueous compartment, as it has been shown that a water soluble membrane impermeable species encapsulated in liposomes and passed through a GPC, does not lose emission upon addition of MV^{2+}.

Experiment B: Behaviour of complex 3.19 over time.

Initial addition of the quencher produces a decrease in intensity of the luminescence as well as a slight (1-2 nm) blue shift of the emission maximum. This decrease in intensity and the blue shift of the emission maximum continues with time. The fact that 3 hours after the addition of the quencher, the emission maximum is placed at 542 nm, *i.e.* 10 mn lower than the starting point, indicates a dynamic process associated with the rhenium dye **3.19.** As the sample had been passed through a column to remove all the luminescent species in the outer part of the liposome prior to the luminescence examination, this confirms the assumption that complex **3.19** is a membrane permeable species. (Initially no Re species are outside the liposome. Over time, the concentration of Re equilibrates therefore, more rhenium is outside the liposome and thus quenched allowing MV^{2+} to have a dominant emission), see **Figure 5.15**.

Increasing time: Complex **3.19**

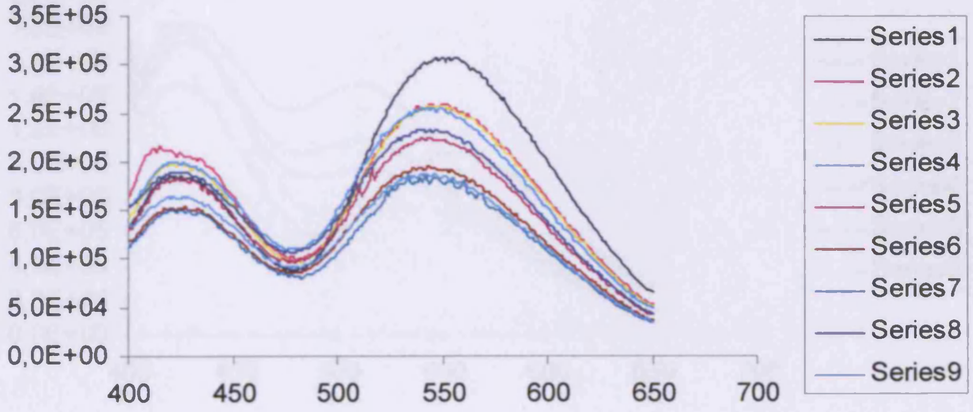

Series 1: No quencher; **Series 2**: 1 µl, MV^{2+}, 0.15 M; **Series 3**: 5 min; **Series 4**: 2 µl, MV^{2+}, 0.15 M; **Series 5**: 35 min; **Series 6:** 1h; **Series 7**: 2h, **Series 8**: 2h 40 min; **Series 9:** 3h.

Figure 5.15 Variation of the emission spectra of liposomes encapsulating complex **3.19** with the time after the addition of MV^{2+}.

5.4.4.2 Non-water soluble rhenium complex .

Experiment A: Titration of complex 2.9.

The same behaviour as that seen for **3.19** was observed for the non-water soluble species **2.9**, *i.e.* a blue shift in the emission maximum, from 554 to 536 nm, and also a drop in intensity, **Figure 5.16**. This can be rationalized by assuming that complex **2.9** is forming part of the lipidic membrane due to its hydrophobicity. It may not show as much localisation within the membrane region as predicted for **3.19** as it does not have the same polar head plus lipid chain as a membrane lipid, although it might have a preference for a lipophilic environment. Therefore an increase of quencher concentration in the outside of the liposome promoted the complete quenching of the luminescence provided by the MLCT state.

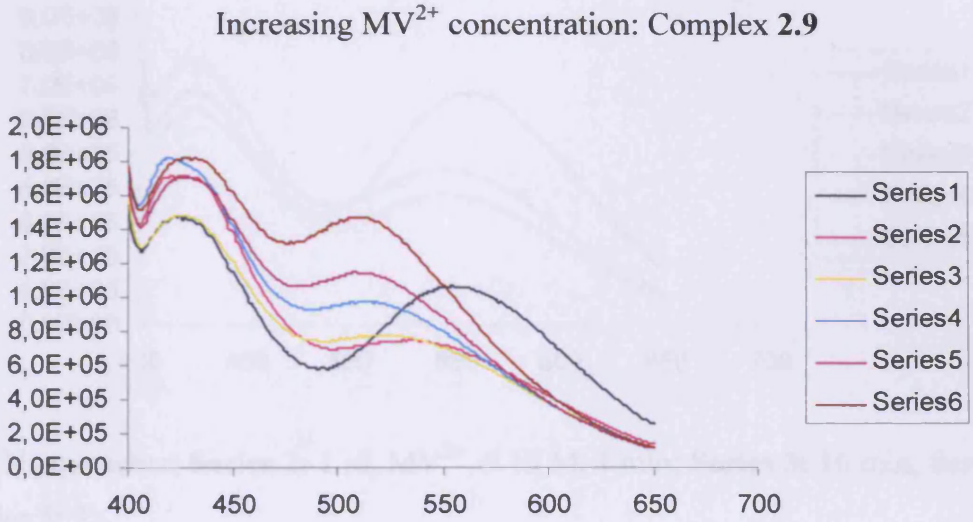

Series 1: No quencher; **Series 2**: 5 µl, MV^{2+}, 0.15 M; **Series 3**: 10 µl, MV^{2+}, 0.15 M; **Series 4**: 15 µl, MV^{2+}, 0.15 M; **Series 5**: 25 µl, MV^{2+}, 0.15 M; **Series 6:** 45 µl, MV^{2+}, 0.15 M.

Figure 5.16. Variation of the emission spectra of liposomes encapsulating complex **5** with an increasing concentration of MV^{2+}.

Experiment B: Behaviour of complex 2.9 over time.

Examination of the change in luminescence with time showed an initial blue shift of the emission maximum from 558 to 546 nm and a large drop in intensity. Over the following three hours, a progressively smaller decay in luminescence intensity accompanied by a slight blue shift to 543 nm was observed (**Figure 5.17**). Once again, these changes suggested the possibility of membrane permeability of the rhenium complex as any change over time indicates a mixing of the MV^{2+} and Re phases, which, given that MV^{2+} is known to be membrane impermeable, implies some permeation of Re from the inner compartment to the outer compartment or membrane. Although **2.9** has low water solubility, a very small quantity could have partitioned into the inner aqueous compartment, and it is presumably the subsequent transport of this portion into a region which is subjected to quenching which is responsible for the small but definite decay in luminescence intensity.

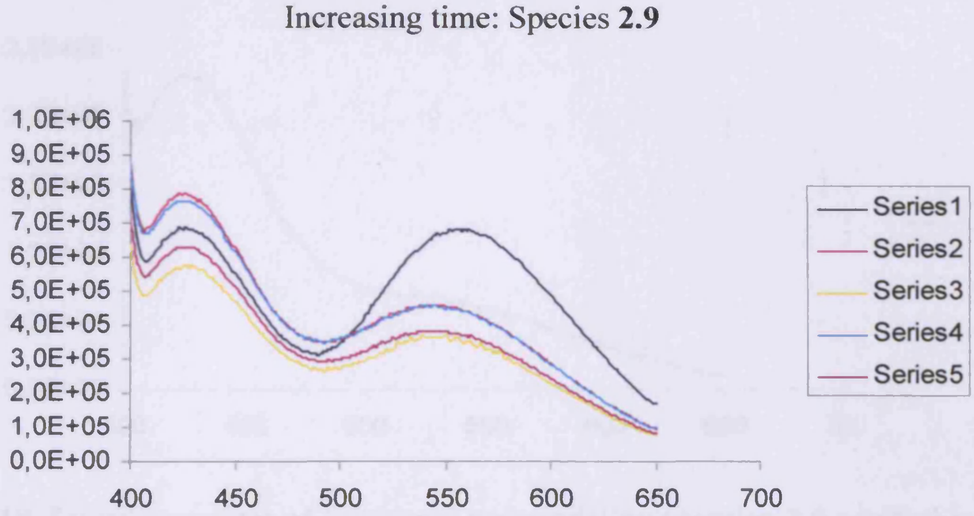

Series 1: No quencher; **Series 2:** 1 μl, MV^{2+}, 0.15 M, 1 min; **Series 3:** 10 min; **Series 4:** 2h min; **Series 5:** 3h.

Figure 5.17. Variation of the emission spectra of liposomes encapsulating complex **2.9** with the time after the addition of MV^{2+}.

Experiment C: Luminescent examination after 48 hours of liposome preparation.

The luminescence of liposomes encapsulating complex **2.9** was examined 48 hours after their generation and dilution with a NaCl buffer solution 0.15 M, see experimental **Section 5.5.2.** This delay time allows the equilibration of the concentration of the encapsulated dye between the outside and inside of the liposome, in case the encapsulated species is membrane permeable. Prior to the measurement, the sample was passed through a GPC column in order to remove any luminescent species which were not encapsulated in the interior compartment or in the liposome membrane. The spectrum obtained showed that there is still MLCT emission but its intensity is much lower than in the previous experiment, see **Figure 5.18.** and compared to **Figure 5.16** or **5.17** (**Series 1**: No quencher), demonstrating the loss of luminescent species, and therefore membrane permeability. *N.B.* the concentration of the sample used for this experiment is similar to the concentration used in previous experiments (5 mM lipidic membrane, 0.045 mM rhenium species). The same treatment of the sample was done when it came to passing it for a second time through a GPC column, see experimental **Section 5.4.3.**

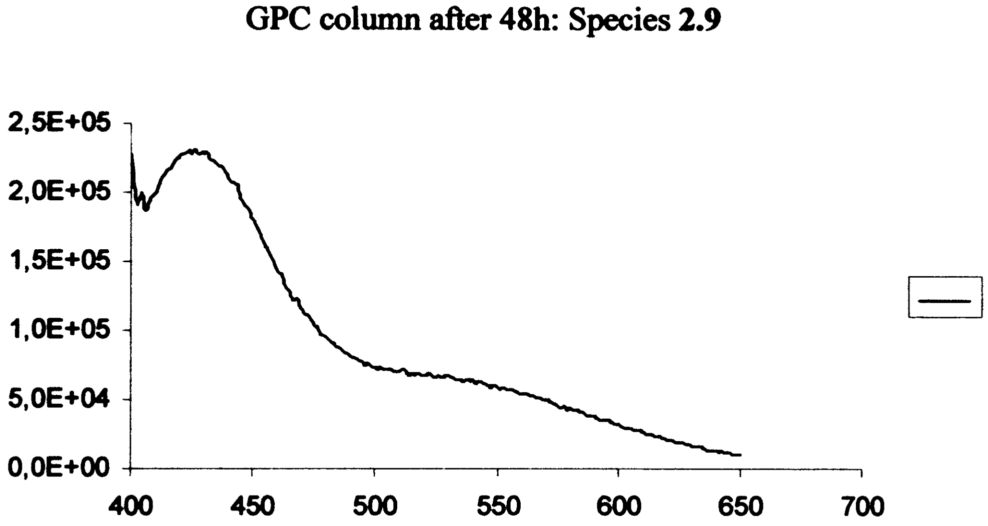
GPC column after 48h: Species **2.9**

Figure 5.18. Emission spectra of liposomes encapsulating complex **2.9** purified on a GPC column 48 hours after being formed.

5.4.4.3 Water soluble rhenium complex.

Experiment A: titration of complex 3.17.

The behaviour of the water soluble complex **3.17** when it was treated with increasing amounts of quencher was completely different from that observed for complexes **3.19** and **2.9** (compare **Figure 5.19** with **Figure 5.13** and **5.16**). These results are highly significant as **3.17**, a highly polar, charged, anionic species was presumed to be membrane impermeable, and thus its behaviour allows confirmation of some of the assumptions made in the discussion of the results for **3.19** and **2.9**. Initial additions of quencher, up to 50 μl, did not affect the emission maximum band as in previous cases and the decrease in the intensity is barely appreciable. This is presumably a result of the slight dilution of the sample and the inner filter effect, as the excitation wavelength (350 nm) is absorbed by

MV^{2+} and thus the intensity of excitation is decreased. It is worth remembering that complex **2.9** and complex **3.19** underwent a blue shift from 554 to 536 ppm and from 554 to 527 ppm respectively after the addition of the first 5 µl of quencher. This time, 500 µl of MV^{2+} was needed in order to obtain a noticeable maximum emission shift, 570 to 525 ppm, indicative of the lipophobicity of the complex **3.17**. As a consequence, the water soluble species **3.17** is assumed to be dispersed in the interior of the aqueous compartment of the liposome and not in contact with the lipidic bilayer (**Figure 5.20**). In this case, there is no possibility of collisional quenching as the complex is separated from MV^{2+} by the membrane, and additionally this assumption avoids any possible quenching process by FRET as the Förster distance would be smaller than the real distance between the quencher and the complex.

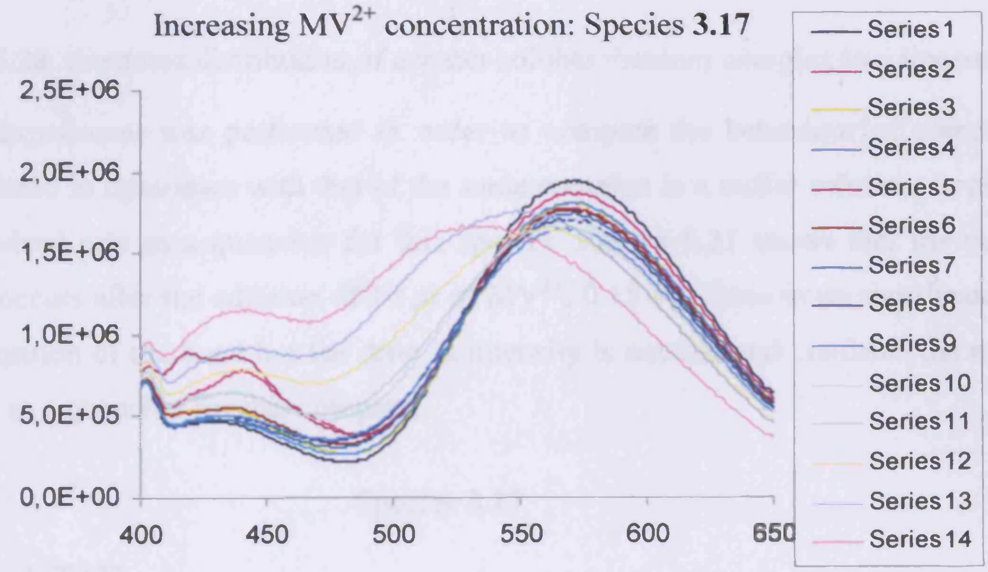

Series 1: No quencher; **Series 2**: 5 µl, MV^{2+}, 0.15 M; **Series 3**: 10 µl, MV^{2+}, 0.15 M; **Series 4**: 15 µl, MV^{2+}, 0.15 M; **Series 5**: 20 µl, MV^{2+}, 0.15 M; **Series 6:** 25 µl, MV^{2+}, 0.15 M; **Series 7**: 30 µl, MV^{2+}, 0.15 M; **Series 8**: 40 µl, MV^{2+}, 0.15 M; **Series 9**: 50 µl, MV^{2+}, 0.15 M; **Series 10**: 70 µl, MV^{2+}, 0.15 M; **Series 11:** 100 µl, MV^{2+}, 0.15 M. **Series 12**: 200 µl, MV^{2+}, 0.15 M; **Series 13**: 300 µl, MV^{2+}, 0.15 M; **Series 14**: 500 µl, MV^{2+}, 0.15 M.

Figure 5.19. Variation of the emission spectra of liposomes encapsulating complex **3.17** with an increasing concentration of MV^{2+}.

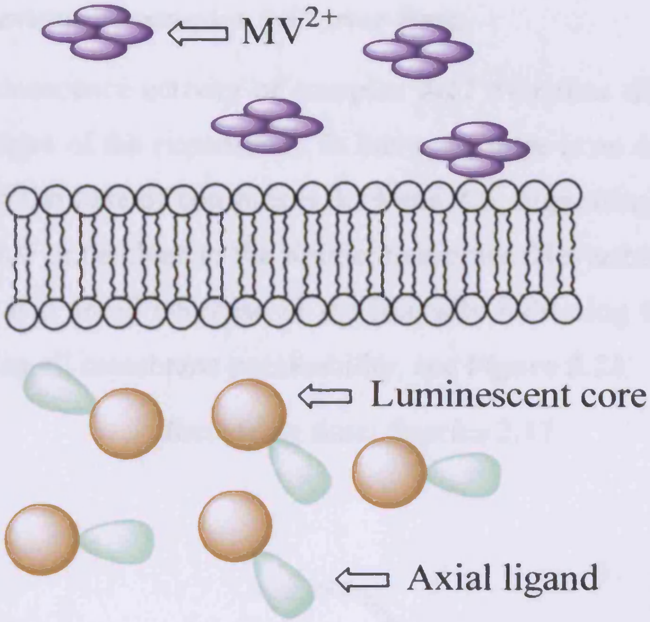

Figure 5.20. Assumed distribution of a water soluble rhenium complex in a liposome.

A new experiment was performed in order to compare the behaviour of complex **3.17** encapsulated in liposomes with that of the same complex in a buffer solution, to prove that MV^{2+} indeed acts as a quencher for this species. **Figure 5.21** shows that the quenching process occurs after the addition of 10 μl of MV^{2+}, 0.15 M. There is no significant change in the position of the band but the drop in intensity is notable and confirms the efficiency of MV^{2+} as a quencher for this complex.

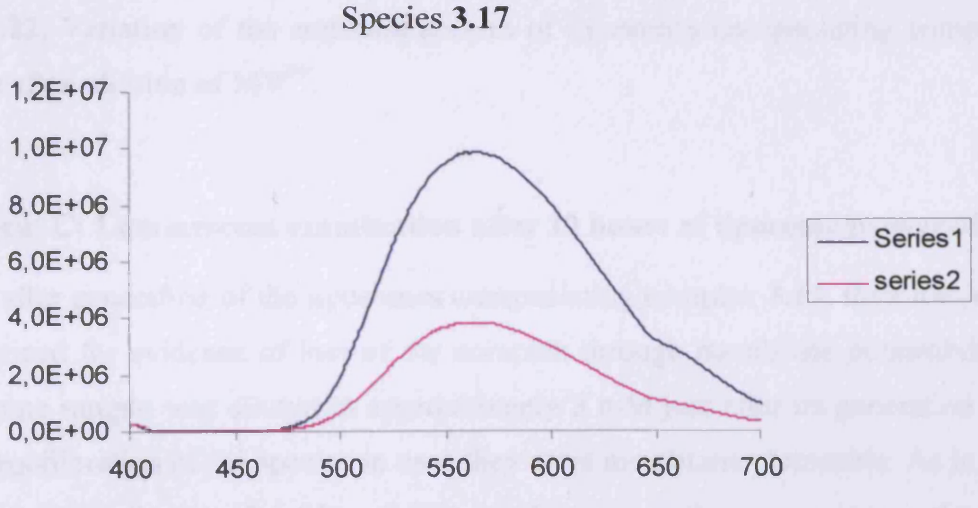

Series 1: No quencher; **Series 2**: 10 μl, MV^{2+}, 0.15 M.

Figure 5.21. Variation of the emission spectra of complex **3.17** in buffer after the addition of 10 μl, MV^{2+}, 0.15 M.

Experiment B: Behaviour of complex 3.17 over time.

The variation in luminescence activity of complex **3.17** over time differs from those seen so far at the initial stages of the experiment. In this case, there is no drop of intensity in the MLCT emission as in the case of complexes **3.19** and **2.9**, suggesting again, that these two complexes might reside or be close to the lipidic membrane. Nevertheless, after three hours of experiment, there is a small decrease in the intensity indicating that the water soluble species retains some small membrane permeability, see **Figure 5.22**.

Increasing time: Species **3.17**

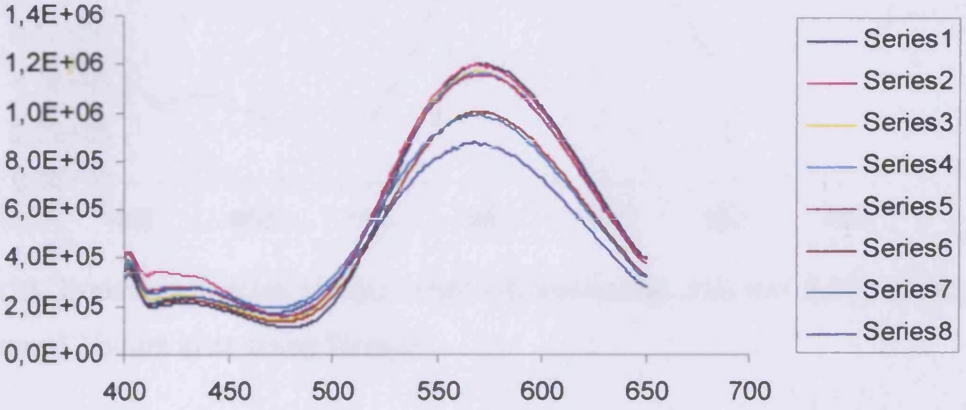

Series 1: No quencher; **Series 2**: 1 μl, MV^{2+}, 0.15 M; **Series 3**: 15 min; **Series 4**: 45 min.; **Series 5**: 1 h 40 min ; **Series 6:** 3 h; **Series 7**: 10 μl, MV^{2+}, 0.15 M; **Series 8**: 4 h 15 min.

Figure 5.22. Variation of the emission spectra of liposomes encapsulating complex **3.17** with time after addition of MV^{2+}.

Experiment C: Luminescent examination after 12 hours of liposome preparation.

12 hours after generation of the liposomes encapsulating complex **3.17**, their luminescence was examined for evidence of loss of the complex through membrane permeability, *N.B.* the liposome sample was diluted to approximately 5 mM just after its generation in order to allow equilibration of the species in case they were membrane permeable. As in the case of **2.9** above (see **Section 5.4.4.2**, experiment C), prior to the measurement, the solution was passed through a GPC column to eliminate external species. The spectrum obtained showed an intense MLCT emission, see **Figure 5.23**, demonstrating the difficulty this species has in crossing the lipidic bilayer, and thus the need for a lipophilic part in any luminescent probe for cell imaging. This could be incorporated, either as a hydrocarbon

chain in the axial ligand or a lipophilic chelate ligand, *e.g.* bipyridine. Finally, the sulphonated ligands which give good water solubility, unless they are balanced with lipid chains, prevent permeation across lipid membranes.

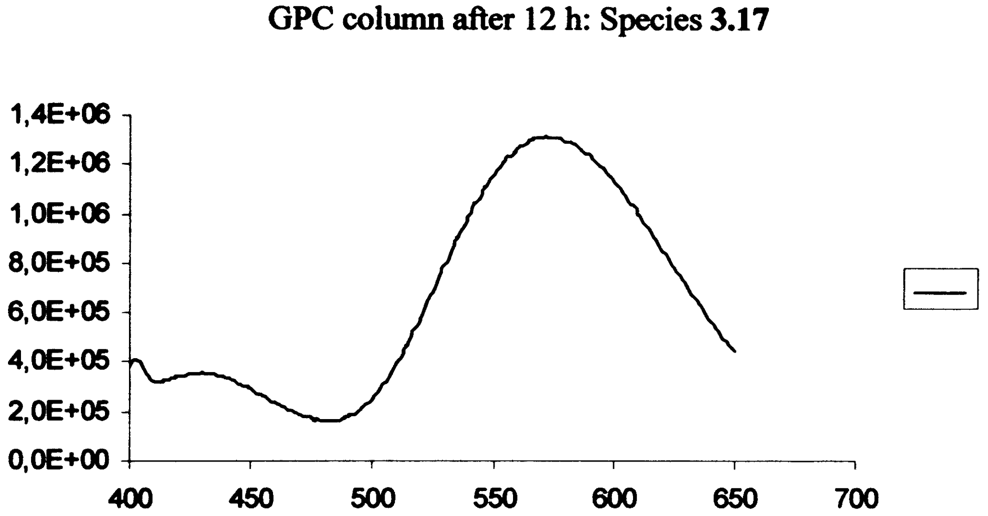

Figure 5.23. Emission spectra of liposomes encapsulating complex **3.17** washed using a GPC column 12 hours after being formed.

5.5 Experimental Procedures For Liposome Generation.

5.5.1 Experimental: Encapsulation of calceine.

Egg phosphatidylcholine (15 mg, 0.02 mmol) was dissolved in chloroform (1 ml). The chloroform was then removed by rotary evaporation, using an adequate spin-speed to obtain a clear film along the walls of the round bottom flask. Further evaporation under high vacuum was carried out for 1 h. The lipid was then hydrated with buffer solution (1 ml, MBSE: 0.15 M NaCl / 0.01 M Mops (pH 7) / 0.1 EDTA) and a calceine buffer solution (2 µl, 0.01 M) was added affording a yellow suspension which was homogenised after further stirring. The solution underwent ten cycles of freezing in a mixture of liquid nitrogen and ethyl acetate and thawing (5 min in frozen solution + 5 min in a warm water bath + 5 min in 50-60°C water bath with high speed stirring) to ensure an equilibration between the trapped and bulk solutions. The initially formed multilamellar vesicles (LMV) were extruded eleven times through a polycarbonate filter (400 nm diameter) using a liposofast pneumatic actuator affording unilamellar vesicles (SUV), see **Figure 5.24**.

a)

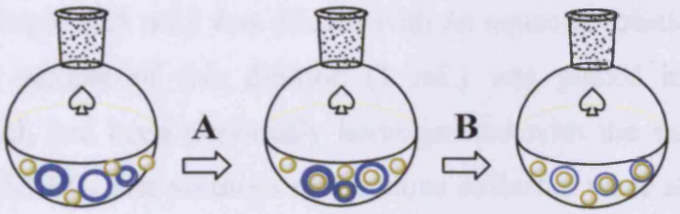

A- Hydration process: the solutes get equilibrated

B- Extrusion process: the LMV are extruded through a polycarbonate filter and SUV are generated

b)

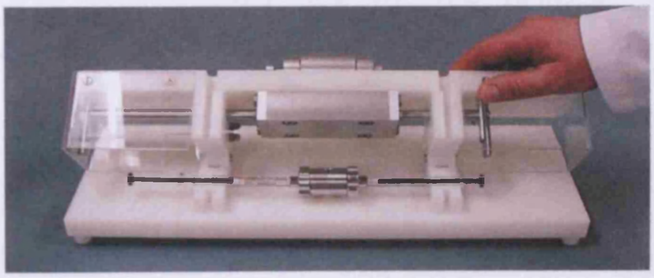

Figure 5.24. a) Illustration of liposome generation, and **b)** the pneumatic liposofast actuator used to convert LMV to SUV.

5.5.2 Experimental: Encapsulation of water soluble species with an internal standard.

The same procedure was followed in each case. Egg phosphatidylcholine (15 mg, 0.02 mmol) was dissolved in chloroform (1 ml). The chloroform was then removed by rotary evaporation, using an adequate spin-speed to obtain a clear film along the walls of the round bottom flask. Further evaporation under high vacuum was carried out for 1 h. The lipid was then hydrated with buffer solution (1 ml, MBSE: 0.15 M NaCl / 0.01 M Mops (pH 7) / 0.1 EDTA) and a bathophenanthroline buffer solution (1 μL, 0.18 mM) and the complex in question (5 μL, 0.18 mM) was added affording a light yellow suspension which was homogenised after further stirring in a 50 °C water bath for 1 h. The solution underwent ten cycles of freezing in a mixture of liquid nitrogen and ethyl acetate and thawing (5 min in frozen solution + 5 min in a warm water bath + 5 min in 50-60°C water bath with high speed stirring) to ensure an equilibration between the trapped and bulk solutions. The initially formed multilamellar vesicles (MLV) were extruded eleven times through a polycarbonate filter (100 nm diameter) using a liposofast pneumatic actuator. Then, a liposome sample (0.5 mL) was diluted with an aqueous solution of NaCl (1.5 mL 0.15 M). Finally a sample of this dilution (1 mL) was placed in the GPC column (Sepharose 4B) which had been previously homogenised with the same buffer (aqueous solution of NaCl, 0.15 M). The volumes of fractions collected were about 1 - 1.5 ml; the clean liposome sample is easily detectable due to its cloudiness. If the column set up is 10 cm of Sepharose in a 1.5 cm diameter column, the liposome is recovered in 4 aliquots after approximately the seventh fraction, see **Figure 5.25**.

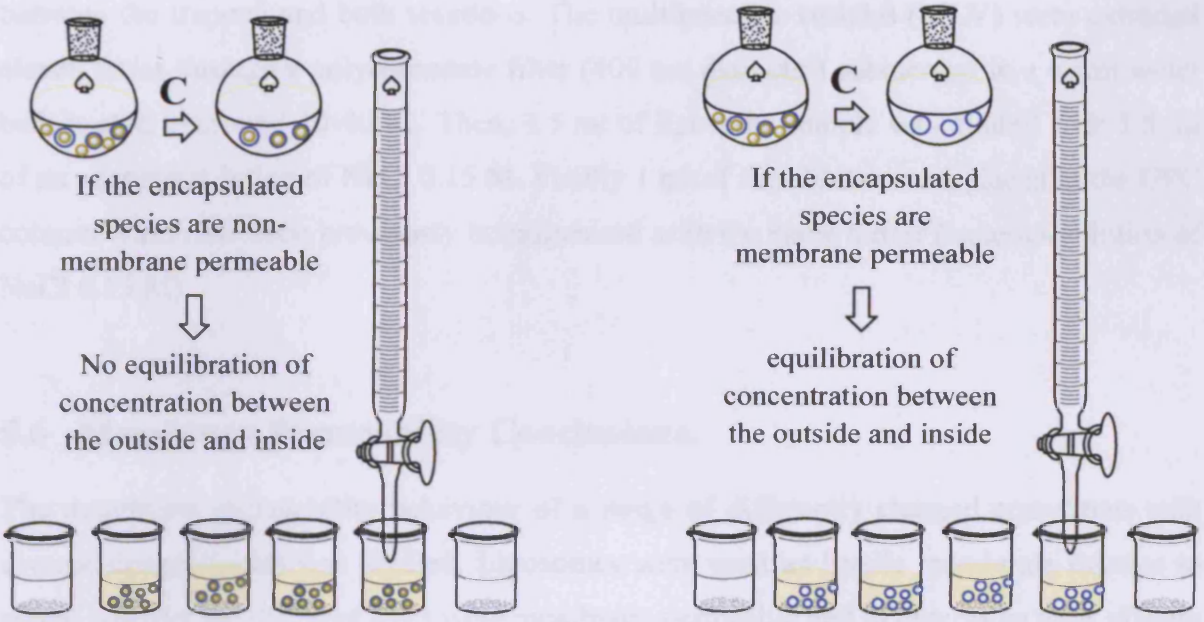

C- GPC: gel permeation chromatography differentiates the solutes by size, *i.e.* entrapping smallest size particles in their pores allowing the elution of larger particules first.

Figure 5.25. Illustration of the process of cleaning the out side liposome using a GPC column.

5.5.3 Experimental: Encapsulation of rhenium complexes in liposomes 20:80 cholesterol phospholipid respectively.

The same procedure was followed in every case except for liposomes encapsulating compound **2.9** which was mixed with the phospholipid and cholesterol at the stage of solubilizing the phospholipids in the organic solvent. Sphingoyelin from chicken egg yolk (11 mg, $16{\cdot}10^{-3}$ mmol) and cholesterol (1.5 mg, $4{\cdot}10^{-3}$ mmol) were dissolved in 1 ml of IPA. Then, the solvent was removed by rotary evaporation, using an adequate spin-speed to obtain a clear film along the walls of the round bottom flask. Further evaporation under high vacuum was carried out for 1 h. Then, the lipid was hydrated with Tris·HCl buffer solution (1 ml, 100 mM, pH 7) and the complex in question ($2{\cdot}10^{-4}$mmol) was added affording a light yellow suspension which was homogenised after sonicating in a water bath at 50 °C for 1 h. The solution underwent ten cycles of freezing in a mixture of liquid nitrogen and ethyl acetate and thawing (5 min in frozen solution + 5 min in a warm water bath + 5 min in 50-60°C water bath with high speed stirring) to ensure an equilibration between the trapped and bulk solutions. The multilamellar vesicles (MLV) were extruded eleven times through a polycarbonate filter (400 nm diameter) submerged in a warm water bath heated to around 30-40 °C. Then, 0.5 ml of liposome sample was diluted with 1.5 ml of an aqueous solution of NaCl 0.15 M. Finally 1 ml of this dilution was placed in the GPC column which has been previously homogenised with the same buffer (aqueous solution of NaCl 0.15 M).

5.6 Membrane Permeability Conclusions.

The membrane permeability behaviour of a range of differently charged complexes with diverse lipophilicities was studied. Liposomes were used as lipidic membrane mimics to assess whether the different dyes were membrane permeable and to determine their affinity for different parts of the vesicle, *i.e.* inner compartment and/or lipidic membrane. Among the variety of quenchers tried ($CoCl_2$, $CrCl_3$, $CuSO_4$, NaI, ascorbic acid and MV^{2+}) only MV^{2+} seems to be suitable to quench the luminescence of rhenium complexes.

The cationic and anionic lipophilic complexes, **2.9** and **3.19** respectively, behaved in a similar manner. An initial addition of quencher (MV^{2+}) decreased the emission intensity considerably, suggesting their affinity for the lipophilic lipidic membrane. Furthermore, examination of the luminescence properties over time suggests an important permeability gradient as the emission maxima shifted gradually towards the quencher emission (514 nm). On the other hand, the anionic and non-lipophilic complex **3.17** showed preferred its affinity for the inner compartment as initial additions of quencher did not affect the luminescence of the dye. In addition, the diffusion of the complex across the lipidic membrane is much slower than for **2.9** and **3.19**.

This study has demonstrated the possibility of tuning the membrane permeability properties of a luminescent rhenium complex of the type $[Re(bisim)(CO)_3L]$, either by a hydrocarbon chain in the axial ligand or by using a organic neutral chromophore as the bisimine ligand. This approach might be useful for design of future luminescent rhenium imaging probes.

5.7 Confocal Fluorescence Microscopy

Electronic imaging systems and imaging processing[16] have had a major impact on fluorescence microscopy due to the demand for better imaging technology with the ability to provide images with a three dimensional architecture. The limitation of ordinary fluorescence microscopy of 'slicing' the species into thin sections to be imaged, and thus the loss of the third dimension information has been overcome with the confocal fluorescence microscopy technique.

Confocal optics allow the operator to focus on a chosen plane in a thick specimen while rejecting the light that comes from the out-of-focus region, *i.e.* above and below that plane, thus imaging an optical section. From a series of optical sections taken at different depths of the imaged specimen, a virtual three dimensional image can then be constructed. This technique involves the illumination by a spotlight onto a single point of the sample, and hence pinpoint illumination is required, *i.e.* a laser. The incident light is aligned by a confocal pinhole orthogonal to the plane of the sample and detector, reflected through a dichroic mirror and focused by the objective lens. The fluorescence emitted from the sample is refocused by the objective lens and transmitted by the dichroic mirror before being collected in a detector though a pinhole. The light from the regions out of the plane of focus of the spotlight is also out of focus at the pinhole detector and thus rejected (see **Figure 5.26**).

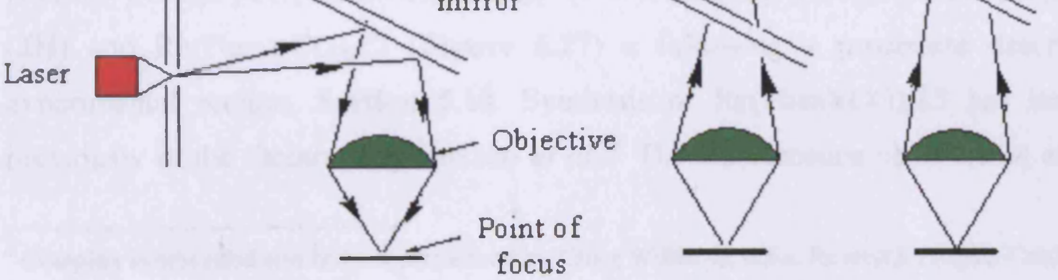

Figure 5.26. Simplified diagram of a basic arrangement of standard confocal fluorescence microscope.[17]

A: Fluorescent sample illuminated with a focused point of light from a pinhole.

B: Emitted fluorescent light from the in-focus point which reaches the pinhole at the detector.

C: Emitted fluorescent light from the out-of-focus point which is excluded from the pinhole at the detector.

As a result, confocal fluorescence microscopy is a powerful, high resolution technique in biological imaging and specific fluorescent staining techniques make it especially useful for diagnostic investigations of tissue samples.

5.8 Confocal Fluorescent Microscopy With Rhenium Complexes In Cells.

In order to test the viability of the species described previously in this thesis to be of use as imaging agents in cell microscopy, the ability of selected complexes to act as microscopy stains was tested, initially in *Spironucleous vortex* and then in yeast, *Saccharomyces Cerevisiae* (IFO 0233) cells and in *Human adenocarcinoma* cells (MCF-7).

5.8.1 Incubation with *Spironucleous vortens.*

Spironucleous vortens, a parasitic flagellate found in many species of fish,[18] was chosen in the first instance as it is known to be a prolific feeder and there was an expectation that the organisms would actively take up the complexes, avoiding any possible consideration about cell-specific issues of active transport. *Spironucleous vortens* suspension was incubated with the different complexes: **2.9**, **3.16**, **3.17**, $[Re(bipy)(CO)_3PyCH_2OCO(CH_2)_{12}CH_3]$[c] **(CW)**, $[Re(bipy)(CO)_3PyCH_2OCO(CH_2)_{16}CH_3]$[d] **(JH)** and $Re(Phen)(CO)_3Cl$ **(Figure 5.27)** a following a procedure described in the experimental section, **Section 5.10**. Synthesis of $Re(Phen)(CO)_3Cl$ has been reported previously in the literature by Itukazo *et al.*[19] The fluorescence observed in all cases was

---

[c] Complex synthesised and fully characterised by Craig Williams, B.Sc. Research Project, Cardiff University, 2006.

[d] Complex synthesised and fully characterised by Jacob B. Hess, B.Sc. Research Project, Cardiff University, 2007.

strongly associated with the cell fragments suggesting a successful fluorophore uptake and the viability of using complexes of the type $[Re(bisim)(CO)_3L]^{-/0/+}$ as cell fluorophores.

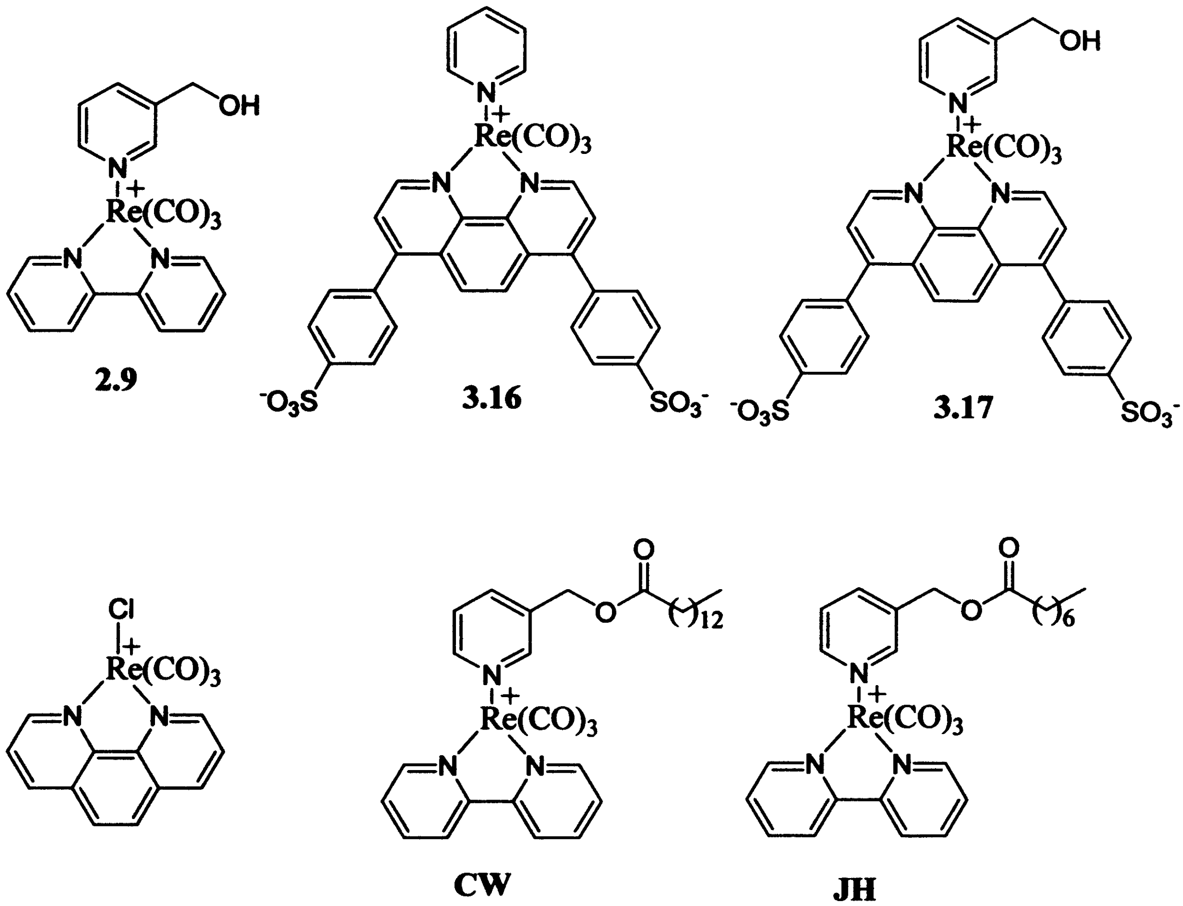

Figure 5.27. Chemical structures of complexes incubated with *Spironucleous vortens*.

The neutral complex, $Re(Phen)(CO)_3Cl$, showed accumulation in the cell domain but it was observed to be toxic, as the cells were immobile (*Spironucleous vortens* is a rapidly moving flagellate and when healthy is difficult to image due to rapid motion) and also to be rapidly photobleached. This photobleaching process cannot be associated with a photo-assisted hydrolysis of the complex, as it was demonstrated that the analogous aqua complex is highly emissive. Fortunately, no other complex appeared to suffer from photobleaching under the same conditions; therefore this undesirable process can be associated with the chloride placed in the axial position, which in the other complexes studied has been substituted by less labile pyridine derivatives.

The most lipophilic complexes **CW** and **JH**, which contain long hydrocarbon chains (C_{13} and C_{17} respectively), showed similar behaviour. Both of them were toxic at high concentrations (40 ml of a 2 mM solution incubated with 200 ml of cell suspension), apparently disrupting the membranes and leading to cell lysis (**Figure 5.28A**). The fluorescence, however, was strongly associated with cell fragments indicating that uptake had occurred. At lower concentrations (20 mL of a 2 mM solution) lysis was avoided and the complexes appeared to be associated with internal membranes partitioning cell compartments and with the constituents within organelles (**Figure 5.28B**).

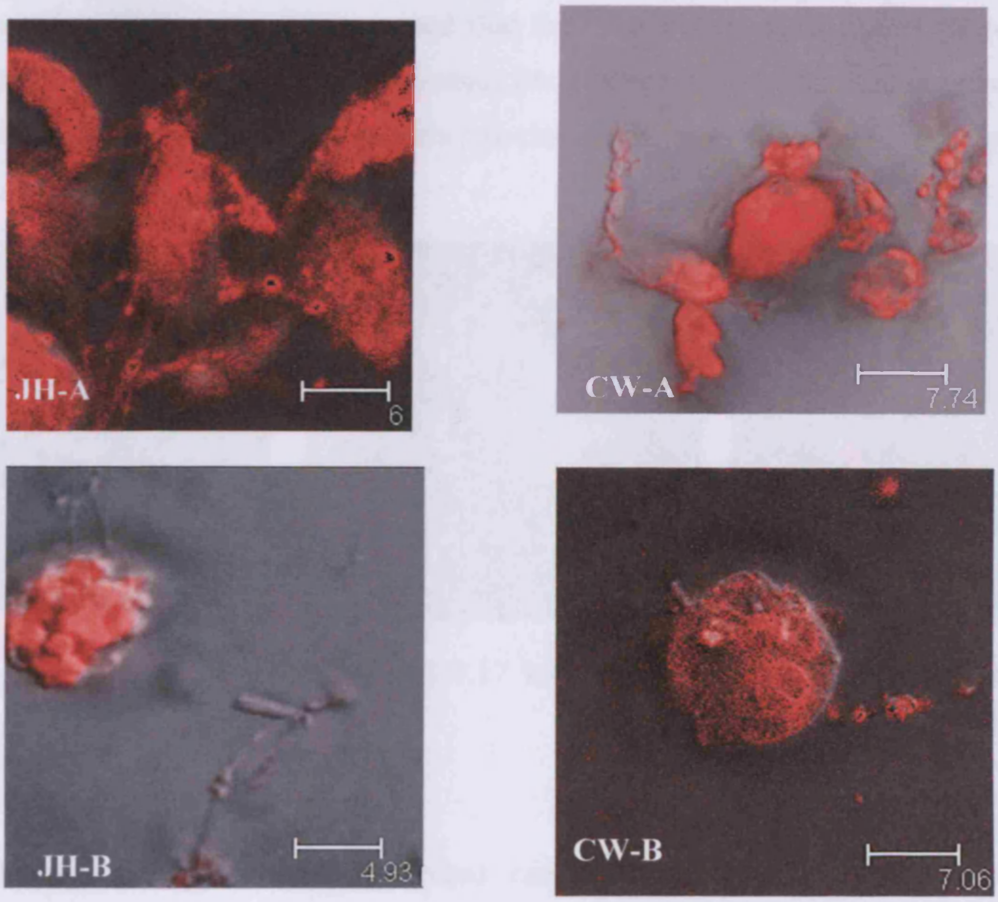

Figure 5.28. Top pictures: complexes **CW** and **JH** incubated with *Spironucleous vortens* at high concentrations. Bottom pictures: complexes **CW** and **JH** incubated with *Spironucleous vortens* at low concentrations (scale in μm).

[Re(bipy)(CO)$_3$PyCH$_2$OH], **2.9**, a simple example of a rhenium bisimine complex with no water solubilising groups, or lipophilic chains, showed accumulation in all the studied cells but it seemed to be more toxic by comparison with its sulphonate analogue, **3.17**, as the cells were dead after 2 hours. Although the images are poor (typical of a dead cell which is losing membrane potential and internal structure) it appears that this complex was localised in certain internal compartments. However, as *Spironucleous vortens* is a poorly characterised species, the nature of these compartments is not clear. The two sulphonated derivatives were the most successful imaging agents as, apart from accumulating in the cell, they were observed to be localized in certain cell domains, which appear to be digestive vacuoles forming during phagocytosis (see **Figure 5.29**). The main difference in properties observed between **3.16** and **3.17** is the toxicity index, as the cells stained with **3.17** were alive after 2 hours of experiment and consequently, moving in the incubation media. These results encouraged us to continue investigating the $[Re(bisim)(CO)_3L]^{-/0/+}$ complexes as possible cell imaging agents since these first applications of rhenium complexes in cell imaging demonstrated that they retain their luminescent properties in biological media and that there is no intrinsic toxicity associated with rhenium complexes. In addition, the observed toxicity of some species can be modulated by tuning the ligands in the complex.

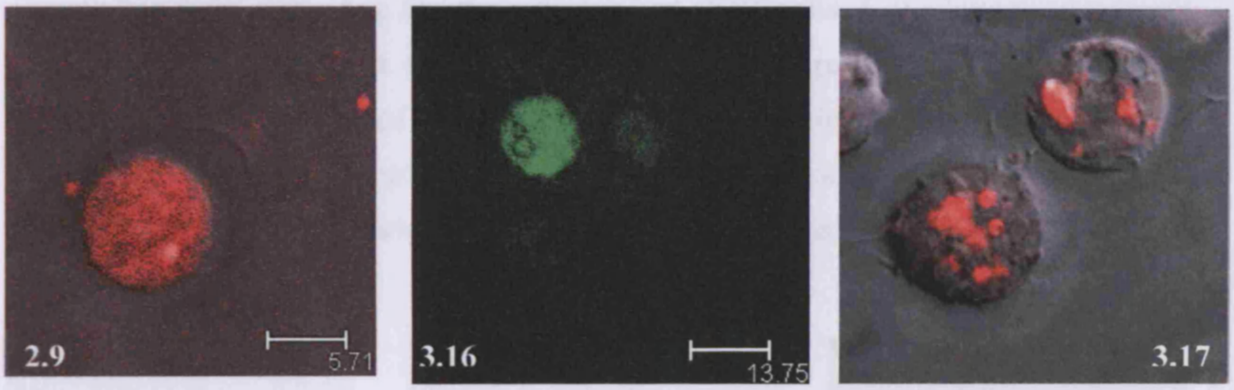

Figure 5.29. Complexes **2.9**, **3.16** and **3.17** incubated with *Spironucleous vortex* cells (scale in μm).

5.8.2 Incubation with human breast cancer cells, MCF-7 adenocarcinoma cells.

As the sulphonate derivatives **3.16** and **3.17** had shown not only accumulation in *Spironucleous vortens,* but also interesting localization and low toxicity, they were incubated with human breast cancer, MCF-7 adenocarcinoma cells, in a tentative experiment to test their behaviour in mammalian cells. In contrast to *Spironucleous vortens* which feeds by engulfing its environment, transport into mammalian cells is much more complex and must occur either by membrane permeation or by an active uptake mechanism (see **Chapter 1, Section 1.1.2**). In addition, species **2.9** and the lipophilic complex **CW** were also incubated with MCF-7 cells in order to allow a comparison between the patterns of uptake and localization of the complexes with different levels of lipophilicity. At this stage, given the lack of literature precedent for the application of rhenium complexes in cell imaging only very tentative predictions of uptake and localisation could be made, and thus the behaviour of all complexes was of interest.

The simplest rhenium complex **2.9** was taken up by the mammalian cells, with the entire population showing high levels of the luminescent species, **Figure 5.30**. As it is not expected that such complexes will be actively transported, it is possible that the lipophilicity, together with the cationic character of the species **2.9** could be the reason for its cell permeability, *i.e.* passive diffusion across the cell membrane due to a positive electrochemical gradient. In addition, the complex appears to be localised in certain organelles in the perimeter of the cytosol within the cell membrane. Apart from an intense luminescence from these specific domains, a slighter luminescence was observed surrounding them, indicating that the complex had also localised, at a lower concentration, in some other organelles in the cytoplasm. This staining pattern, like grains, could be indicative of an interaction of the dye with the endoplasmatic reticulum[e], which is spread throughout the cytoplasm surrounding the nucleus. No nucleus-staining appears to have occurred as seen by the dark centre to the cells (which have larger than usual nuclei, typical of carcinoma cells).

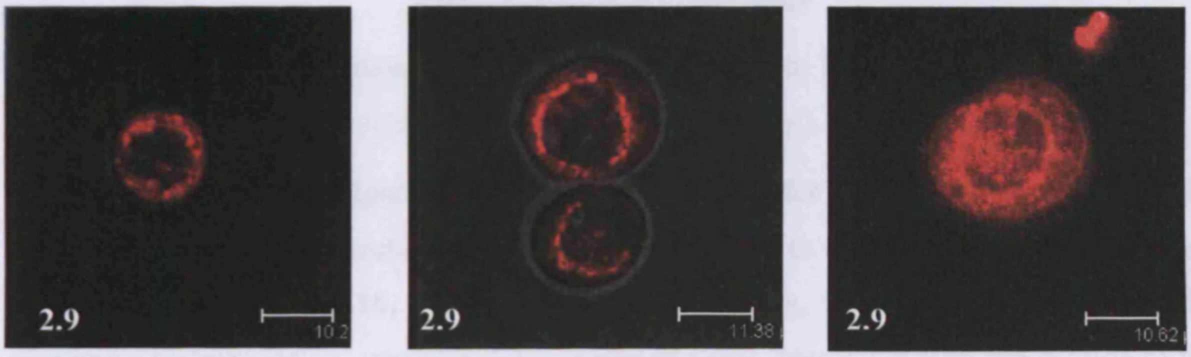

Figure 5.30. Rhenium complex **2.9** incubated with breast cancer cells (scale in μm)

The lipophilic cationic complex, **CW**, also shows accumulation in MCF-7 cells but contrary to its behaviour in *Spironucleous vortens* cells, did not disrupt the cell membrane as the MVF-7 cells appeared to be healthy, **Figure 5.31**. Again, the grainy luminescence observable in the cell could be indicative of localisation in the endoplasmatic reticulum, **Figure 5.32**. An interesting feature is that the cell nucleus seems to be stained as well, as shown by the absence of the dark ring in the centre, which might be explained in terms of the affinity of the anionic bases in the DNA for cationic species.

---

[e] ER is a labyrinthine, membrane bounded organelle.

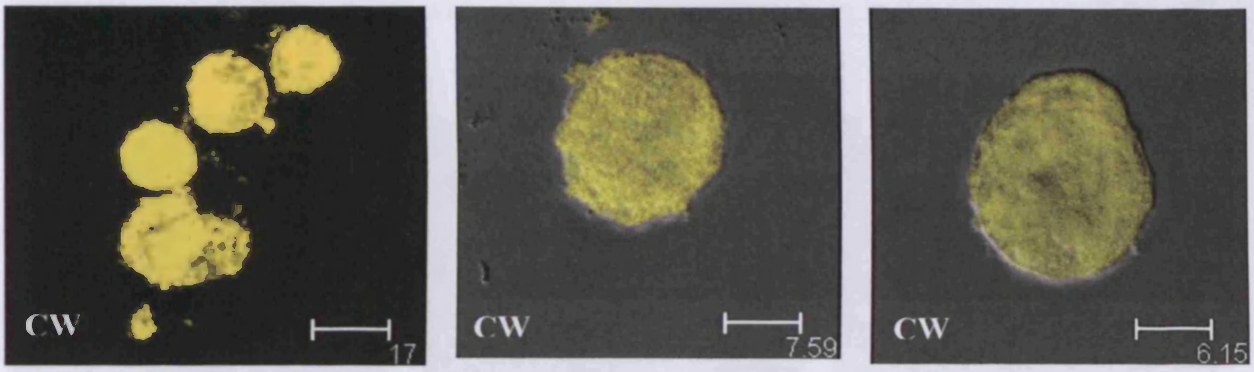

Figure 5.31. Complex **CW** incubated with breast cancer cells (scale in μm).

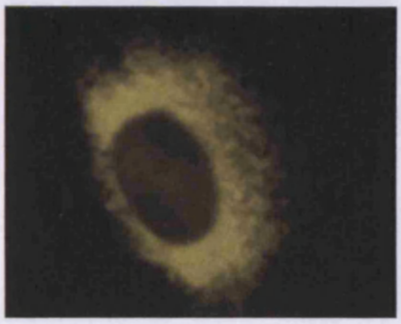

Figure 5.32. This is an image of endoplasmic reticulum in human cancer cells incubated with Calreticulin (note the large dark nucleus) published by Louie Naumovski *et al.*[20]

The two water soluble, sulphonated complexes, which differ in chemical structure only by a hydroxymethyl group, seem to behave very differently to each other in the presence of carcinoma cells. While **3.16,** the simple pyridine complex, was taken up by the cell, the analogous hydroxymethyl complex **3.17** exhibited some interaction with the outside of the cell membrane and no take up process was observed (see **Figure 5.33**). The species **3.16** was distributed throughout the whole cell, with a particularly high concentration in a specific organelle. Its membrane transport could have been mediated by protein channels, narrow hydrophobic pores in the cell membrane, as this kind of species, anionic and highly polar, should not show passive diffusion across the membrane against the potential gradient. On the contrary, species **3.17** seems to stain the outside of the cell, with a higher concentration near the cell membrane. It is likely that the anionic complexes interact with the positively charged choline[f] groups from the lipidic bilayer, allowing a clear definition of the shape of the cell. It is worth noting that, in addition to a strong luminescence arising from the surface of the cell membrane, there is an aureole of light, possibly provided by

---

[f] Phospholipid constitution in the cell membrane: (hydrophobic tail)$_2$--(polar head):(fatty acid)--(glycerol-phosphate-choline).

interactions of the anionic dye with positively charged residues in the glycocalyx,[g] the cell coat.

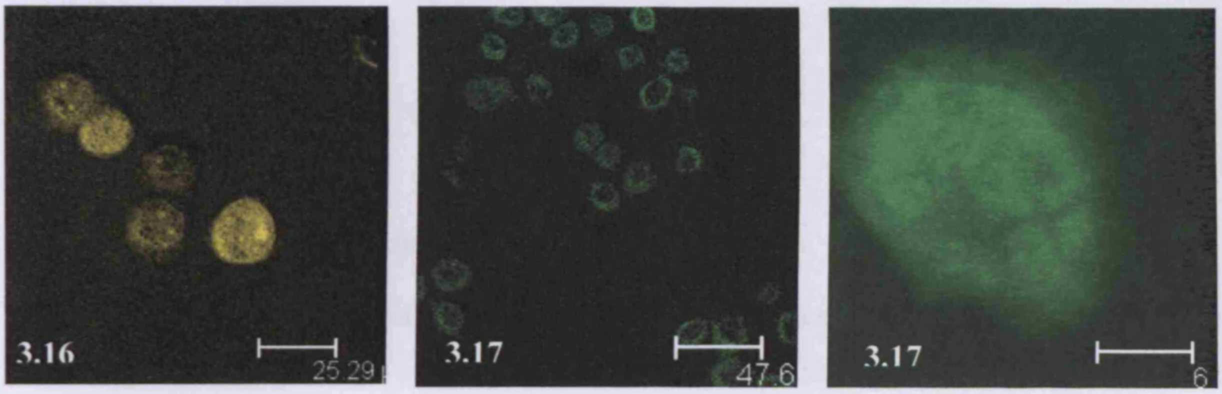

Figure 5.33. Complexes **3.16** and **3.17** incubated with human breast cancer cells (scale in μm).

5.8.3 Incubation with *Saccharomyces Cerevisiae* (IFO 0233) yeast cells.

Further studies were then carried out in order to elucidate which organelles were stained by each of the new dyes. Hence, *Saccharomyces Cerevisiae* (IFO 0233) yeast cells were chosen for the next investigation as this is a well known species, long studied by biologists and where localisation sites of the rhenium dyes within the cells might be identifiable with reference to the literature.

The complexes selected for this experiment were the water soluble sulphonated complexes **3.16** and **3.17,** the lipophilic complexes **CW** and **JH** (*vide supra* **Figure 5.27**) and also complex **4.1** (*vide infra* **Figure 5.34)** to test whether it has the same affinity for thiol-containing biomolecules in a genuine biological environment as was shown *in vitro* in **Chapter 4.**

---

[g] Glycocalyx describes the carbohydrate rich zone on the surface of the cell. They are oligosaccharide chains covalently bound to the membrane proteins (glycoproteins) and polysaccharide chains of the integral membrane proteoglycan molecules.

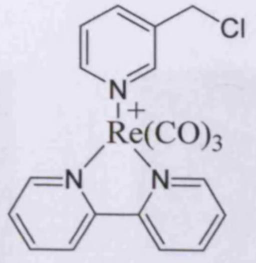

4.1

Figure 5.34. Chemical structure of complex **4.1.**

Examination of the incubated cells with the sulphonated complexes showed a very low percentage of the population had taken up any fluorophore at all; most of the cells showed no luminescence. Moreover, and even more surprisingly, only those cells that were in the budding phase appeared to be the ones that had taken up the fluorophores, suggesting that the sulphonated dyes were able to differentiate between the different stages in the cell life-cycle (**Figure 5.35**). Yeast has a rather substantial cell wall and it may be only at the stage of budding when the wall is weakened at the point of separation that the complex can enter the cells. Furthermore, no specific organelle localization was observed, as the stained cells seemed to have the dye within the entire cytoplasm, indicating that their polar hydrophilic nature makes them more attracted to cytosol (the polar, aqueous, intracellular fluid) than the more lipophilic membranes around many organelles.

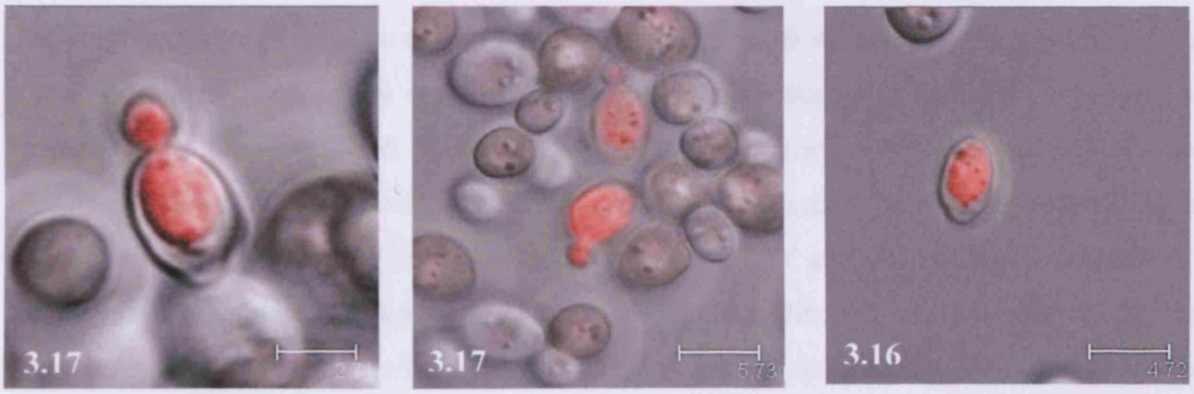

Figure 5.35. Complexes **3.16** and **3.17** incubated with yeast cells (scale in μm).

In the case of the highly lipophilic rhenium complexes **CW** and **JH**, again only a low percentage of cells took up the dye (again, presumably at the budding stage) but contrary to the sulphonated water soluble dyes, **CW** and **JH** seemed to differentiate between organelles and they are localized specifically in certain compartments with no general luminescence observed in the cytosol, **Figure 5.36**.

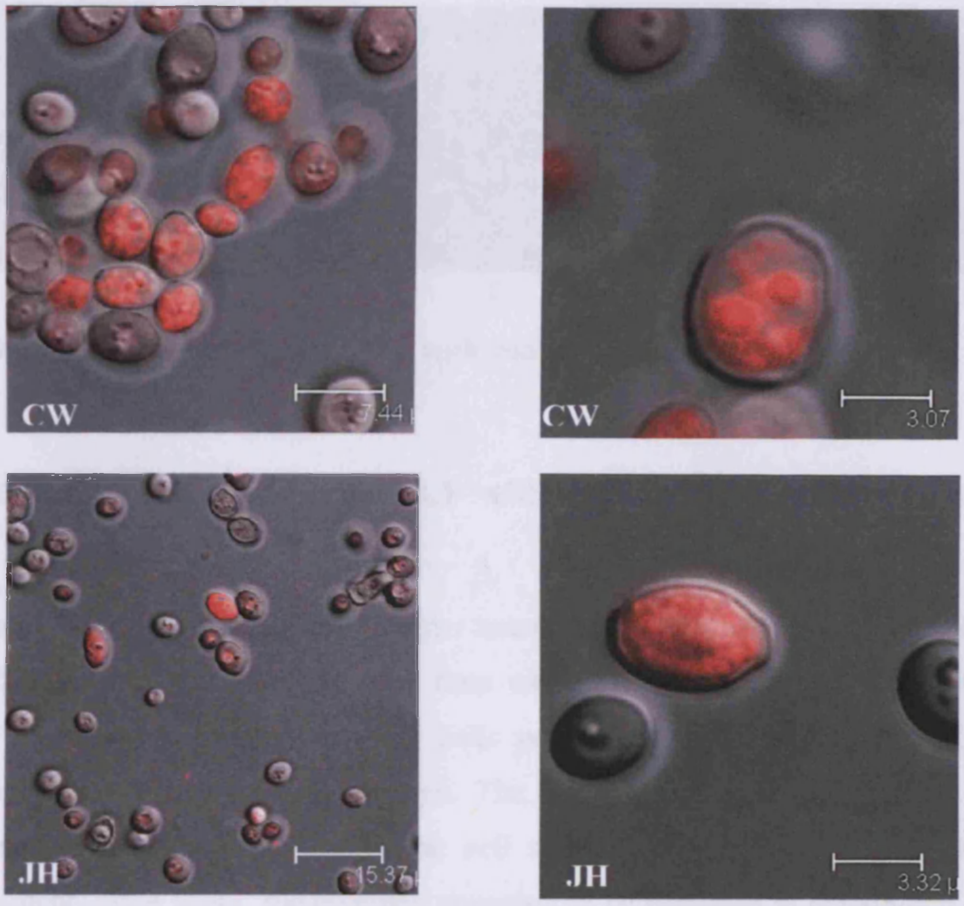

Figure 5.36. Top pictures: complex **CW** incubated with yeast cells. Bottom pictures: complex **JH** incubated with yeast cells (scale in μm).

The selectively thiol-reactive complex, **4.1**, appears to also stain the same kind of cells as in the previous cases, again only those in the budding stage. In addition, complex **4.1** seemed to become localized in some cell domains, mainly organelles near to the cell membrane (**Figure 5.37**). The pattern of localisation seemed to be more specific than the one observed in the case of the lipophilic complexes, **CW** and **JH**, where the domains in which they are localized appear to be more spread throughout the cell rather than concentrated close to the cell membrane. The domains close to the cell membrane are thought to be mitochondria as this is the known distribution of yeast mitochondria, and, moreover mitochondria bear a high concentration of thiol groups for which complex **4.1** has high affinity. Although these results appear to show that **4.1** is a mitochondrial selective agent, given the low level of uptake further proof was needed, and a cell line which does not have the rigid wall of yeast, such as mammalian cells was the next target.

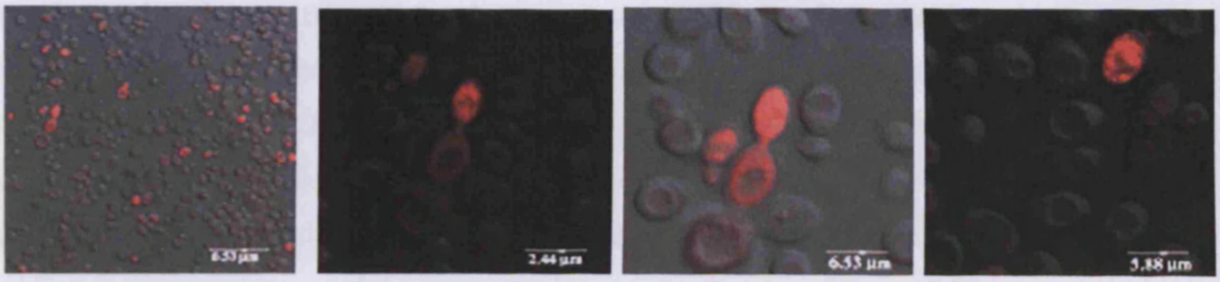

Figure 5.37. Complex **4.1** incubated with yeast cells.

5.8.4 Incubation of complex 4.1 with human breast cancer cells, MCF-7 adenocarcinoma cells.

Further studies were undertaken in order to confirm the assumption that complex **4.1** might specifically stain mitochondria, this time using human mammary adenocarcicoma cells (MCF-7),[21] which unlike the yeast cells possess a less rigid[22] cell wall, which may accelerate the permeation of the dye. The entire population took up the dye and no evidence of toxicity was seen as the cell membrane remained healthy throughout the experiment. Once again, the complex appeared to be localised in certain cell domains that were thought likely to be mitochondria due to their position close to the cell membrane, **Figure 5.38**. These images are somewhat similar to those obtained when the analogous hydroxyl complex was incubated with the mammary adenocarcinoma cells, *vide supra* **Figure 3.30** which was localised in some domains also close to the cell membrane. This similarity is discussed in detail below in **Section 5.8.6**.

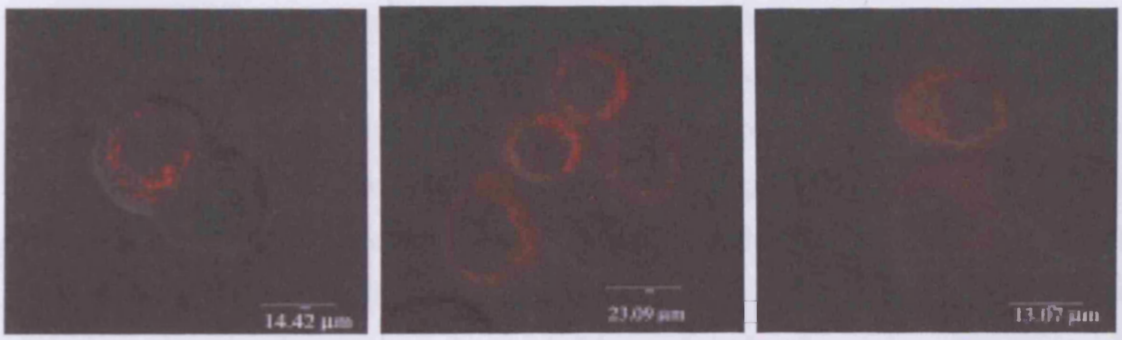

Figure 5.38. Complex **4.1** incubated with human mammary adenocarcinoma cells.

An additional experiment using a commercially available mitochondria-selective dye was performed in order to test the hypothesis that **4.1** was localising in mitochondria.

Tetramethylrhodamine ester (TMRE),[23] a well known specific mitochondrial probe, was incubated with human mammary adenocarcinoma MCF-7 cells under the same conditions as in the case of the rhenium complex **4.1**. Some of the images of the TMRE incubation obtained by confocal fluorescence microscopy are shown in **Figure 5.39.** These do not differ significantly in the shape of the organelle or in the distribution within the cell from pictures taken previously of the rhenium complex **4.1** incubated in the same type of cells, adding further evidence that **4.1** accumulates in mitochondria, **Figure 5.38.**

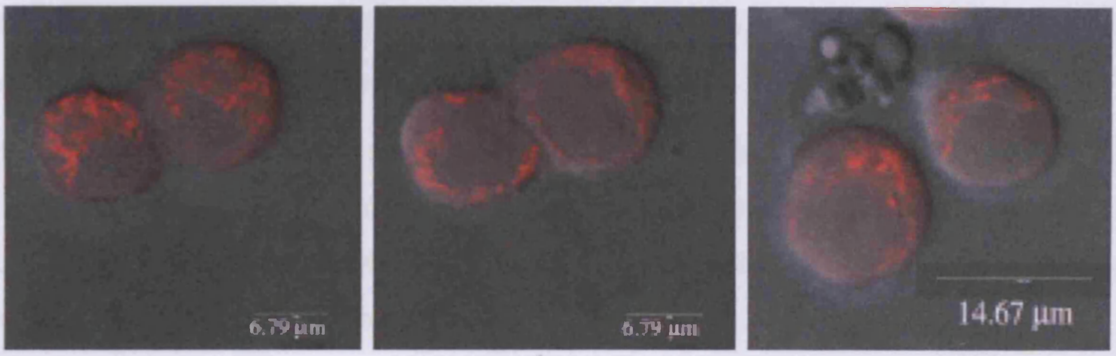

Figure 5.39. Images of TMRE incubated with human mammary adenocarcinoma cells.

5.8.5 Colocalisation experiment: Complex 4.1 and TMRE.

Finally, a co-localization experiment was carried out using the complex **4.1** and the mitochondrial selective dye TMRE as a co-imaging agent. Co-localisation is a technique in which two imaging agents with different emission wavelengths are applied to the same cells simultaneously. Two different images of the emission (and thus localisation) are then recorded first at one wavelength, and then at the other. If the agents have localised in the same organelles then the two images overlap, and the colouring of the overlapped image gives a visual measure of the degree to which the agents localise in the same areas. However, the similar emission properties of the fluorophores ($\lambda em_{max(4.1)}$ = 551nm and $\lambda em_{max(TMRE)}$ = 588 nm) makes it impossible to distinguish their localisation patterns by emission; therefore a different excitation wavelength was used to perform the two measurements ($\lambda exc_{max(4.1)}$ is 364 nm and $\lambda exc_{max(TMRE)}$ is 555 nm). Using a 405 nm laser excitation, emission from **4.1** is observed, **Figure 5.40A**, whereas on excitation at 543 nm only TMRE emission is observed, **Figure 5.40B**. By superposition of both images obtained by confocal microscopy, **Figure 5.40C**, it is clear that both dyes are being localised in the same organelles and thus as TMRE is a selective mitochondrial stain this co-localisation experiment provides final proof that demonstrates that the novel rhenium complex, **4.1**, is also a selective mitochondria fluorescent probe.

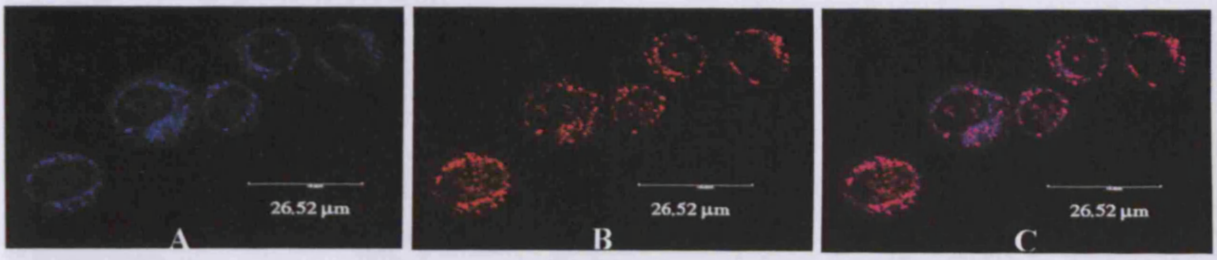

Figure 5.40. Complex **4.1** and TMRE co-localization experiment: **A** exciting at 405 nm, **B** exciting at 543 nm, and **C** superimposed picture.

Figure 5.41A and **B**. show a closer view of both dyes in the same cell making it obvious, at least by eye, how the two dyes are located in the same areas. Even clearer is the cross section shown in **Figure 5.41C,** where it can be seen that the intensities of both dyes are essentially the same along the cell.

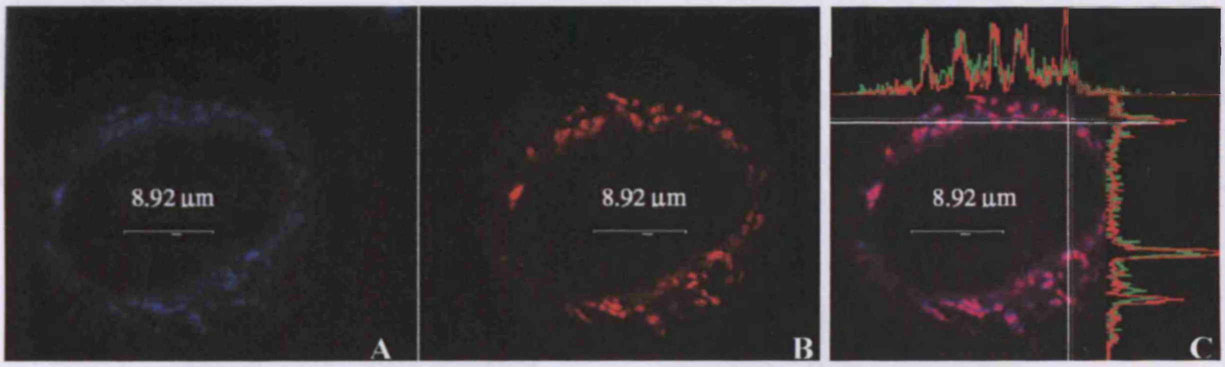

Figure 5.41. Colocalisation of **4.1** and TMRE in MCF-7 close up and cross section.

These results can be also interpreted in a negative way: since the examples seen so far showed the same fluorescent pattern in the cell, it can be thought that the experiment was flawed and cannot differentiate between the two fluorophores. However, by comparison of **Figure 5.42A** and **Figure 5.42B,** another snapshot from the cell population, where the excitation wavelength used was 405 and 544 nm respectively, a different emission pattern is shown, which is confirmed by the superimposition of the two pictures, **Figure 5.42C.** In this case, for a reason that is not known, one cell from the entire population has taken up only **4.1** and not TMRE. We do not know why this cell chose to take up only **4.1**, but by doing so it has validated the experiment, proving that the different excitation technique can differentiate between the two agents. Therefore the technique is validated and it can be assured that the novel complex [Re(bipy)(CO)$_3$PyCH$_2$Cl]PF$_6$ represents the first example of a mitochondrion selective transition metal complex, showing the same localisation as TMRE, but with a large Stokes shift and longer lifetime, which indicates a promising future for ^{3}MLCT biological imaging agents.

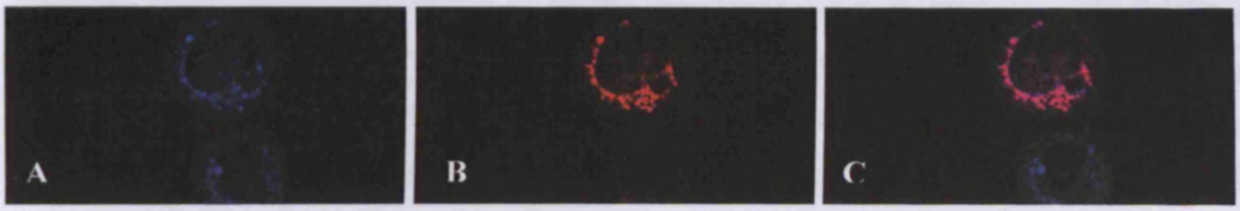

Figure 5.42. Colocalisation of **4.1** and TMRE in MCF-7 showing single uptake in one (bottom) cell.

5.8.6 Comparison between the rhenium complexes 4.1 and 2.9.

Having demonstrated that complex **4.1** is a specific mitochondria marker, it was thought that complex **2.9** would exhibit the same behaviour due to the similar images obtained when it was incubated with human breast cancer cells. However, on closer examination of the images, complex **4.1** (**Figure 5.43** left picture) stains the cell only in some domains specifically (mitochondria) whereas the staining observed by complex **2.9** (**Figure 5.44** right picture) is more spread out through the cytoplasm.

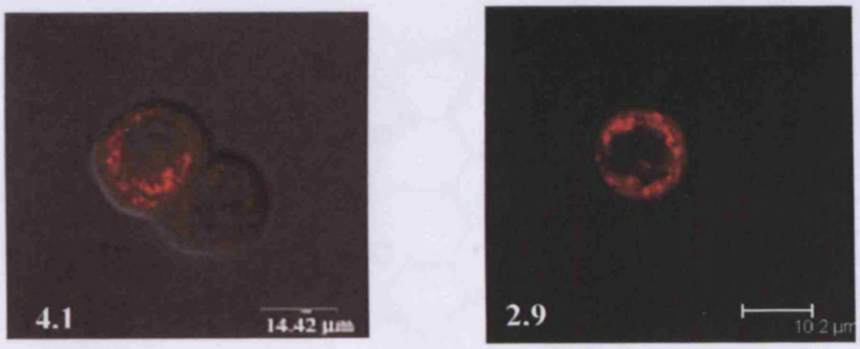

Figure 5.43. Left picture: complex **4.1** incubated with MCF-7. Right picture complex **2.9** incubated with MCF-7.

As both complexes **2.9** and **4.1** are cationic lipophilic species, they should have similar take up and localisation behaviour. Thus, both will be taken up by the cell as they are able to enter by passive diffusion due to their lipophilicity, and, being cationic, to concentrate in the cell due to the potential gradient. Additionally, they will then be further concentrated in the mitochondria which has a greater potential gradient than the remaining cell, and its own membrane, therefore attracting cationic-lipophilic species. However, as the species

4.1 contains a sulfhydryl reactive group (chloromethyl), once inside the mitochondria there is the possibility that it can undergo a chemical reaction with the high concentration of thiols inside the mitochondria, thus preventing the luminescent species from leaving the mitochondria. On the other hand, complex **2.9** does not react with any of the mitochondrial components and therefore it can cross the membrane again to leave the mitochondria. Thus, while **4.1** will become completely localised in the mitochondria as it is chemically bonded there (*i.e.* becomes membrane impermeable), **2.9** will show a higher concentration in mitochondria than in other organelles due to the higher potential gradient, but will be distributed throughout lipophilic units of the cell as it remains membrane permeable. Although this explanation cannot be considered as a scientific probe, it can be used as an initial step for further investigations.

5.8.7 Incubation of complex 3.10 with human breast cancer cells, MCF-7 adenocarcinoma cells.

Although complex **3.10** was not designed to have any substituents sensitive to a biological group and its molecular weight is over 1000 kDa, which implies the necessity of an active transport to cross the cell membrane, its ability as a cell imaging probe was tested (**Figure 5.44**).

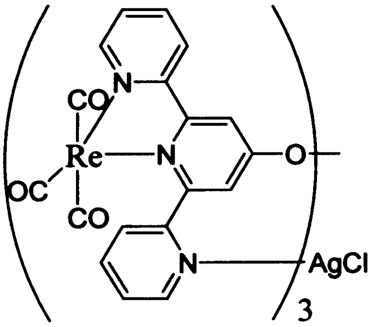

3.10

Figure 5.44. Chemical structure of complex **3.10.**

Complex **3.10** was incubated with human breast cancer cells, MCF-7 adenocarcinoma cells. Not only was the lipophilic cationic species able to cross the cell membrane, but also has affinity for a specific organelle thought to be inside the nuclei, **Figure 5.45**. This preliminary result showed that the dye was taken up by all the cell population getting spread throughout the cytoplasm and the nuclei. In addition, a higher dye concentration is observed in some domains within the nucleus which could be the nucleolus[h]. This initial assumption needs to be studied in more detail in order to draw any conclusions. Therefore, an extensive study of this fascinating complex will be carried out in future to assay its suitability as a chemical sensor and/or cell imaging probe.

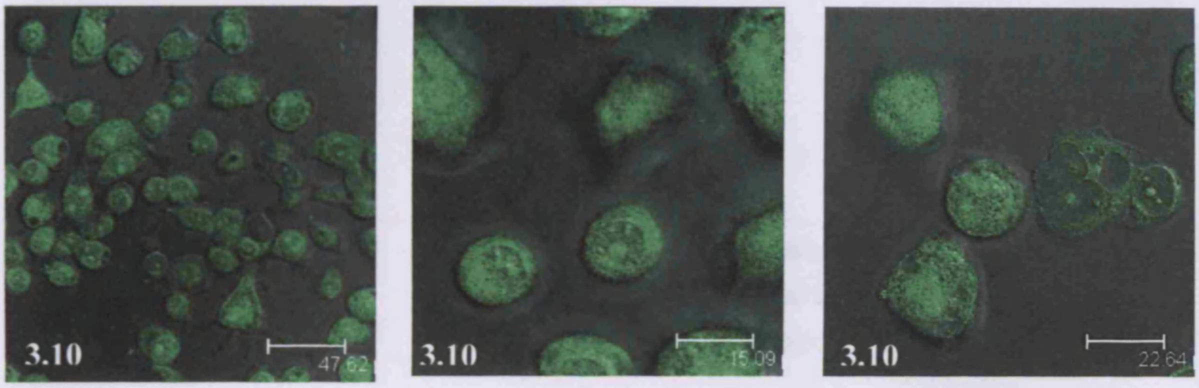

Figure 5.45. Species **3.10** incubated with MCF-7 (scale in µm).

5.9 Confocal Microscopy Conclusions.

Preliminary studies to assess the viability of a variety of differently charged complexes, and with diverse lipophilicities, as possible luminescent cell imaging probes were performed. The selected complexes (**2.9**, **4.1**, **3.10**, **3.16**, **3.17**, **CW**, **JH** and [Re(Phen)$(CO)_3$Cl]) were incubated with different cells (*Spironucleous vortens, Saccharomyces Cerevisiae*-(IFO 0233) yeast cells and human breast cancer cells (MCF-7)-adenocarcinoma cells) giving evidence for the possibility of using rhenium metal complexes as specific cell imaging agents. A summary of the results is shown in **Table 5.3**.

---

[h] Structure in the nucleus where the ribosomal RNA is transcribed and ribosomal subunits are assembled.

	Spironucleous vortens	Yeast cells	Adenocarcinoma cells
2.9	L: certain internal compartments T: more toxic than the sulphonated analogues	--	L: high intensity from certain domains close to the cell membrane, possibly mitochondria and with lower intensity form other organelles in the cytosol, possibly endoplasmatic reticulum
4.1	--	TU: presumably only cells in budding phase L: mitochondria	L: mitochondria
3.10	--	--	L: spread throughout the cytoplasm and the nuclei and with higher concentration in probably the nucleolus
3.16	L: maybe digestive vacuoles occurring during phagocytosis T: more toxic than 3.17	TU: presumably only cells in budding phase L: entire cytoplasm	L: throughout the whole cell, and with a particularly high concentration in a specific organelle.
3.17	L: maybe digestive vacuoles occurring during phagocytosis T: less toxic than 3.16	TU: Presumably only cells in budding phase. L: entire cytoplasm	L: in the outside of the cell, with a higher concentration near the cell membrane.
CW	L: internal membranes and constituents within organelles at low concentration* T: cell lysis at high concentration**	TU: presumably only cells in budding phase L: certain organelles, no cytosol	L: organelles along the cytosol possibly to endoplasmatic reticulum including nucleus
JH	L: internal membranes and constituents within organelles at low concentration* T: cell lysis at high concentration**	TU: presumably only cells in budding phase L: certain organelles, no cytosol	--

L: localization, T: toxicity, TU: taken up, **40 or *20 ml of 2 mM [Re] with 200 ml of cell suspension.

Table 5.3. Summary of cell image results.

5.10 Cell Culture And Imaging.[i]

Spironucleous vortens incubation with 2.9, 3.16, 3.17, CW, JH, RePhen(CO)$_3$Cl. Live cells were harvested by centrifugation, incubated with solutions of each complex in DMSO for 2 h (typically 10–40 ml of a 0.5 mM solution of fluorophore incubated with 200 ml of cell suspension) before being washed in buffer (PBS, pH 7.2) and mounted in methylcellulose to restrict movement. Preparations were viewed using a Leica TCS SP2 AOBS Confocal Scanning Laser Microscope using a ×63 or ×100 objective with excitation at 405 nm and detection at 520-570 nm.

Yeast cell incubation with 2.9, 3.16, 3.17, CW, JH, 4.1. *Saccharomyces cerevisiae* IFO 0233 cells were harvested by centrifugation (1000 g, 3 min), washed twice in phosphate buffer saline (PBS, pH 7.4) before being resuspended in PBS, incubated with the different complexes (final concentration 100 μgml^{-1}) for 30 min. in 0.3 % yeast extract, 1 % peptone, 1 % glucose, rinsed in PBS (×3) and mounted on a slide. Preparations were viewed as above by confocal microscopy.

Human cell incubation with 2.9, 3.10, 3.16, 3.17, CW, 4.1. Human mammary adenocarcinoma cells (MCF-7)[7], obtained from the European Collection of Cell Cultures (Porton Down, Wiltshire, UK) were maintained as adherent cultures in Eagle's Minimum Essential Medium supplemented with 10 % foetal bovine serum, penicillin and streptomycin. Cells were detached from the plastic flask using trypsin and EDTA and were suspended in an excess volume of growth medium. While suspended in this medium, cells were incubated with the luminescent species (final concentration 100 μg. ml^{-1}) on ice for 30 min. Cells were then thrice washed in PBS, harvested by centrifugation (3 min, 3.190 g) before being mounted on a slide and viewed as above by confocal microscopy.

Human cell incubation with TMRE. MCF-7 adenocarcinoma cells were harvested as indicated above, resuspended in EMEM culture medium and incubated with TMRE (final concentration 20 nM) for 2 h at room temperature before being thrice washed in PBS, mounted and viewed as above by confocal microscopy

---

[i] Cell culture and imaging experiments carried out by Coralie Millet, postgraduate student in the School of Bioscience at Cardiff University under the supervision of Prof. David Lloyd.

5.11 Experimental.[j]

Pyridine-3-methyleneoxyoctanoate (JHa)

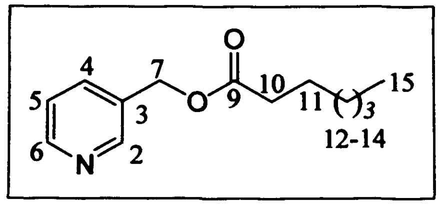

3-Hydroxymethyl pyridine (0.70 ml, 7.2 mmol) was dissolved in DCM (25 ml); subsequently octanoyl chloride (1.12 ml, 6 mmol) was added dropwise. The reaction mixture was then stirred for 3 hours, extracted with sodium bicarbonate solution (sat. aq., 3×10 ml) and dried over MgSO$_4$. The solvent was removed in vacuo to leave **JHa** (0.90 g, 3.83 mmol, 53.23 %) as a colourless oil.[24]

***Fac*-[Re(bipy)(CO)$_3$Py-3-CH$_2$O$_2$C(CH$_2$)$_6$CH$_3$] (JH)**

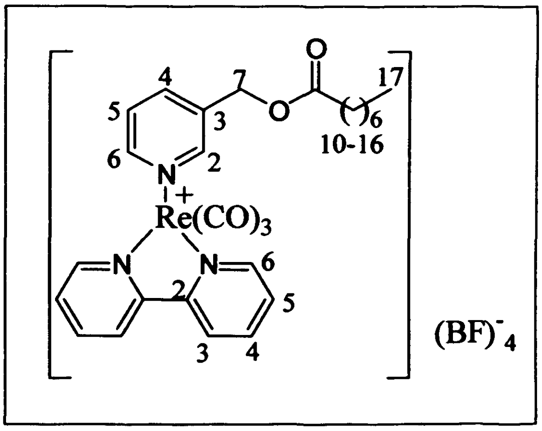

[Re(bipy)(CO)$_3$CH$_3$CN](BF$_4$) (0.080 g, 0.14 mmol), and **JHa** (0.075 g, 0.42 mmol) were dissolved in tetrahydrofuran (20 ml) and heated at 50 °C for 20 hours. The resultant solution was subsequently filtered through Celite prior to the removal of the solvent in vacuo to afford **JH** as a bright yellow solid. δH (CDCl$_3$): 9.02 (2H, d, J = 4.7 Hz, C*H*(6,6') bipy); 8.29 (3H, m, C*H*(2) Py and C*H*(3, 3') bipy), 7.90 (1H, d, J = 8.0 Hz, C*H*(6) Py), 7.69 (3H, m, C*H*(4) Py, C*H*(5) bipy), 7.34 (1H, m, C*H*(5) Py), 4.91 (2H, s, PyC*H*$_2$), 2.24 (2H, m, COC*H*$_2$), 1.25 (10 H, br s, C*H*$_2$), 0.81 (m, 3H, C*H*$_3$); δC (CDCl$_3$): 195.8 173.6, 156.1, 153.2, 151.9, 151.3, 142.1, 140.0, 136.1, 129.4, 127.5, 126.1, 62.4, 34.3, 32.0, 29.4, 29.2, 25.1, 22.9, 14.4 br; ν_{max} (Nujol) 2032, 1917, 1739, (CO) *m/z* (ESI) 660.2 [M-BF4]$^+$; theoretical isotope pattern 660.2 (58%), 661.2 (19%), 662.2 (100%), 663.2 (32%), 664.2 (6%), observed isotope pattern 660.3 (56%), 661.3 (18%), 662.3 (100%), 663.3 (30%), 664.3 (6%); HRMS (ESI) [M-BF$_4$]$^+$ calculated 660.1631 observed 660.1628.

---

[j] Complexes synthesised and fully characterised by Craig Williams (CW) and Jacob B. Hess (JH), B.Sc. Research Projects, Cardiff University, 2006 and 2007 respectively.

Pyridinemethylene-3-oxystearate (CWa)

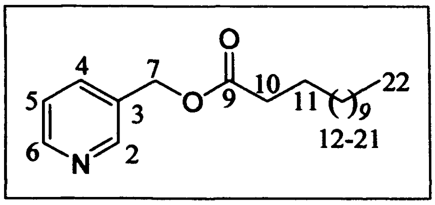

EDCI (2.2 g, 11 mmol) and DMAP (268 mg, 2.2 mmol) were dissolved in DCM (15 ml). To this mixture was added a solution of myristic acid (1.37 g, 6 mmol) in DCM (25 ml) at 0 °C. 15 minutes subsequent to the initial mixing, a solution of 3-hydroxymethyl pyridine (0.55 cm^3, 6 mmol) in DCM (10 ml) was added. The reaction mixture was then left at room temperature for 15 hours with continual stirring. Saturated NH_4Cl (25 ml) was then combined with the reaction mixture and the resultant aqueous layer was extracted with diethyl ether (4 × 25 ml) the organic layer was dried with $MgSO_4$ and concentrated in vacuo. The remaining mixture was purified using column chromatography (40-60 petroleum ether: ethyl acetate, 1:1) to yield compound **CWa** (1.18 g, 68 %) as a white crystalline solid.[25]

Fac-[Re(bipy)(CO)$_3$Py-3-CH$_2$O$_2$C(CH$_2$)$_{12}$CH$_3$] (CW)

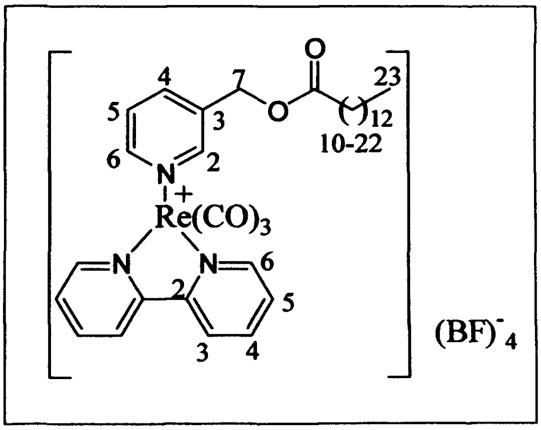

[Re(bipy)(CO)$_3$CH$_3$CN](BF$_4$) (0.161 g, 0.29 mmol) and **CWa** (0.092 g, 0.29 mmol) were dissolved in THF (20 ml) and heated at 50°C for 20 hours. The resultant solution was subsequently filtered through Celite and the product precipitated by the addition of petroleum ether to give **CW** as a bright yellow solid (0.156 g, 64 %), m.p. 123-125 °C. δH (CDCl$_3$): 9.03 (2H, d, *J* = 5.5 Hz, C*H*(6) bipy). 8.65 (2H, d, *J* = 8.0 Hz, C*H*(*3*) bipy), 8.26 (3H, m, C*H*(2) Py, C*H*(*4*) bipy), 7.89 (1H, d, *J* = 7.0 Hz, C*H*(6) Py), 7.71 (3H, m, C*H*(4) Py, C*H*(5) bipy), 7.33 (1H, dd *J* = 7.5, 2.0 Hz C*H*(5) Py), 4.95 (2H, s, PyC*H*$_2$), 2.24 (2H, t, *J* = 7.5 Hz, COC*H*$_2$), 1.22 (20 H, br s 10 × C*H*$_2$), 0.82 (3H, t, *J* = 3.5 Hz, C*H*$_3$); δC (CDCl$_3$) 174.2, 156.6,. 153.3, 151.8, 151.2, 142.5, 139.9, 137.3, 129.3, 127.6, 126.4, 52.4, 34.3, 32.3, multiple peaks 30.1-29.4, 25.2, 23.1, 14.5; ν_{max} (Nujol) 2037, 1938 br, *m/z* (ESI) 746.3 [M-BF$_4$]$^+$ theoretical isotope pattern 744.3 (60%) 746.3 (100%) 747.3 (40 %) 748.3 (10%), observed isotope pattern 744.3 (60%) 746.3 (100%) 747.3 (40 %) 748.3 (10%); HRMS (ESI) [M-BF4]$^+$ calculated mass 744.2570 observed 744.2567.

5.12 References.

[1] T. Bücher, M. Klingenberg, *Angew. Chem.*, **1958**, 70, 552.

[2] F. Q. Schafer, G. R. Buettner, *Free Radical Bio. Med.*, **2001**, 30, 1191.

[3] A. J. Bard, L. R. Faulkner (Eds.), *Electrochemical Methods: Methods And Applications*, 2nd ed., John Wiley & Sons Inc., New York, **2001**.

[4] J. V. Caspar, B. P. Sullivan, T. J. Meyer, *Inorg. Chem.*, **1984**, 23, 2104.

[5] E. Ioachim, E. A. Medlycott, G. S. Hanan, *Inorg. Chim. Acta*, **2006**, 359, 2599.

[6] R. Díaz, A. Francois, A. M. Leiva, B. Loeb, E. Norambuena, M. Yañez, *Helv. Chim. Acta*, **2006**, 89, 1220.

[7] A. Juris, S. Campagna, I. Bidd, J. M. Lehn, R. Ziessel, *Inorg Chem.*, **1988**, 27, 4007.

[8] M. B. Robin, P. Day, *Adv. Inorg. Chem. Radiochem.*, **1967**, 10, 247.

[9] H. Hartmann, W. Kaim, I. Hartenbach, T. Schleid, M. Wanner, J. Fiedler, *Angew. Chem. Int. Ed.*, **2001**, 40, 2842.

[10] D. E Richardson, H. Taube, *Coord. Chem. Rev.*, **1984**, 60, 107.

[11] M. J. Hope, M. B. Bally, G. Webb, P. R. Cullis, *Biochim. Biophys. Acta*, **1985**, 812, 55.

[12] R. C. MacDonald, R. I. MacDonald, B. Ph. M. Menco, K. Takeshita, N. K. Subbarao, L.-R. Hu, *Biochim. Biophys. Acta*, **1991**, 1061, 297.

[13] V. Ramamurthy, K. S. Schanze (Eds.), *Organic and Inorganic Photochemistry*, Vol 2, Marcel Dekker, New York, **1998**.

[14]M. Z. Hoffman, F. Bolletta, L. Moggi, Go. L. Hug, *J. Phys. Chem. Reference Data*, **1989**, 18, 219.

[15] J. C. Luong, L. Nadjo, M. S. Wrighton, *J. Am. Chem. Soc*, **1978**, 100, 5790.

[16] R. D. Allen, *Ann. Rev. Biophys. Chem.*, **1985**, 14, 265.

[17] B. B. A. Dennis, L. Julian, R. Marin, R. Keith, D. W. James (Eds.), *Molecular Biology Of The Cell*, Garland, 3rd ed., New York, 1994.

[18] S. L. Poynton, W. Fraser, R. Francis-Floyd, P. Rutledge, P. Reed, T. A. Nerad, J. Eukaryot, *Microbiol.*, **1995**, 42, 731.

[19] M. K. Itokazu, A. S. Polo, D. L. A. de Faria, C. A. Bignozzi, N. Y. M. Iha, *Inorg. Chim. Acta*, **2001**, 313, 149.

[20] H. M. Lui, J. Chen, L. Wang, L. Naumovski, *Mol. Cancer Res.*, **2003**, 1, 508.

[21] H. D. Soule, J. Vázquez, A. Long, S. Albert, M. Brennan, *J. Nat. Cancer Inst.*, **1973**, 51, 1409.

[22] D. H. Northcote, R. W. Horne, *Biochem. J.,* **1952**, 232.

[23] A) A. Macho, D. Decaudin, M. Castedo, T. Hirsch, S. A. Susin, N. Zamzami, G. Kroemer, *Cytometry,* **1996**, 25, 333; B) R. P. Haugland (Ed.), *A Guide to Fluorescent Probes and Labelling Technologies*, 10th ed., Molecular Probes, Eugene, **2005**.

[24] S. Yang, P. Minkler, C. Hoppel, K.-Y. Tserng, *J. Am. Soc. Mass Spec.,* **2006**, 17, 1620.

[25] L. J. Deterding, M. L. Gross, *Org. Mass Spectrom.,* **1998**, 23, 169.